Nonlinear Dynamics of an Airfoil Forced to Oscillate in Dynamic Stall

John Peter Keleris

Department of Mechanical Engineering

McGill University

Montréal, Canada

March, 1994

Thesis submitted to the Faculty of Graduate Studies and Research in partial fulfilment of the requirements for the degree of Master of Engineering

ABSTRACT

The aeroelastic system studied in this thesis is a rigid NACA 0012 airfoil flexibly suspended in a subsonic flow and forced to oscillate at high angles of attack. In this thesis, a qualitative analysis of the chaotic behaviour caused by the nonlinear aerodynamic forces of dynamic stall is presented.

A semi-empirical numerical model of dynamic stall is utilized to predict the nonlinear aeroelastic forces due to the pitch motion of the airfoil and the aerodynamic forces due to the plunge motion are superimposed using linear aeroelastic theory. The structural forces are modelled using linear torsional and translational springs and the structural damping is neglected.

Four different types of chaotic behaviour are presented for the single degree of freedom (pitch) system. The first two cases show that, under certain conditions, marginally stable periodic attractors and chaotic attractors can exist simultaneously. In the third case, the amplitude of the forcing function is increased and the system is shown to undergo a series of period doubling bifurcations enroute to chaos. The fourth case shows that chaotic vibrations at relatively high forcing frequencies may cause divergent oscillations.

The analysis of the two degree of freedom (pitch and plunge) system is limited to studying the effect of small amplitude plunge oscillations on the stability of two of the aforementioned single degree of freedom cases. The analysis shows that the stability of the system is very sensitive to changes in the ratio of the natural frequencies of the system.

too faint!

SOMMAIRE

Le système aéroélastique étudié dans cette thèse est un profil rigide NACA 0012 placé dans un écoulement subsonique et soumis à des oscillations forcées à des angles d'attaque élevés. Dans cette thèse, une analyse qualitative du comportement chaotique provoqué par les forces aérodynamiques nonlinéaires dues au décrochage dynamique est présentée.

Un modèle numérique semi-empirique du décrochage aérodynamique est utilisé pour prédire les forces aéroelastiques nonlinéaires dues à la rotation du profil, et les forces aérodynamiques dues à la translation y sont ajoutées en utilisant la théorie aéroélastique linéaire. Les forces structurales sout modélisées par des ressorts linéaires en torsion et en translation et l'amortissement dû à la structure est négligé.

Quatre types de comportement chaotique différents sont mis en évidence pour le système à un degré de liberté (en rotation). Les deux premiers cas montrent que sous certaines conditions, des attracteurs périodiques marginalement stables et des attracteurs chaotiques peuvent coexister. Dans le troisième cas où l'amplitude des pulsations forcées est plus grande, on démontre que le système suit une série de bifurcations de doublement de période, qui conduit au chaos. Le quatrième cas montre que les vibrations chaotiques à des fréquences forcées relativement élevées peuvent causer des oscillations divergentes.

L'analyse du système à deux degrés de liberté (translation et rotation) est limitée à l'étude des effets des oscillations en translation de faible amplitude sur la stabilité de deux des cas à un degré de liberté précédemment cités. L'analyse montre que la stabilité du système est intimement liée aux changements du rapport des fréquences naturelles du système.

ACKNOWLEDGEMENTS

The author would like to express his gratitude to Professor S.J. Price for his encouragement and guidance in the research and writing of this thesis. Also, the author would like to express his gratitude to his parents, Ray and Ulda Keleris, and grandparents, John and Ieva Kere, for years of encouragement and support.

Contents

List of Figures

Nomenclature

A	Pitch rate in radians per non-dimensional time
a_h	Non-dimensional distance from the mid-chord to the elastic axis
A_{DM}	Pitch rate at the instant of dynamic stall
a_{OL}	Static lift curve slope
a_{OM}	Static moment curve slope
α	Airfoil angle of attack
α_o	Initial angle of attack
$\bar{\alpha}$	Amplitude of the oscillation in pitch
α_{DM}	Dynamic stall angle of attack
α_E	Effective angle of attack
α_{RE}	Reattachment angle of attack
α_{SS}	Static stall angle of attack
α_{TE}	Angle of attack at the instant the leading edge vortex reaches the trailing edge of the airfoil
α_W	Difference between the geometric angle of attack and the effective angle of attack
α_{WM}	Effective angle of attack at the instant of dynamic stall
b	Semi-chord length
β_1	Parameter in the dynamic stall model = 0.18
β	$\sqrt{1-M^2}$
c	Chord length
C_{AM}	Coefficient in the expression for α_{DM}

C_{AR}	Coefficient in the expression for α_{RE}
C_{AT}	Coefficient in the expression for s_{MT}
$C_{\alpha T}$	Coefficient in the expression for s_{MT}
C_{WM}	Coefficient in the expression for α_{DM}
C_{WR}	Coefficient in the expression for α_{RE}
C_L	Synthesized unsteady lift coefficient
C_{LS}	Static lift coefficient
C_M	Synthesized unsteady moment coefficient
C_{MS}	Static moment coefficient
$C_{M_{1/4}}$	Moment coefficient about the quarter chord
γ	Parameter in the model of a first return map
$\Delta\alpha_1$	Shift in angle of attack in the dynamic stall model
$\Delta\alpha_2$	Shift in angle of attack in the dynamic stall model
ΔC_{L1}	Incremental lift coefficient due to dynamic effects
ΔC_{L2}	Incremental lift coefficient due to vortex effects
Δs	Non-dimensional time step size = $\Delta t U/b$
δ_1	Piece-wise continuous function of the angle of attack
δ_2	Piece-wise continuous function of the angle of attack
ϵ	Parameter in the dynamic stall model of αDM and αRE
ζ_α	Damping ratio in pitch
ζ_ξ	Damping ratio in plunge
h	Plunge variable
η	Generalized co-ordinate
J	Parameter in the Henon map
k	Non-dimensional forcing frequency = $\omega b/U$

K_1	Parameter in the dynamic stall model = 3.0
M	Mach number
m	Mass per unit span of the airfoil
μ	Airfoil air-mass ratio = $m/\pi\rho b^2$
ν	Parameter in the Henon map
ξ	Non-dimensional plunge variable = h/b
$P(s)$	Externally applied force
P_o	Non-dimensional amplitude of the externally applied force = Pb/mU^2
$P_1 ... P_{10}$	Coefficients of the synthesized lift coefficient
$Q(s)$	Externally applied torque
Q_o	Non-dimensional amplitude of the externally applied torque = Q/mU^2
$Q_1 ... Q_7$	Coefficients of the synthesized moment coefficient
Re	Reynolds number of the flow
r_α	Non-dimensional radius of gyration about the elastic axis
ρ	Air density
s	Non-dimensional time = tU/b
σ	Dummy variable of integration
T	Length of a laminar period of an intermittently chaotic system
t	Time
U	Free-stream flow velocity
U^*	Non-dimensional free-stream flow velocity = Ub/ω_α
ϕ_C	Compressibility corrected Wagner function
x_n	General mapping variable
$Z_1 ... Z_6$	Matrices in the aeroelastic equations
ω	Externally applied forcing frequency

ω_α	Natural frequency in pitch
ω_ξ	Natural frequency in plunge
$\bar{\omega}$	Ratio of natural frequencies $= \omega\alpha/\omega xi$

Chapter 1

Introduction

1.1 Introduction to Aeroelasticity

Aeroelasticity can be defined, in general, as the study of the mutual interaction of aerodynamic forces and structural forces; in real aeroelastic systems, these forces are nonlinear and the coupling between them is very complicated. These forces often interact in such a way as to positively reinforce each other, which can lead to divergent oscillations. Therefore, when designing an aeroelastic system, it is critical for the mechanical engineer to have a sound understanding of the possible static and dynamic instabilities of the system.

Aeroelastic systems are not limited to aircraft wings, rotors or other lifting surfaces, they include heat exchangers, nuclear reactor cooling rod arrays and even suspension bridges. However, the study of aeroelastic systems does have its roots in early aircraft design. One of the simplest aeroelastic systems is the linear structural airfoil in a two dimensional, subsonic flow. This system is the focus of this thesis and is utilized here to introduce the topic of aeroelasticity.

The interaction of aerodynamic and structural forces, with regards to the

two degree of freedom airfoil system, can be interpreted as a continuous, circular relationship. Imagine that the airfoil system is in a state of static equilibrium: the flow over the airfoil creates aerodynamic forces, usually represented as a lift force and moment acting at the aerodynamic centre of the airfoil, which exactly balance the structural forces, usually represented as the restoring force and torque of springs acting at the elastic axis of the airfoil. The freestream flow velocity is then perturbed by a small amount. This small perturbation will induce a small change in the aerodynamic forces acting on the airfoil which, in turn, will cause a small change in the deflection of the airfoil. This small change in the deflection of the airfoil will induce another small change in the aerodynamic forces, and so on and so forth. If these alternating induced changes in the forces acting on the system diminish in time, the system will return to its original stable position. However, if these small changes positively reinforce each other, then small changes in the deflection of the airfoil will grow. This means that the original equilibrium state of the airfoil was unstable. In many real aeroelastic systems, this type of instability can lead to catastrophic structural failure.

There are two general types of aeroelastic instabilities: static and dynamic. Static instabilities occur at zero frequency and, thus, they are independent of the inertia of the system. One example of a linear, static aeroelastic instability is the failure of a wing or airfoil by static divergence. For example, if a wing or airfoil is not sufficiently rigid in the pitch degree of freedom then, for sufficiently large values of the dynamic pressure, the effective stiffness of the airfoil can become zero. This aeroelastic phenomenon is caused by a negative stiffness effect induced by the aerodynamic forces and is thought to be the primary reason for the failure of many of the early flying machines developed at the turn of the century. With modern aircraft

analysis and design techniques this particular instability can be easily avoided.

Dynamic aeroelastic instabilities occur at given frequencies of motion of the airfoil and, generally, depend on the coupling of the motion of the airfoil in two degrees of freedom. For example, the coupling can occur between the pitch and plunge motions or between the pitch motion and the motion of a control surface. Since this type of instability depends on the dynamic motion of the airfoil, the inertia of the system plays an important role. One such linear, dynamic aeroelastic instability is known as binary flutter. A complete description of binary flutter is beyond the scope of this thesis, but a brief general description of the phenomenon is given here. As previously stated, a small change in the angle of attack of an airfoil will cause a chain reaction of changes in the aerodynamic and structural forces acting on the system. The dynamic response of the airfoil in both the pitch and plunge degrees of freedom, caused by these changing forces, will occur at certain frequencies which depend on the structural, inertial and aerodynamic characteristics of the system. For values of the dynamic pressure less than a critical value, the oscillatory response of the system will diminish in time; in other words energy from the flow will be dissipated by the system. On the other hand, if the dynamic pressure is greater than this critical value, the amplitude of the oscillations will grow in time; for each cycle of motion of the airfoil, a small amount of energy from the flow is injected into the system through the aerodynamic forces.

This linear dynamic instability is related to the frequencies of the response of the airfoil in pitch and plunge. As the dynamic pressure of the system is increased, the fundamental frequencies of the response in pitch and plunge (accounting for the aerodynamic effects) move closer together. The coalescence of these two frequencies enables the aerodynamic forces to inject a small amount of energy into the system

per cycle, and this small influx of energy causes the oscillatory response of the airfoil to increase in magnitude a small amount per cycle. Therefore, linear analysis of the two degree of freedom airfoil system predicts that, for values of the dynamic pressure greater than a critical value, divergent oscillations will occur.

One important shortcoming of using linear techniques to analyze aeroelastic systems is that linear theory can only give information about the behaviour of the system up to the point of the instability. Linear analysis implies the assumption that the dynamic response of the system will only involve small structural deflections, but this assumption is not valid near the point of instability where linear theory predicts deflections that approach infinity. It is obvious that in order to study the behaviour of aeroelastic systems near the point of linear instability, the nonlinearities inherent in both the structural and the aerodynamic forces must be included in the model of the system.

With recent advances in the field of nonlinear dynamics, and improvements in the performance of affordable computers, it has become possible to study the dynamic behaviour of nonlinear aeroelastic systems numerically. As previously stated, the aeroelastic system being studied in this thesis is a rigid airfoil flexibly mounted in a subsonic flow. The airfoil must be very long in the spanwise direction and mounted far from any boundaries so that the flow around the airfoil can be considered two-dimensional and no boundary effects, such as vortex images, need be considered when calculating the aerodynamic forces. The airfoil is mounted in the flow in such a way that it is constrained by a linear rotational spring to rotate in the pitch degree of freedom, and by a linear translational spring to move perpendicular to the undisturbed free-stream flow. The case of structural nonlinearities in the pitch degree of freedom has been studied by [Lee and LeBlanc, 1986a], [Tang and Dowell, 1992]

and [Price et al., 1993], and systems where aerodynamic nonlinearities dominate have been studied previously by [Tran and Falchero, 1982], [Lee and LeBlanc, 1986b] and [Tang and Dowell, 1992], but these latter systems are still not well understood.

When an airfoil is forced to oscillate at large mean values of the pitch angle, the flow over the airfoil will separate and reattach as the pitch angle changes; this process is known as dynamic stall and is described in detail by [Ericsson and Reding, 1988a] and [Ericsson and Reding, 1988b] and is dealt with in a later section of this thesis. Linear aerodynamic theory is not sufficient to calculate the aerodynamic forces acting on an airfoil undergoing dynamic stall because the nonlinear effects of the unsteady, turbulent wake cannot be accounted for by linear theory. Therefore, a new model of the aerodynamic forces, which takes into account the complicated and unsteady process of flow separation and reattachment, is required.

There are many different models of dynamic stall, such as that developed at ONERA [1] by [Tran and Petot, 1981] and at NASA [2] by [Bielawa et al., 1983]. The semi-empirical ONERA model of dynamic stall assumes that the aerodynamic forces can be written as a function of the variables describing the motion of the airfoil. These functions are obtained by curve fitting expressions to available experimental data. Although the results of this model have shown good agreement with experiment for harmonically oscillating airfoils, there is no attempt made by this approach to model the effects of any of the physical flow phenomena associated with dynamic stall. Furthermore, the amount of information available as to how to implement this model of dynamic stall is limited and, therefore, this model was not utilized in the research presented in this thesis.

---

[1] Office National d'Études et de Recherches Aérospatiales

[2] National Aeronautics and Space Administration

The dynamic stall model utilized in this thesis is a modified form of the semi-empirical Bielawa model. This model describes the effect of the main flow phenomena associated with dynamic stall with semi-empirical numerical expressions which are obtained by least squares curve fitting experimental data. These expressions are then incorporated into the general expressions for the aerodynamic forces, which are also obtained by a curve fitting procedure. The strengths of this model lie in the fact that it gives very good results compared with experiments; it is formulated in the time domain and thus it is easy to implement as part of the solution of the aeroelastic equations; and the structure of the model is such that the aerodynamic loads can be calculated easily from the pitch and pitch rate of the airfoil. Furthermore, there is a detailed account given by [Bielawa et al., 1983] of how this model can be developed from a set of experimental data.

One important drawback concerning this dynamic stall model is that it only accounts for the effects of pitch motion of the airfoil on the dynamic stall events and the unsteady aerodynamic forces. Therefore, it is necessary to make the assumption that the effects of the plunge motion, compared to the effects of the pitch motion, are relatively small in order that the aerodynamic forces due to this motion can be superimposed by linear aerodynamic theory. Due to the errors that result from this assumption, the main focus of this thesis is the study of the single degree of freedom system, in which the airfoil cannot move perpendicular to the flow, and only a brief study of the two-dimensional system is attempted.

The aeroelastic equations used to describe this system are given in [Fung, 1955] and are also given in [Bisplinghoff et al., 1957]. The nonlinear analysis of this system is accomplished by solving these aeroelastic equations numerically by a method developed by [Houbolt, 1950]. This numerical method was implemented because

it possesses the following advantageous qualities: the unknown future position of the airfoil can be expressed in terms of the known positions of the airfoil at previous time steps, and the entire system of equations can be written in the form of matrix equations, making it well suited for use with computers. Furthermore, this numerical method has been shown to posses the desirable property of combining good stability with sufficient accuracy.

1.2 Introduction to Nonlinear Dynamics

Until recently, most aeroelastic systems were approximated by linear equations because the solutions to these equations are unique and their behaviour is well understood. However, with recent advances in the field of nonlinear dynamics, non-unique steady-state solutions have been shown to be meaningful. In a nonlinear dynamical system the response may be chaotic; this implies that the final solution will be very sensitive to the initial conditions of the system. This is profoundly different from the behaviour of linear dynamic systems.

The response of a dynamic system can be viewed in the time domain, with the appropriate position variable shown as a function of time, but a more useful representation is the phase domain (plane), with the same variable and its time derivative shown as a function of time. Ordinarily the time axis is oriented perpendicular to the plane of the page and what is viewed is a projection of the response onto the position and velocity plane. The phase plane is a very convenient way of viewing the response of a nonlinear system because the difference between periodic behaviour and aperiodic behaviour is immediately obvious.

In Figure 1.1 (a), the phase plane plot of a period-four response is shown. As can be seen from the plot, the response is stable and repeats itself every four cycles.

In Figure 1.1 (b), the phase plane of an aperiodic (chaotic) response is shown and the differences between the two cases are obvious. The chaotic response is not stable and does not appear to repeat itself even after many cycles.

The steady-state solution of a nonlinear dynamic system may behave very differently from the steady-state response of a linear system. There is the possibility that the steady-state solution of a nonlinear system will not be unique; which steady-state solution is chosen depends on the initial conditions of the system. When this occurs, the response is may be chaotic. A chaotic response also implies that two solutions that begin very nearly at the same initial conditions, but not exactly, will not be close together after a certain amount of time has passed. In other words, solutions that begin very close together and eventually diverge from one another, but remain bounded, may be chaotic. This is due to the stretching and folding of the different steady-state solutions in the phase plane. The topographical process of stretching and folding is discussed in detail in [Thompson and Stewart, 1986] and [Moon, 1987] and will not be discussed further here; it is sufficient to know that this divergence of similar solutions is caused by the nonlinearities of the system and is not necessarily a consequence of computer or numerical errors.

An interesting question posed by [Thompson and Stewart, 1986] is why bother to numerically integrate a chaotic solution? Since numerical integration is only an approximation, two solutions that begin at exactly the same initial conditions, but are integrated numerically with two different techniques, will eventually diverge from one another due to the chaotic nature of the system. However, there is an entity that will remain common between the two solutions; this entity is known as the chaotic or strange attractor of the response. In this thesis, the attractor of a response is viewed by sampling the phase plane data once every period of the externally applied

harmonic forcing function. After a large number of these data points have been plotted, the attractor of the response becomes visible. This diagram, composed of discrete points in the phase plane, is called a Poincaré section.

If the response of the system is periodic, with the same period as the forcing function, then the attractor will consist of a single point in the phase plane. If the response is chaotic, one might believe that the chaotic attractor will consist of a random placement of points in the phase plane, but this is not the case. A chaotic attractor consists of many points in the phase plane, but there is always an underlying structure to the attractor that is sometimes very complicated, and it is this underlying structure that is common to all the possible steady-state solutions of a chaotic system.

Figure 1.2 (a) shows the Poincaré attractor for the period-four phase plane plot, illustrated in Figure 1.1 (a), over twenty thousand periods. As can be seen, the attractor is comprised of four groups of points. Since these groups are not points, the period-four oscillation is not perfectly stable, but it is almost stable. Figure 1.2 (b) shows the chaotic attractor of the chaotic phase plane plot illustrated in Figure 1.1 (b) over twenty thousand periods. The structure of the chaotic attractor is easily identifiable as a set of curves in the phase plane.

As previously stated, two different initial conditions will lead to two different steady-state solutions, but, the chaotic attractor will be the same in both cases. This settling of solutions to the same chaotic attractor is the result of energy dissipation within the system [Thompson and Stewart, 1986]. The main role of the Poincaré section is to illustrate the underlying structure of the chaotic attractor, and in so doing, provide the common thread between all of the possible chaotic solutions.

The aperiodic nature of a chaotic response can also be viewed by examining

the power spectral density, or Fourier spectrum, of the response. In Figure 1.3 (a), the Fourier spectrum of the period-four response is shown. The frequency of the forcing function is 0.044 and, as the figure shows, this is the frequency corresponding to the largest spike. The three subharmonic spikes in the frequency range below 0.044 indicate that the response is a period-four oscillation. Figure 1.3 (b) shows the Fourier spectrum of the chaotic response. The spike at the forcing frequency is still evident but, the subharmonic range is now dominated by broadband noise. This noise is not caused by any external sources but is a product of the nonlinearities of the system and is a signature of chaos.

In nonlinear dynamic systems, multiple attractors are common and chaotic and periodic attractors can even be present at the same time. Furthermore, as the various parameters of a nonlinear system are varied, different attractors will appear and others will disappear. This implies that as a system parameter is varied across a certain critical value, a change in the steady-state or long term behaviour of the system can occur. This change in behaviour is known as a bifurcation. Bifurcations can be viewed qualitatively in a bifurcation diagram. These are constructed by recording the values of the system parameter at which changes in the long term behaviour of the system take place over a given range of the parameter. In this thesis, bifurcation diagrams are constructed by recording the maximum and minimum values of the pitch at increasing values of a certain system parameter. A typical bifurcation diagram is shown in Figure 1.4.

The above discussion of nonlinear dynamic theory and qualitative analysis techniques is only intended as an introduction to what is to come in this thesis. For a more detailed discussion of the theory of chaos in nonlinear systems the reader is referred to [Thompson and Stewart, 1986] and [Moon, 1987].

The study of the effect of nonlinear aerodynamics on the linear airfoil system has been attempted previously. The nonlinear analysis of the dynamics of a NACA [3] 0012 airfoil forced to oscillate at large initial angles of attack and for large amplitudes was undertaken by [Lee and LeBlanc, 1986b]. However, since this research pre-dates many of the recent developments of nonlinear dynamics theory it did not take advantage of the qualitative nonlinear analysis techniques now available and, subsequently, there are areas of the report that can be further explored. The aeroelastic system consisting of a linear NACA 0012 airfoil structure and nonlinear aerodynamic stall model was also studied by [Tran and Falchero, 1982] and [Tang and Dowell, 1992], but, in these cases, the dynamic stall model utilized was the ONERA model, and an in depth discussion of the chaotic dynamics was not given. At present, there has been no detailed investigation of the dynamic response of a linear airfoil with nonlinear aerodynamics modelled using the Bielawa model of dynamic stall.

1.3 Motivation

The previous discussion on aeroelastic systems led to the following conclusion: in order to understand the behaviour of airfoils oscillating at high angles of attack, or for large amplitude oscillations, the nonlinearities inherent in the system must be included in the numerical model of the system. Nonlinear aeroelasticity implies that either the structural components that comprise the system are nonlinear in nature, the aerodynamic forces are nonlinear, or both. The nonlinear behaviour of an aeroelastic system is an extremely important consideration for mechanical engineers designing systems such as airplanes, helicopters, free-standing towers, heat

[3]National Advisory Committee for Aeronautics

exchangers, nuclear reactor cooling rod arrays and suspension bridges. In these systems, understanding the types of nonlinear instabilities that occur is essential to avoiding structural fatigue and catastrophic failure.

Nonlinear structural forces can arise in a system in many ways. For example, when a flexible component of a structure is displaced from its equilibrium position by a sufficiently large amount to cause plastic deformations in the material, or when there is freeplay in a joint, the resultant structural forces are nonlinear. Nonlinear aerodynamic forces can also be caused in different ways. Unsteady flow phenomena, such as the separation of the flow around sharp corners or moving boundaries, the turbulent flows found in high speed turbomachinery applications and the formation of local shocks in transonic flow around airfoils are all examples of aeroelastic systems in which the aerodynamic forces are nonlinear. The case of an airfoil forced to oscillate in dynamic stall is an example of a nonlinear aeroelastic system that is presently not well understood.

In general, modelling a three-dimensional nonlinear aeroelastic system, such as an aircraft or suspension bridge, is, to say the least, a very complicated problem. In the nonlinear analysis of such complicated systems, it is advantageous to simplify the system as much as possible, while retaining only the most important nonlinearities. The aeroelastic system that is being analyzed in this thesis is a rigid airfoil flexibly mounted in a subsonic flow. Since the airfoil is rigid it does not deform under the aerodynamic loads but, because it is flexibly suspended in the flow, it does move under the influence of these forces. This airfoil is forced to oscillate at large angles of attack, and, therefore, the flow around the airfoil does not always remain attached. Because of the high angles of attack and the subsequent flow separation and reattachment, the resultant aerodynamic forces are nonlinear. The study of the

dynamic behaviour of this simplified system is of fundamental importance to the understanding of the behaviour of more complicated aeroelastic systems.

Since many high performance aircraft and turbines operate at high angles of attack, understanding the dynamic behaviour of an airfoil forced to oscillate in dynamic stall is extremely important. It is hoped that the qualitative analysis presented herein will further the understanding of the different types of chaotic instabilities that can result from the nonlinear aerodynamic forces of dynamic stall.

1.4 Objectives of this Thesis

The main objective of this research is to give a qualitative description of the types of chaotic behaviour that the modified Bielawa model of dynamic stall predicts for a single degree of freedom airfoil system. This includes explanations of how the response of the system changes from periodic behaviour to chaotic behaviour, as well as explanations of the different types of chaotic behaviour exhibited by the system. This thesis also examines the effect of adding the plunge degree of freedom on the response of the system, and the effect that the ratio of the natural frequencies of the system has on the stability of the response.

In Chapter 2, the dynamic stall process is explained in terms of the physical properties and structures of the flow. It also discusses, in detail, the modified Bielawa model of dynamic stall, including how the major dynamic stall events are modelled numerically and how these expressions are incorporated into a comprehensive model of the unsteady aerodynamic forces. This Chapter also contains a description of the general two degree of freedom aeroelastic equations and a discussion of the assumptions that were made that allow these equations to be simplified. There is also a discussion of Houbolt's numerical procedure for solving this system of equations.

The one degree of freedom system is discussed in detail in Chapter 3. It begins with a description of the system, including all necessary assumptions and simplifications. Next, the nonlinear analysis techniques are defined and discussed. These techniques include bifurcation diagrams, phase plane plots, Fourier spectra and Poincaré sections. The analysis is divided into four cases based on the values of the system parameters at which the chaotic behaviour occurs and the type of chaotic behaviour that is observed. The dynamics of the system as a whole are analyzed by exploring the system dynamics over a wide range of values of certain system parameters; this is accomplished with the use of bifurcation diagrams. The regions of potentially chaotic behaviour are then studied in further detail with more detailed bifurcation diagrams, time histories, phase plane plots, Fourier spectra and Poincaré sections and maps. Wherever possible, the Poincaré maps are compared with maps from known analytical systems, or they are modelled by simple sets of equations, in order to obtain an improved understanding of the dynamics of the system.

Chapter 4 briefly describes the two-dimensional system and the limitations of superimposing linear aerodynamic theory. The main objectives of this Chapter are to show the effect of adding the plunge degree of freedom on the chaotic responses of the single degree of freedom system and to show how the ratio of the natural frequencies in pitch and plunge affect the stability of the system. This is accomplished by examining bifurcation diagrams that illustrate the stability of the response, and Poincaré sections that qualitatively show the long term behaviour of the response.

The analysis of the dynamics of a linear structural airfoil with nonlinear aerodynamic forces that is given in this thesis is not a typical aeroelastic analysis. The chaotic instabilities that are encountered in the analysis are not self-excited; there is an externally applied forcing function that is always driving the system.

Therefore, the focus of this thesis is to analyze the different types of chaotic behaviour exhibited by the system and not to find flutter boundaries or other self-excited instabilities.

The final Chapter of this thesis gives the main conclusions of the nonlinear analysis and also includes recommendations for areas of possible future research. It is hoped that at the conclusion of this section the reader will have a clear understanding of the different types of chaotic behaviour that are exhibited by this system and some understanding as to how this chaotic behaviour develops.

(a)

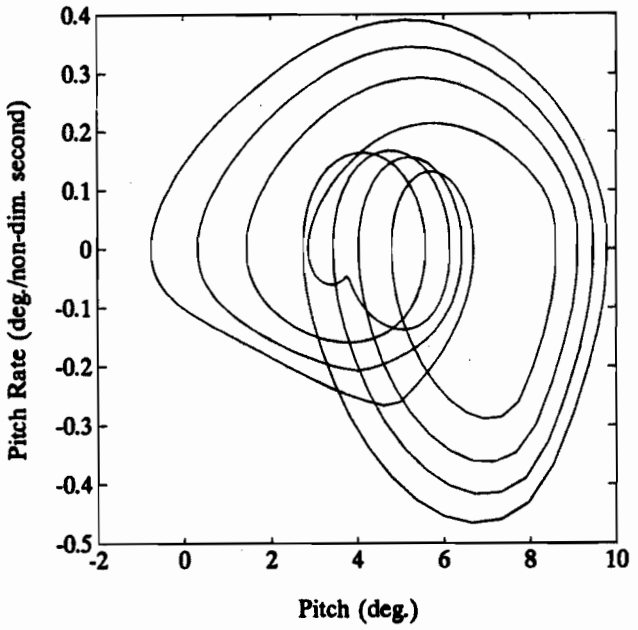

(b)

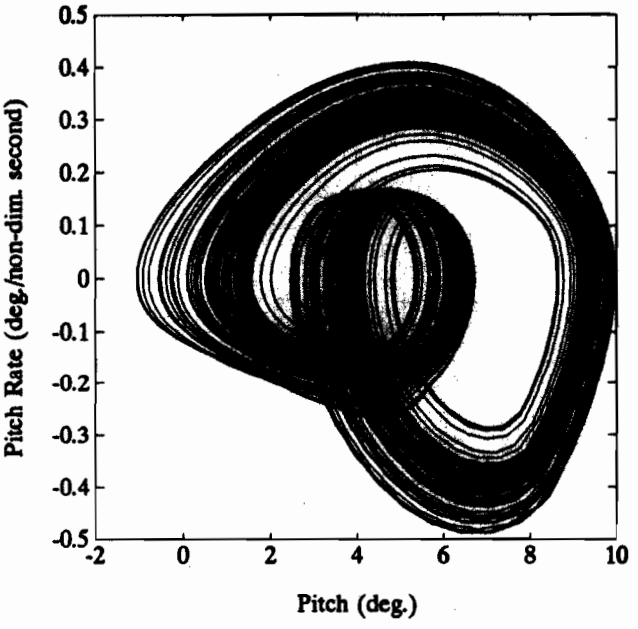

Figure 1.1: The phase plane plot of (a) a period-four response and (b) a chaotic response.

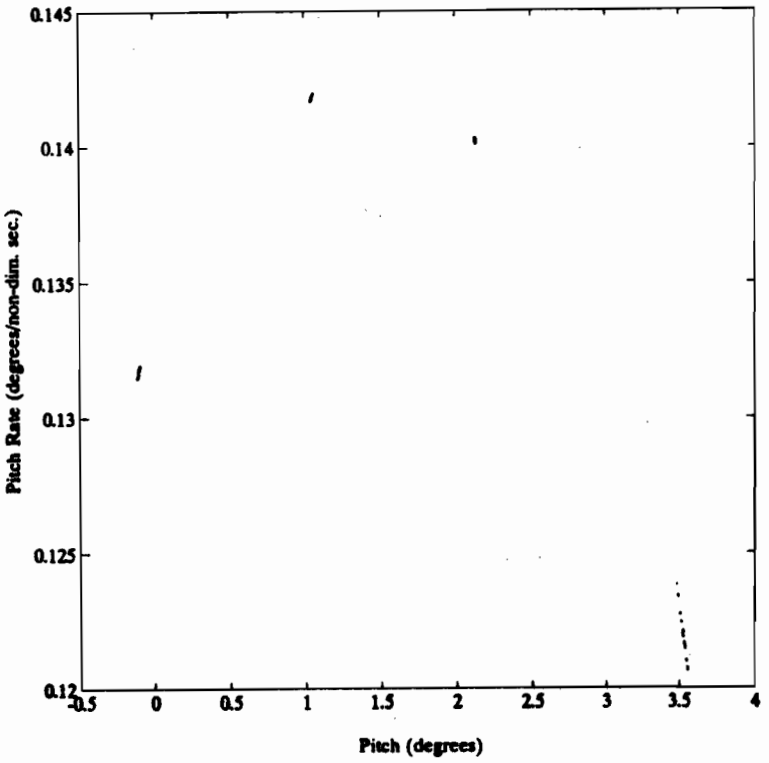

(a)

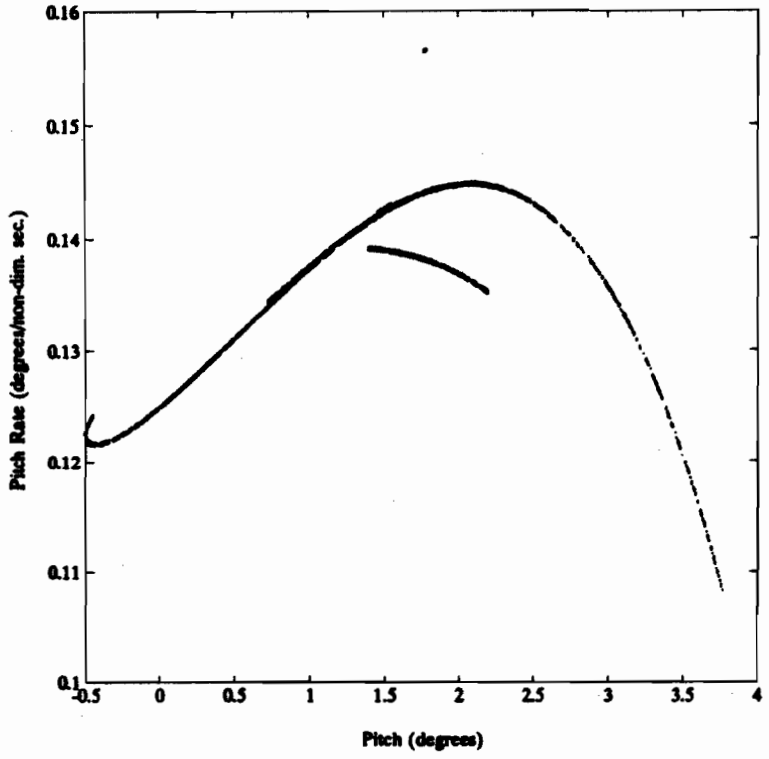

(b)

Figure 1.2: The Poincaré sections, showing the attractors, of (a) a period-four response and (b) a chaotic response.

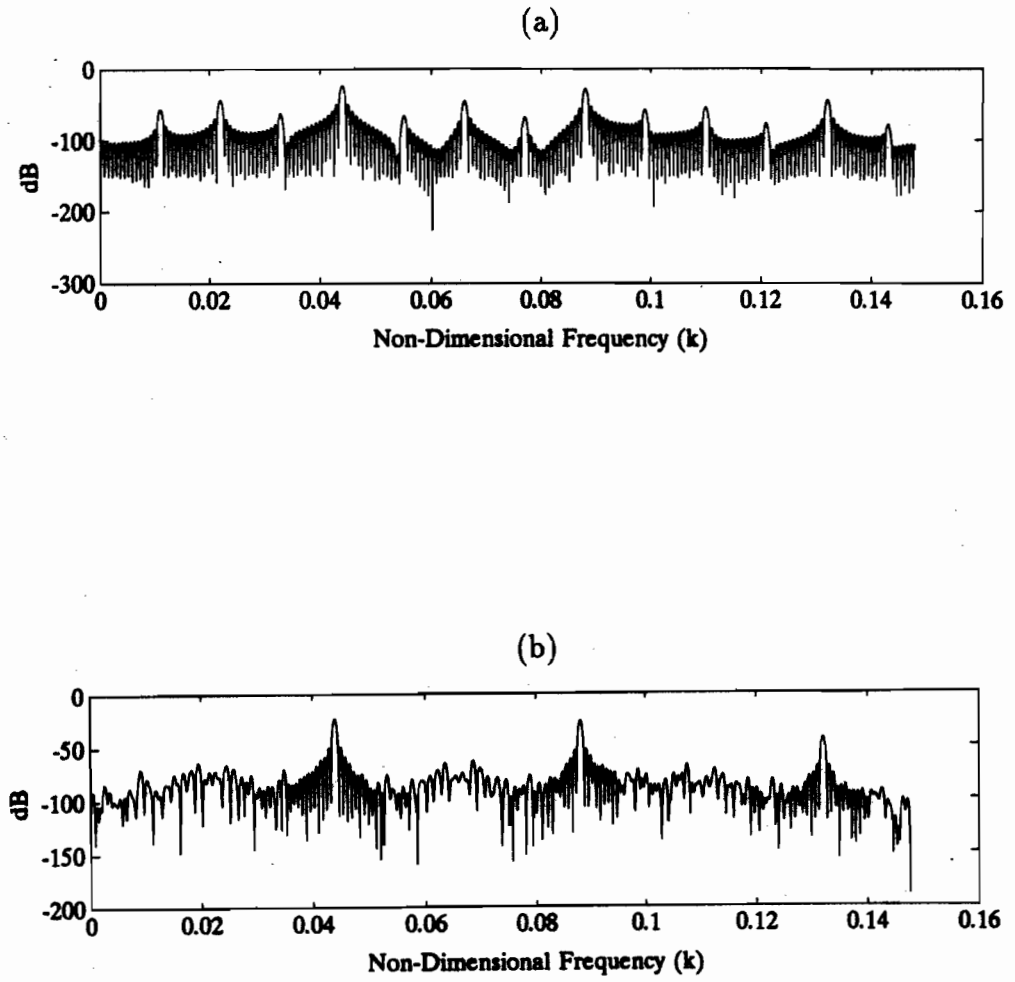

Figure 1.3: The Fourier spectrum of (a) a period-four response and (b) a chaotic response.

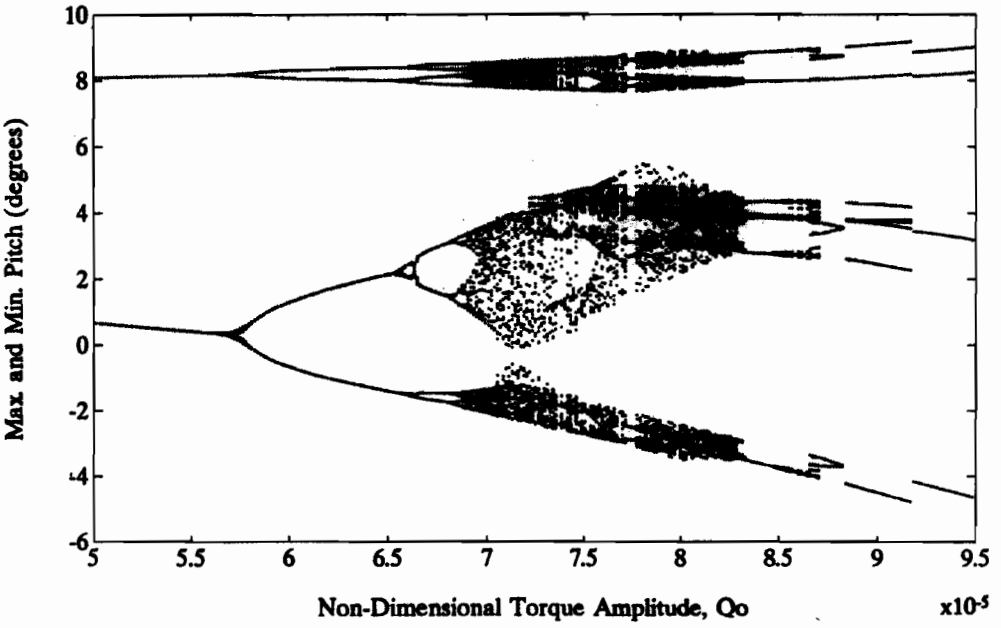

Figure 1.4: The bifurcation diagram of a typical nonlinear system showing the changes in the long term behaviour of the system as a system parameter is varied.

Chapter 2

The Dynamic Stall Model and Numerical Techniques

2.1 Characteristics of Dynamic Stall

Dynamic stall of an airfoil undergoing an oscillatory motion in the pitch degree of freedom is a highly nonlinear process. Therefore, it is difficult to predict analytically the aerodynamic loads acting on the airfoil. The three main events of the dynamic stall process are illustrated in Figure 2.1. The first event is the formation of a leading edge vortex, which occurs as the angle of attack of the airfoil is increased beyond the static stall angle. As the angle of attack of the airfoil continues to increase, the leading edge vortex grows until it detaches from the leading edge of the airfoil and is convected downstream by the free stream flow. This vortex shedding process is associated with an almost instantaneous decrease in the circulation around the airfoil, which causes a rapid loss of lift. As the low pressure centre of this vortex travels downstream near the surface of the airfoil, the distribution of lift on the airfoil is altered, as illustrated in Figure 2.2. The second significant event of the

dynamic stall process arises as the shed vortex approaches the trailing edge of the airfoil. The localized area of low pressure associated with the centre of the vortex causes an increase in the local lift coefficient near the trailing edge of the airfoil. It is this increase in the local lift coefficient which induces a sharp decrease in the moment coefficient (measured positive in the nose up direction) as the vortex leaves the trailing edge of the airfoil. The final significant event in the dynamic stall process is the reattachment of the flow over the airfoil. This usually occurs after the vortex has left the trailing edge of the airfoil and the angle of attack of the airfoil has decreased below the static stall angle.

Typical graphs of the lift coefficient and moment coefficient versus angle of attack for an airfoil undergoing simple harmonic motion in pitch are shown in Figure 2.3. This Figure illustrates that a significant amount of nonlinear hysteresis exists in the aerodynamic loads of an airfoil experiencing dynamic stall as compared to static stall. This nonlinear hysteresis in the lift and moment coefficient curves, caused by characteristic delays in the boundary layer separation and reattachment, is impossible to accurately predict using any of the present analytical, aerodynamic theories.

The main parameters that influence the amount of hysteresis in the dynamic lift and moment curves are the mean angle of attack and the amplitude and frequency of the oscillation. Other parameters that influence the static lift and moment curves, as well as the dynamic curves, are the airfoil shape, the Mach number and the Reynolds number of the flow. These parameters strongly influence the three most significant events that occur during dynamic stall: the production and the subsequent shedding of a leading edge vortex, the time at which this vortex reaches the trailing edge of the airfoil and the reattachment of the flow around the airfoil. These events cause the observed overshoot and undershoot of the dynamic lift coefficient as compared to the

static lift coefficient, and the characteristic sharp decrease in the moment coefficient typical of airfoils undergoing dynamic stall [Bielawa et al., 1983].

The observed overshoot of the dynamic lift coefficient as compared to the static lift coefficient, as the angle of attack is increased beyond the static stall angle, is due to a delay in the separation of the boundary layer near the leading edge of the airfoil. The boundary layer is made less susceptible to separation near the leading edge of the airfoil by a combination of two main effects. The first is due to the induced acceleration of the flow near the surface of the leading edge, caused by the motion of the airfoil. This induced acceleration causes a decrease in the pressure gradient along the surface of the airfoil, as compared to the static pressure gradient at the same angle of attack. Therefore, the downstream separation of the boundary layer is delayed, in the dynamic case, because the boundary layer profile is made less susceptible to separation by the more favourable upstream pressure gradient [Ericsson and Reding, 1988a]. The second effect is due to the moving boundary of the airfoil which improves the boundary layer profile immediately downstream of the stagnation point. The motion of the surface of the airfoil, in the direction of the freestream flow, as the angle of attack of the airfoil is increased, has the net effect of increasing the flow velocity component tangential to the airfoil surface. This increases the amount of kinetic energy in the boundary layer flow nearest to the surface of the airfoil, thus strengthening the boundary layer and delaying separation. This moving boundary effect is also greatly responsible for the delayed reattachment of the flow as the angle of attack of the airfoil is decreased below the static stall angle [Ericsson and Reding, 1988a].

2.2 An Empirical Model of Dynamic Stall

The model utilized herein to predict the unsteady, stalled aerodynamic loads acting on an airfoil undergoing a general pitching motion was developed by [Bielawa et al., 1983]. The model involves several analytical expressions, which are simple mathematical models of the main dynamic stall events, to describe the aerodynamic loads acting on the airfoil in the time domain. The analytical expressions are comprised of numerous unknown coefficients, which are determined by curve fitting data from wind tunnel tests of oscillating airfoils to the expressions using a least squares minimization technique. Since this dynamic stall model describes the lift and moment coefficients in the time domain, the main parameters utilized to predict the unsteady aerodynamic loads are the airfoil geometric angle of attack and pitch rate, which are simple to define both physically and mathematically. The model does not utilize the frequency of the airfoil oscillation as a parameter because of the difficulty of mathematically defining the instantaneous frequency of an airfoil undergoing quasi-periodic or chaotic motion.

2.2.1 Definition of Dynamic Parameters

In order to at least partially account for the time history of the airfoil's motion, an unsteady decay parameter, α_W, is defined. The physical interpretation of this parameter is that it represents the difference between the instantaneous, geometric angle of attack, α, and the effective angle of attack, α_E,

$$\alpha_W = \alpha - \alpha_E. \tag{2.1}$$

This interpretation of the unsteady decay parameter is only strictly correct when the flow over the airfoil is attached. However, this parameter is also utilized to predict

certain dynamic stall events and to approximate the aerodynamic loads even when the airfoil is stalled. The effective angle of attack, for attached flow, can be defined using Duhamel's integral as:

$$\alpha_E = \alpha(0)\phi_C(s, M) + \int_0^s \frac{\partial \alpha}{\partial \sigma}\beta\phi_C(s-\sigma, M)d\sigma \tag{2.2}$$

where $\alpha(0)$ is the initial angle of attack of the airfoil, $\beta = \sqrt{1-M^2}$ (in this thesis $M = 0.6$), and the non-dimensional time is given by $s = Ut/b$, where U is the freestream flow velocity and b is the semi-chord. The quantity ϕ_C is a form of the Wagner function, which has been corrected for compressibility effects, and gives the response of the airfoil to a step change in the angle of attack. The expression for ϕ_C is as follows:

$$\phi_C(s, M) = (1 - 0.165exp(-0.0455(1-M^2)s) - 0.335exp(-0.3(1-M^2)s))/\sqrt{1-M^2} \tag{2.3}$$

For an airfoil undergoing a general pitch oscillation, the following recursive relationships were utilized to obtain the angle of attack (α_n), the pitch rate (A_n) and the unsteady decay parameter ($(\alpha_W)_n$) at each time step [Bielawa et al., 1983]:

$$\alpha_n = \theta_n \tag{2.4}$$

$$A_n = \frac{(\Delta\theta)_n}{(\Delta s)_n} \tag{2.5}$$

$$(\alpha_W)_n = x_n + y_n \tag{2.6}$$

$$x_n = x_{n-1}exp(-0.0455(1-M^2)(\Delta s)_n) + 0.165(\alpha_n - \alpha_{n-1}) \tag{2.7}$$

$$y_n = y_{n-1}exp(-0.3(1-M^2)(\Delta s)_n) + 0.355(\alpha_n - \alpha_{n-1}) \tag{2.8}$$

where θ_n is the geometric angle of attack at time step 'n'.

2.2.2 Modelling the Dynamic Stall Events

In order to accurately model the unsteady aerodynamic loads acting on an airfoil undergoing dynamic stall, it is important to be able to predict the onset of the three major dynamic stall events: the formation and shedding of a leading edge vortex (onset of dynamic stall), the arrival of this vortex at the trailing edge and the reattachment of the flow over the airfoil.

Dynamic stall occurs after the angle of attack of the airfoil has exceeded the static stall angle, and occurs at the angle of attack at which the leading edge vortex breaks away from the leading edge of the airfoil. The model used herein to predict the instantaneous angle of attack at which dynamic stall occurs utilizes a semi-empirical relationship between the instantaneous angle of attack and the main factors influencing dynamic stall. The model assumes that the main factors influencing dynamic stall include the airfoil shape, the Mach and Reynolds numbers of the flow, and the pitch rate and effective angle of attack of the airfoil. The static stall of an airfoil depends on the first three factors stated above, and therefore the effect of these factors on the dynamic stall is taken into account by incorporating the static stall angle into the empirical equation for the dynamic stall angle. The effective angle of attack of the airfoil is taken into account by the unsteady decay parameter, α_W, defined in equations (2.1) and (2.2). The model assumes a functional relationship between the instantaneous angle of attack of the airfoil at dynamic stall and the static stall angle, the pitch rate and the effective angle of attack of the airfoil. By linearizing this functional relationship about the quasi-static stall angle, (i.e. $\alpha_{QSS} = (1+\epsilon)\alpha_{SS}$), an empirical expression for the dynamic stall angle of attack is obtained and is given by,

$$\alpha_{DM} = (1 + \epsilon + C_{AM}A_{DM} + C_{WM}\alpha_{WM})\alpha_{SS} \tag{2.9}$$

where α_{DM} is the instantaneous angle of attack, A_{DM} is the pitch rate and α_{WM} is the unsteady decay parameter at the point of dynamic stall, and ϵ, C_{AM} and C_{WM} are empirically determined constants. The last two terms in equation (2.9) account for the difference between the angle of attack at dynamic stall and the angle of attack at quasi-static stall.

After dynamic stall, the leading edge vortex is convected downstream over the upper surface of the airfoil and it strongly influences the aerodynamic loads on the airfoil. The lift produced by the airfoil, while the vortex is being convected, can vary depending on the strength of the vortex and the distance between the vortex and the surface of the airfoil. The main effect of the vortex on the distribution of lift around the airfoil is to increase the negative (nose down) pitching moment of the airfoil. The negative pitching moment reaches a maximum when the vortex arrives at the trailing edge of the airfoil. The model utilizes a semi-empirical relationship to predict the amount of non-dimensionalized time (s_{MT}) required for the vortex to travel from the leading edge to the trailing edge of the airfoil. The expression for s_{MT} is given below:

$$s_{MT} = \frac{1.0}{C_{AT}A_{DM} + C_{\alpha T}\alpha_{DM}} \tag{2.10}$$

where C_{AT} and $C_{\alpha T}$ are empirically determined coefficients.

The instantaneous angle of attack at which the flow around the airfoil becomes reattached is denoted by α_{RE}. The method for predicting the reattachment angle of attack is the same as for predicting the dynamic moment stall angle of attack α_{DM}. The appropriate expression is given below:

$$\alpha_{RE} = (1 - \epsilon + C_{AR}A_{DM} + C_{WR}\alpha_{WM})\alpha_{SS} \tag{2.11}$$

where ϵ is the same as in equation (2.9), but C_{AR} and C_{WR} are not the same as C_{AM} and C_{WM}.

2.2.3 The Unsteady Lift and Moment Coefficients

Dynamic lift stall is a phenomenon characterized by a sudden loss of lift due to the increased distance between the shed leading edge vortex and the upper surface of the airfoil. It can also be interpreted as a sudden loss of lift due to the almost instantaneous loss of circulation around the airfoil contained in the shed leading edge vortex. The model used herein to describe the aerodynamic loads acting on an airfoil undergoing dynamic moment stall takes into account this sudden loss of lift implicitly with the following expressions [Bielawa et al., 1983]:

$$C_L = C_{LS}(\alpha - \Delta\alpha_1 - \Delta\alpha_2) + a_{OL}\Delta\alpha_1 + \Delta C_{L1} + \Delta C_{L2} \tag{2.12}$$

$$\Delta\alpha_1 = (P_1 A + P_2\alpha_W + P_3)\alpha_{SS} \tag{2.13}$$

$$\Delta\alpha_2 = \delta_2\alpha_{SS} \tag{2.14}$$

$$\Delta C_{L1} = P_4 A + P_5\alpha_W + P_6(\frac{\alpha}{\alpha_{SS}}) + P_7(\frac{\alpha}{\alpha_{SS}})^2 \tag{2.15}$$

$$\Delta C_{L2} = P_8\delta_1 + P_9\Delta\alpha_2 + P_{10}\alpha_{DM}^2[\frac{1 - exp(-(\beta_1 s_M)^3)}{(\beta_1 s_M)^2}] \tag{2.16}$$

where the following definitions apply:

$$s_M = \frac{U(t - t_{DM})}{b} \tag{2.17}$$

$$\delta_1 = \begin{cases} 0, & \text{for } \alpha \leq \alpha_{SS} \\ (\frac{\alpha}{\alpha_{SS}} - 1), & \text{for } \alpha_{SS} < \alpha \leq \alpha_{DM} \\ (\frac{\alpha_{DM}}{\alpha_{SS}} - 1)(1 - (\frac{s_M}{s_{MT}})^2), & \text{for } 0 \leq s_M \leq s_{MT} \\ 0, & \text{for } s_M > s_{MT} \end{cases} \tag{2.18}$$

$$\delta_2 = \begin{cases} 0, & \text{for } \alpha \leq \alpha_{SS} \\ (\frac{\alpha}{\alpha_{SS}} - 1), & \text{for } \alpha_{SS} < \alpha \leq \alpha_{DM} \\ (\frac{\alpha_{DM}}{\alpha_{SS}} - 1), & \text{for } 0 \leq s_M \leq s_{MT} \\ (\frac{\alpha_{DM}}{\alpha_{SS}} - 1)\frac{\alpha - \alpha_{RE}}{\alpha_{TE} - \alpha_{RE}} & \text{for } \alpha_{RE} \leq \alpha \leq \alpha_{TE} \\ 0, & \text{for } \alpha < \alpha_{RE} \end{cases} \tag{2.19}$$

In the above equations, the parameter β_1 is an empirically determined constant, given by [Bielawa et al., 1983] to be equal to 0.18, and s_M is the non-dimensionalized time measured from the instant that dynamic moment stall occurs until the instant the vortex reaches the trailing edge of the airfoil (i.e. when $s_M = s_{MT}$ then $\alpha = \alpha_{TE}$). As can be seen in equation (2.12), the total lift coefficient, C_L, is expressed as a sum of the static lift coefficient curve [Abbott and von Doenhoff, 1959] at a shifted angle of attack, $\alpha - \Delta\alpha_1 - \Delta\alpha_2$, plus the static lift curve slope, a_{OL}, multiplied by the incremental angle of attack, $\Delta\alpha_1$, plus the sum of two incremental lift coefficients, ΔC_{L1} and ΔC_{L2}. The incremental angle of attack, $\Delta\alpha_1$, is present at all times, whereas the incremental angle of attack, $\Delta\alpha_2$, is only non-zero when the flow over the airfoil is stalled; therefore, it must at least in part account for the effects associated with dynamic moment stall and flow reattachment. The incremental lift coefficient, ΔC_{L1}, is primarily responsible for the difference between the unsteady lift coefficient and the steady lift coefficient, especially when the flow over the airfoil is unstalled, whereas the incremental lift coefficient, ΔC_{L2}, is responsible only for the lift effects of the shed leading edge vortex as it is convected over the surface of the airfoil. The coefficients, $P_1 ... P_{10}$, are empirical constants determined by least squares curve fitting available data from wind tunnel tests of oscillating airfoils to the above expression for C_L.

The model to predict the unsteady moment coefficient, C_M, utilizes a similar set

of equations as those described above. The equation for C_M is given below.

$$C_M = C_{MS}(\alpha - \Delta\alpha_2) + a_{OM}\Delta\alpha_2 + \Delta C_M \tag{2.20}$$

where the following definition applies:

$$\Delta C_M = Q_1 A + Q_2 \alpha_W + Q_3(\frac{\alpha}{\alpha_{SS}}) + Q_4 \mid \alpha_W \mid + Q_5\delta_1 + Q_6\Delta\alpha_2 + Q_7\alpha_{DM}A_{DM}s_M \tag{2.21}$$

The parameter a_{OM} is the static moment coefficient curve [Abbott and von Doenhoff, 1959] slope at zero angle of attack, which is zero for symmetric airfoils. The last term of equation (2.21) represents the effects of the shed leading edge vortex, and the constants, $Q_1 ... Q_7$, are determined by curve fitting windtunnel data to the above expressions using a least squares technique. The coefficients of the dynamic stall model are given in Appendix A.

2.2.4 Modification and Verification of the Dynamic Stall Model

Two simple modifications were made to the dynamic stall model described above, keeping in mind that the lift and moment coefficient curves must be at least piecewise continuous in the time domain and that they must always take on physically realizable values.

The first modification was to restrict the domains of the dynamic moment stall angle of attack, α_{DM}, and the flow reattachment angle of attack, α_{RE}. The reason for introducing this restriction was to ensure that both α_{DM} and α_{RE} obtained physically realizable values for cases when the airfoil was undergoing extreme oscillations, such as very high or very low frequencies or large amplitudes. The domain of α_{DM} was restricted to values greater than the static stall angle of attack, α_{SS}, and the domain

of α_{RE} was restricted to values less than α_{SS}. It can be argued that α_{DM} must always be greater than α_{SS} due to the boundary layer improvements, discussed in Section 2.1, caused by the dynamics of the airfoil as the angle of attack is increasing. Similarly, it can be argued that α_{RE} must always be less than α_{SS} since the dynamic effects are also present as the angle of attack of the airfoil is decreasing, and these effects will act to destabilize the boundary layer and delay reattachment of the flow. Unfortunately, in the case of the flow reattachment angle of attack, this is not always the case. Since static stall can be induced by local shocks for Mach numbers greater than about 0.6 it is possible for the flow to reattach at an angle of attack greater than α_{SS}. Therefore, by introducing the previous assumptions the model is restricted to cases where stall is not induced by local shocks.

The second modification to the dynamic moment stall model was made in order to ensure that the lift and moment coefficient curves remained at least piece-wise continuous. Very often the model correctly predicted that the shed vortex did not reach the trailing edge of the airfoil before the angle of attack of the airfoil had decreased below the predicted flow reattachment angle. In other words, the two conditions, $s_M < s_{MT}$ and $\alpha < \alpha_{RE}$, existed simultaneously. It can be seen from equations (2.18) and (2.19) that the model does not allow for this occurrence. The result was that the function δ_2 was discontinuous because the stage where the shed vortex is gone, $s_M > s_{MT}$, but the flow is not yet reattached, $\alpha_{RE} < \alpha < \alpha_{TE}$, was omitted, therefore, the lift and moment coefficient curves were also discontinuous. To avoid this discontinuity, the expressions for δ_2, ΔC_{L2} and ΔC_M were modified for the instances when both conditions, $s_M < s_{MT}$ and $\alpha < \alpha_{RE}$, occur simultaneously. The modified expressions are:

$$\delta_2 = (\frac{\alpha_{DM}}{\alpha_{SS}} - 1)[1 - exp(K_1(s_M - s_{MT}))] \tag{2.22}$$

$$\Delta C_{L2} = P_8\delta_1 + P_9\Delta\alpha_2$$

$$+ P_{10}\alpha_{DM}^2[1 - \frac{exp(-\beta_1 s_M)^3}{(\beta_1 s_M)^2}][1 - exp(K_1(s_M - s_{MT}))] \quad (2.23)$$

$$\Delta C_M = Q_1 A + Q_2\alpha_W + Q_3\frac{\alpha}{\alpha_{SS}} + Q_4 \mid \alpha_W \mid + Q_5\delta_1$$

$$+ Q_6\Delta\alpha_2 + Q_7\alpha_{DM}A_{DM}s_M[1 - exp(K_1(s_M - s_{MT}))] \quad (2.24)$$

where the parameter, K_1, is a constant equal to 3.0. The terms that are modified are those that are supposed to be zero as the vortex detaches from the leading edge, $s_M = s_{MT}$, and reach a certain value as the flow reattaches after the vortex has been shed. However, since the model predicts that the flow will reattach before the vortex is shed, these terms are multiplied by the expression $[1 - exp(K_1(s_M - s_{MT}))]$, which ensures that they will tend to the appropriate values as s_M becomes increasingly larger than s_{MT}. The value of K_1 was determined empirically by comparing the modified expressions with the actual wind tunnel data.

In Figure 2.4, the lift and moment coefficient curves from wind tunnel tests are plotted versus angle of attack and compared to the predicted lift and moment coefficient curves of the modified and unmodified dynamic stall models for a case where $\alpha_{TE} < \alpha_{RE}$. As can clearly be seen, the two dynamic stall models give identical results until the stage where the angle of attack, α, decreases to less than α_{RE} but is still greater than α_{TE}. Through this range the modified dynamic stall model is continuous, but the unmodified dynamic stall model is discontinuous at the point when $\alpha = \alpha_{TE}$.

The curve fitting of the windtunnel test data to the expressions for the unsteady lift and moment coefficients was done with the use of the 'Amoeba' subroutine found in [Press et al., 1986] and a least squares method. Eighteen data loops from [Gray and Liiva, 1968] were utilized in determining the unknown coefficients, thus ensuring that the model would be valid over a wide range of non-dimensional

frequencies, $k(0.044,\ldots,0.256)$, amplitudes $\bar{\alpha}(2.5^o,\ldots,7.5^o)$, and mean angles of attack $\alpha_0(0.0^o,\ldots,10.0^o)$. In Figures 2.5 and 2.6 some typical comparisons are made between the lift and moment coefficient curves from the windtunnel test data and the lift and moment curves predicted by the modified dynamic stall model for four different non-dimensional frequencies, amplitudes and mean angles of attack. Appendix B contains most of the data-model comparisons of the lift and moment coefficient data for a Mach number of 0.6 and a Reynolds number of $6.2 * 10^6$ given in [Gray and Liiva, 1968].

2.3 Two Degree of Freedom Airfoil System

The details of the two degree of freedom airfoil system are illustrated in Figure 2.7. The angle of attack, α, is measured positive in the nose up direction, and the non-dimensionalized vertical displacement, $\xi = h/b$, is measured positive downwards. The elastic axis is located a distance $a_h b$ behind the midchord of the airfoil, and the centre of mass of the airfoil is located a distance $x_\alpha b$ behind the elastic axis.

The non-dimensionalized two degree of freedom aeroelastic equations, from [Fung, 1955], are:

$$\ddot{\xi} + x_\alpha \ddot{\alpha} + 2\zeta_\xi \frac{\bar{\omega}}{U^*}\dot{\xi} + \frac{(\bar{\omega})^2}{(U^*)^2}\xi = -\frac{1}{\pi\mu}C_N(s) + \frac{P(s)b}{mU^2} \tag{2.25}$$

$$x_\alpha \ddot{\xi} + r_\alpha^2 \ddot{\alpha} + 2\zeta_\alpha \frac{r_\alpha^2}{U^*}\dot{\alpha} + \frac{r_\alpha^2}{(U^*)^2}\alpha = \frac{2}{\pi\mu}C_M(s) + \frac{Q(s)}{mU^2} \tag{2.26}$$

where ζ_α and ζ_ξ are the viscous damping ratios in the pitch and plunge degrees of freedom, respectively, $\bar{\omega} = \omega_\xi/\omega_\alpha$ is the ratio of uncoupled natural frequencies and $U^* = U/b\omega_\alpha$ is the non-dimensional velocity. The airfoil air-mass ratio is defined as $\mu = m/\pi\rho b^2$, where m is the airfoil's mass per unit span, ρ is the air density and b is the semi-chord. The non-dimensionalized radius of gyration about the elastic

axis is r_α. $C_N(s)$ and $C_M(s)$ are the lift and moment coefficients, respectively, taken about the elastic axis and $P(s)$ and $Q(s)$ are the externally applied force and torque, respectively, applied at the elastic axis.

For the two degree of freedom airfoil system studied herein, it is assumed that the plunge oscillations are very small compared to the pitch oscillations. This implies that the stiffness of the airfoil in the plunge degree of freedom is much greater than the stiffness in the pitch degree of freedom, or that $\bar{\omega}$ is large. Furthermore, as $\bar{\omega}$ tends to infinity, the system tends to a single degree of freedom in pitch. Since the pitch degree of freedom dominates the motion of the airfoil, the main contribution to the aerodynamic loads must be from the pitch oscillation and therefore, the effect of the plunge motion can be added on using linear aerodynamic theory (see [Mazelsky, 1952] and [Mazelsky and Drischler, 1952]). It should be noted that if the above assumption is not employed, calculation of the aerodynamic forces becomes extremely difficult and is beyond the scope of this thesis.

2.4 Solution of the Aeroelastic Equations

The finite difference method employed to solve the aeroelastic equations, (2.25) and (2.26), was Houbolt's implicit method [Houbolt, 1950]. This method approximates the derivatives at the current time step with difference equations that depend on the position of the airfoil at the current time step and the three previous time steps. The finite difference equations for a general coordinate, η, are:

$$\dot{\eta}_n = \frac{1}{6\epsilon}[11\eta_n - 18\eta_{n-1} + 9\eta_{n-2} - 2\eta_{n-3}] \tag{2.27}$$

$$\ddot{\eta}_n = \frac{1}{\epsilon^2}[2\eta_n - 5\eta_{n-1} + 4\eta_{n-2} - \eta_{n-3}] \tag{2.28}$$

where ϵ is the constant time step size. After substituting the appropriate expressions for the derivatives of α and ξ into equations (2.25) and (2.26), the equations can be solved for α_n and ξ_n The complete equations are given in Appendix C and only the matrix formulation is given below.

$$\begin{aligned} Z_1\xi_n + Z_2\alpha_n &= Z_3 \\ Z_4\xi_n + Z_5\alpha_n &= Z_6 \end{aligned} \tag{2.29}$$

where Z_3 and Z_6 are functions of the variables at the previous time steps and Z_1, Z_2, Z_4 and Z_5 are constants.

Since Houbolt's method requires that the position of the airfoil be known for three previous time steps, a special procedure must be implemented for the first time step, when only the initial conditions are known. Given that the aerodynamic loads can be found at the initial conditions, equations (2.25) and (2.26) can be solved for the second derivatives of α and ξ at time zero. By using the second derivatives in a Taylor expansion around time zero, the position of the airfoil at times $s = +\Delta s$ and $s = -\Delta s$ can be approximated [Lee and LeBlanc, 1986b]. The position of the airfoil is now known for $s = -\Delta s$, $s = 0$ and $s = +\Delta s$; therefore, Houbolt's implicit method can be utilized to find the position of the airfoil at $s = +2\Delta s$.

Houbolt's method requires that the aerodynamic loads at time step 'n' be known in order to calculate the position of the airfoil at time step 'n'. However, because the aerodynamic loads at time step 'n' depend on the position of the airfoil at time step 'n', a recursive predictor-corrector procedure must be implemented. The first step of this procedure is to calculate the aerodynamic loads at time step 'n' based on the position of the airfoil at time step '$n-1$'. Next, these aerodynamic loads are used to calculate the predictor position of the airfoil at time step 'n', and based on this predictor value, the aerodynamic loads are recalculated. Finally, these recalculated aerodynamic loads are used to find the corrector position of the airfoil. If the absolute

difference between the predictor value and the corrector value is within a specified tolerance (approximately 1.0E-06), then the corrector value is accepted and the time step is successful. If the absolute difference is greater than the tolerance, then the entire procedure must be halted. A time step control algorithm cannot be utilized to converge to an acceptable solution because the Houbolt's method that was utilized assumes that the time step remains constant.

The convergence of this corrector-predictor method was verified using two different methods: the first method utilized different techniques to calculate the predictor values and the second method involved utilizing different time step sizes.

There are many techniques and levels of accuracy that can be utilized to calculate the predictor values of the pitch and pitch velocity of the airfoil: the lowest-order approximation of these variables is to use the values at the previous time step and higher order approximations utilize the pitch velocity and acceleration at a previous time step to estimate the pitch and pitch velocity at the next time step. If the solution is a periodic oscillation, the method and accuracy of calculating the predictor values does not influence the final corrector solution. However, if the solution is chaotic, the different methods of calculating the predictor values lead to solutions that are initially almost identical but, after a number of oscillations, these solutions diverge from one another. This type of behaviour is typical of chaotic solutions - the presence of chaos implies that knowledge of initial conditions is lost after many oscillations [Moon, 1987]. Most importantly, the chaotic behaviour of the system was found to occur regardless of the method utilized to calculate the predictor values.

The convergence of the numerical procedure was also verified using different time step sizes. For periodic solutions, the choice of the time step size, within reasonable limits, did not affect the final corrector solution and for chaotic solutions, the different

solutions would begin almost identically and then diverge from one another as time continued. For sufficiently small time steps, the recursive predictor-corrector method was found to converge for almost all cases. The only exceptions to this are cases in which the airfoil undergoes high frequency chaotic oscillations or when the airfoil is very near divergence.

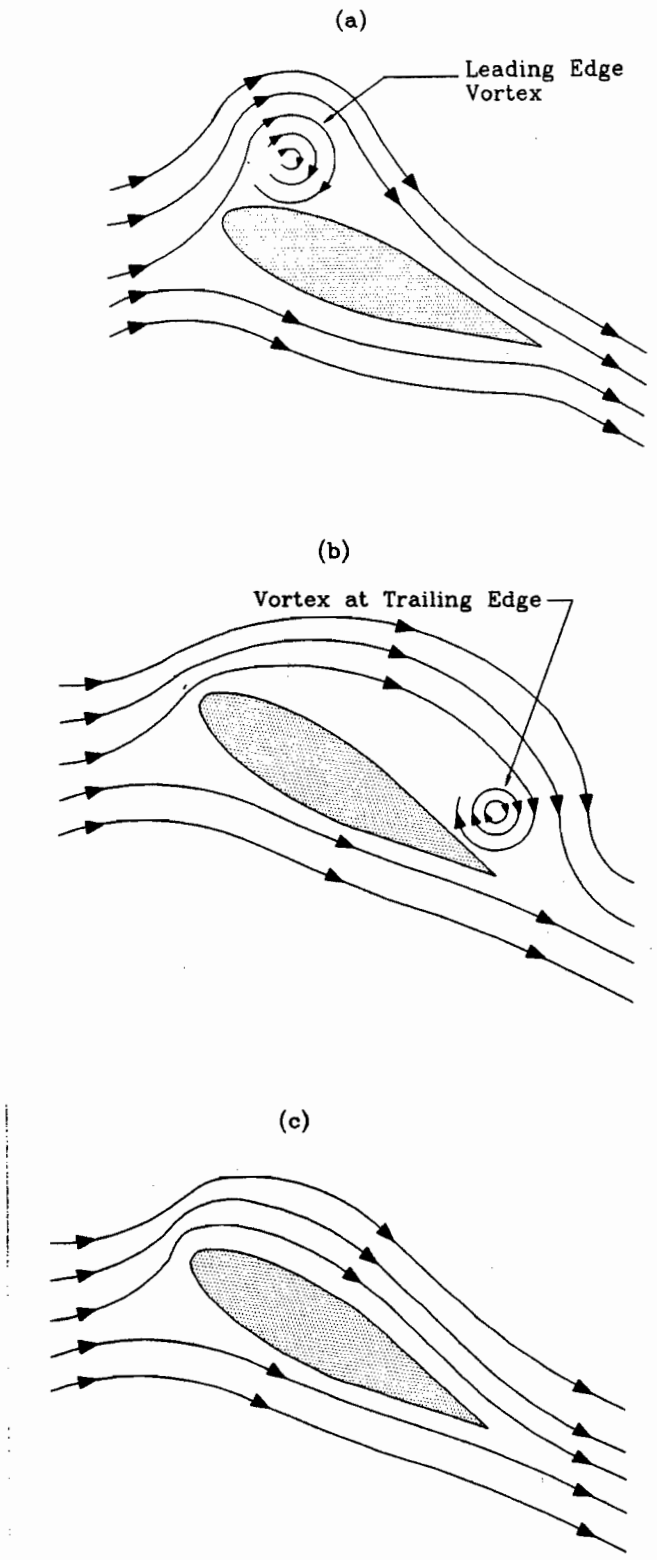

Figure 2.1: A conceptual presentation of the three main events of dynamic stall: (a) the leading edge vortex is shed from the leading edge of the airfoil, (b) the vortex arrives at the trailing edge and (c) the flow reattaches around the airfoil.

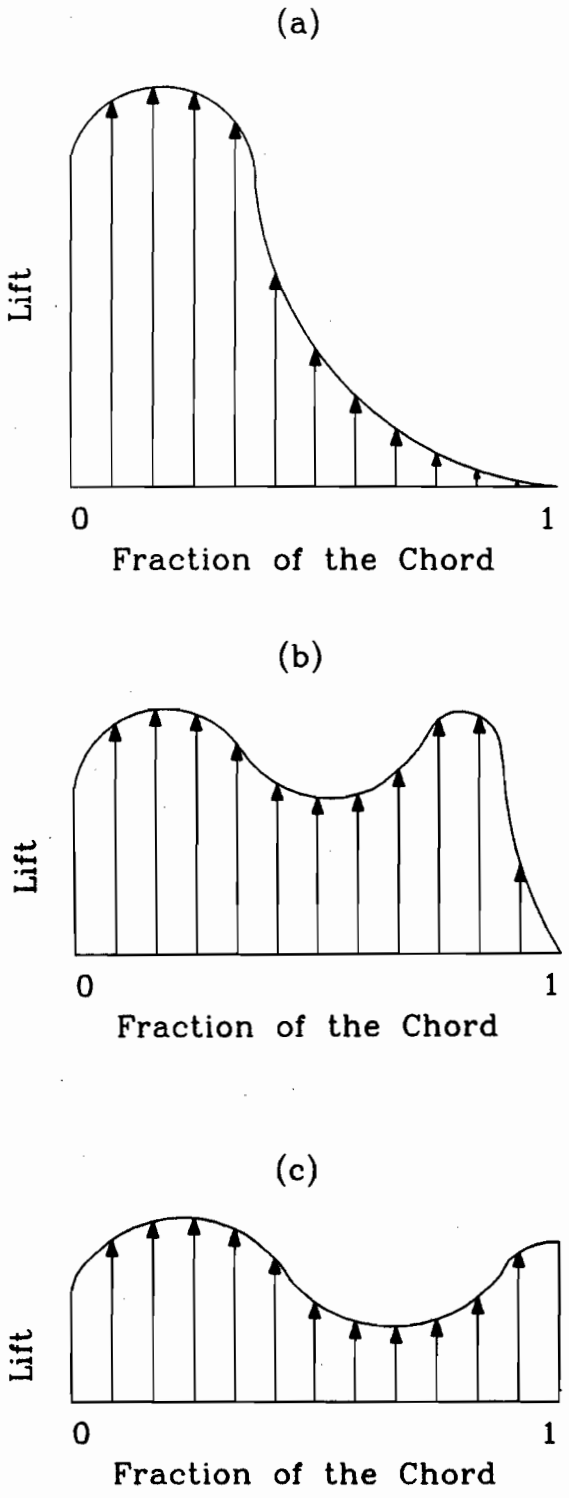

Figure 2.2: The lift distribution as a function of the chord as the leading edge vortex is convected downstream: (a) vortex at the leading edge, (b) vortex approaching the trailing edge, (c) vortex at the trailing edge.

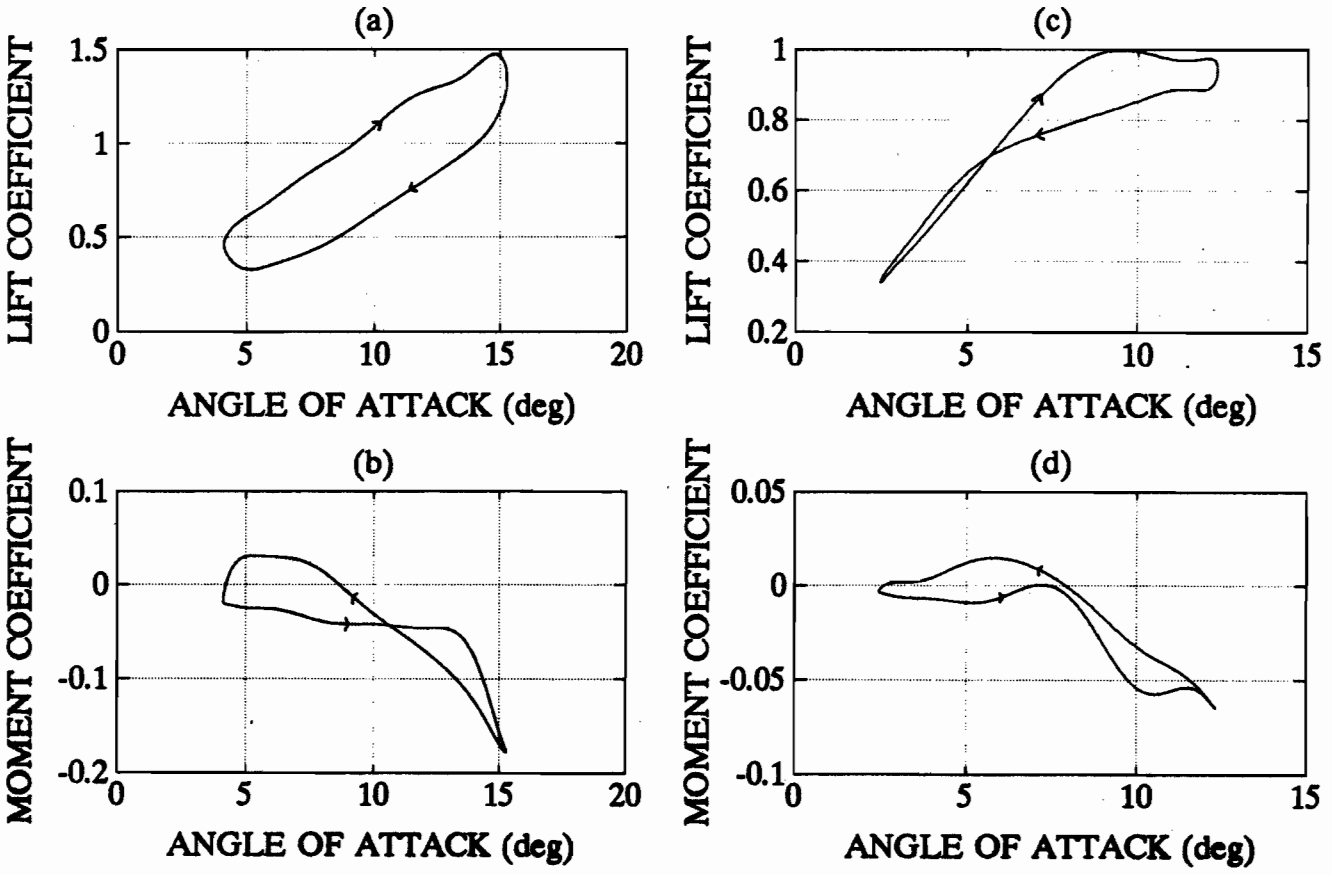

Figure 2.3: Lift and moment coefficient curves as a function of angle of attack for an oscillating NACA 0012 airfoil: (a) and (b) $k = 0.211$, $\alpha_o = 9.70^o$ and $\bar{\alpha} = 5.59^o$, (c) and (d) $k = 0.045$, $\alpha_o = 7.39^o$ and $\bar{\alpha} = 4.94^o$. (From ref. Gray, L. and Liiva, J. (1968))

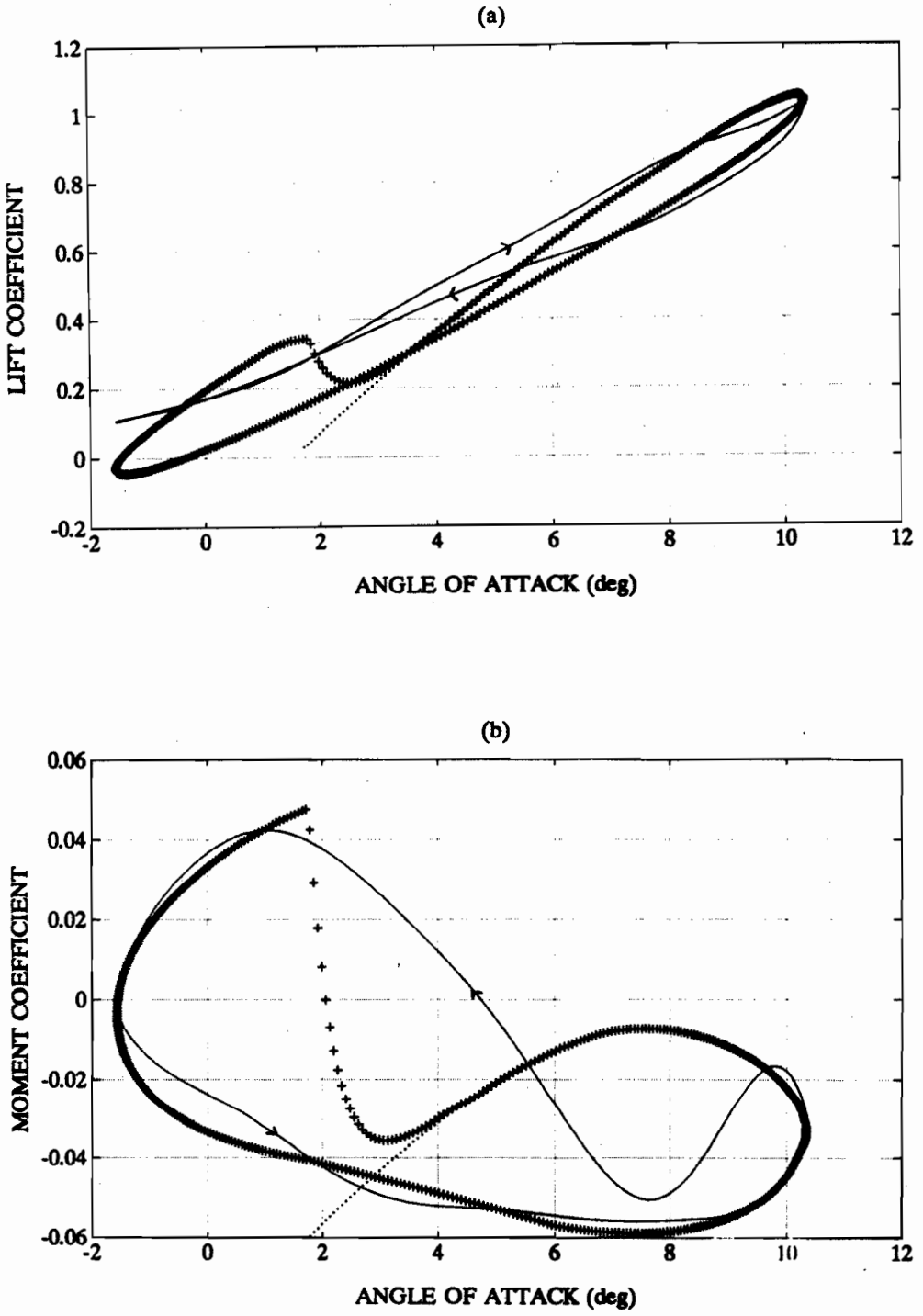

Figure 2.4: Comparison of the (a) lift coefficient and (b) moment coefficient of the actual data (solid line) with the Bielawa model (dotted line) and the modified Bielawa model ('x' line) for the cases $k = 0.252$, $\alpha_o = 4.39°$ and $\bar{\alpha} = 5.96°$.

(a)

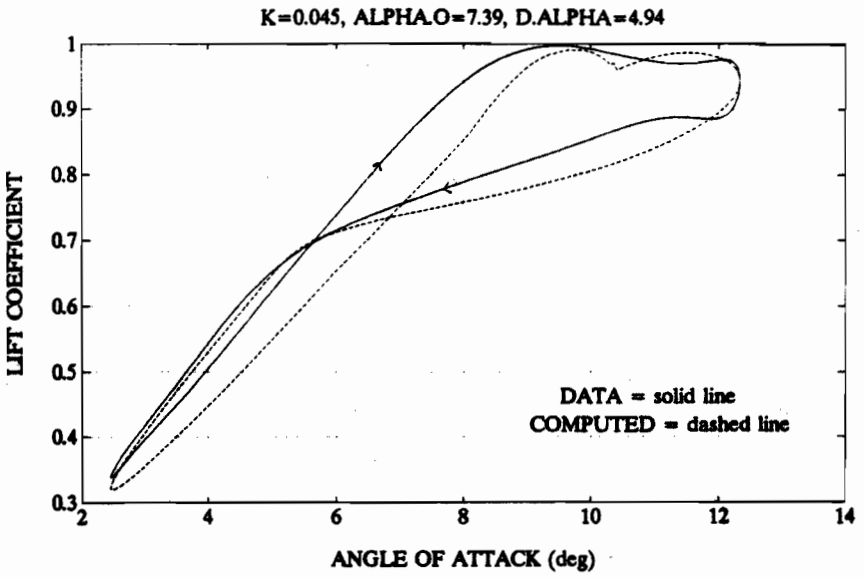

(b)

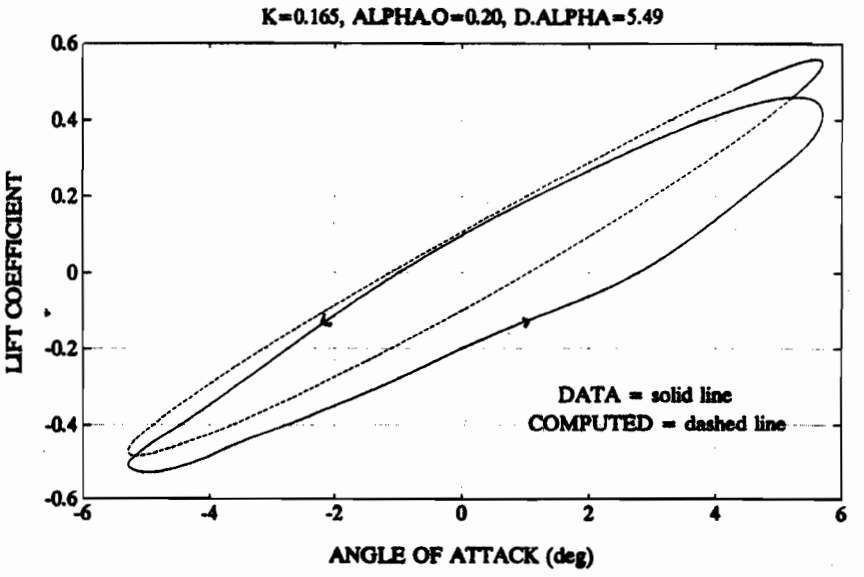

Figure 2.5: Comparison of actual lift coefficient data (solid line) with the lift coefficient predicted by the modified Bielawa model (dashed line) for cases: (a) $k = 0.045$, $\alpha_o = 7.39°$, $\bar{\alpha} = 4.94°$; (b) $k = 0.165$, $\alpha_o = 0.20°$, $\bar{\alpha} = 5.49°$; (c) $k = 0.088$, $\alpha_o = 9.75°$, $\bar{\alpha} = 5.01°$; and (d) $k = 0.129$, $\alpha_o = 7.62°$, $\bar{\alpha} = 5.28°$.

(c)

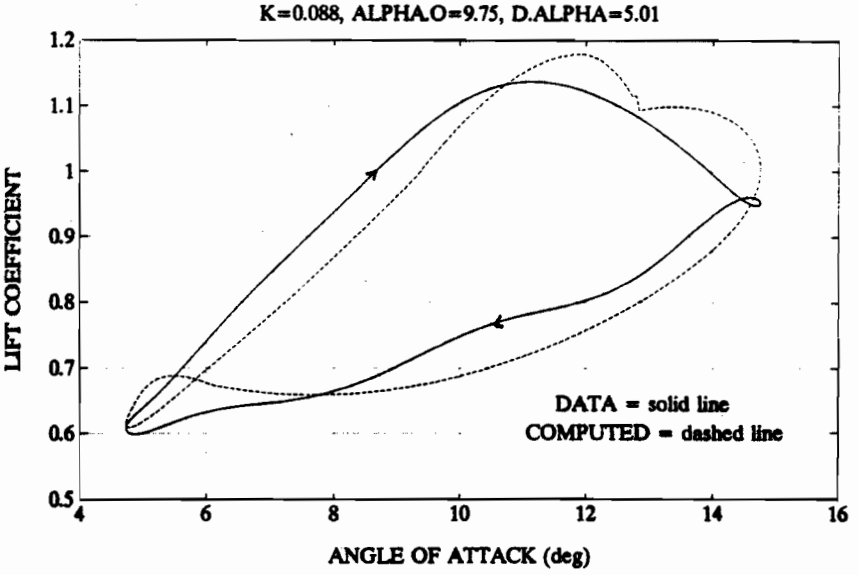
K=0.088, ALPHA.O=9.75, D.ALPHA=5.01
LIFT COEFFICIENT
ANGLE OF ATTACK (deg)
DATA = solid line
COMPUTED = dashed line
1.2
1.1
1
0.9
0.8
0.7
0.6
0.5
4
6
8
10
12
14
16

(d)

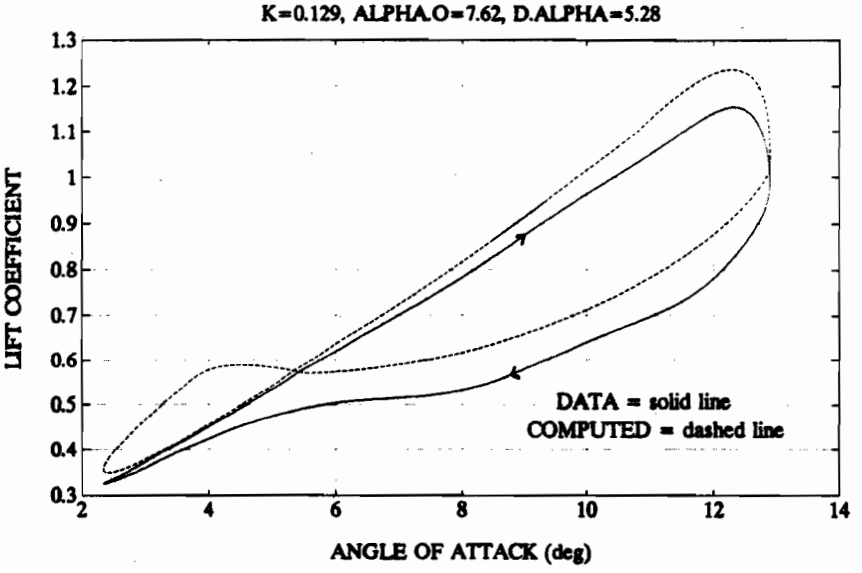
K=0.129, ALPHA.O=7.62, D.ALPHA=5.28
LIFT COEFFICIENT
ANGLE OF ATTACK (deg)
DATA = solid line
COMPUTED = dashed line
1.3
1.2
1.1
1
0.9
0.8
0.7
0.6
0.5
0.4
0.3
2
4
6
8
10
12
14

(a)

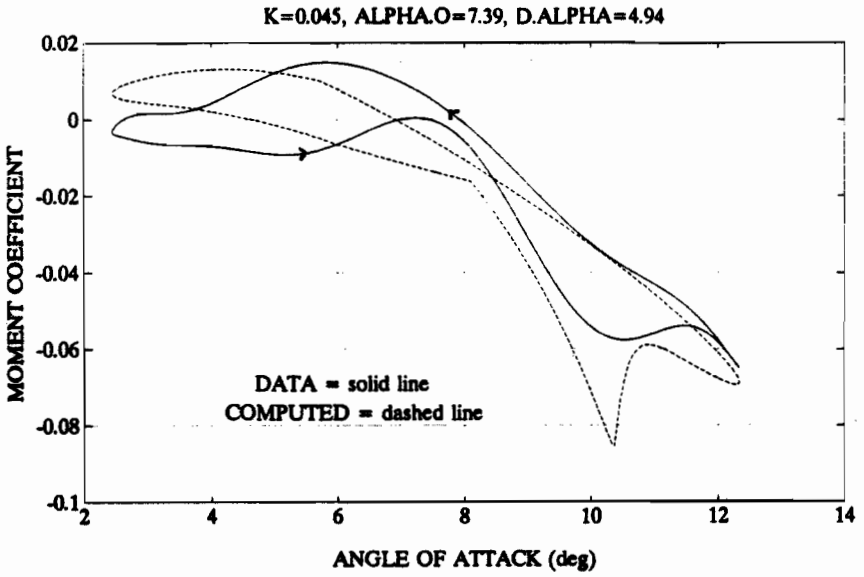

(b)

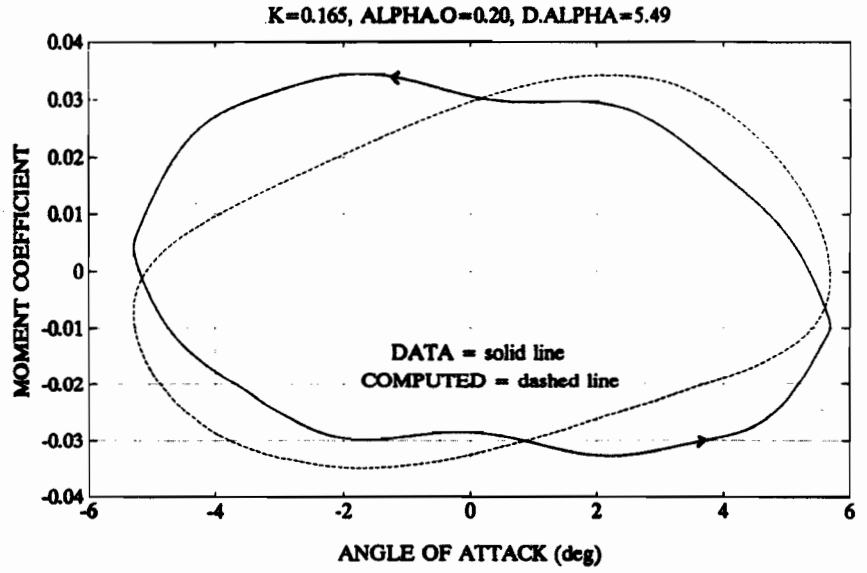

Figure 2.6: Comparison of actual moment coefficient data (solid line) with the moment coefficient predicted by the modified Bielawa model (dashed line) for cases: (a) $k = 0.045$, $\alpha_o = 7.39°$, $\bar{\alpha} = 4.94°$; (b) $k = 0.165$, $\alpha_o = 0.20°$, $\bar{\alpha} = 5.49°$; (c) $k = 0.088$, $\alpha_o = 9.75°$, $\bar{\alpha} = 5.01°$; and (d) $k = 0.129$, $\alpha_o = 7.62°$, $\bar{\alpha} = 5.28°$.

(c)

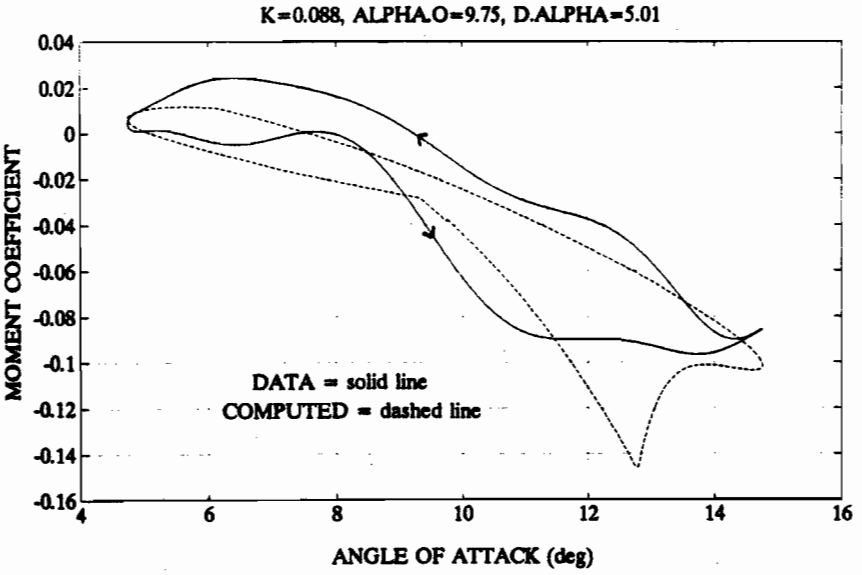
K=0.088, ALPHA.O=9.75, D.ALPHA=5.01
MOMENT COEFFICIENT
0.04
0.02
0
-0.02
-0.04
-0.06
-0.08
-0.1
-0.12
-0.14
-0.16
4
6
8
10
12
14
16
DATA = solid line
COMPUTED = dashed line
ANGLE OF ATTACK (deg)

(d)

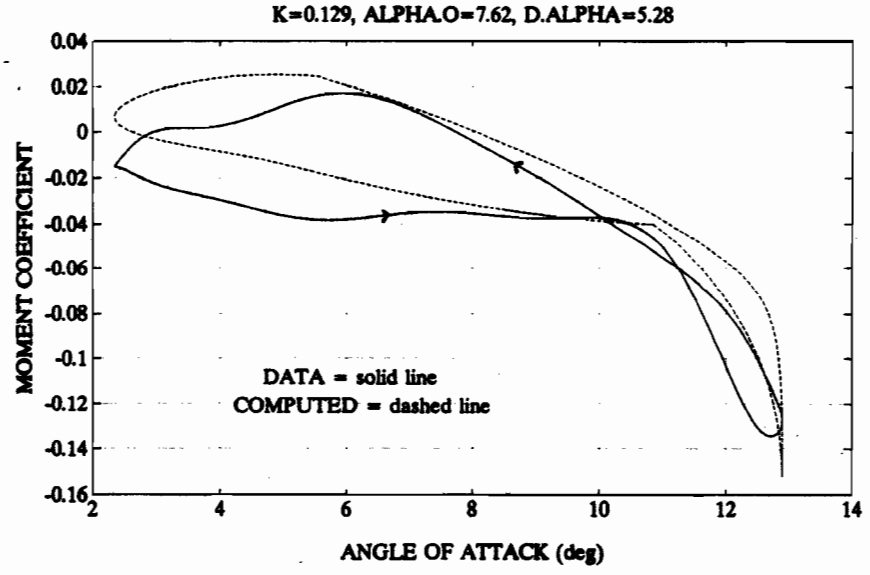
K=0.129, ALPHA.O=7.62, D.ALPHA=5.28
MOMENT COEFFICIENT
0.04
0.02
0
-0.02
-0.04
-0.06
-0.08
-0.1
-0.12
-0.14
-0.16
2
4
6
8
10
12
14
DATA = solid line
COMPUTED = dashed line
ANGLE OF ATTACK (deg)

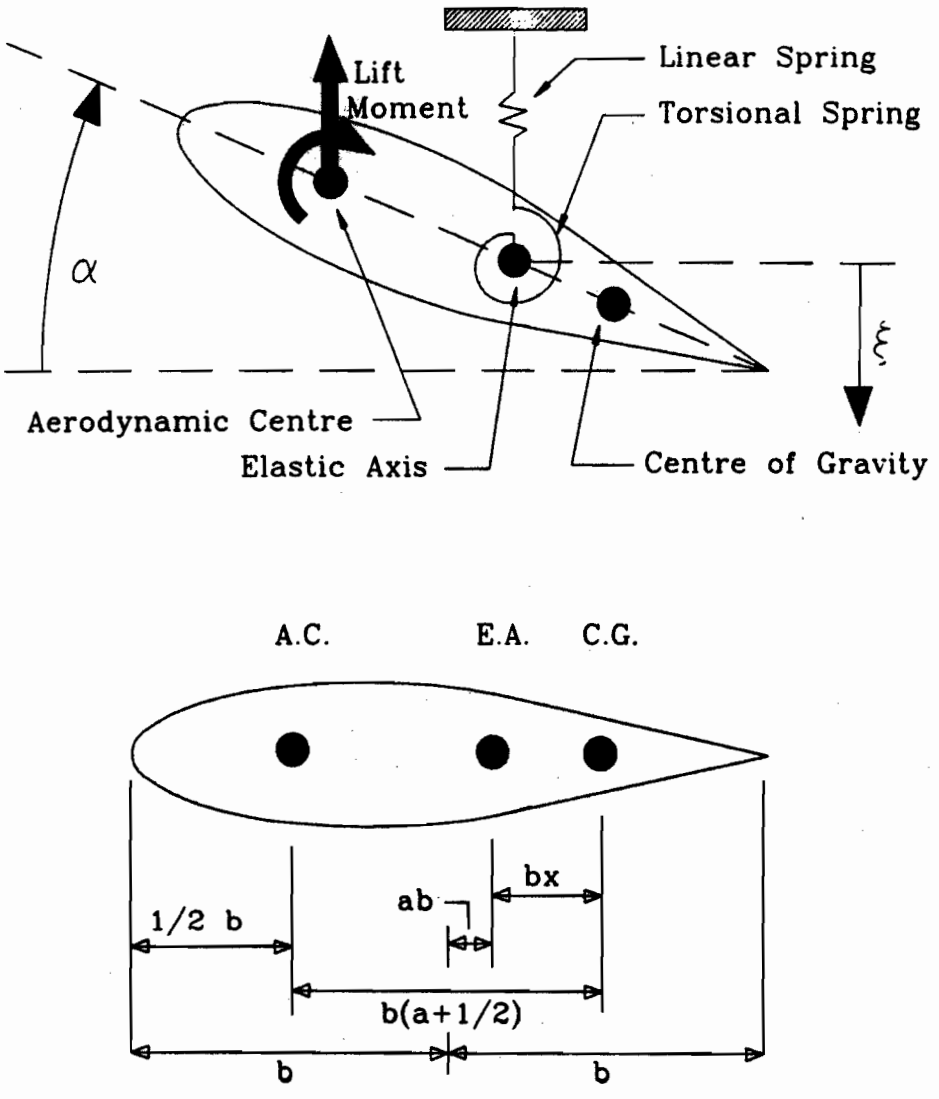

Figure 2.7: The two degree of freedom airfoil system.

Chapter 3

The One Degree of Freedom System

3.1 System Description

The general two degree of freedom system is represented by equations (2.25) and (2.26). When the ratio of uncoupled natural frequencies, $\bar{\omega}$, is very large, the stiffness in the plunge degree of freedom, ξ, is much greater than the stiffness in the pitch degree of freedom, α, and therefore, any plunging motion can be assumed to be negligible. With this assumption the two degree of freedom system reduces to the following one degree of freedom system:

$$r_\alpha^2 \ddot{\alpha} + \frac{2r_\alpha^2 \zeta_\alpha}{U^*}\dot{\alpha} + \frac{r_\alpha^2}{(U^*)^2}\alpha = \frac{2}{\pi\mu}C_M(s) + Q(s) \tag{3.1}$$

where $C_M(s) = C_{M_{c/4}} + C_{L_{c/4}}(\frac{a_h}{2} + \frac{1}{4})$ is the total moment coefficient about the elastic axis, a_h is the non-dimensional distance from the mid-chord to the elastic axis, $s = \frac{Ut}{b}$ is the non-dimensional time, $Q(s) = Q_o \sin ks$ is the non-dimensional externally applied torque about the elastic axis, $k = \frac{\omega b}{U}$ is the non-dimensional frequency of the externally applied torque and $U^* = \frac{U_b}{\omega_\alpha}$ is the non-dimensional velocity. The one

degree of freedom system is illustrated in Figure 3.1.

The lift and moment coefficients, obtained using the dynamic stall model described in the previous chapter, are about the one-quarter chord position and the unsteady lift and moment coefficient data, taken from [Gray and Liiva, 1968], are for a NACA 0012 airfoil oscillating about the one-quarter chord position. Thus, in order to most closely approximate the actual oscillating airfoil system, the position of the elastic axis was taken to be at the one-quarter chord position, hence $a_h = -0.5$ and $C_M(s) = C_{M_{c/4}}(s)$, for all the simulations that were done as part of this thesis. The centre of mass was positioned one eighth of a chord behind the elastic axis ($x_\alpha = 0.25$), the non-dimensional radius of gyration about the elastic axis, r_α, was chosen to be 0.5 and the airfoil air-mass ratio, μ, was fixed at a value of 100.

A further simplification of the system described by equation (3.1) is possible as the structural damping term is known to be small compared to the aerodynamic damping term. Therefore, the structural damping coefficient, ζ_α, is assumed to be zero in all the simulations done as part of this research.

It is not obvious from equation (3.1) what range of values of the magnitude of the externally applied torque, Q_o, should be utilized in order to obtain airfoil oscillations with reasonable amplitudes (i.e. in the range of five to fifteen degrees). Although the appropriate values of Q_o will depend on the magnitudes of all the terms in equation (3.1), as a first order approximation the appropriate values of Q_o should be of the same order of magnitude as the aerodynamic moment term, $\frac{2}{\pi\mu}C_M(s)$. Therefore, by substituting the average value of C_M into equation 3.1, it is possible to obtain an approximation of the appropriate order of magnitude of the term Q_o.

For large amplitude oscillations at very high angles of attack, the magnitude of the moment coefficient, C_M, can instantaneously be as large as 0.2, but the average

value is typically near 0.05. Substituting this average value of C_M into equation (3.1) yields a value of approximately $3*10^{-4}$ as the magnitude of the aerodynamic moment term. Therefore, the appropriate values of Q_o for reasonable amplitude oscillations should on the order of 10^{-4}.

3.2 Non-Linear Analysis Techniques

The focus of this non-linear analysis is to find when the response of the system. given by equation (3.1), becomes unpredictable or chaotic, and to describe how the transition from predictable behaviour to chaotic behaviour occurs. Since the system has only one degree of freedom and all the structural terms in equation (3.1) are linear, any chaotic vibrations could only be caused by the non-linear aerodynamic loads. The aerodynamic model, discussed in the previous chapter, is not analytical and, therefore, most of the analytical techniques developed for studying non-linear systems cannot be utilized. However, many numerical techniques exist to find and characterize chaotic vibrations. The techniques utilized herein include bifurcation diagrams, spectral analysis, phase plane plots and Poincaré sections and maps.

The first step in analysing the very complicated system dynamics was to choose a set of system parameters and generate a set of bifurcation diagrams. A bifurcation denotes a sudden change in the steady state response of a system; for example when a stable fixed point changes to a stable or unstable limit cycle motion [Moon, 1987]. Bifurcation diagrams can be constructed in many ways. In this thesis the maximum and minimum value of the angle of attack was stored over a certain number of periods, typically about 50. Then one of the system parameters was incremented and this process was repeated until a predetermined range of the system parameter was analyzed. These diagrams give a good qualitative description of how the response

of the system changes as a system parameter is varied. They also make it easy to pinpoint critical values of a system parameter at bifurcation points and they highlight regions where the oscillations may be chaotic or quasi-periodic.

The next step in the analysis was to determine if the regions found in the bifurcation diagrams were chaotic or quasi-periodic. This was done by examining the time histories, phase plane plots, Fourier spectra and Poincaré sections of the response of the system at certain values of the system parameters. The Poincaré sections were obtained by storing the value of the angle of attack and pitch rate once every period of the sinusoidal forcing function, $Q = Q_o \sin ks$. Thus, if the response of the system was periodic the Poincaré section would consist of a finite number of points, if the response was quasi-periodic it would reveal a closed curve and if the response was chaotic it would reveal a chaotic or 'strange' attractor [Moon, 1987]. As further proof of chaotic behaviour, the Poincaré maps were, wherever possible, compared to simpler analytical maps which either were known to be chaotic, or for which analytical methods could be utilized to show that the response was chaotic. A system response was labelled chaotic only if all of the aforementioned techniques yielded results that exhibited the characteristics of chaotic behaviour.

3.3 Discussion of Results

The aerodynamic loads acting on an airfoil oscillating at large angles of attack are highly nonlinear making the dynamic response of the single degree of freedom system very complicated. Furthermore, there are three independent system parameters that, when varied, strongly influence the dynamic response of the system; these are the amplitude of the non-dimensional externally applied torque, Q_o, the non-dimensional velocity, U^*, and the non-dimensional frequency of the externally applied torque, k.

A close examination of the single degree of freedom equation (3.1) reveals that the inverse of the non-dimensional velocity represents the non-dimensional structural natural frequency of the airfoil. Thus, the product of the non-dimensional frequency of the externally applied torque, k, and the non-dimensional velocity, U^*, gives the ratio of the forcing frequency to the structural natural frequency. Another important point to note, which is not obvious from equation (3.1), is that the structural natural frequency and the natural frequency of the system will not, in general, be the same because the aerodynamic moment term, $\frac{2}{\pi\mu}C_M(s)$, will contain stiffness terms. Furthermore, due to the complicated nature of the aerodynamic loads, the natural frequency of the system cannot be calculated explicitly.

The non-linear analysis attempted herein is divided into four different case studies based on the values of the system parameters for which chaotic oscillations were found and the type of chaos that occurred. The first case study is for low frequency, high velocity, intermittent chaos; the second is for low frequency, low velocity intermittent chaos; the third is for low frequency, high velocity, classical chaos; and the fourth case study is for high frequency, high velocity, classical chaos.

3.3.1 Case I: Low Frequency, High Velocity, Intermittent Chaos

This section considers the possibility that chaotic vibrations occur for airfoils forced to oscillate at high initial angles of attack, α_o (this is the angle of attack of the airfoil at time zero), low non-dimensional frequencies, k, and high non-dimensional velocities, U^*. The first stage in this investigation is to develop a general picture of the overall behaviour of the system as certain system parameters are varied over a wide range of values. Bifurcation diagrams are presented in which the amplitude of the non-dimensional externally applied torque, Q_o, the non-dimensional velocity, U^*, and the non-dimensional frequency of the externally applied torque, k, are varied over a wide range of values in an effort to discover any regions of potentially chaotic behaviour. Next, these potentially chaotic regions are more closely examined by providing more detailed bifurcation diagrams that focus only on the range of parameters for which the response may be chaotic. The response in these regions is explored further by comparing the time traces, phase plots and Fourier spectra for four separate cases in order to illustrate how the response changes as one of the system parameters is varied. The Poincaré sections for these cases are then examined to show the long term behaviour of the system and to help classify the response as either chaotic or quasi-periodic.

Bifurcation Diagrams

The first set of system parameters considered were: the initial angle of attack, $\alpha_o = 8.90^o$, the non-dimensional velocity, $U^* = 21.0227$, and the non-dimensional forcing frequency, $k = 0.044$. The first bifurcation diagram, Figure 3.2, was obtained by allowing the value of Q_o to vary over the range $(0.0 < Q_o < 1.18 * 10^{-4})$,

while the rest of the system parameters were held constant. In Figure 3.2, it can be seen that the amplitude of the response of the airfoil increases almost linearly as the magnitude of Q_o increases. Furthermore, the system undergoes two period doubling bifurcations, the first at approximately $Q_o = 0.20 * 10^{-4}$ and the second at approximately $Q_o = 0.88 * 10^{-4}$. A region of possibly chaotic motion can be seen to exist in the range $(1.00 * 10^{-4} < Q_o < 1.09 * 10^{-4})$, and for values of Q_o larger than $1.09 * 10^{-4}$ the system returns to a stable period two oscillation.

The next bifurcation diagram was obtained by fixing the value of $Q_o = 1.02 * 10^{-4}$, which is in the apparently chaotic region of Figure 3.2, and allowing the value of U^* to vary over the range $(5.0 < U^* < 23.0)$. The results, illustrated in Figure 3.3, show that the amplitude of the response generally increases as the magnitude of U^* increases, and that the system undergoes a period doubling bifurcation at approximately $U^* = 10.4$. A region of possibly chaotic motion exists for values of U^* in the range $(20.5 < U^* < 21.2)$.

To create the third bifurcation diagram, Q_o and U^* were held constant at values of $1.02 * 10^{-4}$ and 21.0227, respectively, while the non-dimensional forcing frequency, k, was varied over the range $(0.02 < k < 0.225)$. The value of $U^* = 21.0227$ corresponds to a non-dimensional structural natural frequency of 0.0476. The results, illustrated in Figure 3.4, reveal that the response of the system increases to a maximum near $k = 0.075$ and decreases for larger values of k. The system can be seen to undergo several different types of bifurcations, and there are two regions of possibly chaotic behaviour. The focus of the remainder of this section will be on the low frequency region, near $k = 0.044$. The higher frequency region, near $k = 0.170$, will be discussed in a later section.

The bifurcation diagrams in Figures 3.2,...,3.4 give the amplitude of oscillations

that are obtained as certain system parameters are varied over a wide range of values. However, the most interesting system dynamics occur in the narrow regions where the response is potentially chaotic. In Figures 3.5 - 3.7, the bifurcation diagrams are expanded in the regions where the response of the system changes from periodic motion to chaotic or quasi-periodic motion.

In the bifurcation diagram shown in Figure 3.5, Q_o is varied over a small range of values ($0.98 * 10^{-4} < Q_o < 1.10 * 10^{-4}$). This corresponds to the region in Figure 3.2 where the response of the system begins to appear chaotic or quasi-periodic. As Q_o is increased from $0.98 * 10^{-4}$ the well defined lines, characteristic of periodic motion, begin to spread out or diffuse into one another. Furthermore, at values of Q_o equal to approximately $1.003 * 10^{-4}$ and $1.0062 * 10^{-4}$, the system appears to undergo complicated bifurcations; these are indicated by the appearance of many new lines or regions where the lines diffuse suddenly. These new lines are unstable and diffuse quickly as Q_o is increased indicating that the oscillations corresponding to these lines are not very stable. According to this bifurcation diagram, the response of the system is chaotic or quasi-periodic for Q_o greater than approximately $1.0062 * 10^{-4}$, and the transition from periodic to chaotic or quasi-periodic behaviour is a gradual decrease in the stability of the periodic oscillations. This bifurcation diagram does not provide a means of clearly defining a critical value of the parameter Q_o. A critical value should divide the region of periodic behaviour from the chaotic or quasi-periodic region, but in fact the chaotic or quasi-periodic behaviour tends to creep gradually into the solutions. After Q_o exceeds a value of approximately $1.079 * 10^{-4}$, the response returns to a stable, period two oscillation. Within the apparently chaotic region ($1.0062 * 10^{-4} < Q_o < 1.079 * 10^{-4}$), there are smaller regions where the response is stable and periodic, for example near $Q_o = 1.058 * 10^{-4}$ and $Q_o = 1.065 * 10^{-4}$.

In Figure 3.6, the non-dimensional velocity, U^*, is varied over the apparently chaotic region, ($20.00 < U^* < 21.38$) of Figure 3.3. The system undergoes bifurcations at several values of U^*, including 20.13, 20.19 and 20.46. The response of the system appears to become chaotic or quasi-periodic for values of U^* greater than approximately 20.66. However, once again it is difficult to define a critical value with certainty because the transition to chaotic or quasi-periodic motion is gradual. The system returns to a stable, period two oscillation for values of U^* greater than approximately 21.35.

The small chaotic or quasi-periodic region shown in Figure 3.4, near $k = 0.044$, is shown in more detail in Figure 3.7. As the non-dimensional frequency, k, is increased to values greater than approximately 0.041, the response of the system can be seen to undergo a series of bifurcations. The response appears to be chaotic or quasi-periodic for values of k greater than approximately 0.0434, whereas, for k greater than approximately 0.045, the response suddenly returns to a stable, period-two oscillation. Furthermore, just prior to the onset of the chaotic or quasi-periodic motion at $k = 0.0433$, the response is stable and periodic, and other smaller regions within the chaotic or quasi-periodic region also show signs of periodic behaviour.

Case Studies

The next stage in the nonlinear analysis consists of comparing the time histories, phase plane plots and Fourier spectra for four different test cases. In these test cases the non-dimensional velocity, U^*, and the non-dimensional frequency, k, were fixed at 21.0227 and 0.044, respectively, while the value of Q_o was set at $1.00 * 10^{-4}, 1.006 * 10^{-4}, 1.02 * 10^{-4}$ and $1.05 * 10^{-4}$.

Figure 3.8 shows a small section of the time history of the response for each of the four different test cases. In Figure 3.8 (a), the response is a stable, period-four

oscillation. The responses shown in Figure 3.8 (b), (c), and (d) exhibit some higher order periodic, or even quasi-periodic behaviour. The pattern of the response repeats itself over the time interval shown in Figure 3.8 (b) and (d), and the period of the response in Figure 3.8 (c) is of the order of the time interval shown.

Figure 3.9 shows the phase plane plots, over the same time interval as in Figure 3.8, for the four different test cases. In Figure 3.9 (a), the response remains in a stable, period four oscillation, while, in Figure 3.9 (b), the stable curve begins to break down and the plot suggests a higher order periodic response. In Figure 3.9 (c), the period reaches a maximum, and it is not obvious whether the response repeats itself over the given time interval, whereas, in Figure 3.9 (d), the response returns to a high order periodic oscillation.

The Fourier spectra of the four different responses are shown in Figure 3.10. Figure 3.10 (a) confirms that the response for the case in which $Q_o = 1.00 * 10^{-4}$ is a period four oscillation. The largest spike occurs at the forcing frequency, $k = 0.044$, with three other subharmonic spikes at $k = 0.011, k = 0.022$ and $k = 0.033$. The higher frequencies shown are the higher order harmonics of these four main frequency components. In Figure 3.10 (b), there are many well defined subharmonic spikes, indicating that the response, over the given time interval, is periodic. In Figure 3.10 (c), it is difficult to define any subharmonic spikes; instead the response has more of a broad band spectrum, indicating that the response may be chaotic. The Fourier spectrum shown in Figure 3.10 (d) contains many well defined spikes confirming that the response is once again periodic over the given time interval.

Poincaré Sections

The next step in the analysis involves studying the long term behaviour of the response by examining the Poincaré sections. Each Poincaré section was constructed

with a minimum of twenty thousand points, corresponding to a time interval equal to twenty thousand periods of the forcing function. Furthermore, before any points were retained, the system was allowed to run for a minimum of one hundred periods to allow time for any transient motions to die out.

The Poincaré section for the case where $Q_o = 1.00 * 10^{-4}$ is shown in Figure 3.11 (a). The four groups of points shown in this plot indicate that the response of the system is a period four oscillation. However, since the groups are not exact points. this period-four oscillation is not perfectly stable. In Figure 3.11 (b), each pitch data point is plotted versus the number of the period for which that data point was obtained, therefore, the x-axis can be interpreted as a discretized time variable. This method of plotting the Poincaré data is useful in helping to determine the long term behaviour of the system since the general characteristics of the long term behaviour can be captured with very few data points. Figure 3.11(b) shows that the period-four response remains stable for approximately the first ten thousand periods, but becomes slightly unstable for an almost equally long time before settling back down to the original period four oscillation. The response is not chaotic while the period four attractor is slightly unstable, instead it changes from one high order periodic state to another, as indicated by the different lines that appear in the plot. These new higher order periodic states may exist for only a few periods or they may exist for several hundred periods.

The next Poincaré section, for the case where $Q_o = 1.006 * 10^{-4}$, is given in Figure 3.12 (a). The four groups of points observed in Figure 3.11 (a) have diffused into fine lines and a pattern is beginning to emerge in the way the data points are distributed in the phase plane. This pattern is normally referred to as an attractor. Figure 3.12 (b) illustrates that the response changes from one periodic state to another, and

that each state may remain stable for up to several hundred periods. Occasionally as the response of the system is changing from one of these periodic states to another, it will become very highly periodic, perhaps even quasi-periodic or chaotic, but this behaviour lasts only for a very short period of time, on the order of about ten periods.

The structure of the attractor is clearly visible in the Poincaré section for $Q_o = 1.02 * 10^{-4}$, shown in Figure 3.13 (a). Aside from one small area near the top of the plot, all the data points fall along several very well defined curves. From Figure 3.13 (b), the long term behaviour of the system can be seen to be very complicated. Initially the response is a high-order periodic oscillation and it remains in this state for approximately the first 2500 periods, then the response goes through approximately 500 oscillations where it is either quasi-periodic or chaotic, then it returns to a periodic oscillation that remains stable for approximately 5000 periods.

The periodic response then suddenly becomes unstable. During this unstable phase the response undergoes frequent transitions from high order periodic phases to quasi-periodic or chaotic phases, and the number of different high order periodic phases is very large. As can be seen from the plot, these high order periodic phases appear in a seemingly random fashion and can remain stable for as long as several hundred periods. On the other hand, the quasi-periodic or chaotic phases are usually very short, on average lasting only about ten periods before the response restabilizes into a new and different high order periodic phase. After approximately 8000 periods the response stabilizes into another periodic oscillation, this time a period-one oscillation. After approximately 4000 periods this response becomes unstable and the more complicated behaviour returns.

The attractor shown in the Poincaré section in Figure 3.14 (a) is for the case in which $Q_o = 1.05 * 10^{-4}$. The overall shape of this attractor is very similar to the

shape of the attractor in Figure 3.13 (a), for the case where $Q_o = 1.02 * 10^{-4}$, except that it has been stretched into a slightly different orientation in the phase plane. This different orientation of the attractor results in a different overall pattern of the response, which is illustrated in Figure 3.14 (b). The response does not remain in any periodic state for as long as in the previous case as the maximum time span for a periodic state to exist is reduced from approximately 5000 to 1000 periods. However these periodic states occur more frequently so that the periods of chaotic or quasi-periodic behaviour are distributed more evenly over the time interval shown.

The attractors in Figures 3.13 (a) and 3.14 (a) are not as one-dimensional as the Figures suggest. The regions outlined in boxes in Figure 3.13 (a) are shown in detail in Figure 3.15 (a) and (b). In these enlarged views, the attractor can be seen to vary in thickness with definite boundaries defining its shape. Within the boundaries of the attractor there is an internal structure: the data points are distributed in short, discrete, quasi-parallel groups that are approximately perpendicular to the orientation of the attractor.

Poincaré Maps and Intermittent Chaos

To examine how the complicated behaviour illustrated in Figures 3.13(b) and 3.14(b) arises, the case where $Q_o = 1.02 * 10^{-4}$ will be studied in further detail by examining the Poincaré data in the form of first and second return maps. The first return map plots the '$n+1$' pitch data point versus the 'n' pitch data point, similarly the second return map plots the '$n+2$' pitch data point versus the 'n' pitch data point. With these maps, the response of this system can be shown to share some similarities with systems that exhibit intermittent chaos.

Intermittent chaos is observed in theoretical systems, such as the Lorenz model, and also in experimental systems, such as Rayleigh-Bérnard convection

[Bergé et al., 1986]. The response of a system exhibiting classical intermittent chaotic behaviour will be periodic for a certain length of time, then there will be a short burst of chaotic activity followed by a return to the same periodic behaviour. The transition from a chaotic burst back to periodic behaviour is known as the relaminarization of the response. There are three different types of classical intermittency, types I, II and III, each having different qualitative characteristics.

Type I intermittency involves the destabilization of a periodic trajectory, for values of a system parameter greater than a critical value, caused by the crossing of an eigenvalue of the Floquet matrix with the unit circle of the complex plane at +1 [Bergé et al., 1986]. The main characteristic of type I intermittency is that a laminarization channel exists in the first return map. This channel is a region of the attractor that lies near the identity line (the 45° line) and is tangent to the identity line at some point, a typical channel is illustrated in Figure 3.16 (a). The response enters this channel at a point near the bottom end and, with successive iterations of the map, it moves through the channel as shown. While the response is in the channel it is reasonably stable and therefore the behaviour of the system appears periodic. The length of time required for the response to move through the channel can be relatively long depending on the width of the channel. After the system leaves the channel it moves to another part of the phase plane where the attractor is chaotic, this corresponds to a chaotic outburst in the response. The system will remain in the chaotic region of the phase plane until it is mapped back to the beginning of the channel, this is the relaminarization process. The length of time that the response spends in the laminar phase depends on the type of intermittency, for type I intermittency the probability of the response remaining in a laminar phase of length 'T' is given by the characteristic distribution shown in Figure 3.16 (b). The

shape of this distribution indicates that for type I intermittency there will be many laminar phases of approximately the same length, some very short laminar phases and there is a definite maximum laminar phase length which is system dependant.

Type II intermittency is caused by two complex conjugate eigenvalues of the Floquet matrix crossing the unit circle of the complex plane [Bergé et al., 1986]. The theory of type II intermittency is reasonably well understood but, as of yet, there have been no examples of systems, either numerical or experimental, which have been proven to exhibit type II intermittent chaos.

Type III intermittency is caused by an eigenvalue of the Floquet matrix crossing the unit circle of the complex plane at -1 [Bergé et al., 1986]. The laminarization channel for this type of intermittency is found in the second return map and is illustrated in Figure 3.17 (a). This characteristic shape in the second return map is caused by the first return map crossing the identity line at a slope slightly less than -1. While the system is in this channel the response is periodic, as in type I intermittency, an important characteristic of this type of intermittency is that the approach of the chaotic outburst is signalled by the growth of a subharmonic oscillation. This subharmonic oscillation increases in amplitude until at some point there is a chaotic burst, usually in the form of a sudden increase in the amplitude of the response. The characteristic probability distribution of the average lengths of time of the laminar phases is shown in Figure 3.17 (b). This distribution illustrates that for type III intermittency there is a definite minimum length of the laminar phases and that some laminar phases can last for a very long time.

The first return map for the case of $Q_o = 1.02 * 10^{-4}$ is shown in Figure 3.18 (a). The attractor can be divided into three separate regions: the first, for angles of attack less than approximately 0.9 degrees, consists of an almost straight line; the second,

for angles of attack between 0.9 and 3.6 degrees, consists of three curves, two of which cross the identity line at slopes less than -1; the third, for angles of attack greater than 3.6 degrees, consists of a single short line. The corresponding second return map, shown in Figure 3.18 (b), is composed of several curves distributed throughout the plane. The first and second return maps for the case where $Q_o = 1.05 * 10^{-4}$, shown in Figures 3.19 (a) and (b) respectively, are very similar in appearance.

These return maps do not show the type of characteristics described previously for systems that exhibit classical type I or type III intermittency. Furthermore, the long term behaviour of the system, as illustrated in Figures 3.13 (b) and 3.14 (b), is not typical of these types of intermittency in two respects. Firstly, the responses show regions of very long periodic phases and very short periodic phases. This is especially true for the case illustrated in Figure 3.13 (b), which suggests that the behaviour is a combination of type I and type III intermittency, and secondly, after each chaotic burst the system does not return to the same periodic oscillation but instead tends to find a new periodic state.

The reason the response can be labelled as intermittently chaotic is because of the time scale of the chaotic behaviour and the marginal stability of the response. To illustrate the time scale of the chaos consider the following: if the response is analyzed over any short period of time (less than approximately 200 periods), one may find that it is periodic and stable, however, if a longer time scale is chosen the response will be chaotic because, even though the behaviour is mostly periodic, the final state of the system is completely unpredictable. Furthermore, since the response of the system spends most of its time in a periodic oscillation, and the unstable phases are usually very short, the behaviour of the system can be described as marginally stable. It is these two characteristics that the system shares with other

systems that exhibit the more classical types of intermittency.

One of the purposes of comparing the intermittently chaotic behaviour of this system with systems that exhibit classical intermittency is to illustrate that there are important differences in the long term behaviour of the two cases. It is important to remember that the type of intermittently chaotic behaviour found herein is a direct result of the numerical dynamic stall model. Therefore, like any other numerical model, the long term behaviour of the system, as illustrated by the Poincaré sections and maps, should show behaviour similar to other numerical models regardless of their origin. However, the type of marginally stable long term behaviour exhibited by this system seems to be unique to this particular model. Furthermore, since this behaviour is a product of the numerical model it cannot be stated absolutely that it is the result of the dynamic stall phenomenon, only that it is the result of this particular dynamic stall model.

Analytical Modelling of the Return Maps

In order to better understand the complicated behaviour of this system, the first return map was modelled by the analytical system given below:

$$x_{n+1} = \begin{cases} -0.6x_n + 0.645, & \text{for } 0 <= x_n < 0.4 \\ (x_n + 0.6)^{-\gamma}, & \text{for } 0.4 <= x_n <= 1.0 \end{cases} \tag{3.2}$$

This model of the first return map was obtained by inspection and it should be noted that it is not identical to the system first return map; it is not multi-valued and the region being mapped has been scaled to fit the region ($0 <= x_n <= 1.0$). However, the general shape of the attractor, shown in Figures 3.18 (a) and 3.19 (b), is captured by this model with only a single parameter, γ.

In Figures 3.20 (a), (b) and (c) the first return map , the second return map and the long term behaviour of this analytical system, respectively, are shown for

the case where the value of γ is equal to 11.00. These plots illustrate that the behaviour of the system is periodic, however, a large number of iterations of the map are required before the system repeats itself. In Figures 3.21 (a), (b) and (c) the value of γ is increased to 11.05 and, as can be seen from the plots, this almost imperceptible change in the orientation of the attractor results in a significant change in the dynamics of the map. The value of γ is increased to 11.10 in Figures 3.22 (a), (b) and (c) and the system dynamics once again undergo a significant change back to a periodic state. It is evident from the plots in Figures 3.20 to 3.22 that for very small changes in the value of the parameter γ, resulting in slight changes in the orientation of the attractor, a wide range of highly periodic and chaotic responses can be created.

The Lyapunov spectrum for this analytical system is shown in Figure 3.23 for a narrow range of values of the parameter γ. It should be noted that the Lyapunov exponent for the case where $\gamma = 11.00$ is greater than zero, which indicates a chaotic response, however, from Figures 3.20 (a) - (c) it is obvious that the response is not chaotic. In this case, the periodicity of the map is so large that an infinite number of iterations of the map would be required for the Lyapunov exponent to approach zero. These highly periodic states are the dominant type of response for the system for values of the parameter γ in the range $(10.0 < \gamma < 13.2)$.

In Figure 3.24 the region outlined by the boxes in Figure 3.18 (a), which is the first return map for the case where $Q_o = 1.02 * 10^{-4}$, is shown in greater detail. The internal structure of the attractor consists of short lines or small groups of data points, similar to those in Figures 3.15(a) and (b). Different combinations of these groups of data points correspond to different periodic solutions. The quantized structure of the attractor implies a periodic response because it consists of a finite

number of groups of points, but, since these groups of points have a two dimensional structure and are not one dimensional points, the periodic responses are unstable.

An example of the implications of this quantized internal structure can be seen from the data for the case where $Q_o = 1.02 * 10^{-4}$. According to Figure 3.13 (b), after approximately 16500 periods the system begins a marginally stable period-one oscillation that persists for approximately 4000 periods. In order for a marginally stable period one oscillation to exist the attractor of the first return map must intersect the identity line at a slope slightly greater than -1 or slightly less than $+1$, otherwise successive iterations of the map will quickly move away from the intersection point and the period-one oscillation will be unstable. The orientation of the attractor for the first return map, shown in Figure 3.18(a), shows that the slope of the attractor at the intersection point is significantly less than -1, therefore, no stable period-one oscillation should exist. However, as seen in Figure 3.24, the microscopic structure of the attractor makes it possible for two of the internal structures of the attractor to intersect the identity line at slopes that result in a marginally stable period-two oscillation. The two internal structures are so close to the identity line that, at the normal scale of the Poincaré map, this marginally stable period-two oscillation appears as a period-one oscillation.

By examining the Poincaré data at the microscopic level, it is obvious that the internal structure of the attractor plays an important role in the marginal stability of this type of chaotic response. However, how this particular internal structure develops is still unclear.

Evidence of Transient Chaos

Continuing the discussion of the long term behaviour of the system, the Poincaré section for the case where $Q_o = 1.05 * 10^{-4}$ was obtained for the time interval from

twenty thousand periods to fifty thousand periods of the forcing function, and is shown in Figure 3.25(a). The long term behaviour of the system, shown in Figure 3.25(b), indicates that the previously described complicated behaviour persists for up to approximately forty thousand periods, however, after this point a pattern begins to emerge. This pattern is comprised of blocks, approximately 4000 periods in length, which repeat themselves. This indicates that the response has undergone a transition from unpredictable, chaotic oscillations to predictable, quasi-periodic oscillations.

Further evidence of this transition from chaotic to quasi-periodic behaviour can be seen by studying the internal structure of the attractor; the region of the attractor outlined by the box in Figure 3.25(a) is shown in greater detail in Figure 3.26. The pattern of the attractor repeats itself as the entire structure appears to drift downward and slightly to the left in the phase plane. It is not unreasonable to extrapolate these results and assume that if the simulation were allowed to continue for many thousands more periods the structure of the attractor would trace a closed curve in the phase plane. As stated earlier, a Poincaré section that traces a closed curve in the phase plane is indicative of a quasi-periodic response.

The preliminary indications from this very long term analysis of the response is that the intermittent chaotic oscillations, characterized by phases of periodic behaviour mixed with phases of quasi-periodic or chaotic behaviour, may be transient in nature. However, due to the limits imposed by the amount of memory required to run a simulation of the system for the required length of time, confirmation of the possible transient nature of the chaos will have to be left for future investigation.

3.3.2 Case II: Low Frequency, Low Velocity, Intermittent Chaos

In this section, the system dynamics are analyzed for a case where the airfoil is forced to oscillate at a relatively low non-dimensional frequency, $k = 0.088$, low non-dimensional velocity, $U^* = 12.20$, and high initial angle of attack, $\alpha_o = 9.76^o$. The response of the system is first presented in a bifurcation diagram in which Q_o is varied over a wide range of values, then the region where the response is quasi-periodic or chaotic is presented in a more detailed bifurcation diagram. The response of the system is then analyzed for many different test cases within the apparently chaotic region and for each of these test cases the time histories, phase plane plots, Fourier spectra and Poincaré sections are analyzed.

Bifurcation Diagrams

In Figure 3.27, the bifurcation diagram for the case where $\alpha_o = 9.76^o$, $k = 0.088$, $U^* = 12.20$ and where the value of Q_o is varied over the range $(5.0 * 10^{-5} < Q_o < 12.0 * 10^{-5})$ is presented. The large region $(6.3 * 10^{-5} < Q_o < 7.2 * 10^{-5})$, where the response becomes either quasi-periodic or chaotic, is the main focus of this section. There are other regions where the response appears to go unstable, for example at approximately $Q_o = 7.8 * 10^{-5}$ and $Q_o = 8.4 * 10^{-5}$, however, due to time constraints, these regions will have to be left for future studies.

The region $(6.12 * 10^{-5} < Q_o < 7.30 * 10^{-5})$ is shown in more detail in Figure 3.28. The response can be seen to undergo many bifurcations as the value of Q_o is increased and it appears to be either quasi-periodic or chaotic for Q_o greater than approximately $6.4 * 10^{-5}$. The general appearance of Figure 3.28 is very similar to the bifurcation diagram shown in Figure 3.5. The similarities include the gradual

decrease in the stability of the periodic oscillations and regions of periodic behaviour that frequently disrupt the apparently chaotic regions. Furthermore, these islands of periodic behaviour appear and disappear without warning, for example, in Figure 3.28 the region of apparently chaotic behaviour is subdivided by a region of periodic behaviour near $Q_o = 6.8 * 10^{-5}$, and the transitions to periodic behaviour and back to quasi-periodic or chaotic behaviour are very sudden.

The response of the system in the region shown in Figure 3.28 is studied in more detail by analysing the time histories, phase plane plots, Fourier spectra and Poincaré sections for different test cases.

Case Studies

The case studies analyzed in this section will focus on the values of the parameter Q_o for which the response undergoes the transition from periodic behaviour to quasi-periodic or chaotic behaviour. In the first such region, $(6.30 * 10^{-5} < Q_o < 6.60 * 10^{-5})$, the transition is gradual, and in the second region, $(6.81 * 10^{-5} < Q_o < 7.00 * 10^{-5})$, the transition is very abrupt.

In Figures 3.29, 3.30 and 3.31 (a) - (d), the time histories, phase plane plots and Fourier spectra of the responses, for the first transition region, are shown for the cases where Q_o equals $6.30 * 10^{-5}$, $6.35 * 10^{-5}$, $6.4 * 10^{-5}$ and $6.6 * 10^{-5}$, respectively. As can be seen from these Figures, the response is a stable period-five oscillation for $Q_o = 6.30 * 10^{-5}$, and as Q_o is increased to $6.35 * 10^{-5}$ the periodicity of the response increases. Although there are many well defined spikes in the Fourier spectrum of Figure 3.31 (b), some of these spikes are nearly of the same order as the background noise. Therefore, it is difficult to define the periodicity of the response. As Q_o is increased further to $6.40 * 10^{-5}$, the response becomes increasingly higher order periodic. The time history of the response, Figure 3.29 (c), appears periodic and

stable, however, the phase plane plot, Figure 3.30 (c), is becoming increasingly unstable, and the Fourier spectrum, Figure 3.31 (c), shows signs of a period-five response. It also has a broadband structure indicating that the response is not stable. For the case where Q_o is increased to $6.60 * 10^{-5}$, the time history of the response, Figure 3.29 (d), appears stable, but the phase plane plot, Figure 3.30 (d), is not characteristic of a stable response, and the Fourier spectrum, Figure 3.31 (d), has many subharmonic spikes indicating that the response may be quasi-periodic.

In Figures 3.32 to 3.34 the time histories, phase plane plots and Fourier spectra are shown for test cases in the second transition region. These test cases are for Q_o equal to $6.815927 * 10^{-5}$, $6.815928 * 10^{-5}$ and $7.00 * 10^{-5}$, respectively. Figures 3.32 (a), 3.33 (a) and 3.34 (a) show that for $Q_o = 6.815927 * 10^{-5}$ the response is a stable period-two oscillation. However, if the value of Q_o is increased by the slightest amount to $6.815928 * 10^{-5}$, the response immediately becomes unstable, as illustrated in Figures 3.32 (b), 3.33 (b) and 3.34 (b). In Figures 3.32 (c), 3.33 (c) and 3.34 (c), the response for the case where $Q_o = 7.00 * 10^{-5}$ is also shown to be unstable.

The evidence from the time histories, phase plane plots and Fourier spectra does not prove that the response goes from periodic behaviour to chaotic behaviour, moreover, since the Fourier spectra for some of the unstable cases show definite subharmonic spikes, the evidence does suggest that the response may become quasi-periodic. Conclusive evidence of chaotic behaviour can only be found in the long term behaviour of the responses, which are illustrated by the Poincaré data discussed in the following section.

Poincaré Sections

The Poincaré sections and the long term behaviour of the responses, for each of the above test cases, are shown in Figures 3.35 to 3.41.

For the first transition region, the response for the case where $Q_o = 6.30 * 10^{-5}$ is a stable period-five oscillation; the Poincaré section, shown in Figure 3.35 (a), is a five point attractor and the long term behaviour, shown in Figure 3.35 (b), shows five lines. In Figures 3.36 (a) and (b), Q_o is increased to $6.35*10^{-5}$, and the corresponding Poincaré section shows fourteen distinct groups of data points indicating that the response is a period-fourteen oscillation, however, the long term behaviour of the response shows that this periodic oscillation is slightly unstable. As Q_o is increased to $6.40 * 10^{-5}$, the finite number of points shown in the previous Poincaré section begin to form curves in the phase plane, as illustrated in Figure 3.37 (a). The long term behaviour of the response, as illustrated in Figure 3.37 (b), shows that the response has become even more unstable and that it alternates between marginally stable phases of periodic and quasi-periodic behaviour. In Figures 3.38 (a) and (b), the value of Q_o is increased to $6.60 * 10^{-5}$ and the corresponding Poincaré section has become more complex and the long term behaviour shows that the response has become increasingly unstable.

In the second transition region, the response of the system starts out as a stable, period-two oscillation, for the case where $Q_o = 6.815927 * 10^{-5}$, as illustrated in the Poincaré section and the long term behaviour shown in Figures 3.39 (a) and (b), respectively. However, as Q_o is increased only slightly to a value of $6.815928 * 10^{-5}$, the response of the system immediately becomes unstable, as illustrated by the complicated Poincaré section and long term behaviour shown in Figures 3.40 (a) and (b), respectively. The Poincaré section and long term behaviour of the response are shown in Figures 3.41 (a) and (b), respectively, for the case where $Q_o = 7.00 * 10^{-5}$.

The long term behaviour of the responses illustrated in Figures 3.38 (b) and 3.41 (b), is very similar in appearance to the responses shown in Figures 3.13 (b) and 3.14

(b), however, the shapes of the Poincaré sections in these cases are not very similar. In Figures 3.37 (a) and 3.38 (a) the Poincaré attractors are very complicated structures, comprised of many curves, whereas, in Figures 3.13 (a) and 3.13 (b), the attractors are simple structures, comprised of only a few curves. The connection between the different shapes of the Poincaré sections and the similarity of the responses in these two cases lies in the internal structure of the Poincaré sections. In Figure 3.42, the internal structure of the Poincaré section outlined by the box in Figure 3.41 (a) is shown. The data points seem to be organized in quasi-parallel groups, this type of internal structure is very similar to the internal structure of the Poincaré section illustrated in Figures 3.15 (a) and (b). Furthermore, it was shown in the previous section that this internal structure was necessary for marginally stable periodic and quasi-periodic states to exist.

The marginally stable, or intermittently chaotic, responses discussed in Cases I and II are one type of chaotic behaviour that is observed in this system. The route to this intermittently chaotic behaviour begins with a stable periodic oscillation and, as the value of Q_o is increased, this periodic oscillation becomes increasingly unstable. When the instability is at a maximum the long term response of the system is dominated by many different periodic and quasi-periodic states which remain stable for unpredictable lengths of time.

3.3.3 Case III: Low Frequency, High Velocity, Chaos

In this section, the response of the system is analyzed at higher values of the non-dimensional velocity than in case II. The analysis begins with a series of bifurcation diagrams that give a general overview of the response and also focus on the transition regions where the dynamics are most interesting. Then, several case studies are presented, the purpose of which is to illustrate the transition of the response from periodic behaviour to chaotic behaviour. Finally, Poincaré sections are presented for several different examples within the chaotic region, and these results are then compared with other theoretical systems that exhibit similar behaviour.

Bifurcation Diagrams

In Figure 3.43, the following system parameters are held fixed: the non-dimensional frequency, $k = 0.088$, the initial angle of attack, $\alpha_o = 9.76°$ and the amplitude of the non-dimensional externally applied torque, $Q_o = 0.82 * 10^{-4}$. The value of the non-dimensional velocity, U^*, is varied over the range $(5.0 < U^* < 28.0)$. Two separate regions of chaotic behaviour are shown: the first region, near the low velocity end of the bifurcation diagram, was studied in the previous section and the second region, near $U^* = 25.0$, is the main focus of this section.

In Figure 3.44, the value of U^* is fixed at 25.2 and the value of Q_o is varied over the range $(0.0 < Q_o < 1.0 * 10^{-4})$. The amplitude of the response increases as Q_o is increased, and at Q_o equal to approximately $5.75 * 10^{-5}$ the response undergoes a period doubling bifurcation. The response can be seen to undergo another period doubling bifurcation at approximately $Q_o = 6.5 * 10^{-5}$ and after this bifurcation the system quickly becomes unstable, the instability reaches a maximum near $Q_o = 7.2 * 10^{-5}$, and then restabilizes into a period-two oscillation at approximately

$Q_o = 9.00 * 10^{-5}$.

The unstable region, shown in Figure 3.44, is shown in more detail in Figure 3.45. In this diagram the period doubling bifurcations are easily identified; as Q_o increases, the system undergoes a series of period doubling bifurcations until, at approximately $Q_o = 6.90 * 10^{-5}$, the response appears chaotic.

Case Studies

In this section, the period doubling cascade and chaotic response are verified by examining a number of different test cases. The period doubling phenomena begins with the response of the system in a period-one oscillation and, at Q_o, equal to approximately $5.75 * 10^{-5}$, the response undergoes a bifurcation to a period-two oscillation. The value of Q_o is then increased to approximately $6.60 * 10^{-5}$, where the period of the response changes to a period-four oscillation and, at a value of Q_o equal to approximately $6.86 * 10^{-5}$, the period of the response doubles again to a period-eight oscillation. For values of Q_o greater than approximately $6.86 * 10^{-5}$, the response is chaotic.

In Figures 3.46, 3.47 and 3.48 (a) to (d) the time histories (for a short time interval), phase plane plots and Fourier spectra, respectively, are shown for four different test cases at different values of Q_o along the period doubling cascade. This is done in order to verify that the period of the response is actually doubling at each bifurcation point. In case (a) $Q_o = 5.50 * 10^{-5}$, the response is a period-one oscillation and at $Q_o = 6.40 * 10^{-5}$ the response changes to a period-two oscillation, shown in case (b). In case (c) $Q_o = 6.75 * 10^{-5}$, the response has undergone another period doubling bifurcation and is a period-four oscillation. As Q_o is increased beyond this value the period of the response increases quickly and for case (d) $Q_o = 6.92 * 10^{-5}$, the response is chaotic.

According to the bifurcation diagram shown in Figure 3.45, the chaotic behaviour reaches a maximum near $Q_o = 7.3 * 10^{-5}$. In Figure 3.49 the time history, phase plane plot and Fourier spectra are shown for this case. The Fourier spectrum shows an obvious broadband frequency characteristic that is typical of a chaotic response.

Poincaré Sections and Maps

In this section, the Poincaré sections, maps and long term behaviour of the system are shown for several different cases for which the response is chaotic. As the value of Q_o is increased in each case, the Poincaré attractor can be seen to changes its shape and orientation in the phase plane. The evolution of the Poincaré attractor, maps and long term behaviour of the response is then compared to the Henon map - a well documented, two-dimensional, analytical map that is known to exhibit chaotic behaviour - in order to help in discovering the source of the chaotic behaviour.

In Figure 3.50 (a), the Poincaré section for the case in which $Q_o = 6.90 * 10^{-5}$ (this is near the onset of the chaotic region of Figure 3.45) is shown. The general shape of the attractor indicates that the response follows a period-four attractor. The second return map for this case is shown in Figure 3.50 (b): two curves are located near the larger values of the pitch and two other curves intersect near the identity line at the lower values of the pitch. The long term behaviour of the response is shown in Figure 3.50 (c): the four part attractor is evident in this diagram as the chaotic behaviour is confined to within four distinct bands. The two overlapping curves of the second return map attractor correspond to the two overlapping bands evident in the lower values of the pitch.

The Poincaré section for the case where $Q_o = 7.00 * 10^{-5}$ is shown in Figure 3.51 (a). The four part attractor structure, evident in Figure 3.50 (a), has evolved into a two part attractor; the two pairs of curves of the previous attractor have

grown to overlap each other's domain so that only two independent curves can be distinguished. The second return map, shown in Figure 3.51 (b), illustrates how these curves have grown into one another. The distinctive feature of this attractor is the section at the lower values of pitch that resembles an 'α' shape. The long term behaviour of the response, shown in Figure 3.51 (b), indicates that the chaotic behaviour is now confined to within two distinct bands, while the previous four part attractor is still partially evident as indicated by the darker sections of the two bands.

The Poincaré section for the case where Q_o is increased to a value of $7.30 * 10^{-5}$. shown in Figure 3.52 (a), is considerably different in appearance from the previous two cases. In this case, some bending or folding of the attractor is evident. This is indicated by the two-dimensional banded structure of the attractor - the attractor no longer appears as a collection of one dimensional curves, but now each independent curve is composed of a series of parallel curves very closely spaced. In the second return map, shown in Figure 3.52 (b), the attractor has the same general shape as for the previous case, but the shape has become more complicated with more smaller attractors and a folded type structure. The long term behaviour of the response, shown in Figure 3.52 (c), is considerably different than for the previous two cases. The wide bands that contained the chaotic behaviour in the two previous cases are gone, and they have been replaced with thinner bands. There are at least eleven distinguishable bands, but, the chaotic behaviour is not always confined within these bands. At seemingly random intervals the chaotic behaviour will burst out of this multi-banded structure for a short period of time, and fill a large, two banded structure in which the first band contains the upper six bands of the multi-banded structure and the second band contains the lower five bands of the multi-banded structure.

In Figure 3.53 (a), the Poincaré section for the case where $Q_o = 7.60 * 10^{-5}$ is shown. The overall shape of this attractor is very similar to the previous case with the folded type structure still apparent. However, the second return map, shown in Figure 3.53 (b), has changed considerably in its shape and orientation: the 'α'-type structure of the previous two attractors is no longer evident and there are at least six different sections to the new attractor. The long term behaviour of the system, shown in Figure 3.53 (c), has also changed considerably from the previous case. The most significant change is that the double banded structure has returned, indicating that the response is no longer wandering around the unstable periodic attractor of the previous case.

The Poincaré section for the case where $Q_o = 8.20 * 10^{-5}$ is shown in Figure 3.54 (a) and the second return map is shown in Figure 3.54 (b). The general characteristics of the two plots are similar to the previous case, however, the long term behaviour of the response, shown in Figure 3.54 (c), indicates that the dynamics are different. The two banded structure is still evident, however, at certain times the response can be seen to change from chaotic to periodic behaviour. These intervals of periodic behaviour occur several times over the time period studied but, they do not remain stable for more than approximately one thousand periods. Furthermore, the dark and light bands within the double banded structure are aligned with the periodic regions, this implies that the chaotic behaviour is confined to wander around an unstable periodic attractor.

In Figure 3.55, a small section of the Poincaré attractor, for the case shown in Figure 3.51 (a) ($Q_o = 0.7 * 10^{-4}$), is illustrated in order to show the internal structure of the attractor. The data points within the attractor can be seen to be organized into distinct, quasi-parallel groups of points. This 'striped' internal structure was

also evident in cases I and II.

Comparison with the Henon Map

The Henon map is given in equation (3.3).

$$\begin{aligned} x_{n+1} &= 1 - \nu x_n^2 + y_n \\ y_{n+1} &= -J x_n \end{aligned} \tag{3.3}$$

It is a two dimensional map that stretches ($|J| > 1$) or contracts ($|J| < 1$) and bends areas in the x-y plane. The result of many iterations of this map, corresponding to many contractions and foldings of areas in the phase plane, is that information about the initial conditions is lost and the behaviour becomes chaotic [Moon, 1987]. In the examples of this map shown as part of this thesis, the value of J is fixed at -0.3 and the value of the parameter ν is varied. The results of the Henon map, for different values of the parameter ν, are presented and then compared qualitatively with the results of the Poincaré sections and maps presented in the previous section. The goal of this qualitative comparison is to gain insight into the possible cause of the chaotic behaviour of the oscillating airfoil system, by comparing its behaviour with that of an analytical system.

In Figure 3.56, the bifurcation diagram of x_n versus ν is shown for the case where J is fixed at -0.3 and ν is varied from 0.9 to 1.1. The importance of this diagram is that it shows qualitatively that the route to chaos for this system is period doubling.

The phase plane plot of y_n versus x_n, which is similar to the Poincaré section for a continuous system, for the case where ν is equal to 1.065 is shown in Figure 3.57 (a). The attractor, composed of four distinct curves in the phase plane, is similar in appearance to the four piece attractor shown in Figure 3.50 (a). The fourth return map for the x variable, shown in Figure 3.57 (b), shares a common

physical characteristic with the second return map shown in Figure 3.50 (b), namely the development of a small loop structure near the identity line. The long term behaviour of the response, shown in Figure 3.57 (c), is illustrated by plotting each value of the x variable against the number of the iteration for each data point. This figure shares the same banded structure as shown in Figure 3.50 (c). Furthermore, within these bands can be seen some darker and lighter bands, which is also a common characteristic of the two systems.

In Figures 3.58 (a), (b) and (c) the value of the parameter ν is increased to 1.077, and the corresponding phase plane plot, fourth return map and long term behaviour, respectively, are shown. The important changes to the attractor are as follows: the distinct curves of the four piece attractor of the phase plane plot have lengthened, the loop type structure of the attractor in the fourth return map has become more pronounced and the bands of chaotic activity, shown in the long term behaviour, have widened. As the parameter ν is increased even further, several important qualitative changes in the attractor become apparent.

In Figures 3.59 (a), (b) and (c) the value of ν is increased to 1.089. The phase plane attractor, illustrated in Figure 3.59 (a), has developed into a two piece attractor and the shape of each of the curves has developed a folded appearance. This folded, two piece attractor is qualitatively very similar to the attractor shown in Figure 3.51 (a). Also, the pronounced loop type structure of the fourth return map, shown in Figure 3.59 (b), is similar to the type of structure seen in the second return map of Figure 3.51 (b). Furthermore, the long term behaviour of the system, illustrated in Figure 3.59 (c), shows the same double banded structure with dark and light internal bands as the long term behaviour of the system illustrated in Figure 3.51 (c).

While it is not surprising that the oscillating airfoil system becomes chaotic

after a series of period doubling bifurcations, similar to the Henon system, it is very surprising that the Poincaré sections and maps and the long term behaviour of a system designed to model an aerodynamic system should strongly resemble the corresponding plots of a system designed to model the contraction and folding of areas in the phase plane. The Henon map is known to become chaotic due to the fact that the stable and unstable manifolds of the Poincaré section intersect an infinite number of times in the phase plane. The result is that if a Poincaré point lies near one of these intersection points it will be mapped to all the other intersection points in future iterations, the curve on which these points lie is called a homoclinic orbit [Moon, 1987]. It cannot be proven that the stable and unstable manifolds of the oscillating airfoil system intersect and that a homoclinic orbit exists, (if it can be proven it is well beyond the scope of this thesis), but, homoclinic orbits are known to be of fundamental importance in the type of chaotic behaviour found in horseshoe-type maps such as the Henon map. The similarities in the Poincaré data of the oscillating airfoil system and the Henon system suggest that the chaotic behaviour in both systems may be caused by the same type of phenomena, namely, the existence of a homoclinic orbit. However, due to the overwhelming complexity of proving such a link between the two systems, further study along these lines will have to be left as a possible topic of future research.

3.3.4 Case IV: High Frequency, High Velocity, Chaos

The fourth type of chaotic behaviour found in the single degree of freedom system involves high non-dimensional velocities and higher frequency oscillations than in the previous cases. The analysis begins with bifurcation diagrams, in which the non-dimensional frequency, k, or the non-dimensional forcing amplitude, Q_o, are varied, which pinpoint the regions of chaotic behaviour. Next, a series of examples are presented that focus on the transition to chaos and the types of bifurcations which the system undergoes. Finally, Poincaré sections and the long term behaviour of the response, for several different chaotic cases, are presented.

Bifurcation Diagrams

The bifurcation diagram shown in Figure 3.60 illustrates how the maximum amplitude of the response changes as the non-dimensional frequency, k, is increased for the case where $\alpha_o = 7.62^o$, $U^* = 20.265$ and $Q_o = 8.40 * 10^{-5}$. The maximum amplitude of the response occurs at a frequency of approximately $k = 0.068$, this implies that the natural frequency of the entire system, including the aerodynamics, lies near this value. For completeness the structural natural frequency of the system is shown on the plot in order to illustrate that the two frequencies are not the same. The response becomes either quasi-periodic or chaotic at a value of approximately $k = 0.150$, and then restabilizes at approximately $k = 0.215$.

In the next bifurcation diagram, shown in Figure 3.61 (a), the initial angle of attack, α_o, and the non-dimensional velocity, U^*, remained unchanged at 7.62^o and 20.265, respectively, and the frequency was fixed at $k = 0.156$ while Q_o was varied over the range $(0.00 < Q_o < 1.50 * 10^{-4})$. The plot illustrates a number of different characteristics of the response: the maximum amplitude of the response generally

increases as Q_o increases, secondly, the response undergoes a series of bifurcations that eventually lead to an unstable response, and finally, the observed unstable response persists over a wide range of values of Q_o before it restabilizes in a period-two oscillation.

The bifurcation diagram shown in Figure 3.61 (b) is a detailed view of the transition region of Figure 3.61 (a). In this plot the bifurcations leading to the chaotic response are clearly visible. At Q_o equal to approximately $3.40 * 10^{-5}$, the response changes from a period-one oscillation to a period-four oscillation and then, at Q_o equal to $3.90 * 10^{-5}$, the response changes from period-four to period-six. The response undergoes another bifurcation at Q_o equal to approximately $4.15 * 10^{-5}$ to a higher order periodic oscillation and then, at Q_o equal to $4.24 * 10^{-5}$ the response suddenly becomes unstable and may be chaotic.

Case Studies

The four case studies discussed in this section are from the different regions of Figure 3.61 (b) where the response changes to higher order periodic states leading to the potentially chaotic region. The values of Q_o for these test cases are: (a) $3.6*10^{-5}$, (b) $4.0*10^{-5}$, (c) $4.2*10^{-5}$ and (d) $4.3*10^{-5}$, all of the other system parameters remain the same as in Figures 3.61 (a) and (b): $\alpha_o = 7.62^o$, $U^* = 20.265$ and $k = 0.156$.

In Figures 3.62, 3.63 and 3.64 (a) - (d), the time histories, phase plane plots and Fourier spectra for each of the four values of Q_o are shown, respectively. In case (a), the value of Q_o is $3.6 * 10^{-5}$, and the response is a stable period-four oscillation, in case (b) the value of Q_o is increased to $4.0 * 10^{-5}$ and the period of the response increases to period-six. In case (c) the value of Q_o is increased to $4.2 * 10^{-5}$ and from the time history and Fourier spectrum the response can be seen to be a stable period-nine oscillation. In case (d), the value of Q_o is increased to $4.3 * 10^{-5}$ and is

within the unstable region of Figure 3.61 (b). As indicated by the phase plane plot, the response does not repeat itself over the sampled time period (the time history does not show all of the data that was sampled to obtain the phase plane plot and Fourier spectrum). Furthermore, the Fourier spectrum shows a definite spike at the forcing frequency, $k = 0.156$, and a broadband spectrum in the subharmonic range which is typical of chaotic signals.

An important point to note regarding the above case studies is that the response of the system does not period double before the onset of the chaotic behaviour, as was the case in the previous section. However, the system does undergo a series of bifurcations that increase the periodicity of the response until, at a value of the forcing amplitude of approximately $4.24 * 10^{-5}$, the response becomes chaotic.

Poincaré Sections

In this section, the Poincaré sections and long term behaviour of the response are illustrated for three different test cases within the unstable region of Figure 3.61 (b), and one high frequency test case from case I.

In Figures 3.65, 3.66 and 3.67 (a) and (b), the Poincaré sections and long term dynamics of the response are illustrated for these three different test cases. In each case, the parameters $\alpha_o = 7.62°$, $k = 0.156$ and $U^* = 20.265$ are the same and only the value of Q_o is different.

The attractor shown in Figure 3.65 (a), for the case where $Q_o = 4.30 * 10^{-5}$, has a definite structure within the phase plane that is characteristic of a strange or chaotic attractor; the data points are formed into a complex but highly organized structure comprised of many intersecting curves. The long term behaviour of the response, shown in Figure 3.65 (b), has the same general type of pattern found in cases I and II (the intermittent type chaos), however, in this case, the response always returns to

the same periodic oscillation after each outburst of chaotic behaviour. This indicates that the response is under the influence of a weak periodic attractor.

In Figures 3.66 and 3.67 (a) and (b), the Poincaré sections and long term behaviour of the system are illustrated for the cases where $Q_o = 4.45 * 10^{-5}$ and $Q_o = 4.70 * 10^{-5}$, respectively. The similarity between the shapes of these two Poincaré attractors is unmistakable, in fact they are nearly identical. The differences between these Poincaré attractors and those of cases I, II and III (see Figures 3.13 (a), 3.40 (a) and 3.51 (a), respectively) is also evident; the Poincaré attractors for these high frequency chaotic cases have more of a two-dimensional structure than the attractors in the other lower frequency chaotic cases. From Figures 3.66 (b) and 3.67 (b), it can be seen that the long term behaviour is not confined to within definite bands, as in case III, and is not intermittent or marginally stable, as in cases I and II, although there are regions in Figure 3.66 (b) that appear periodic they are very unstable and quickly disappear.

In general, the type of chaotic behaviour found in this high velocity - high frequency case is different from the previous cases in at least one significant way: the high frequency chaotic response is much more unpredictable or chaotic than the lower frequency chaotic responses. The meaning of the term predictable can best be defined as how close the response is to being stable or periodic. This difference in behaviour is best illustrated by comparing the time histories of the response for test cases from each of the four cases studied, as shown in Figures 3.68 (a) - (d). The responses illustrated in Figures 3.68 (a) through (c) have been shown in previous sections to be chaotic, however, these oscillations do not appear to be completely unstable - in other words, the position of the airfoil cannot be predicted exactly from a previously known position, however, the oscillations do not tend to behave

in an extremely erratic manner either, therefore, these responses can be described as only 'weakly' chaotic. On the other hand, the response illustrated in Figure 3.68 (d), for the high frequency chaotic case, is extremely unpredictable. This response has regions of small amplitude oscillations and regions of large amplitude oscillations that appear at seemingly random intervals and when compared with the three other cases is far more unstable. Therefore, this response is characterized as 'strongly' chaotic.

The type of behaviour illustrated in Figures 3.65 - 3.67 is typical of the behaviour that is found when the system is forced at a frequency in the range ($0.150 < k < 0.185$), with large initial angles of attack and high velocities. For example, in Figures 3.69 (a) and (b), the Poincaré section and long term behaviour, respectively, are shown for the case in which $\alpha_o = 8.90^o$, $k = 0.165$, $U^* = 21.0227$ and $Q_o = 1.02 * 10^{-5}$, this is a high frequency case using other parameters equal to those for case I (see Figures 3.13 (a) and (b)). The Poincaré attractor and the long term behaviour are remarkably similar to the cases shown in Figures 3.65 - 3.67. The complicated internal structure of this Poincaré attractor is revealed in the magnified view shown in Figure 3.70. On the microscopic scale, the data points are organized into well defined groups of parallel curves and are not randomly distributed within the attractor. This internal organization of the data points, or fractal structure, is a characteristic of all chaotic, or strange, attractors [Moon, 1987].

The instability of the numerical method (discussed in Chapter 2) is evident in Figure 3.68 (b). The solution converges for approximately nineteen thousand periods of the forcing function, and then it diverges. The error at each time step is approximated by the difference between the predictor and corrector values of the pitch. This estimated error is usually well below the predetermined tolerance level

$(1 * 10^{-6})$, but the high-velocity chaos is prone to sudden large increases in the amplitude of the response which causes sudden increases in the estimated error. Occasionally, these increases in the estimated error become greater than the tolerance level and the time step cannot be accepted. It is not obvious what causes these large increases in the estimated error but, in the future, a more accurate method of calculating the predictor values of the pitch and pitch rate may decrease the magnitude of the estimated error and allow the simulation to continue.

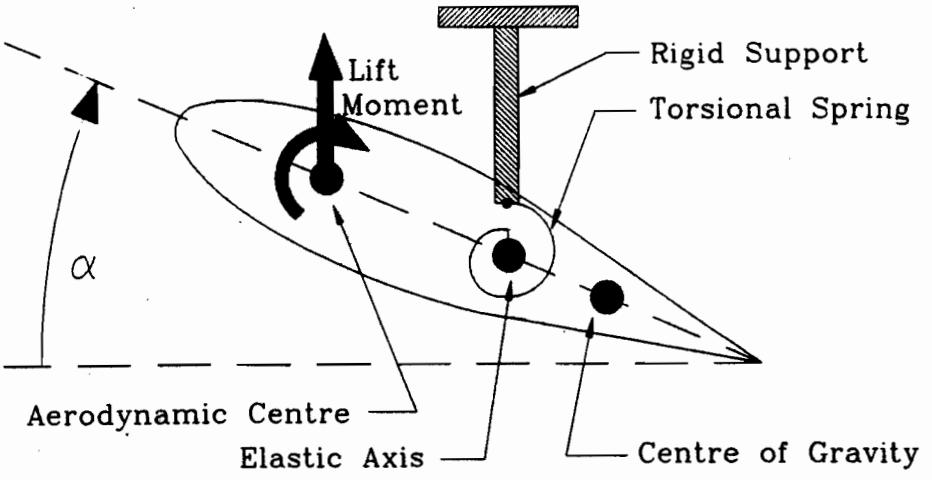

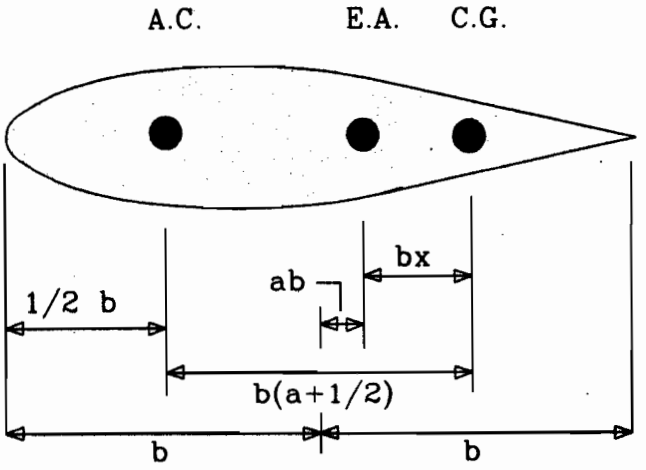

Figure 3.1: The single degree of freedom airfoil system.

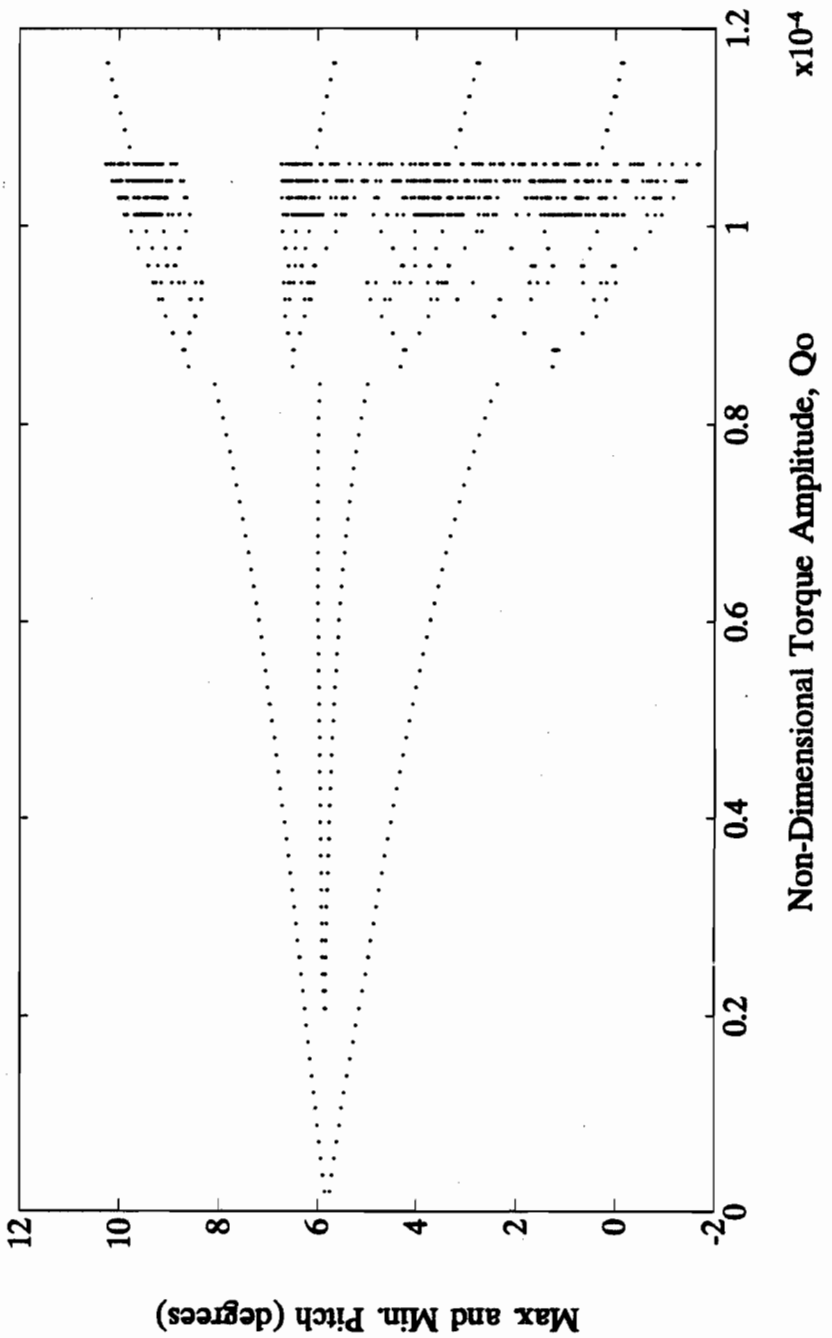

Figure 3.2: Bifurcation diagram for the case: $\alpha_o = 8.90°$, $U^* = 21.0227$, $k = 0.044$ and $0.0 < Q_o < 1.18 * 10^{-4}$.

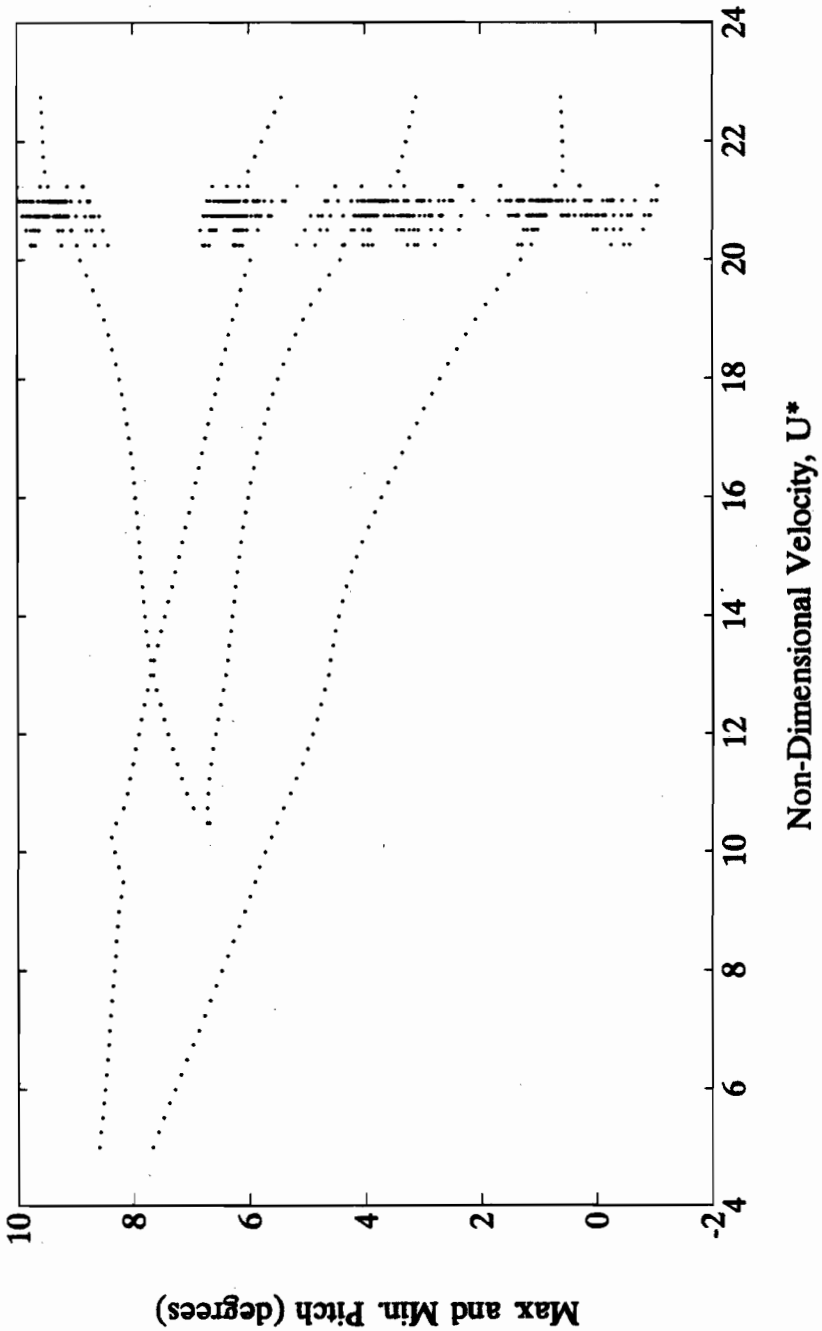

Figure 3.3: Bifurcation diagram for the case: $\alpha_o = 8.90°$, $Q_o = 1.02 * 10^{-4}$, $k = 0.044$ and $5.0 < U^* < 23.0$.

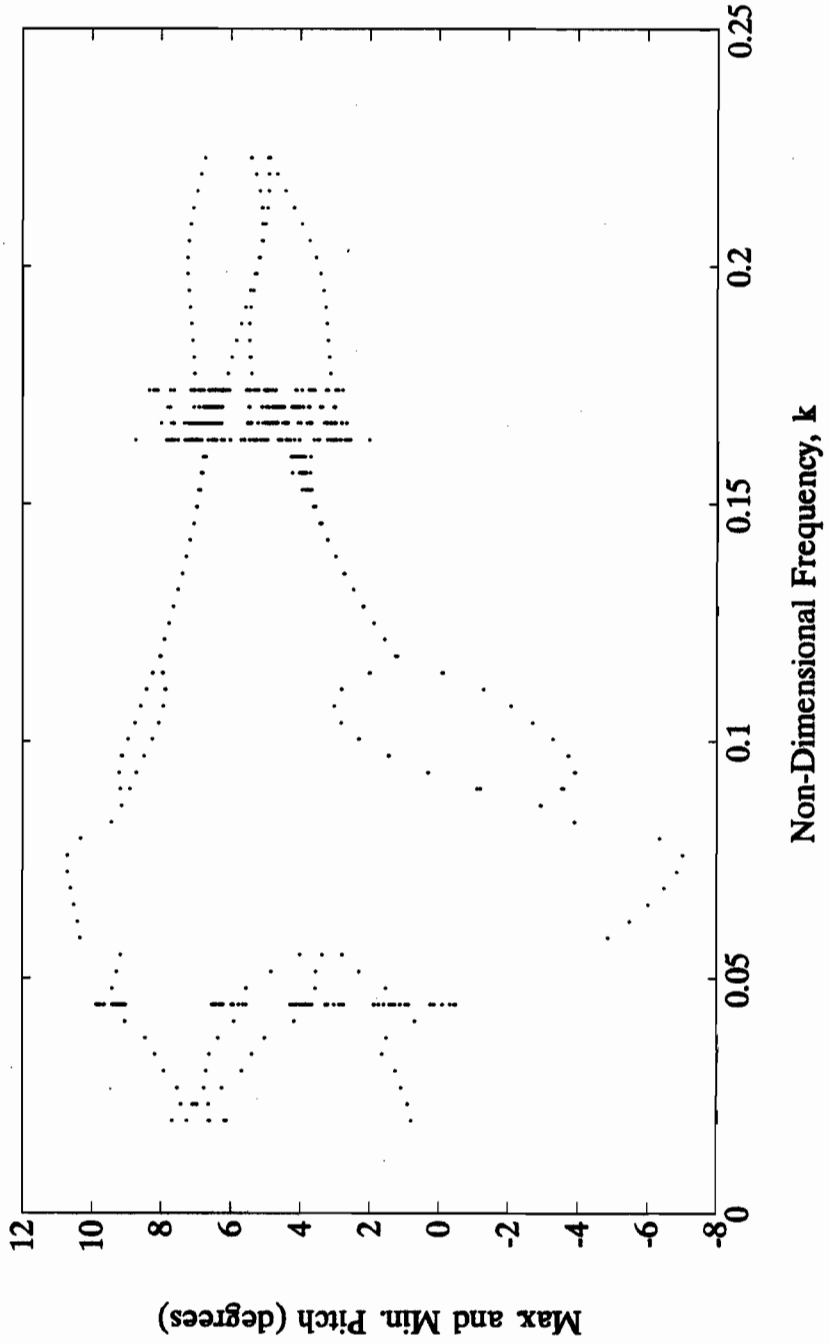

Figure 3.4: Bifurcation diagram for the case: $\alpha_o = 8.90°$, $Q_o = 1.02 * 10^{-4}$, $U^* = 21.0227$ and $0.02 < k < 0.225$.

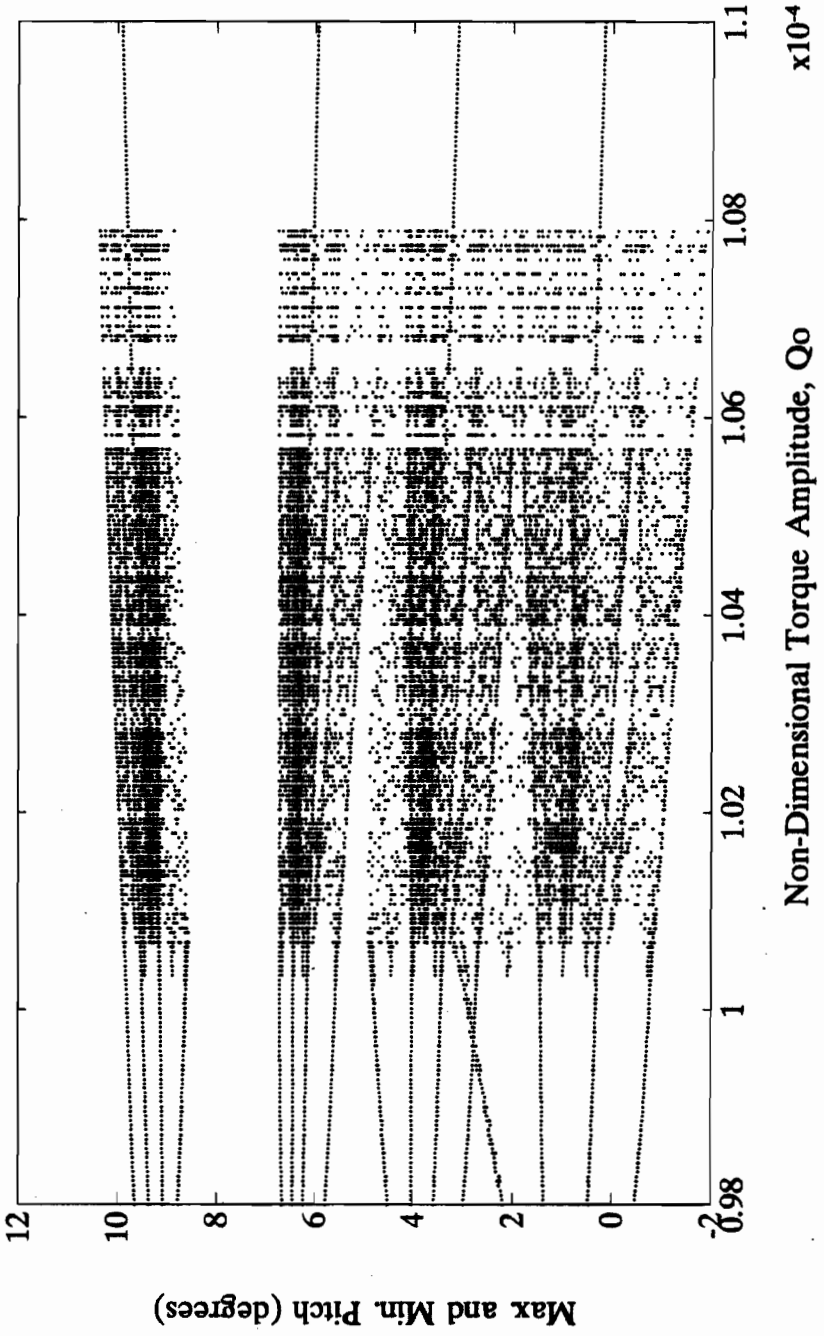

Figure 3.5: Bifurcation diagram for the case: $\alpha_o = 8.90^o$, $U^* = 21.0227$, $k = 0.044$ and $0.98 * 10^{-4} < Q_o < 1.10 * 10^{-4}$.

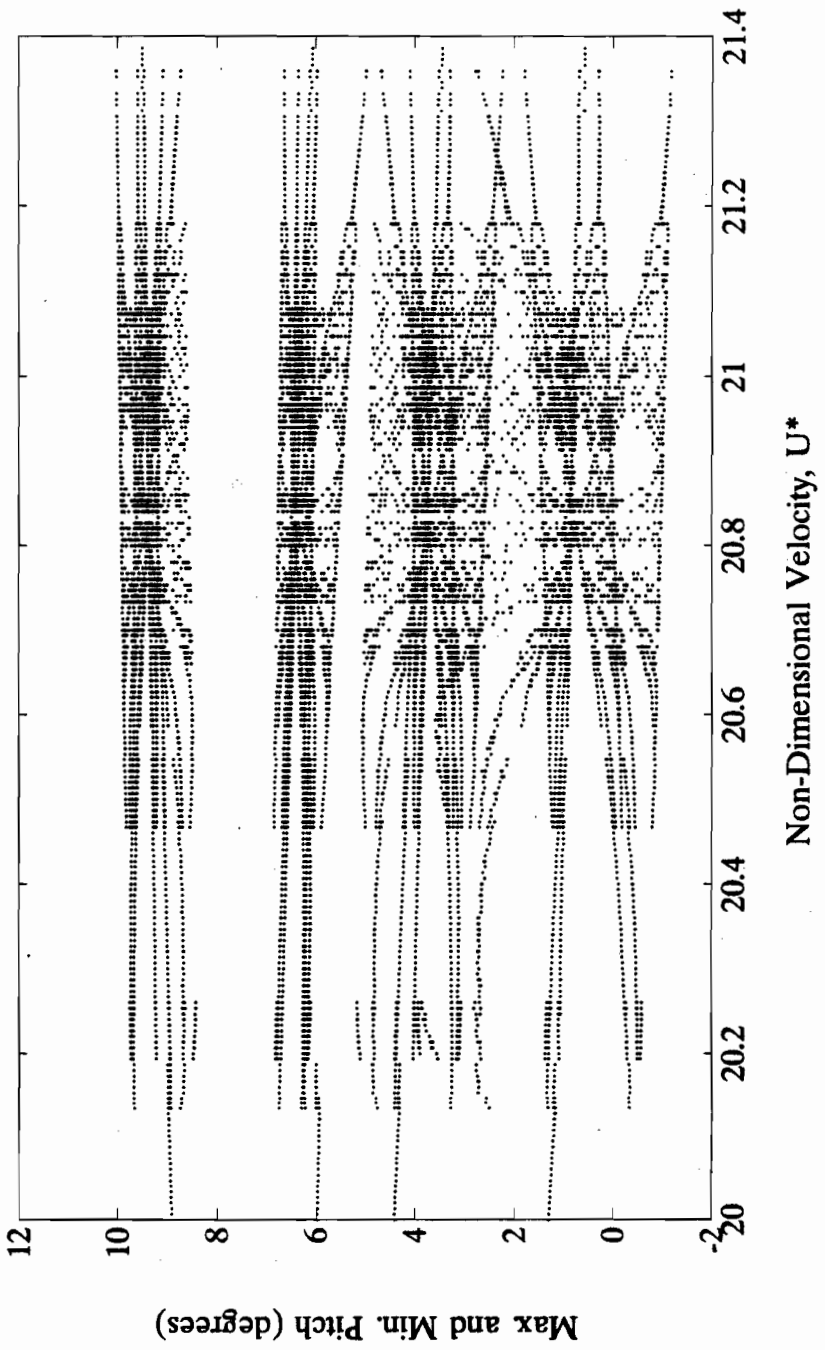

Figure 3.6: Bifurcation diagram for the case: $\alpha_o = 8.90°$, $Q_o = 1.02 * 10^{-4}$, $k = 0.044$ and $20.0 < U^* < 22.0$.

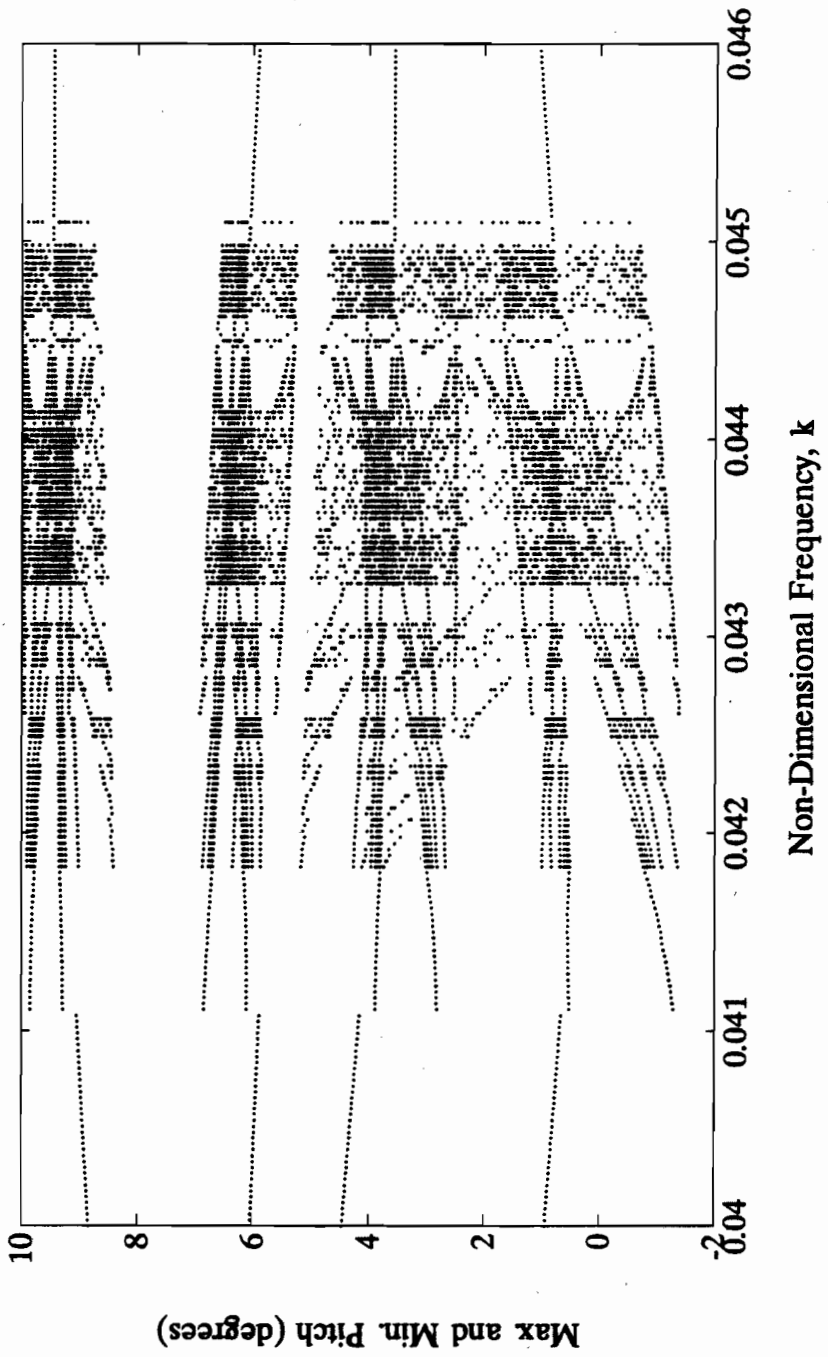

Figure 3.7: Bifurcation diagram for the case: $\alpha_o = 8.90°$, $Q_o = 1.02 * 10^{-4}$, $U^* = 21.0227$ and $0.040 < k < 0.046$.

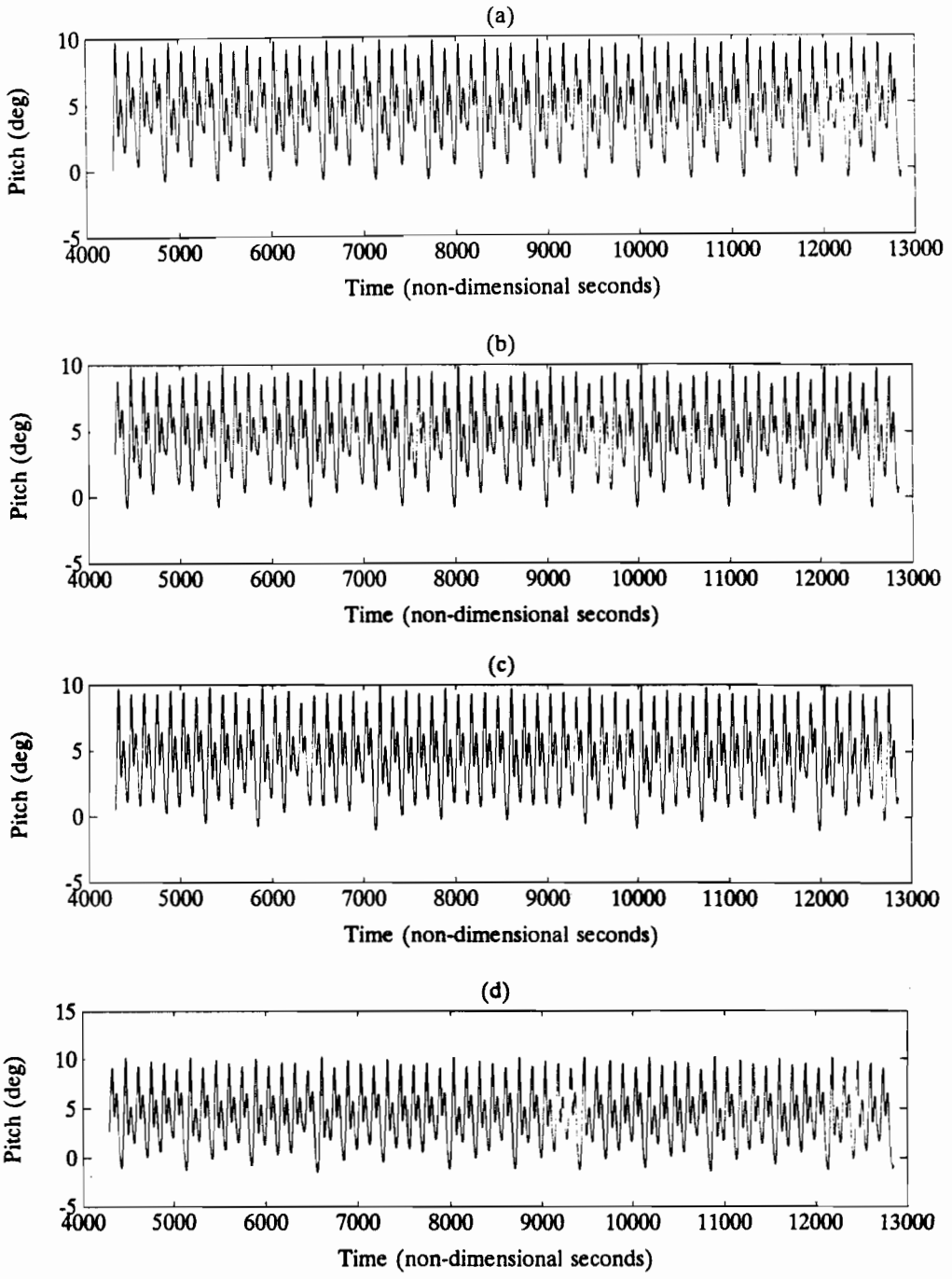

Figure 3.8: The **time histories** of the response of the airfoil for the cases: $\alpha_o = 8.90°$, $U^* = 21.0227$ and $k = 0.044$ and (a) $Q_o = 1.000 * 10^{-4}$, (b) $Q_o = 1.006 * 10^{-4}$, (c) $Q_o = 1.020 * 10^{-4}$ and (d) $Q_o = 1.050 * 10^{-4}$.

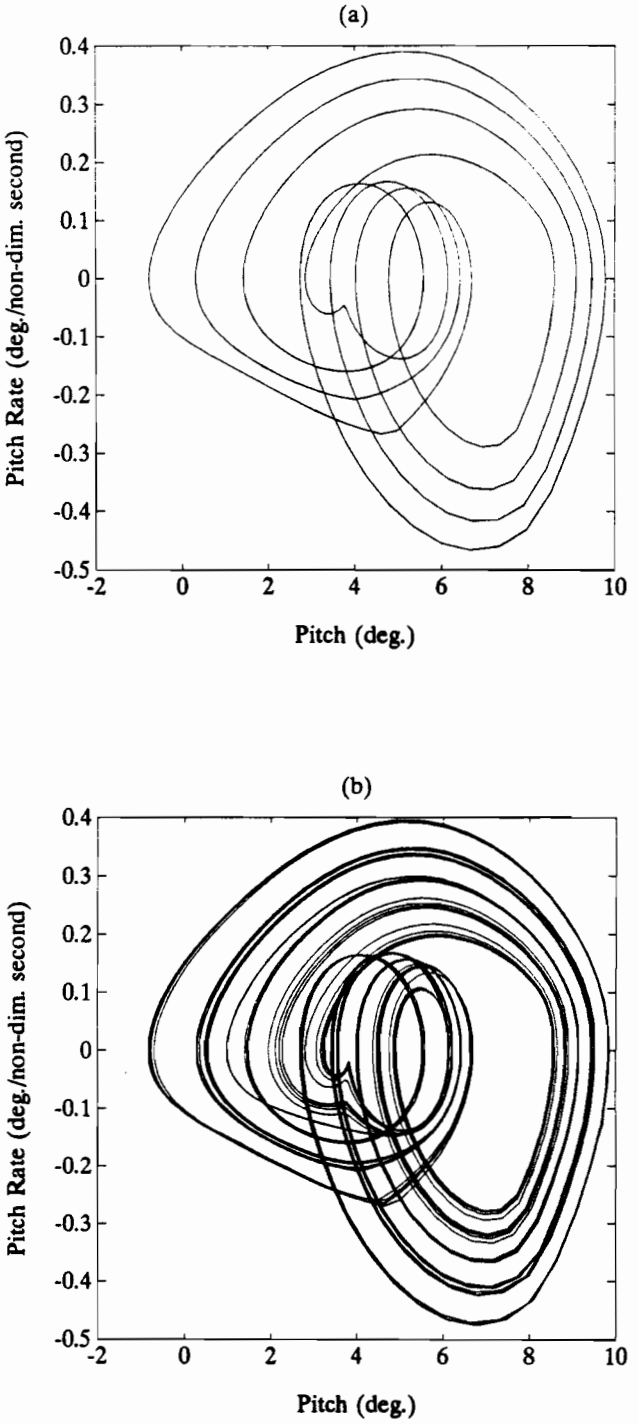

Figure 3.9: The **phase plane plots** of the response of the airfoil for the cases: $\alpha_o = 8.90^o$, $U^* = 21.0227$ and $k = 0.044$ and (a) $Q_o = 1.000 * 10^{-4}$, (b) $Q_o = 1.006 * 10^{-4}$, (c) $Q_o = 1.020 * 10^{-4}$ and (d) $Q_o = 1.050 * 10^{-4}$.

(c)

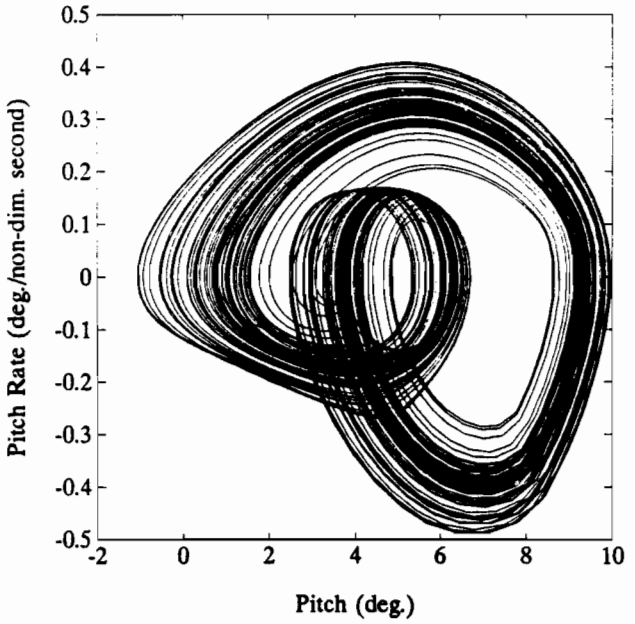
Pitch Rate (deg./non-dim. second)
0.5
0.4
0.3
0.2
0.1
0
-0.1
-0.2
-0.3
-0.4
-0.5
-2
0
2
4
6
8
10
Pitch (deg.)

(d)

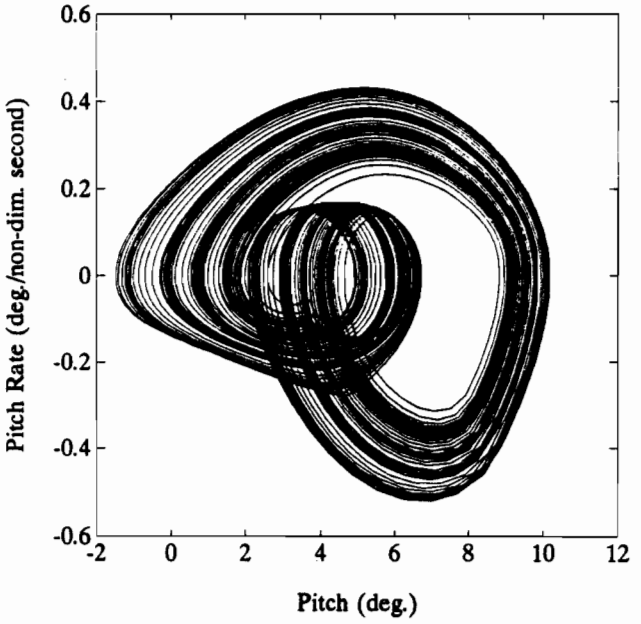
Pitch Rate (deg./non-dim. second)
0.6
0.4
0.2
0
-0.2
-0.4
-0.6
-2
0
2
4
6
8
10
12
Pitch (deg.)

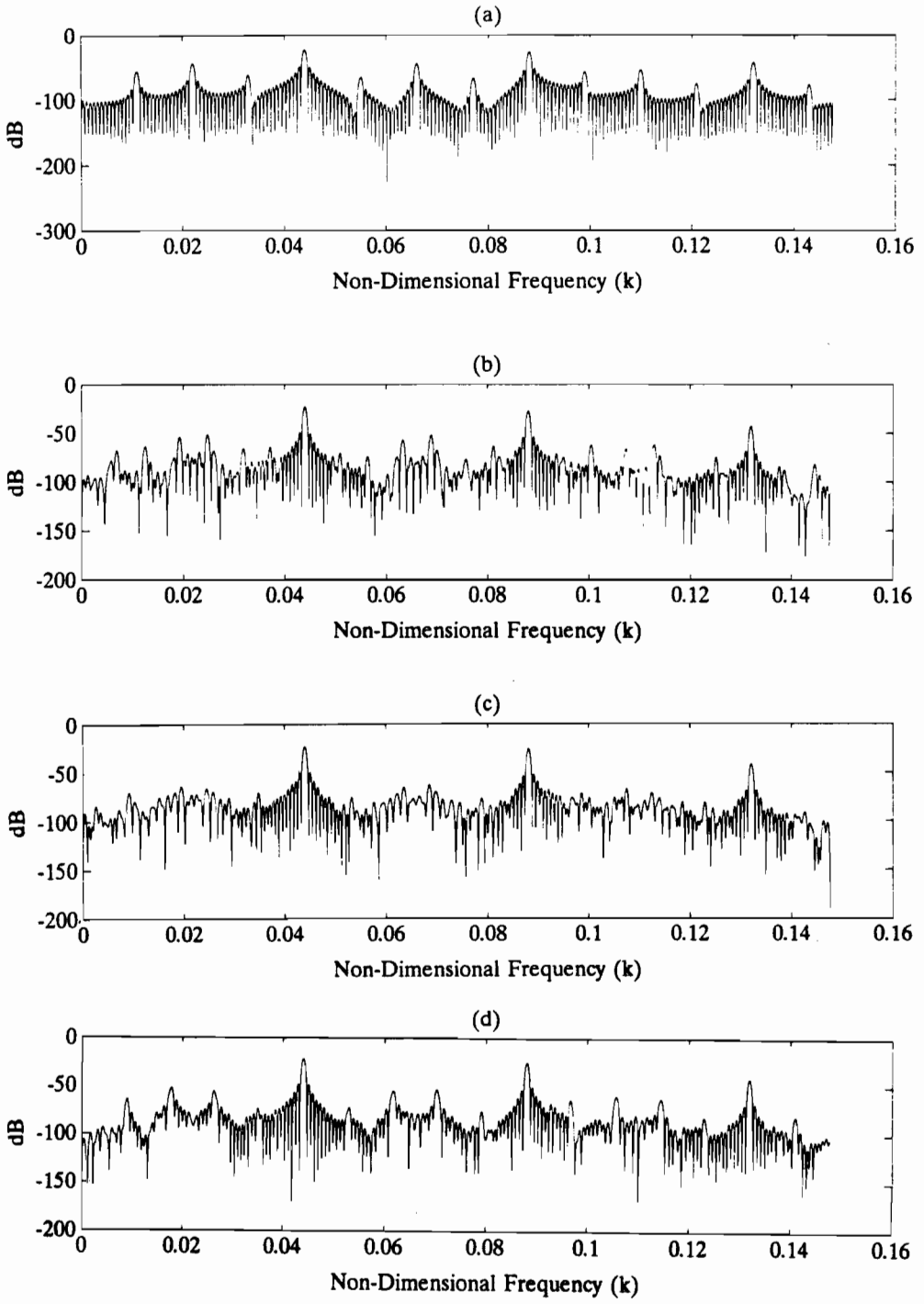

Figure 3.10: The **Fourier spectra** of the response of the airfoil for the cases: $\alpha_o = 8.90^o$, $U^* = 21.0227$ and $k = 0.044$ and (a) $Q_o = 1.000 * 10^{-4}$, (b) $Q_o = 1.006 * 10^{-4}$, (c) $Q_o = 1.020 * 10^{-4}$ and (d) $Q_o = 1.050 * 10^{-4}$.

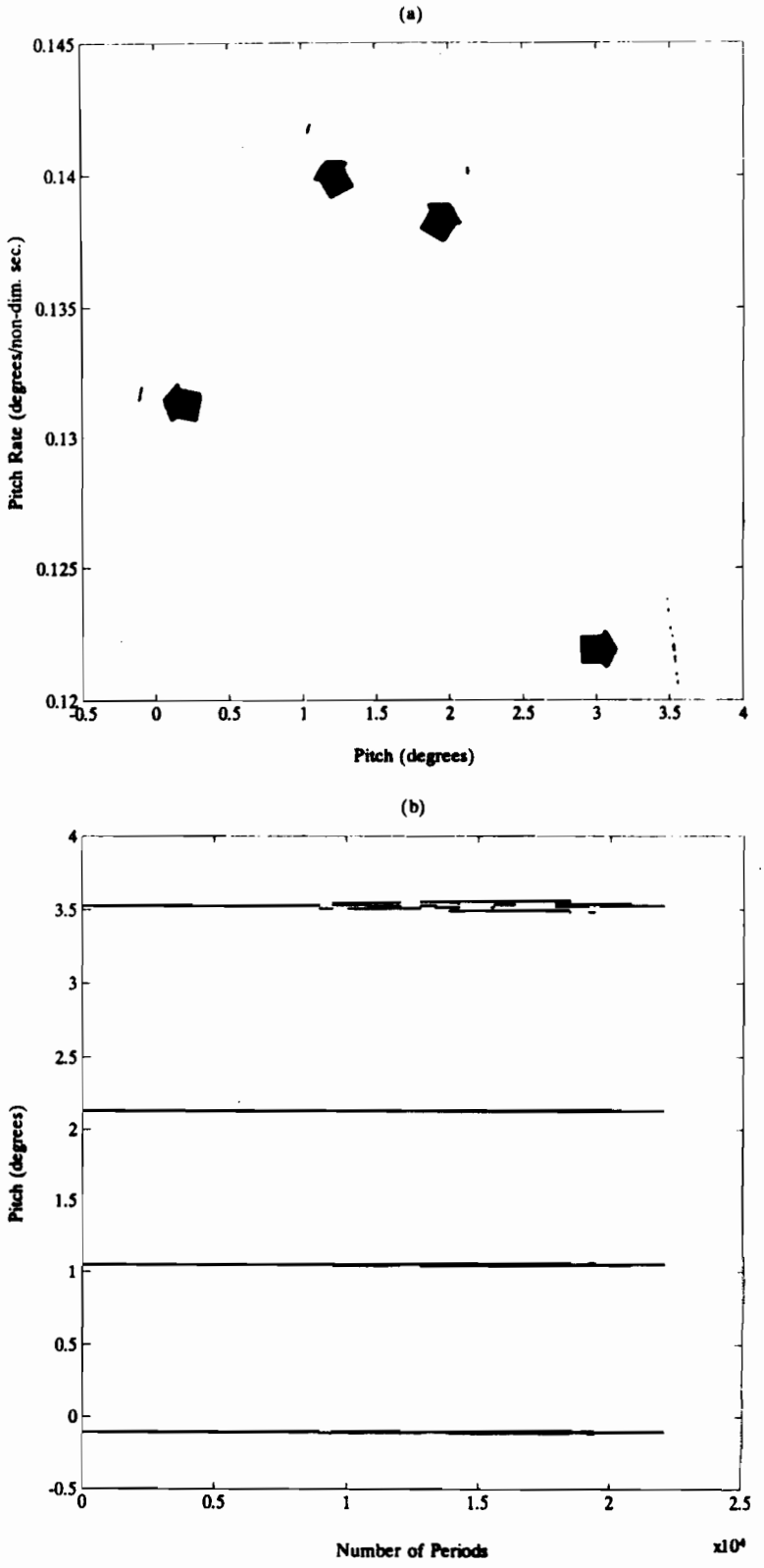

Figure 3.11: (a) The Poincaré section and (b) the long term behaviour of the system for the case: $\mathbf{Q_o = 1.000 * 10^{-4}}$, $\alpha_o = 8.90°$, $U^* = 21.0227$ and $k = 0.044$.

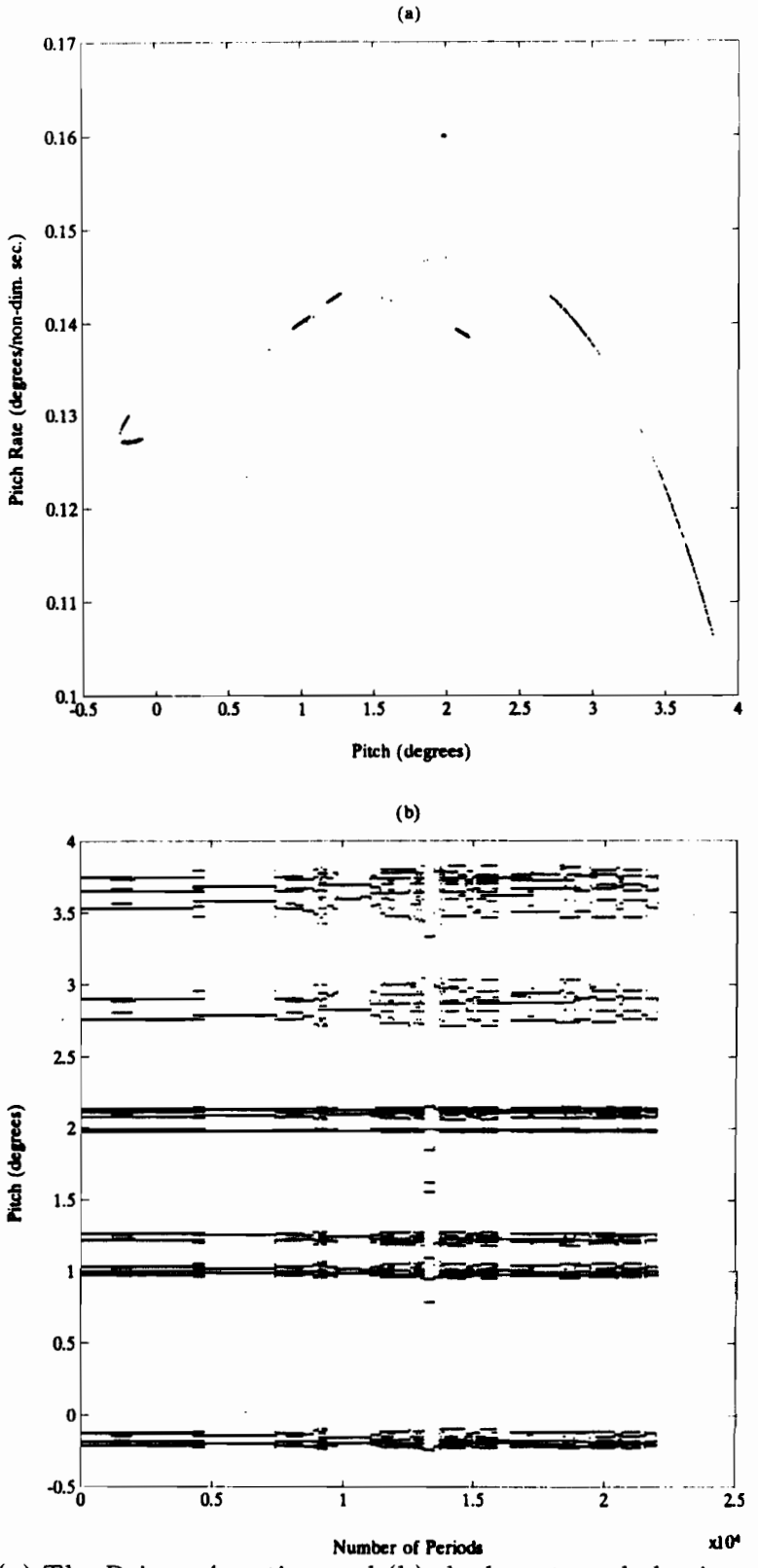

Figure 3.12: (a) The Poincaré section and (b) the long term behaviour of the system for the case: $\mathbf{Q_o = 1.006 * 10^{-4}}$, $\alpha_o = 8.90°$, $U^* = 21.0227$ and $k = 0.044$.

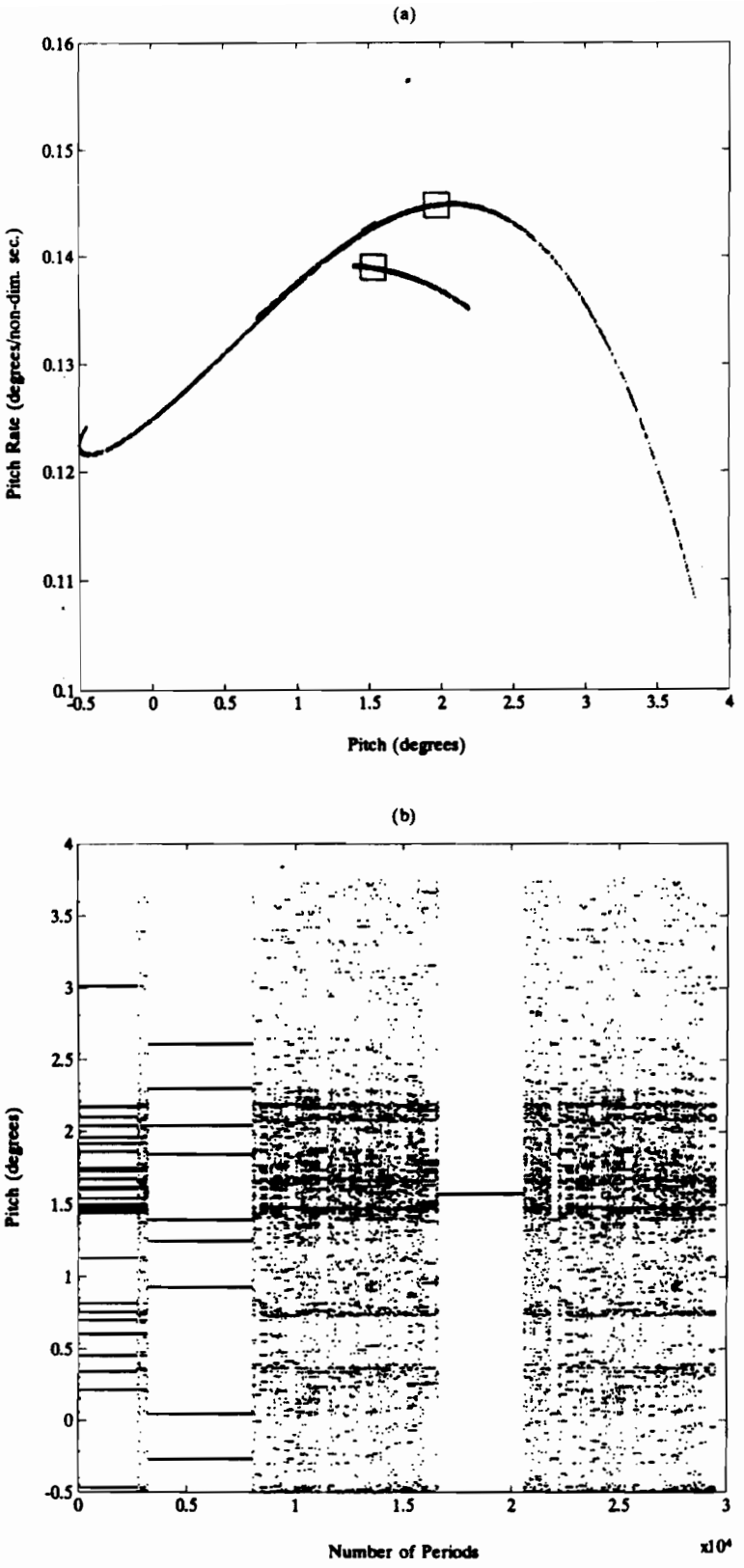

Figure 3.13: (a) The Poincaré section and (b) the long term behaviour of the system for the case: $\mathbf{Q_o = 1.020 * 10^{-4}}$, $\alpha_o = 8.90°$, $U^* = 21.0227$ and $k = 0.044$.

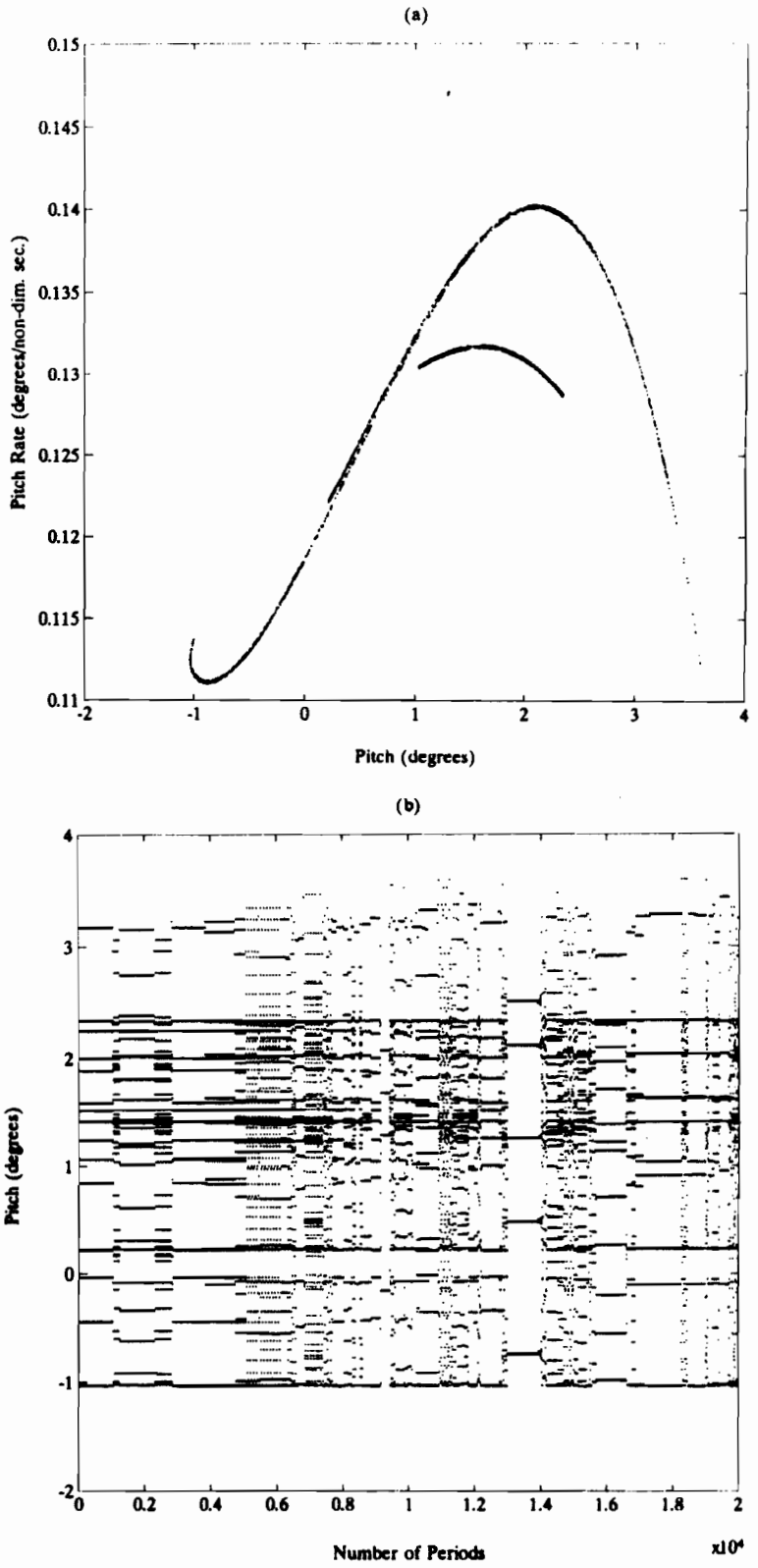

Figure 3.14: (a) The Poincaré section and (b) the long term behaviour of the system for the case: $\mathbf{Q_o = 1.050 * 10^{-4}}$, $\alpha_o = 8.90°$, $U^* = 21.0227$ and $k = 0.044$.

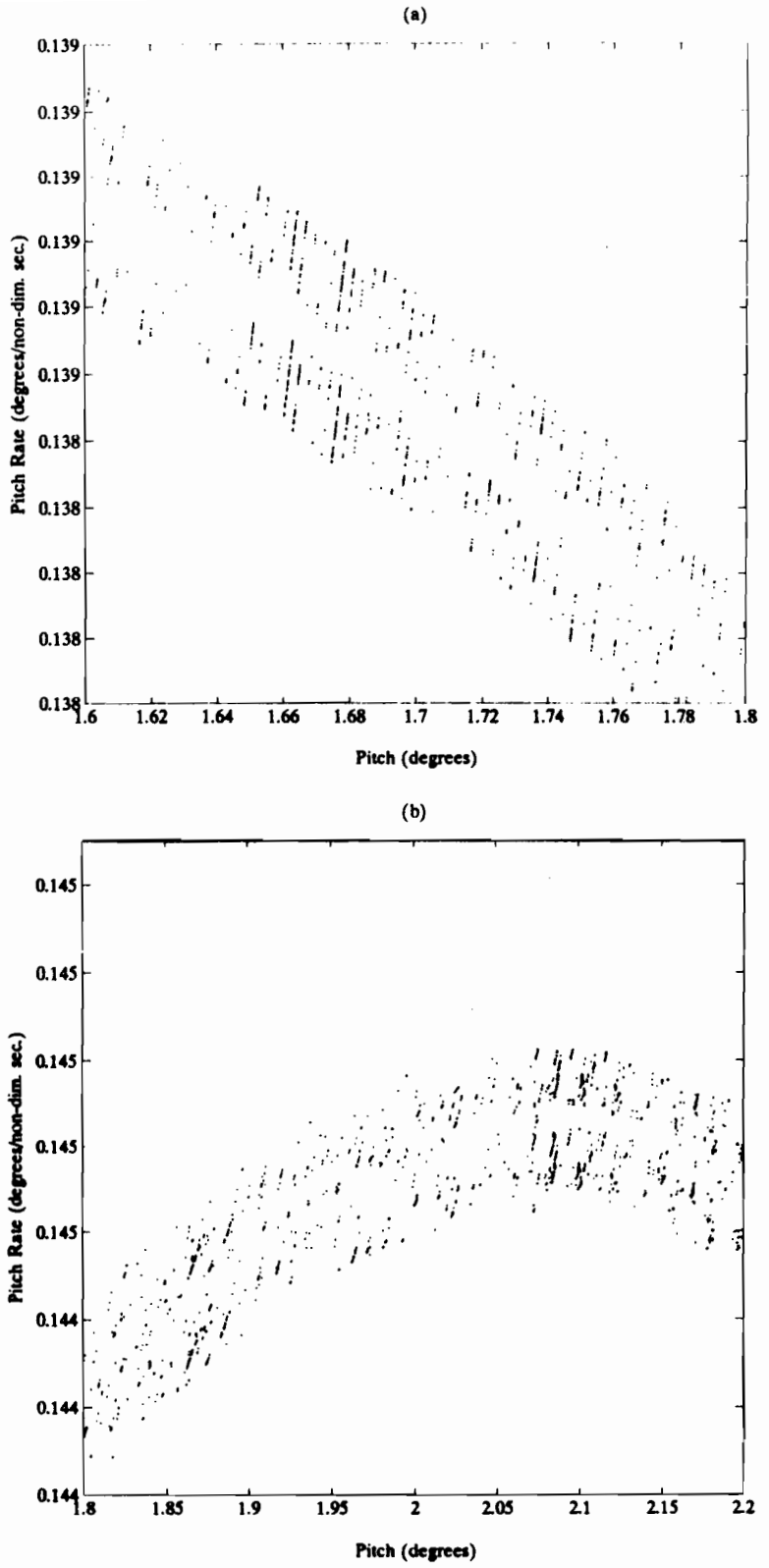

Figure 3.15: The micro-structure of the Poincaré attractor is shown for two separate regions, (a) and (b), of the case: $Q_o = 1.020 * 10^{-4}$, $\alpha_o = 8.90^o$, $U^* = 21.0227$ and $k = 0.044$ (see Figure 3.13(a)).

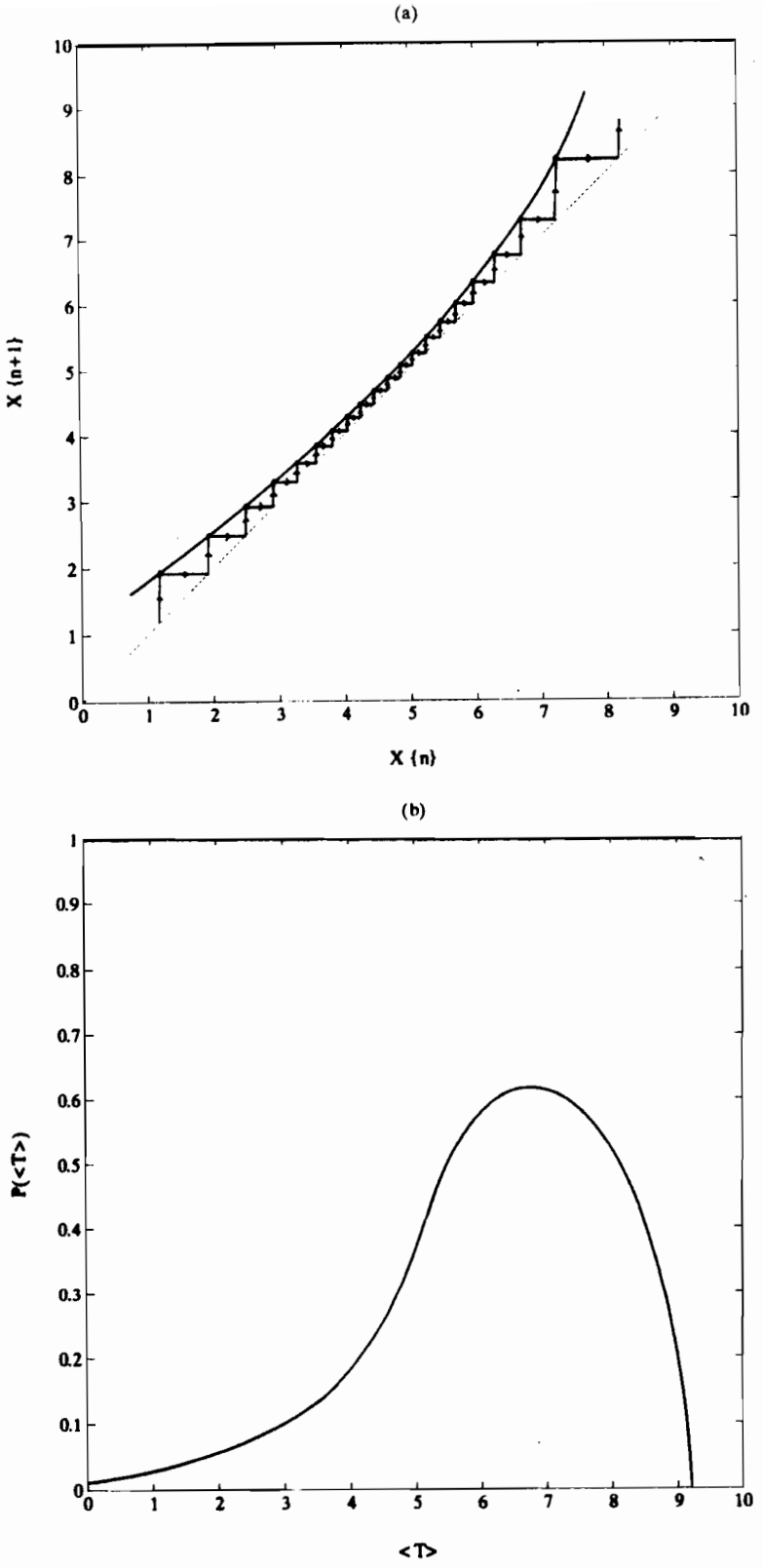

Figure 3.16: (a) The general shape of the relaminarization channel for type I intermittency and (b) the general shape of the probability distribution of finding a laminar phase of length 'T' for type I intermittency.

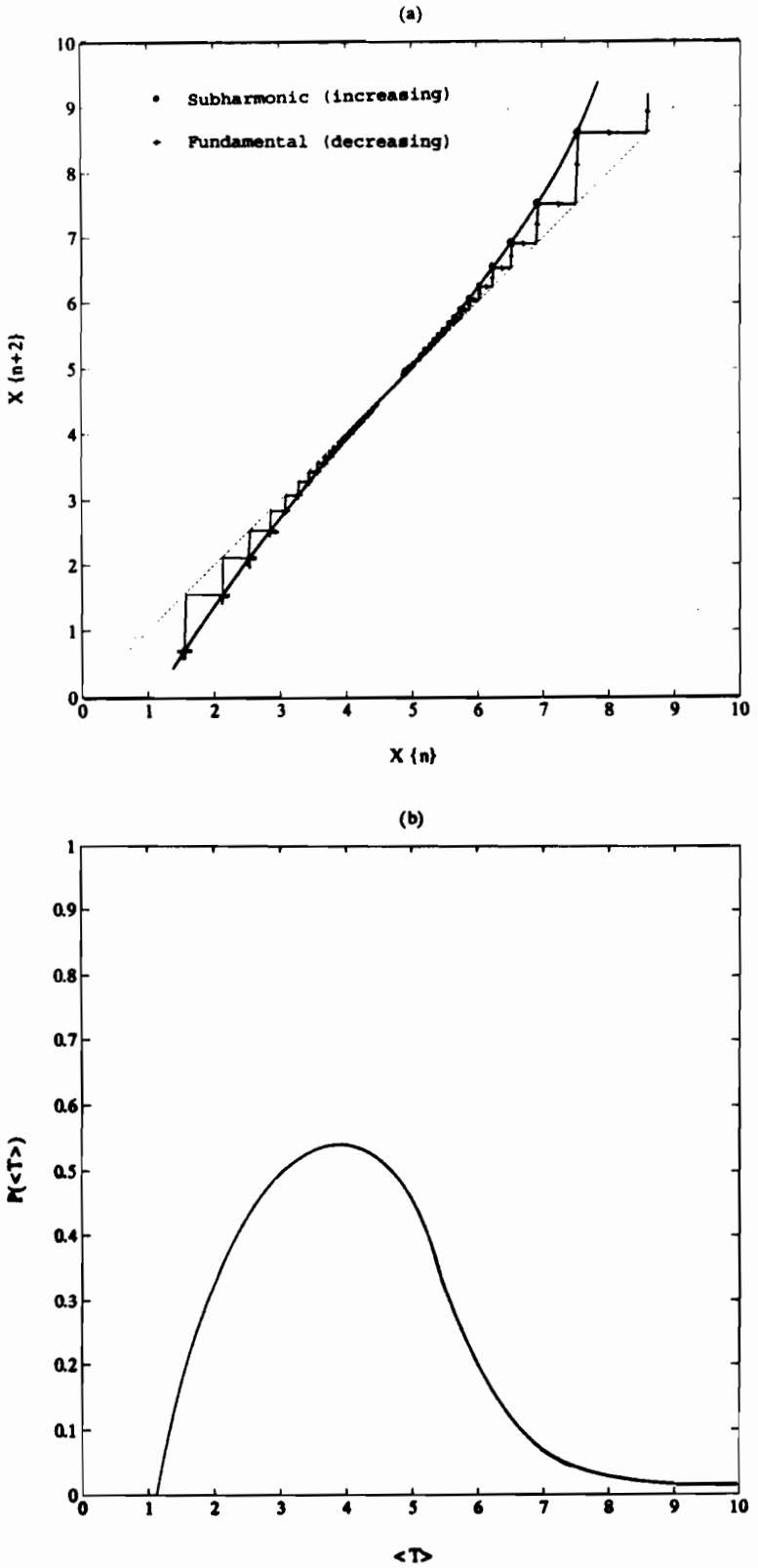

Figure 3.17: (a) The general shape of the relaminarization channel for type III intermittency and (b) the general shape of the probability distribution of finding a laminar phase of length 'T' for type III intermittency.

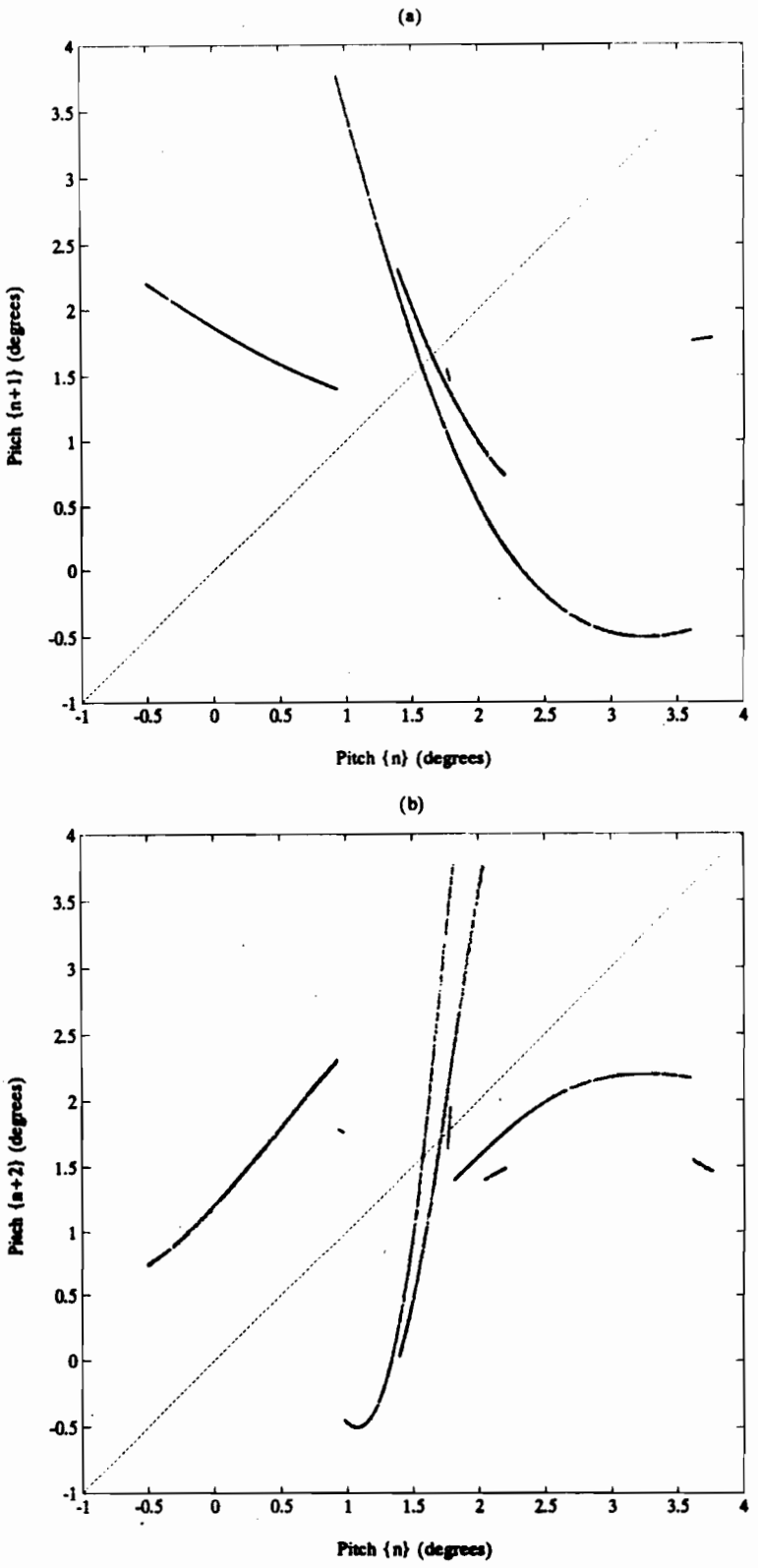

Figure 3.18: (a) The first return map and (b) the second return map of the Poincaré data for the case: $\mathbf{Q_o = 1.020 * 10^{-4}}$, $\alpha_o = 8.90°$, $U^* = 21.0227$ and $k = 0.044$.

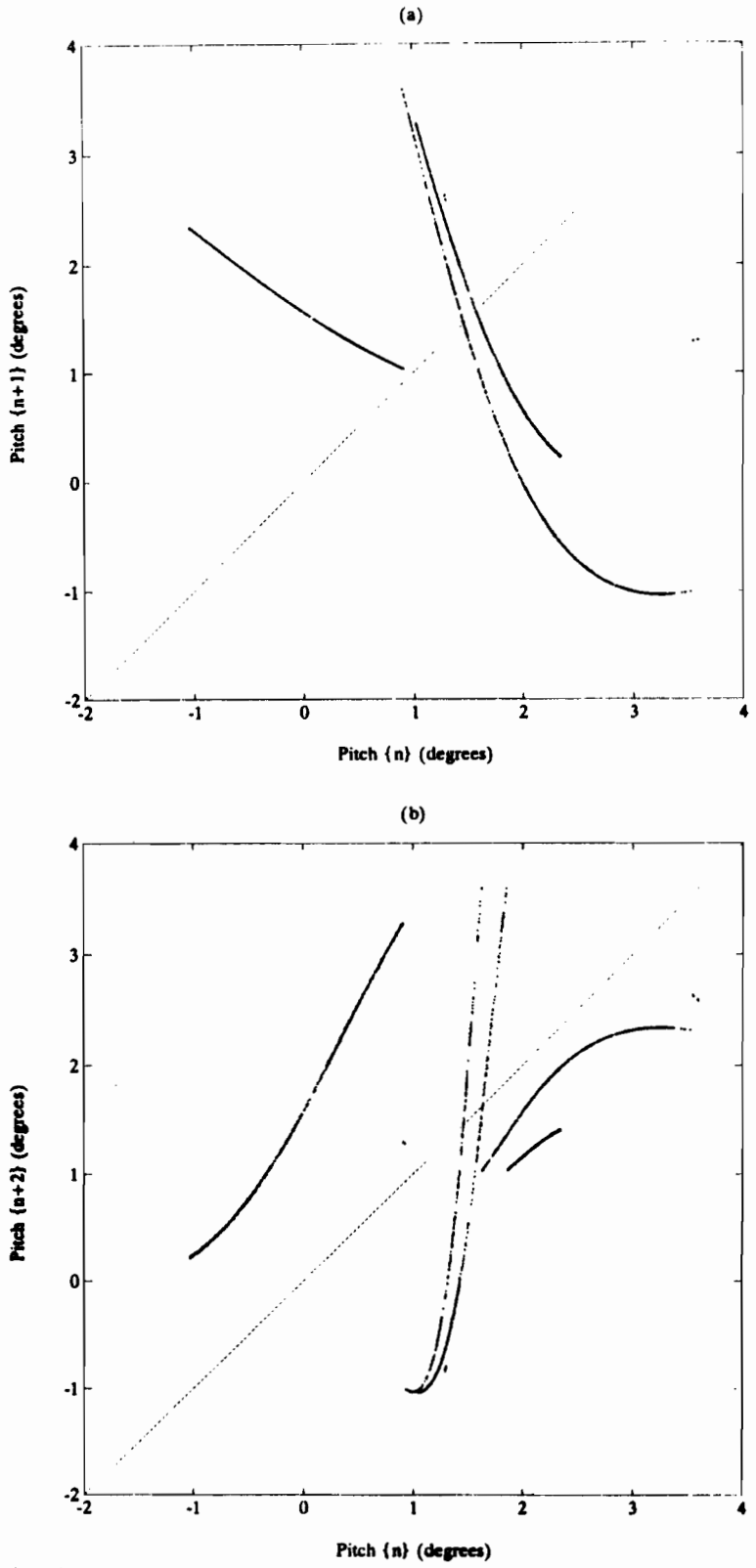

Figure 3.19: (a) The first return map and (b) the second return map of the Poincaré data for the case: $\mathbf{Q_o = 1.050 * 10^{-4}}$, $\alpha_o = 8.90°$, $U^* = 21.0227$ and $k = 0.044$.

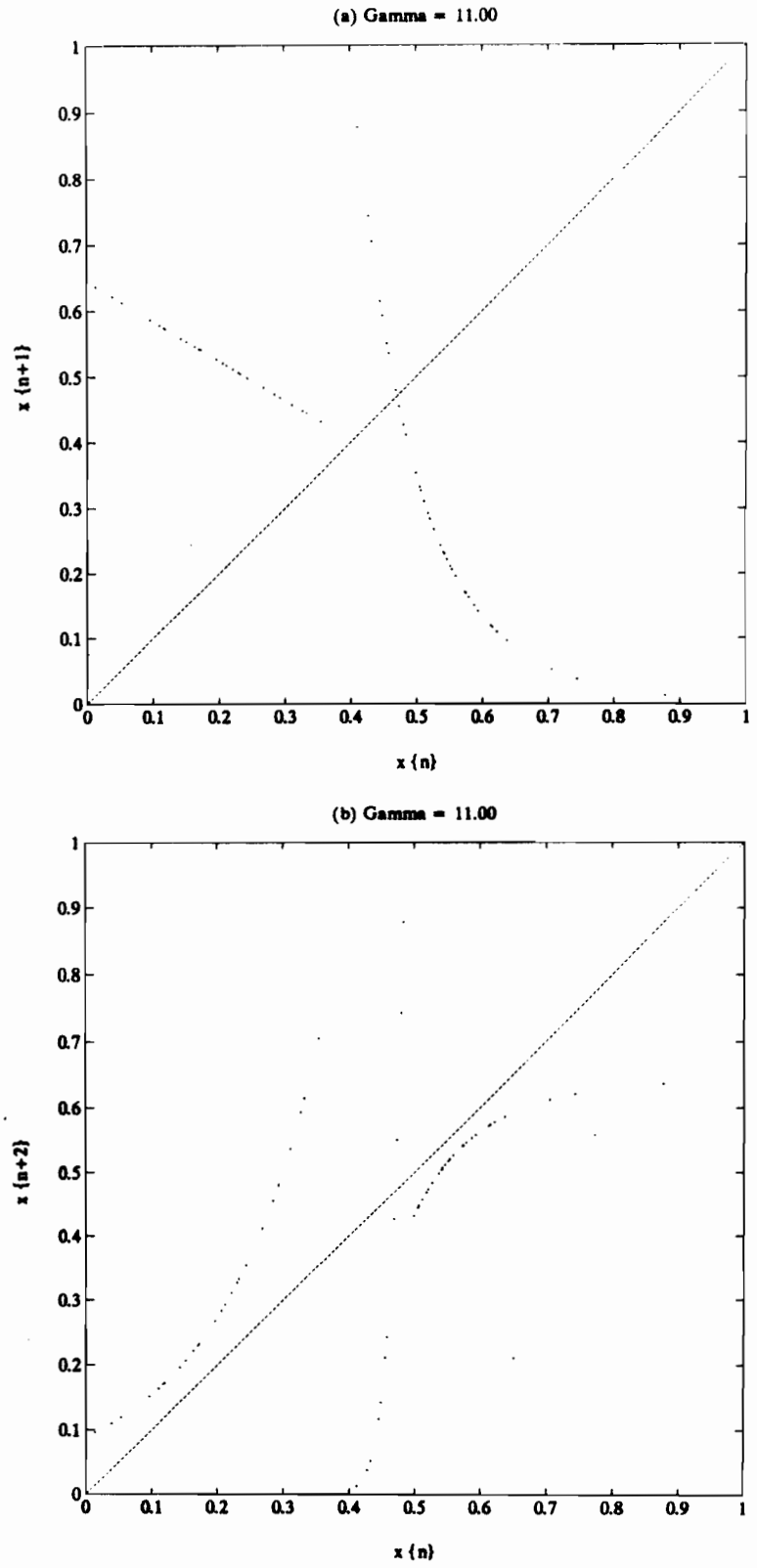

Figure 3.20: (a) The first return map, (b) second return map and (c) long term behaviour of the analytical system given by equation (3.2) for the case of $\gamma = 11.00$.

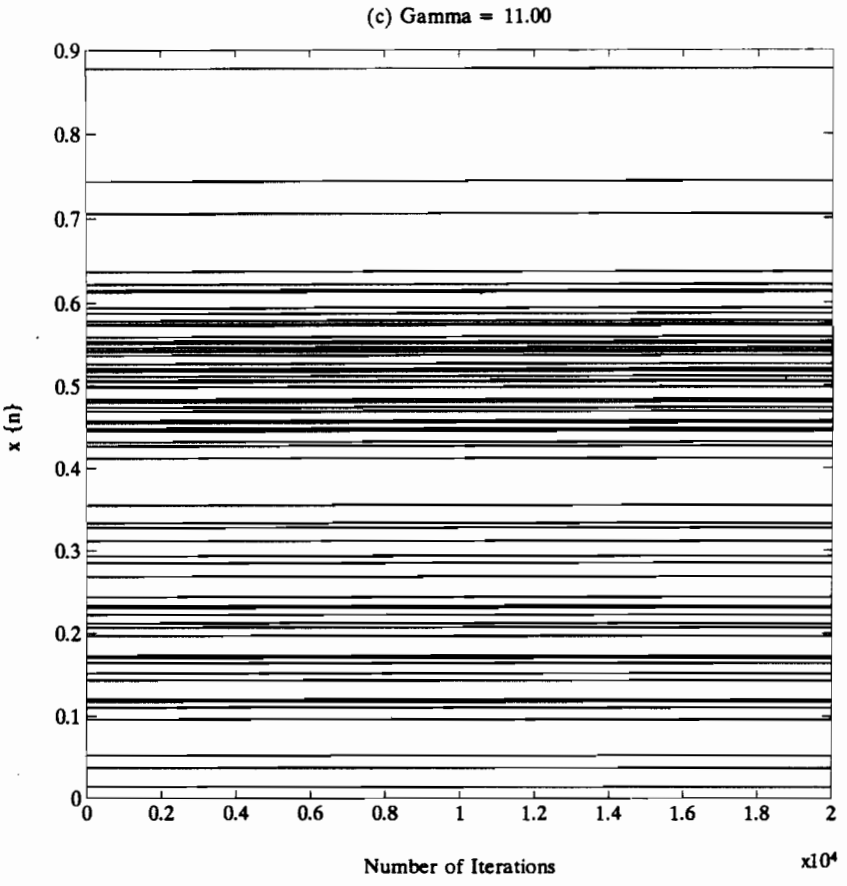
(c) Gamma = 11.00
0.9
0.8
0.7
0.6
0.5
0.4
0.3
0.2
0.1
0
x {n}
0
0.2
0.4
0.6
0.8
1
1.2
1.4
1.6
1.8
2
Number of Iterations
x10^4

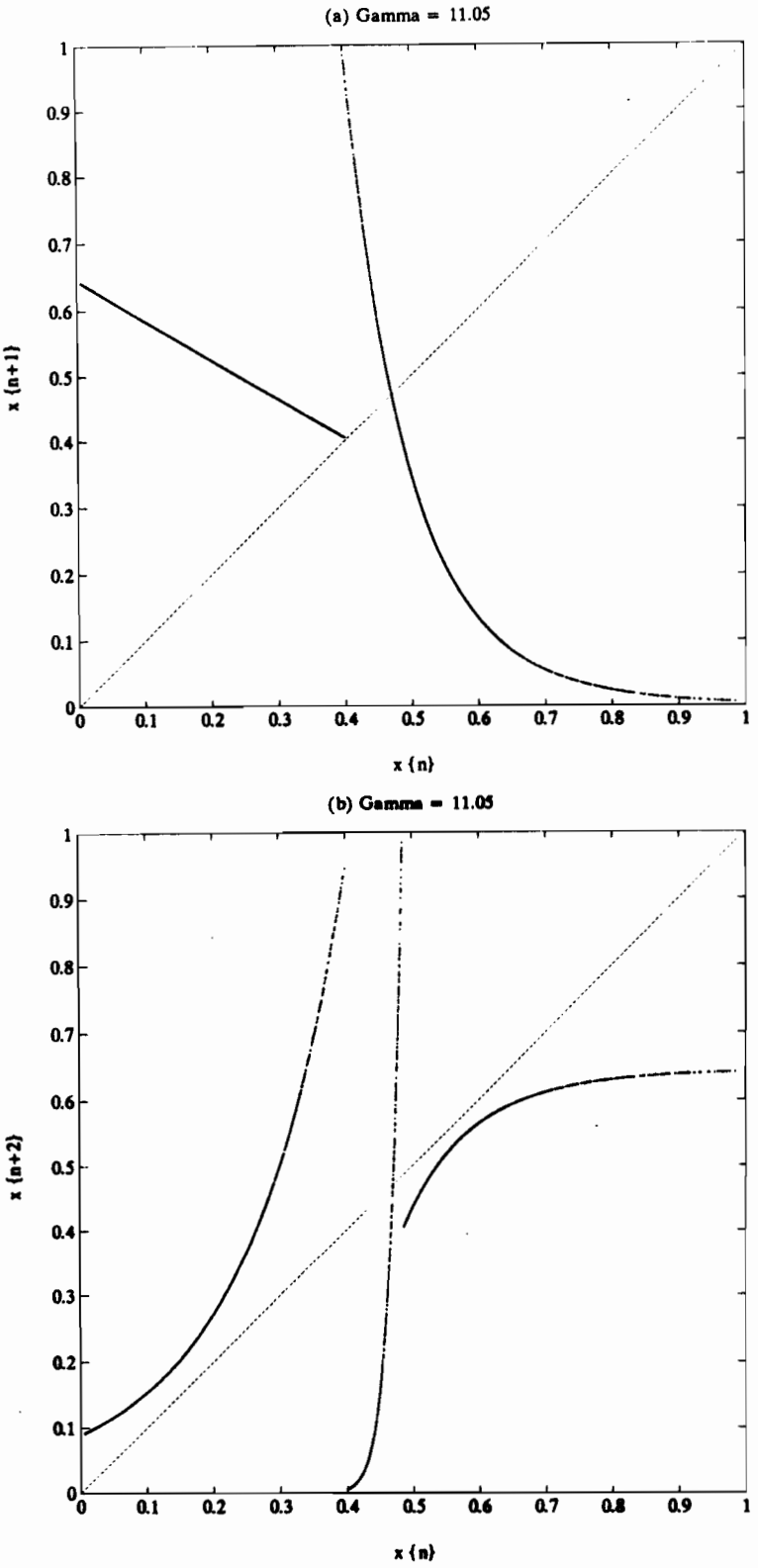

Figure 3.21: (a) The first return map, (b) second return map and (c) long term behaviour of the analytical system given by equation (3.2) for the case of $\gamma = 11.05$.

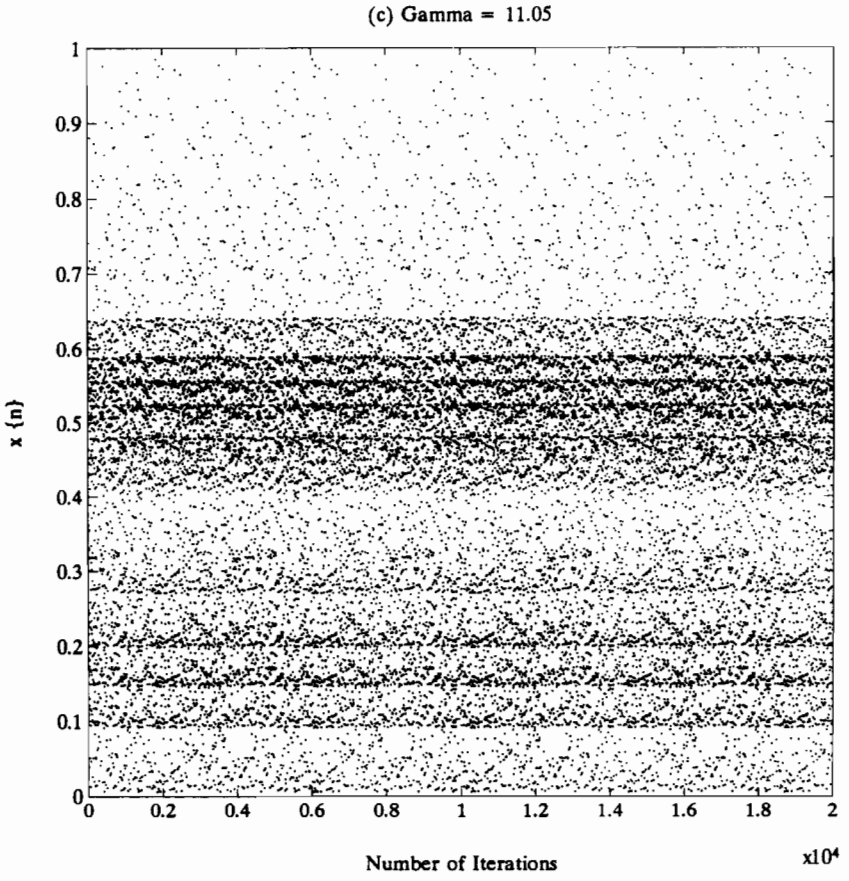
(c) Gamma = 11.05
x (n)
Number of Iterations
x10^4
0
0.1
0.2
0.3
0.4
0.5
0.6
0.7
0.8
0.9
1
0.2
0.4
0.6
0.8
1
1.2
1.4
1.6
1.8
2

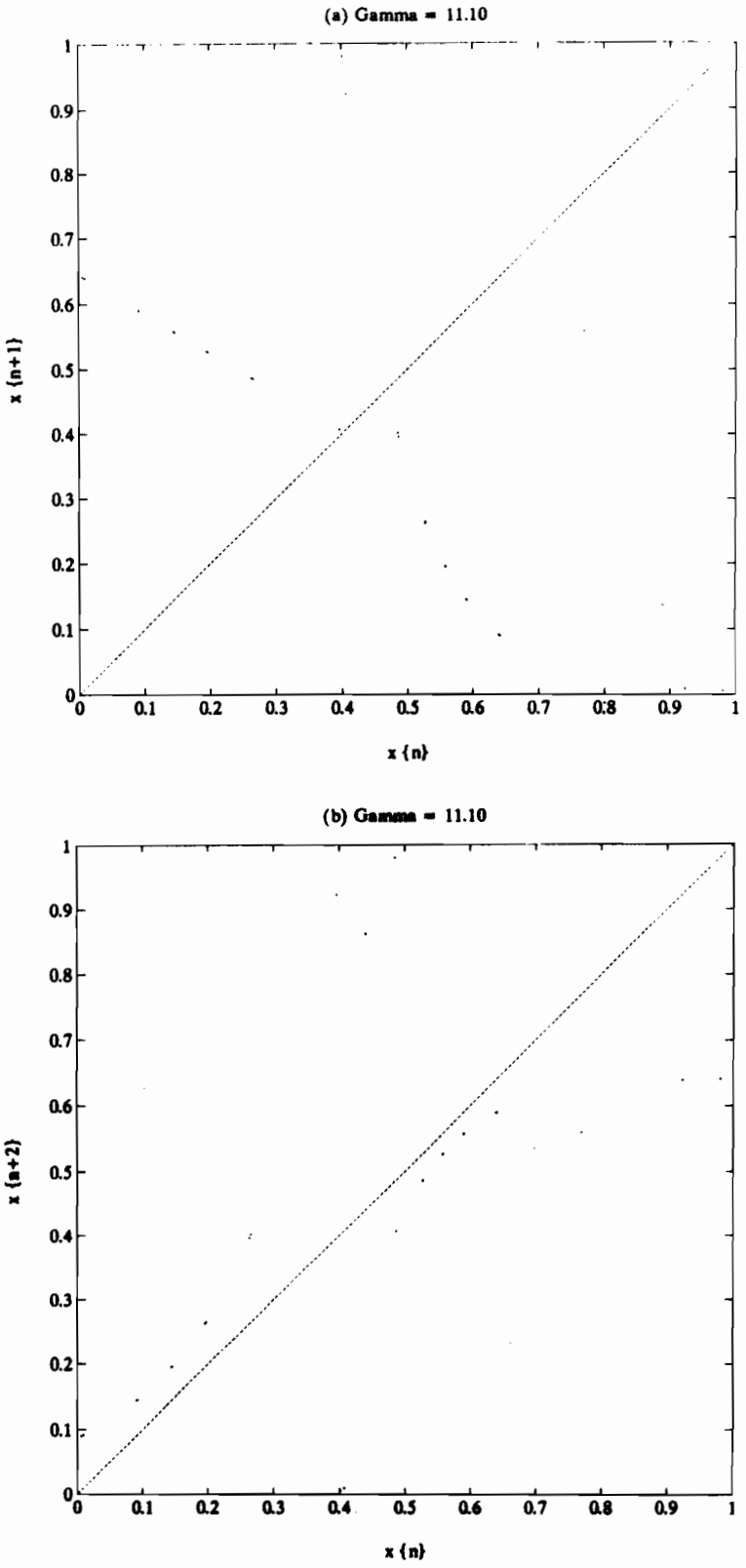

Figure 3.22: (a) The first return map, (b) second return map and (c) long term behaviour of the analytical system given by equation (3.2) for the case of $\gamma = 11.10$.

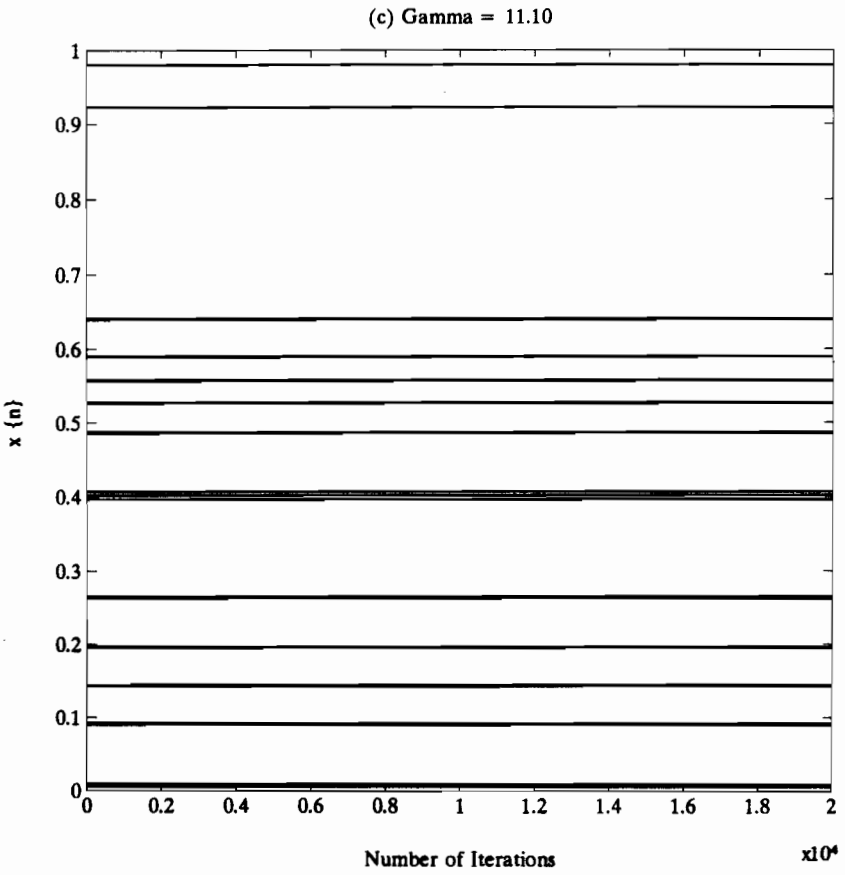
(c) Gamma = 11.10
x (n)
1
0.9
0.8
0.7
0.6
0.5
0.4
0.3
0.2
0.1
0
0
0.2
0.4
0.6
0.8
1
1.2
1.4
1.6
1.8
2
Number of Iterations
x10⁴

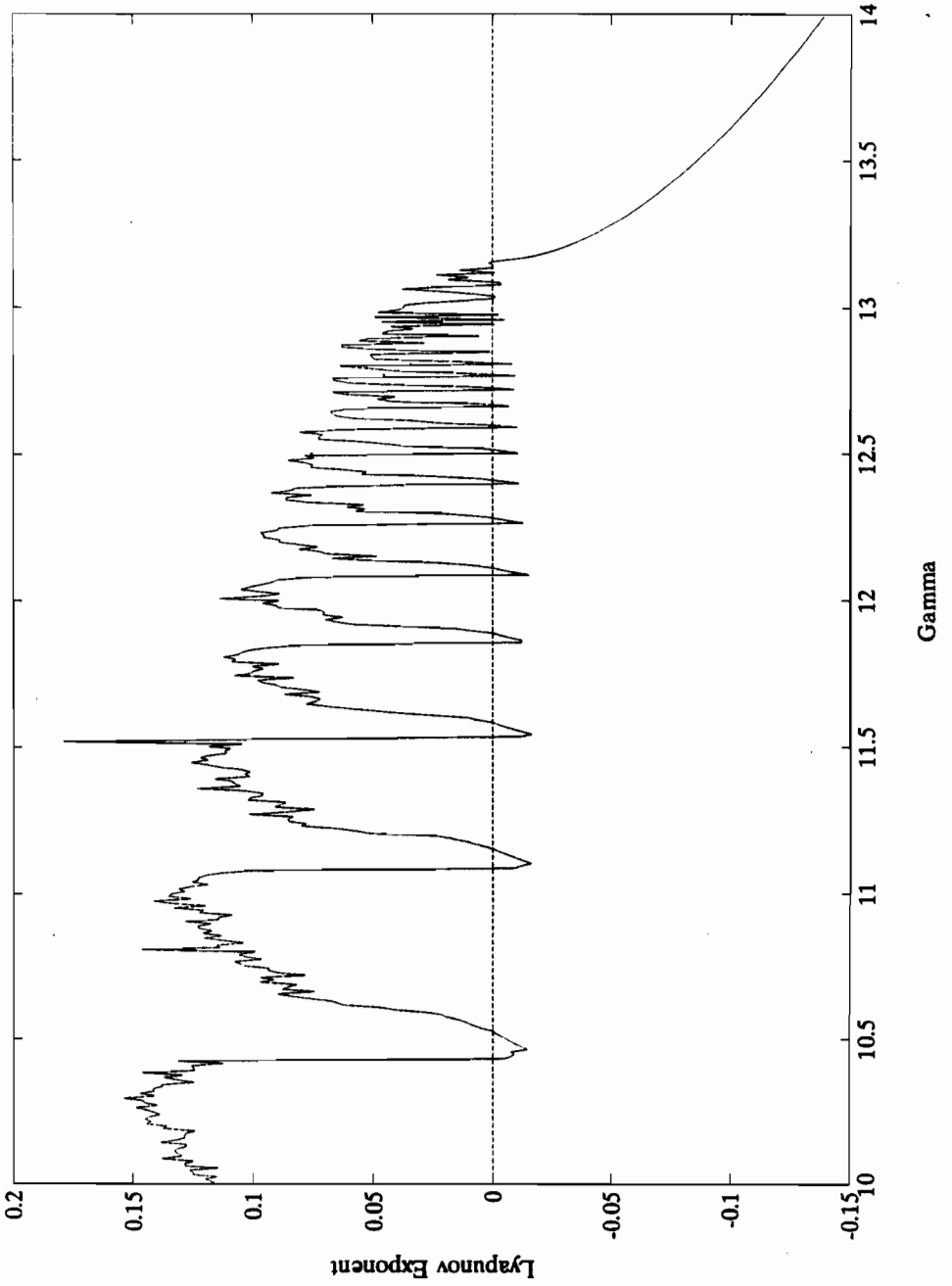

Figure 3.23: The Lyapunov exponent versus the variable γ of the analytical system given by equation (3.2).

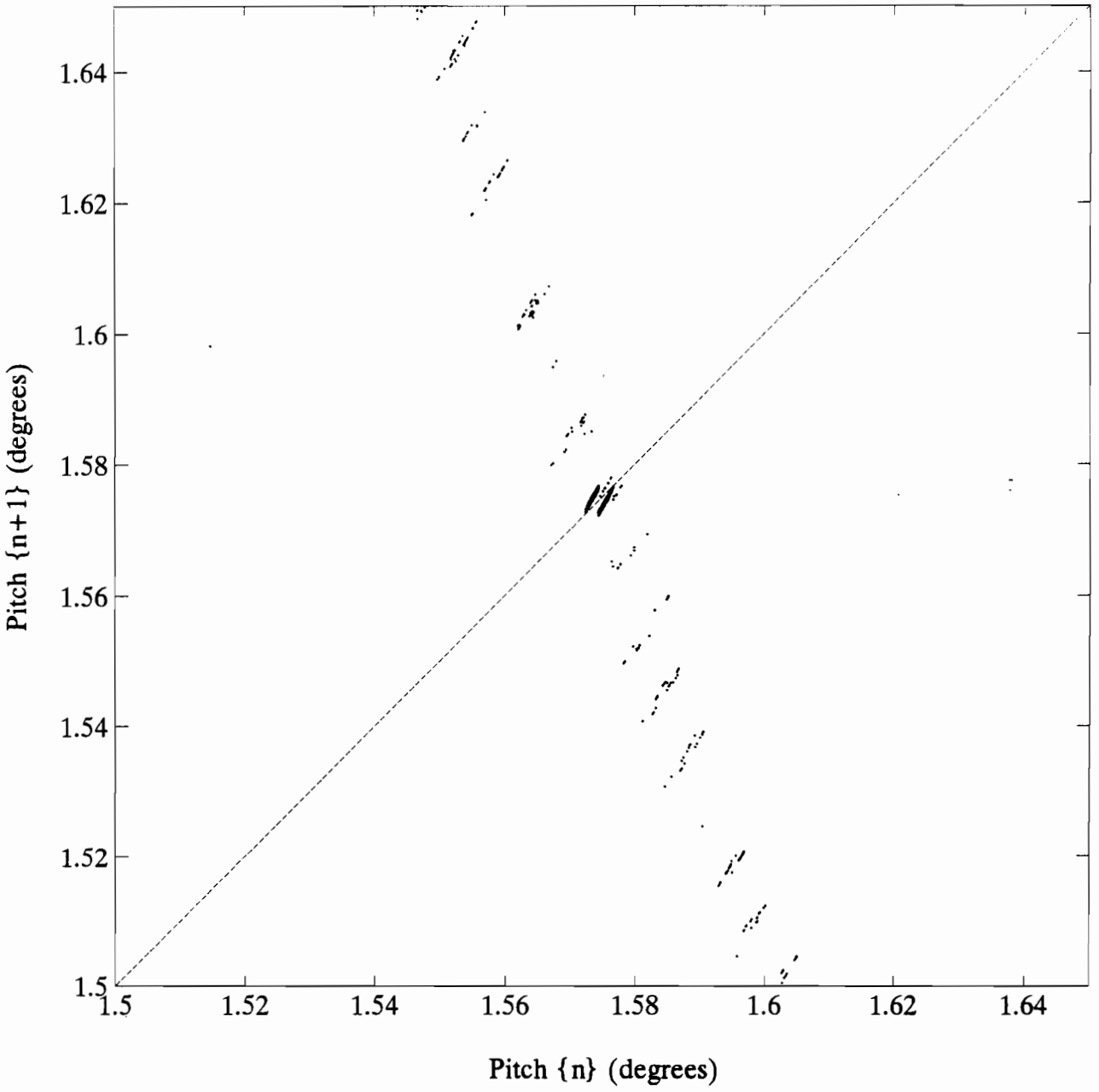

Figure 3.24: The micro-structure of the first return map attractor for the case: $Q_o = 1.020 * 10^{-4}$, $\alpha_o = 8.90°$, $U^* = 21.0227$ and $k = 0.044$ (see Figure 3.18(a)).

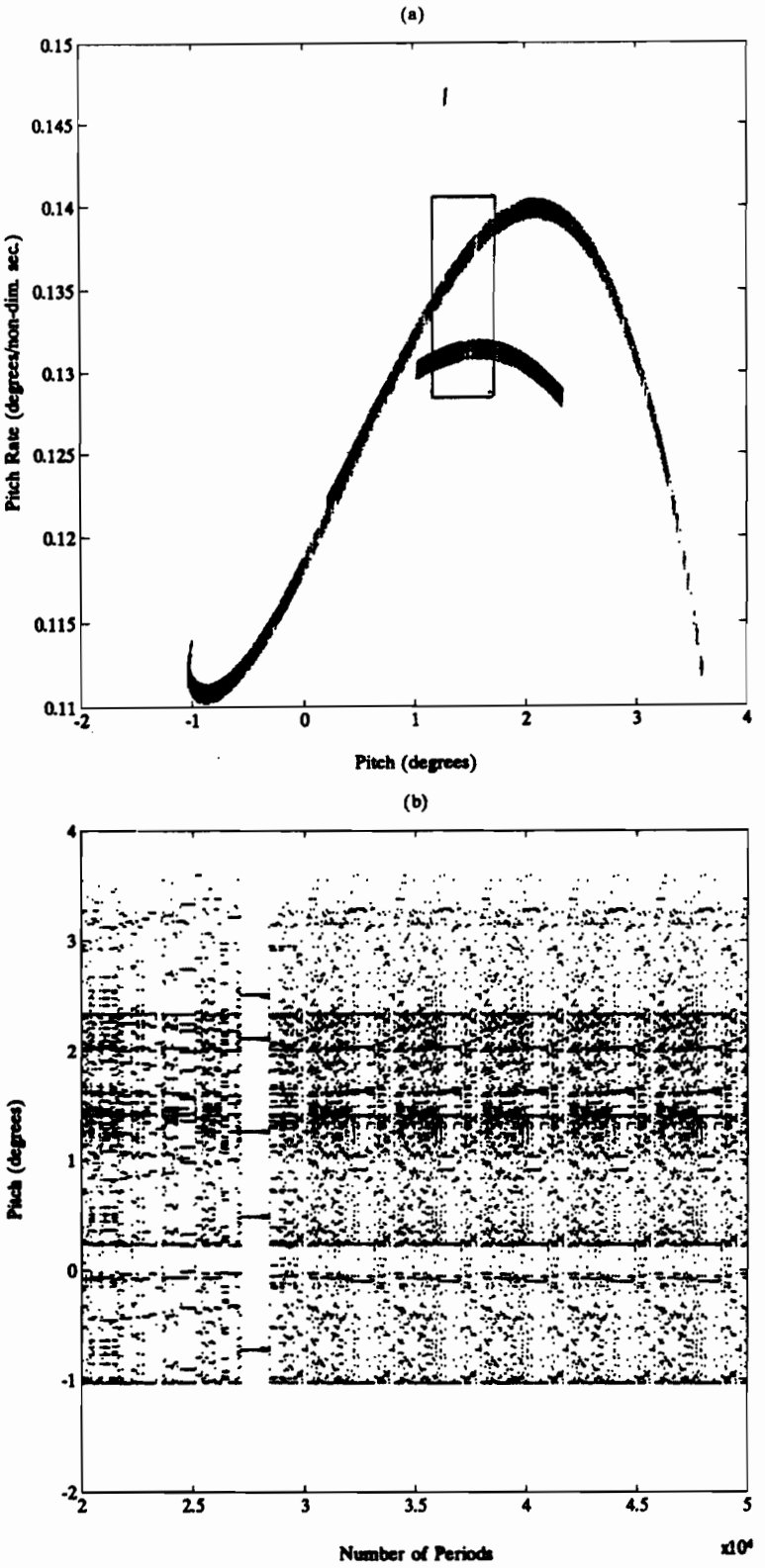

Figure 3.25: (a) The Poincaré section and (b) the long term behaviour for the case: $Q_o = 1.050 * 10^{-4}$, $\alpha_o = 8.90°$, $U^* = 21.0227$ and $k = 0.044$ for the time period of 20,000 to 50,000 periods of the forcing frequency.

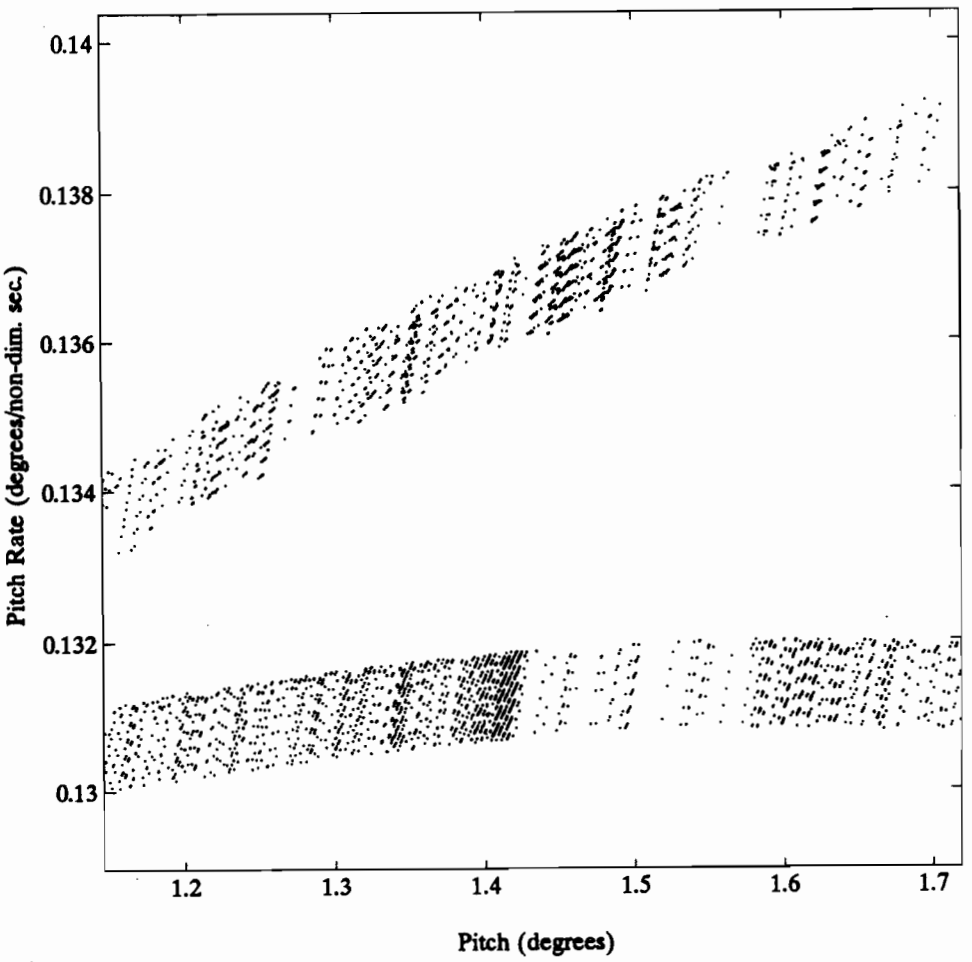

Figure 3.26: The micro-structure of the Poincaré attractor for the case: $Q_o = 1.050 * 10^{-4}$, $\alpha_o = 8.90°$, $U^* = 21.0227$ and $k = 0.044$ for the time period of 20,000 to 50,000 periods of the forcing frequency (see Figure 3.25(a)).

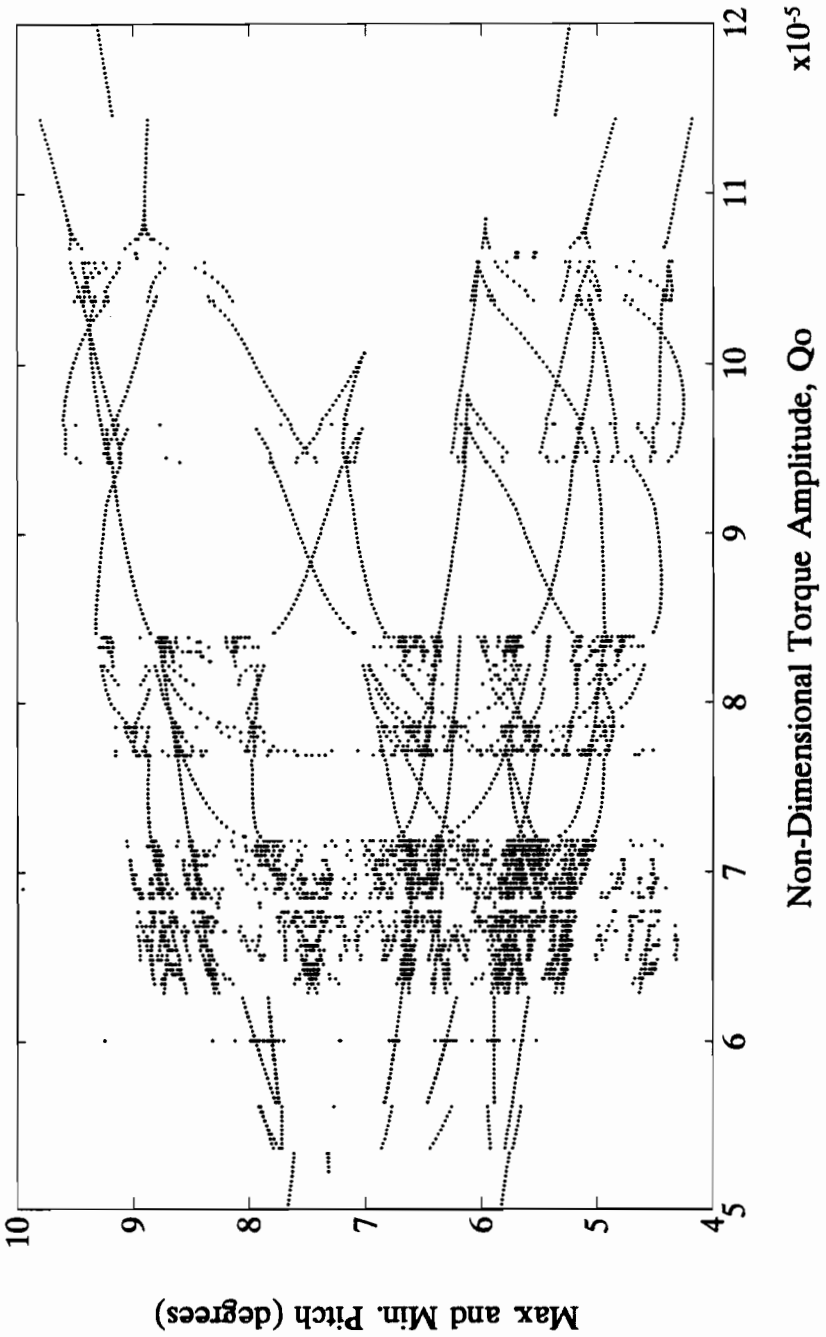

Figure 3.27: Bifurcation diagram for the case: $\alpha_o = 9.76^o$, $U^* = 12.20$, $k = 0.088$ and $5.0 * 10^{-5} < Q_o < 12.0 * 10^{-5}$.

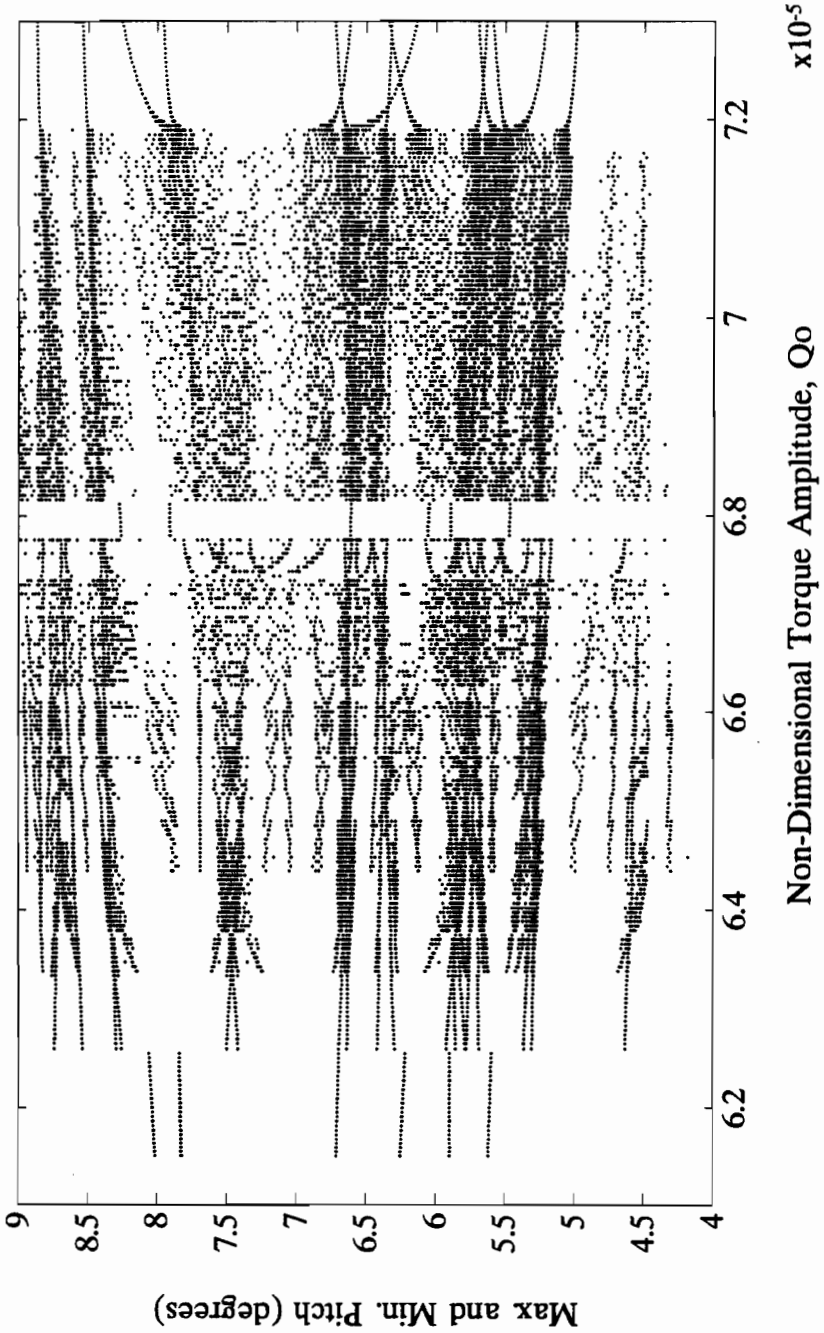

Figure 3.28: Bifurcation diagram for the case: $\alpha_o = 9.76°$, $U^* = 12.20$, $k = 0.088$ and $6.12 * 10^{-5} < Q_o < 7.30 * 10^{-5}$.

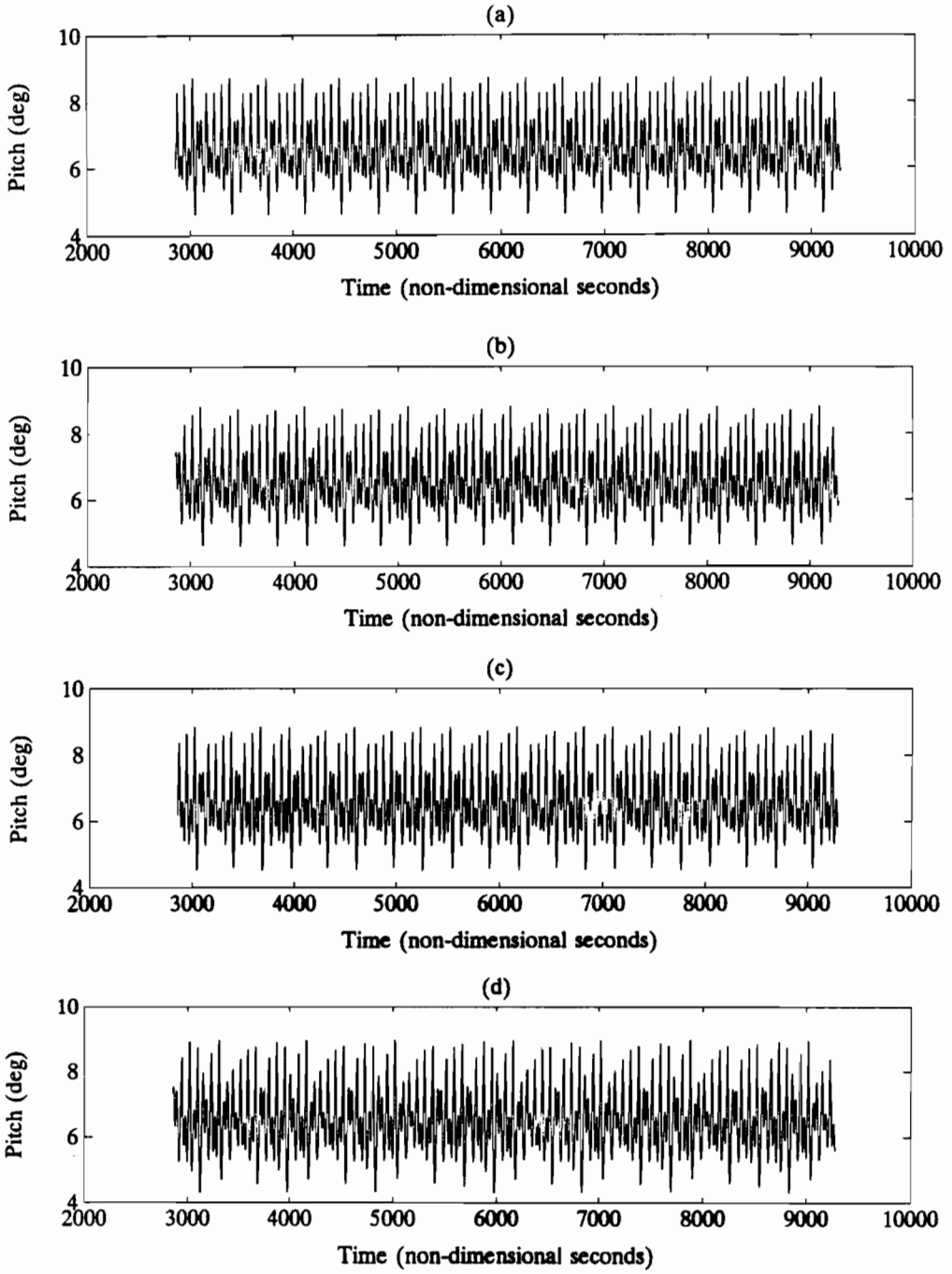

Figure 3.29: The **time histories** of the response of the airfoil for the cases: $\alpha_o = 9.76^o$, $U^* = 12.20$ and $k = 0.088$ and (a) $Q_o = 0.630{*}10^{-4}$, (b) $Q_o = 0.635{*}10^{-4}$, (c) $Q_o = 0.640 * 10^{-4}$ and (d) $Q_o = 0.660 * 10^{-4}$.

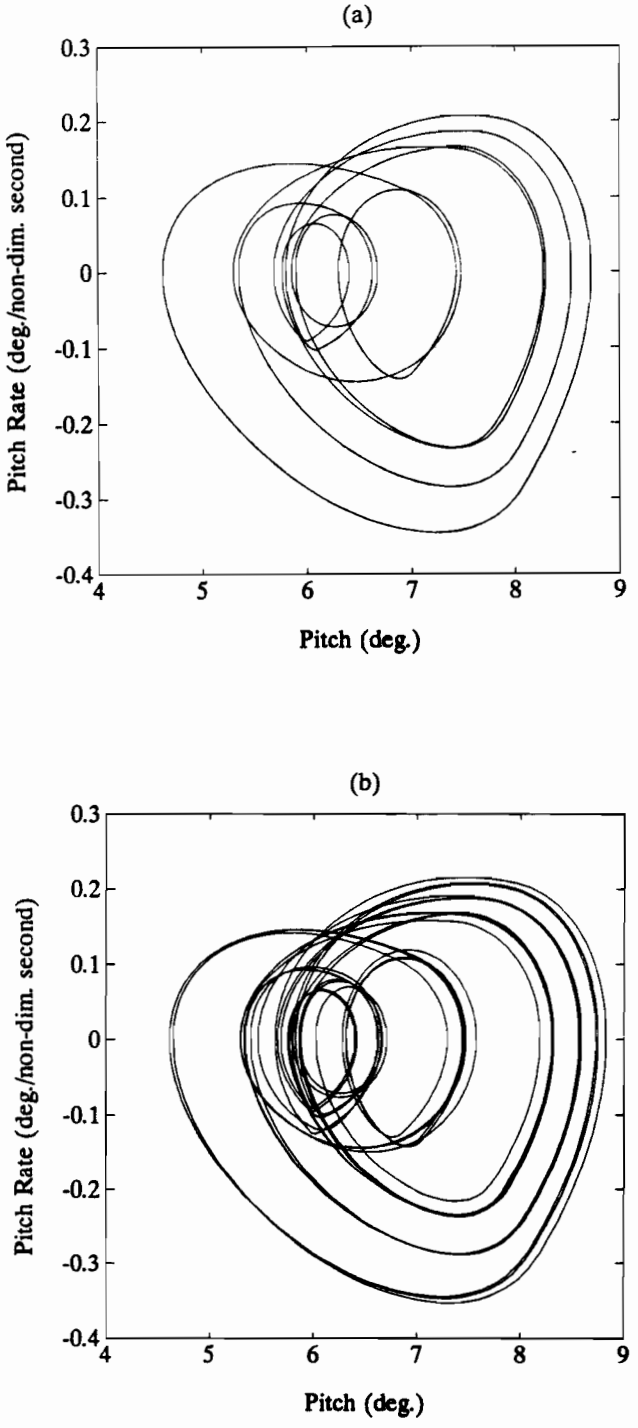

Figure 3.30: The **phase plane plots** of the response of the airfoil for the cases: $\alpha_o = 9.76°$, $U^* = 12.20$ and $k = 0.088$ and (a) $Q_o = 0.630{*}10^{-4}$, (b) $Q_o = 0.635{*}10^{-4}$, (c) $Q_o = 0.640 * 10^{-4}$ and (d) $Q_o = 0.660 * 10^{-4}$.

(c)

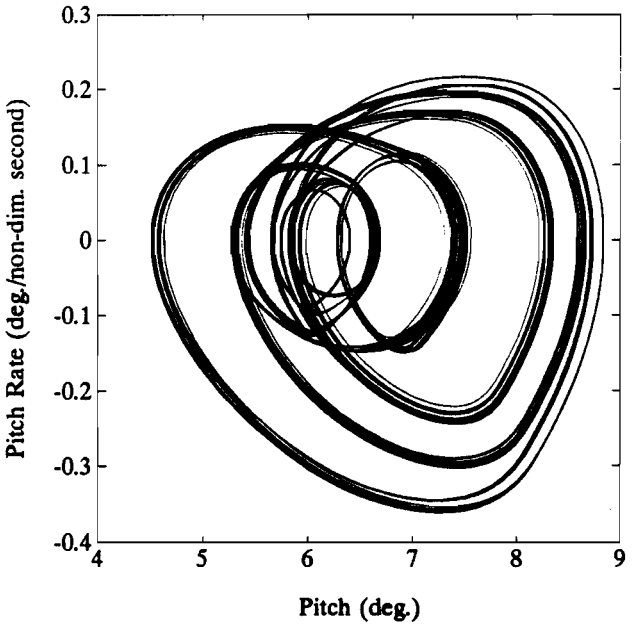
0.3
0.2
0.1
0
-0.1
-0.2
-0.3
-0.4
4
5
6
7
8
9
Pitch Rate (deg./non-dim. second)
Pitch (deg.)

(d)

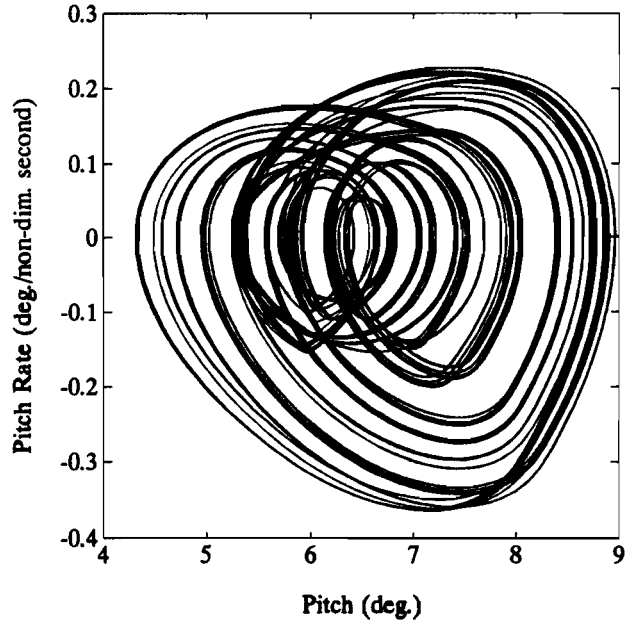
0.3
0.2
0.1
0
-0.1
-0.2
-0.3
-0.4
4
5
6
7
8
9
Pitch Rate (deg./non-dim. second)
Pitch (deg.)

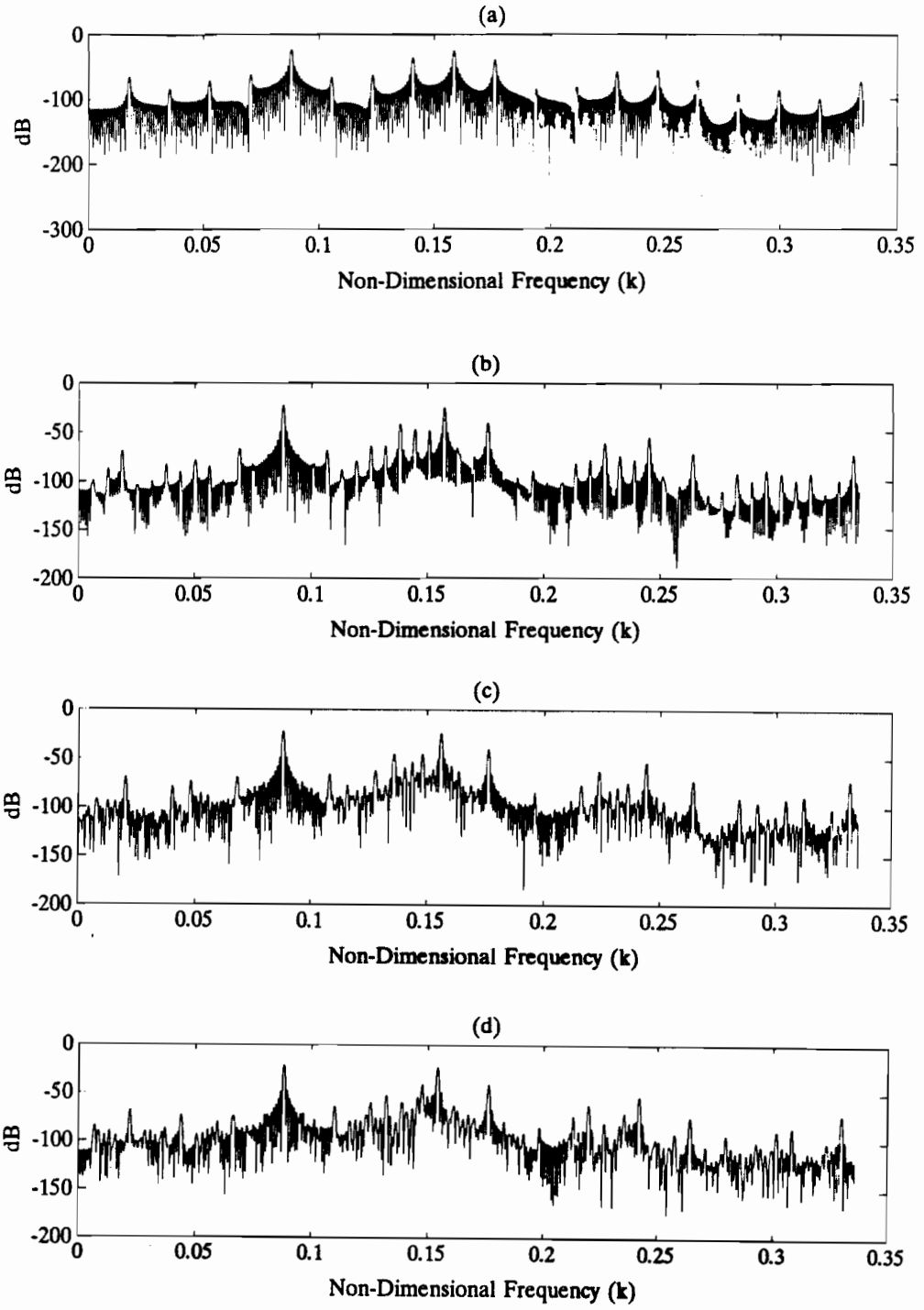

Figure 3.31: The **Fourier spectra** of the response of the airfoil for the cases: $\alpha_o = 9.76^o$, $U^* = 12.20$ and $k = 0.088$ and (a) $Q_o = 0.630{*}10^{-4}$, (b) $Q_o = 0.635{*}10^{-4}$, (c) $Q_o = 0.640 * 10^{-4}$ and (d) $Q_o = 0.660 * 10^{-4}$.

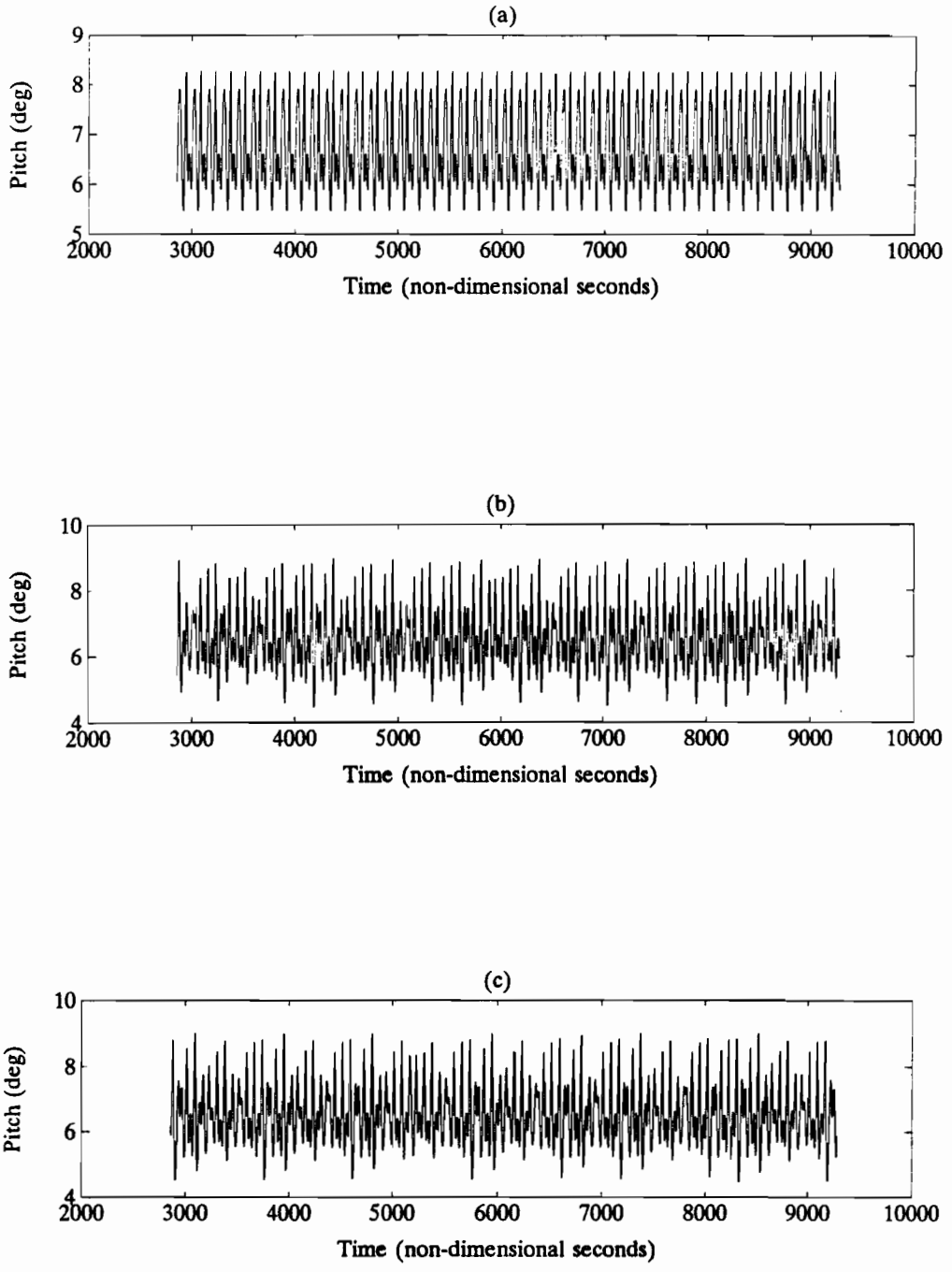

Figure 3.32: The **time histories** of the response of the airfoil for the cases: $\alpha_o = 9.76^o$, $U^* = 12.20$ and $k = 0.088$ and (a) $Q_o = 0.6815927 * 10^{-4}$, (b) $Q_o = 0.6815928 * 10^{-4}$ and (c) $Q_o = 0.700 * 10^{-4}$.

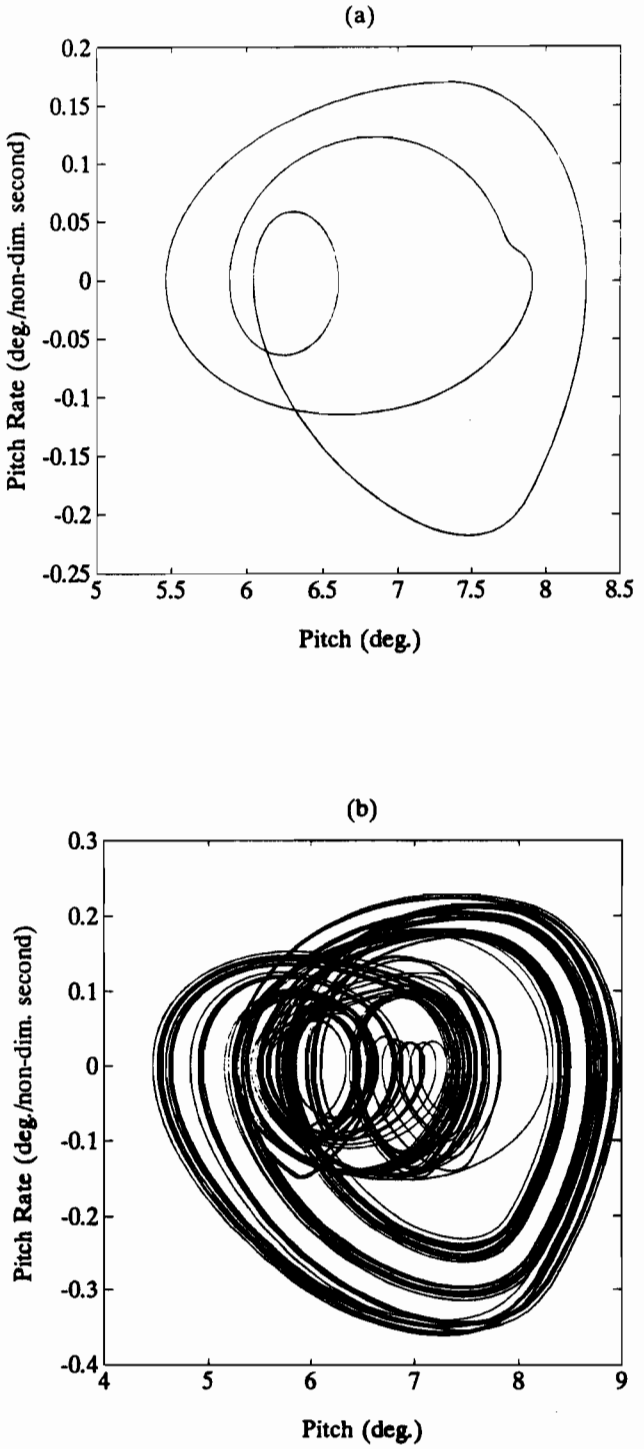

Figure 3.33: The **phase plane plots** of the response of the airfoil for the cases: $\alpha_o = 9.76^o$, $U^* = 12.20$ and $k = 0.088$ and (a) $Q_o = 0.6815927 * 10^{-4}$, (b) $Q_o = 0.6815928 * 10^{-4}$ and (c) $Q_o = 0.700 * 10^{-4}$.

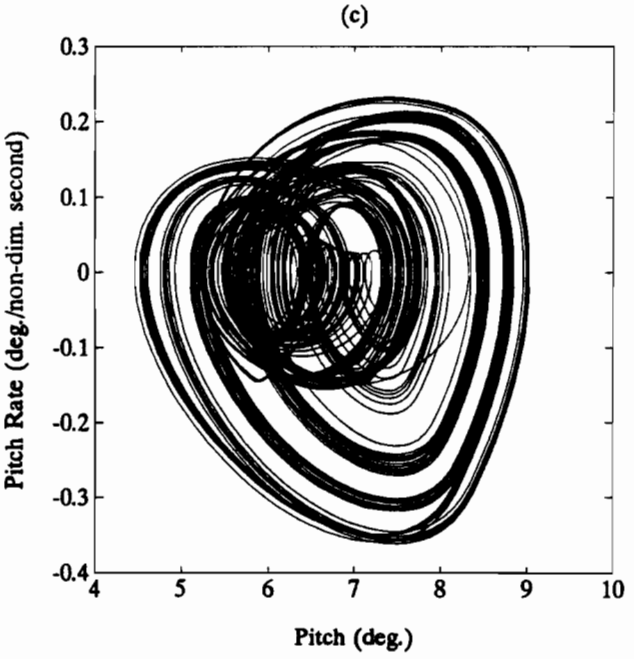
(c)
0.3
0.2
0.1
0
-0.1
-0.2
-0.3
-0.4
4
5
6
7
8
9
10
Pitch Rate (deg./non-dim. second)
Pitch (deg.)

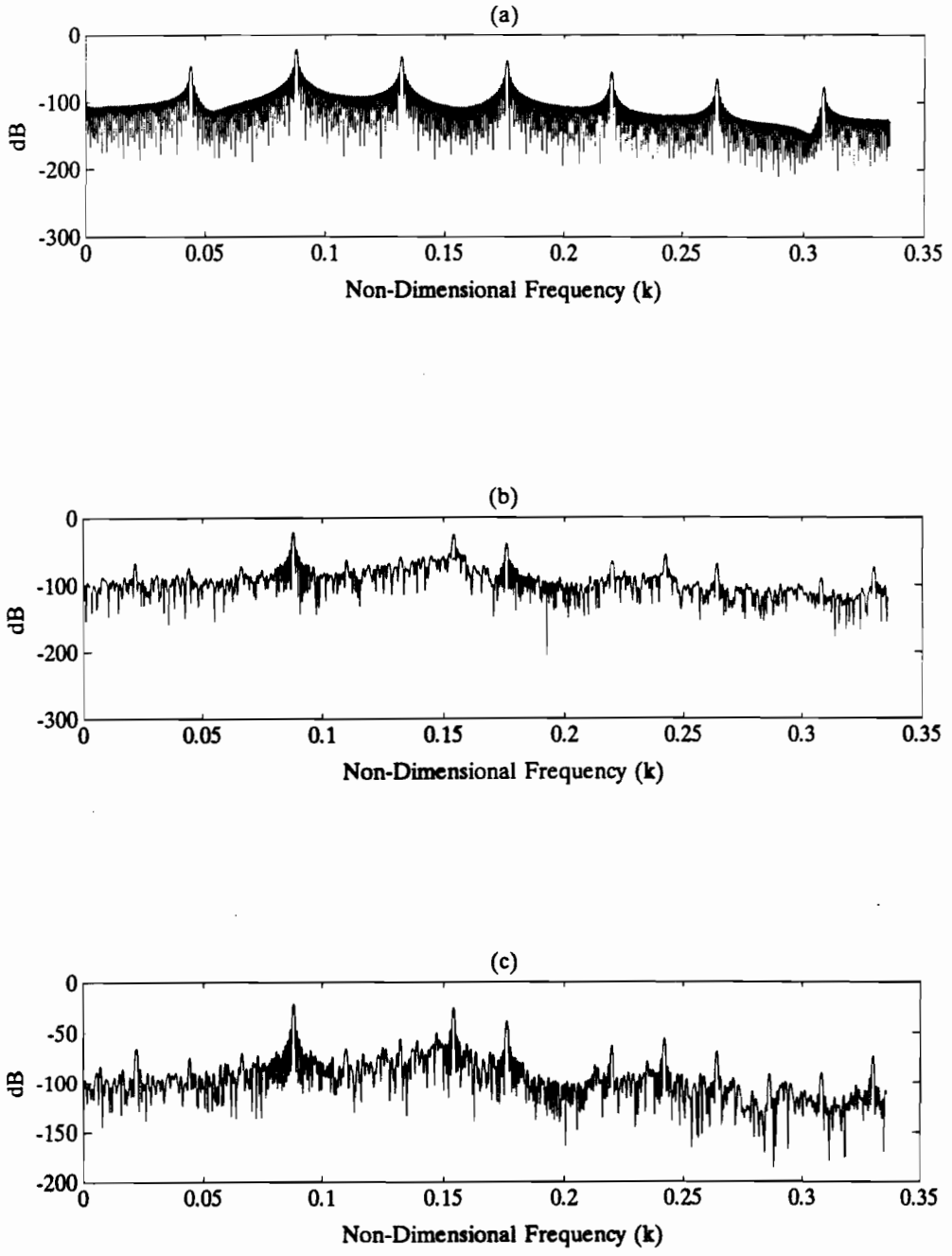

Figure 3.34: The **Fourier spectra** of the response of the airfoil for the cases: $\alpha_o = 9.76^o$, $U^* = 12.20$ and $k = 0.088$ and (a) $Q_o = 0.6815927 * 10^{-4}$, (b) $Q_o = 0.6815928 * 10^{-4}$ and (c) $Q_o = 0.700 * 10^{-4}$.

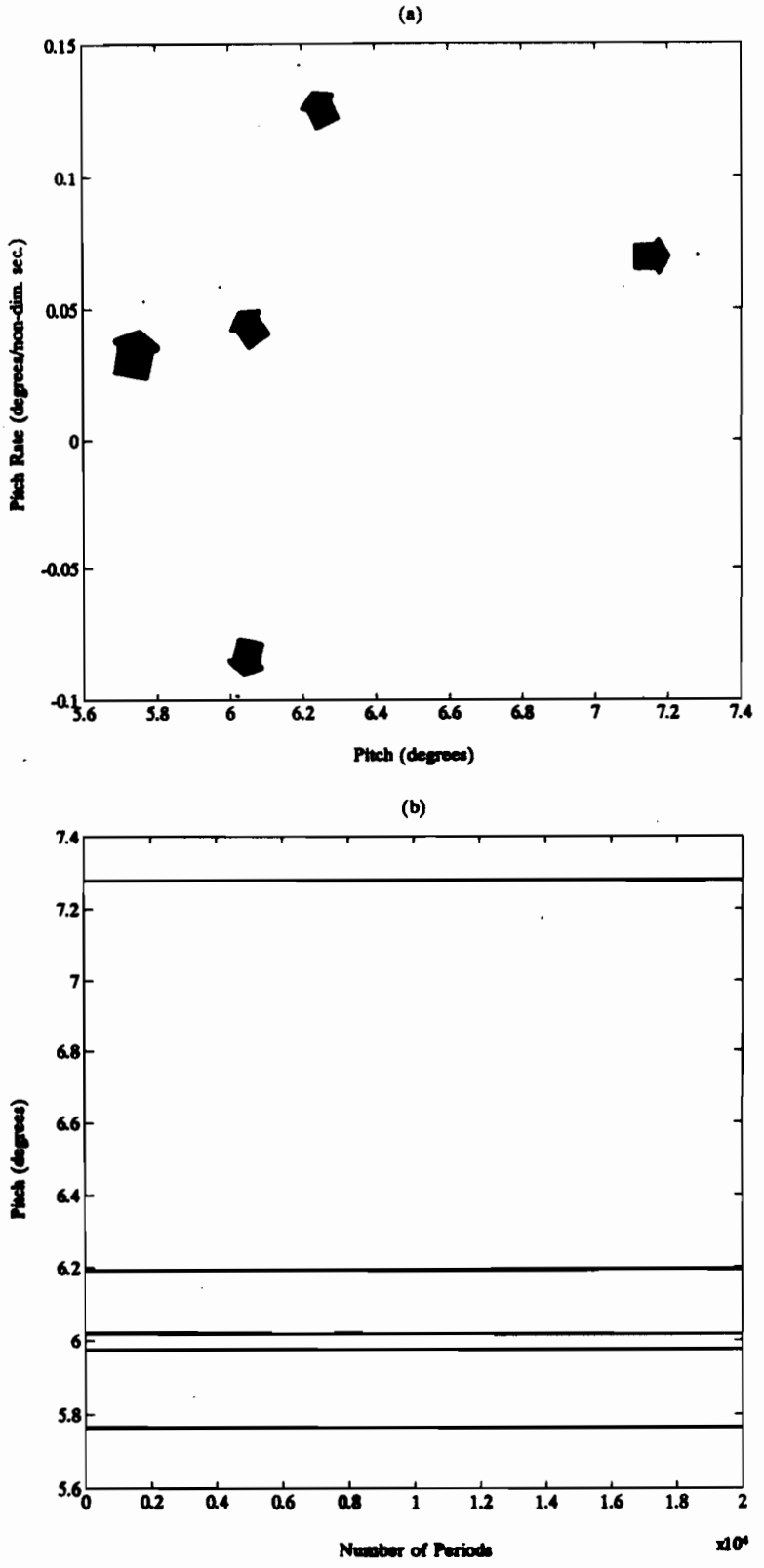

Figure 3.35: (a) The Poincaré section and (b) the long term behaviour of the system for the case: $\mathbf{Q_o = 0.630 * 10^{-4}}$, $\alpha_o = 9.76^o$, $U^* = 12.20$ and $k = 0.088$.

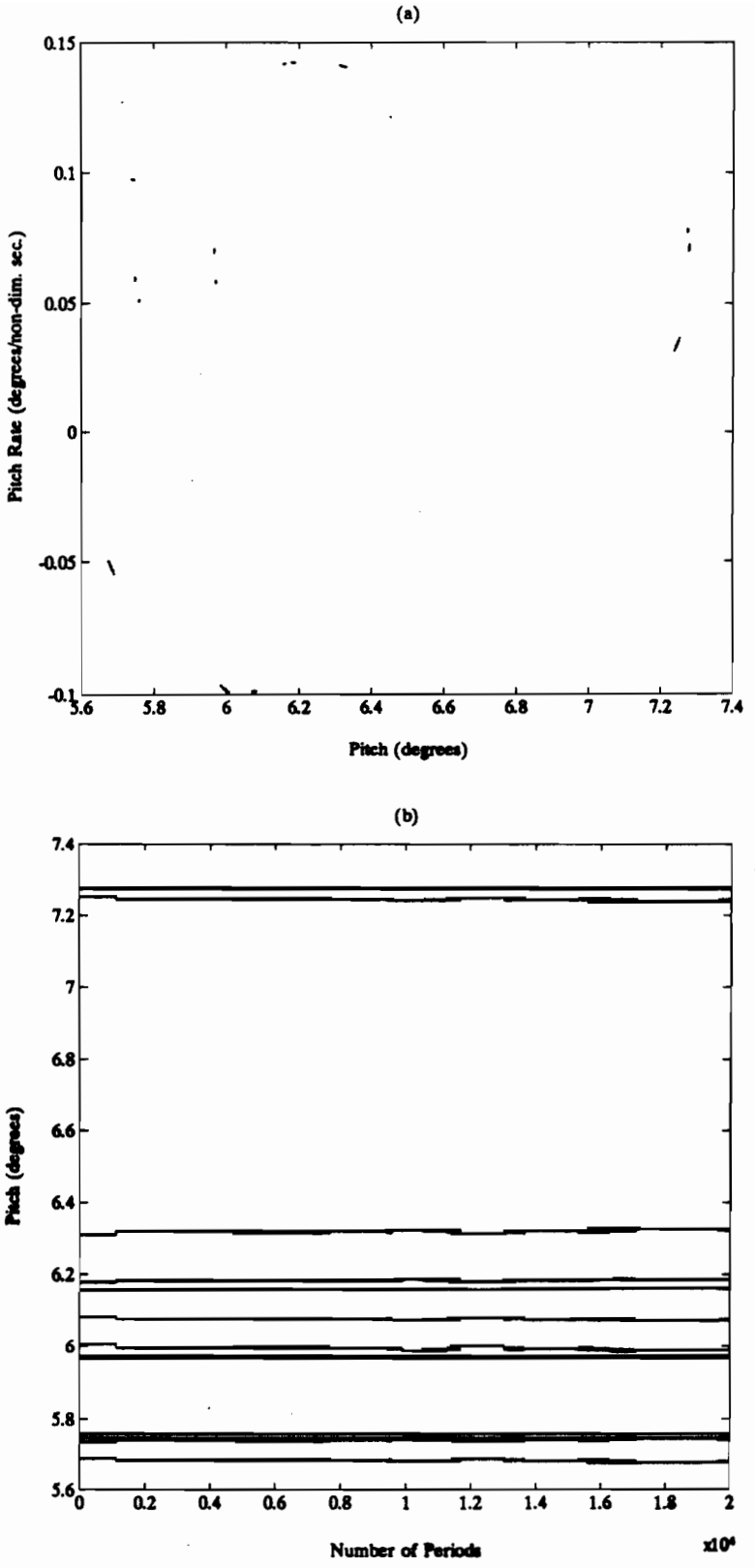

Figure 3.36: (a) The Poincaré section and (b) the long term behaviour of the system for the case: $\mathbf{Q_o = 0.635 * 10^{-4}}$, $\alpha_o = 9.76^o$, $U^* = 12.20$ and $k = 0.088$.

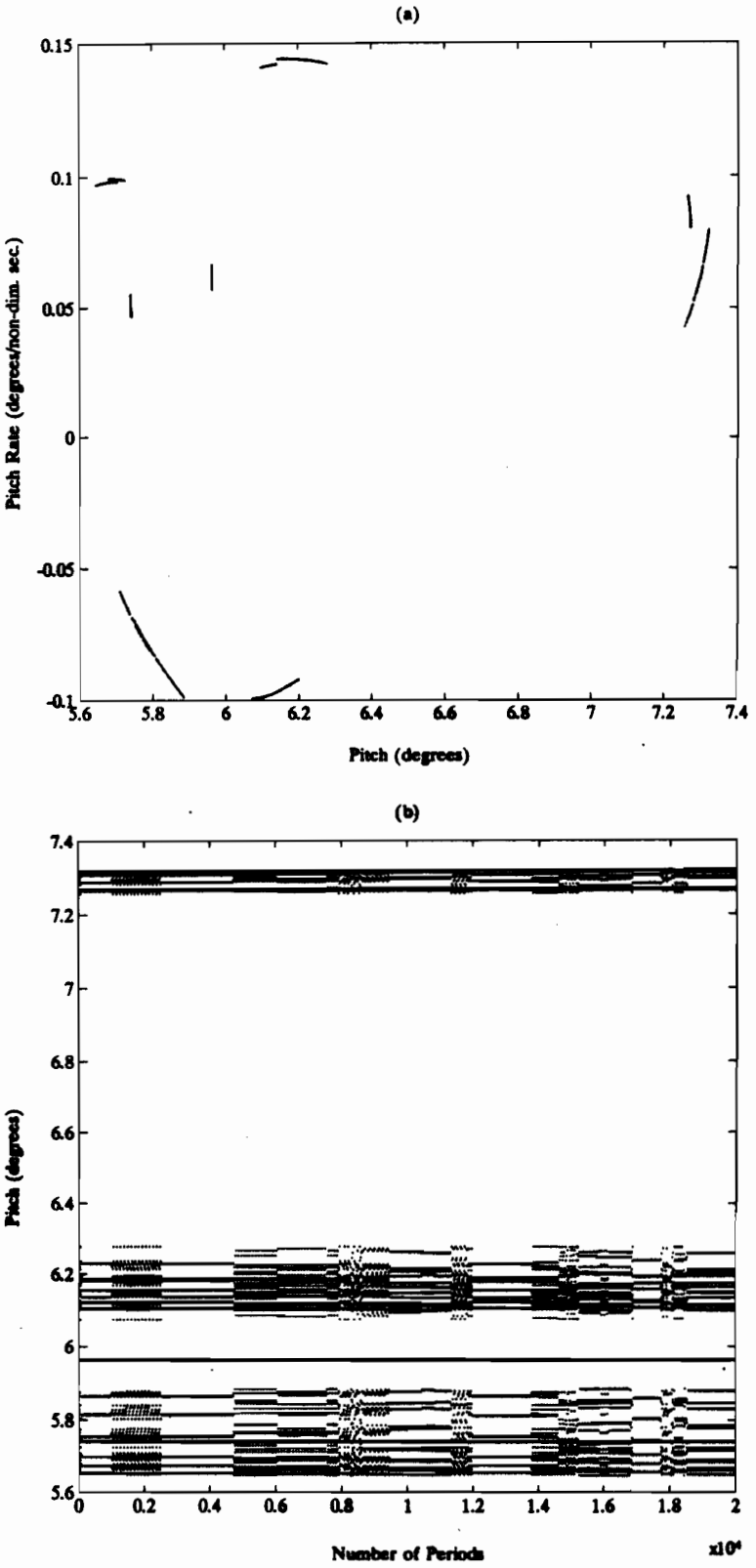

Figure 3.37: (a) The Poincaré section and (b) the long term behaviour of the system for the case: $\mathbf{Q_o = 0.640 * 10^{-4}}$, $\alpha_o = 9.76^o$, $U^* = 12.20$ and $k = 0.088$.

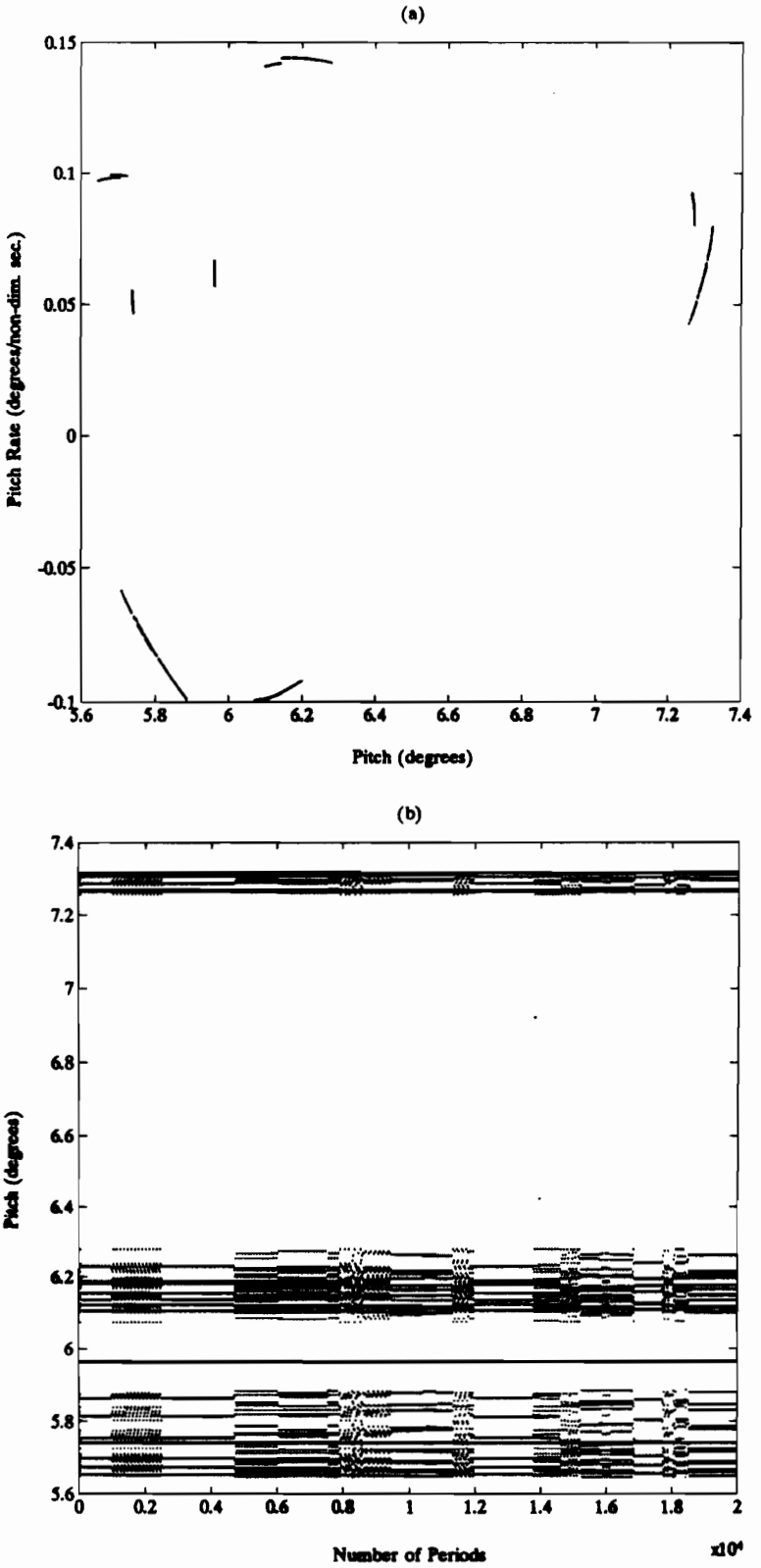

Figure 3.38: (a) The Poincaré section and (b) the long term behaviour of the system for the case: $\mathbf{Q_o = 0.660 * 10^{-4}}$, $\alpha_o = 9.76°$, $U^* = 12.20$ and $k = 0.088$.

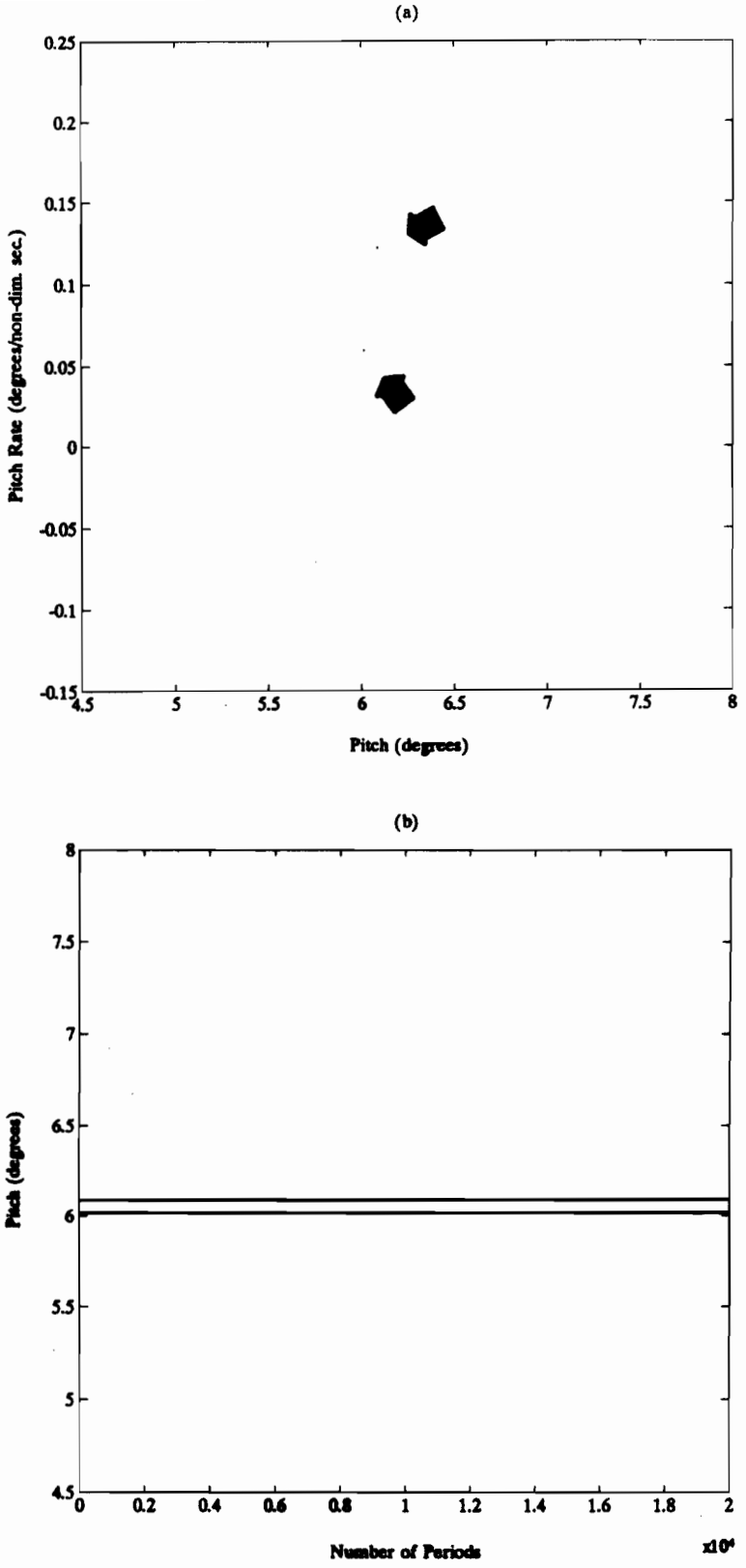

Figure 3.39: (a) The Poincaré section and (b) the long term behaviour of the system for the case: $\mathbf{Q_o = 0.6815927 * 10^{-4}}$, $\alpha_o = 9.76°$, $U^* = 12.20$ and $k = 0.088$.

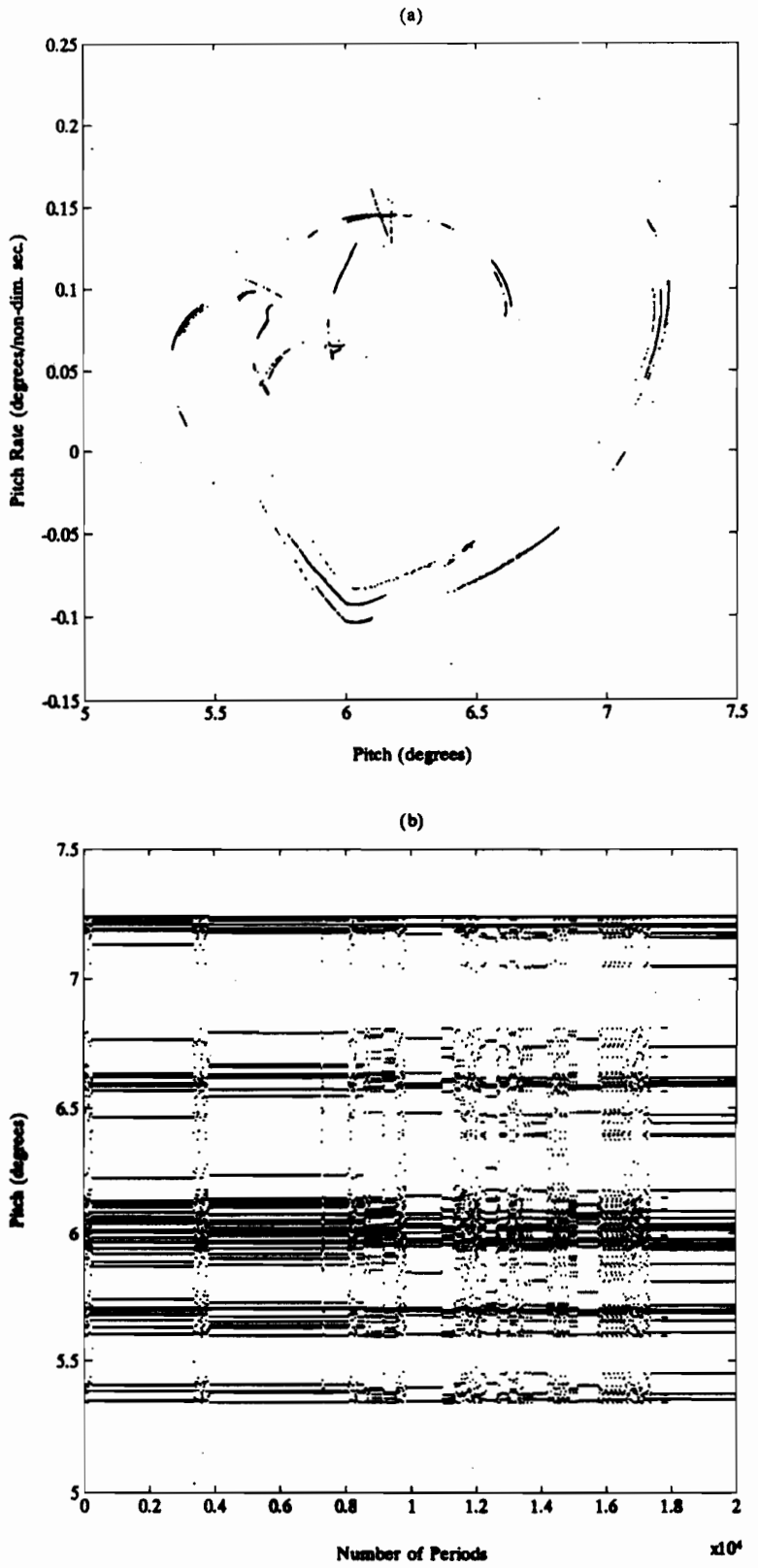

Figure 3.40: (a) The Poincaré section and (b) the long term behaviour of the system for the case: $\mathbf{Q_o = 0.6815928 * 10^{-4}}$, $\alpha_o = 9.76°$, $U^* = 12.20$ and $k = 0.088$.

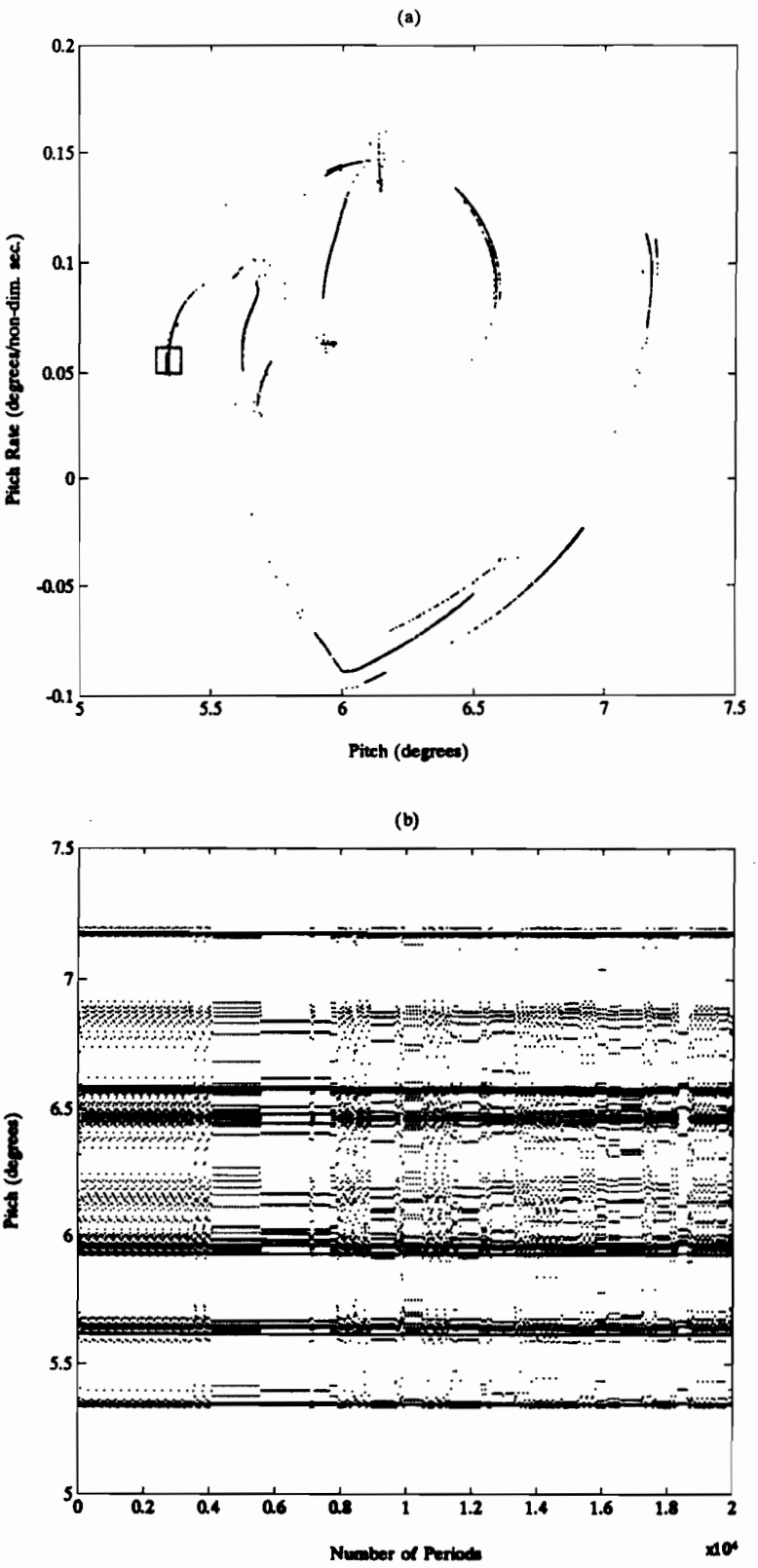

Figure 3.41: (a) The Poincaré section and (b) the long term behaviour of the system for the case: $\mathbf{Q_o = 0.700 * 10^{-4}}$, $\alpha_o = 9.76°$, $U^* = 12.20$ and $k = 0.088$.

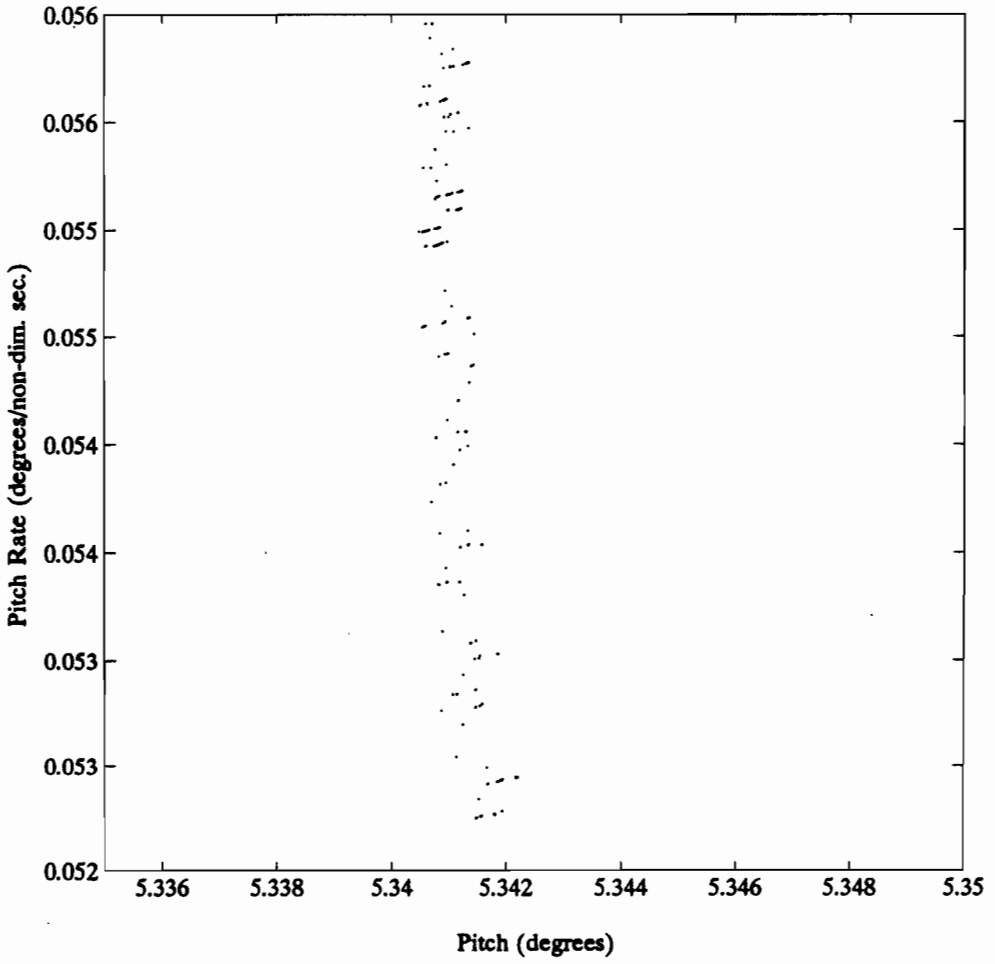

Figure 3.42: The micro-structure of the Poincaré attractor for the case: $Q_o = 0.700 * 10^{-4}$, $\alpha_o = 9.76°$, $U^* = 12.20$ and $k = 0.088$ (see Figure 3.41(a)).

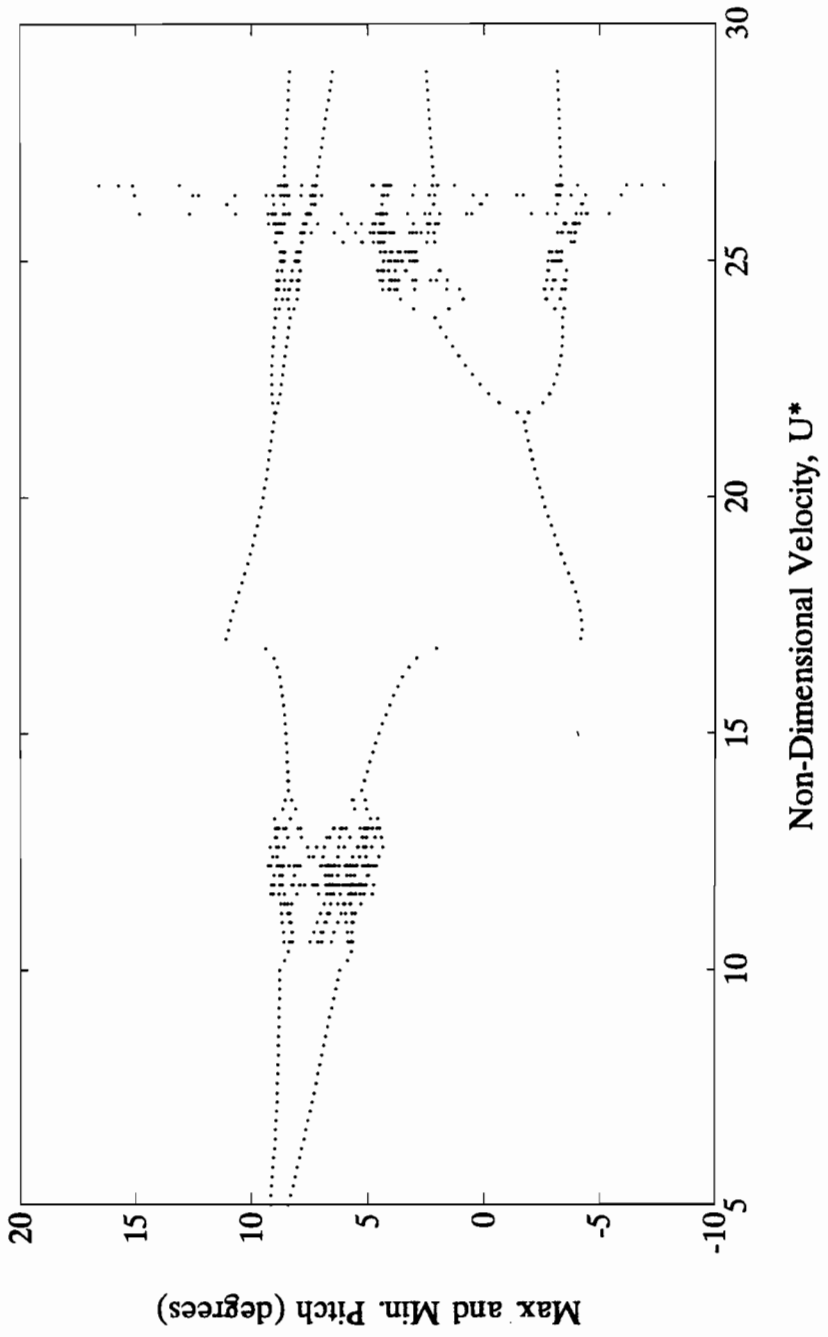

Figure 3.43: Bifurcation diagram for the case: $\alpha_o = 9.76^o$, $Q_o = 0.820 * 10^{-4}$, $k = 0.088$ and $5.0 < U^* < 28.0$.

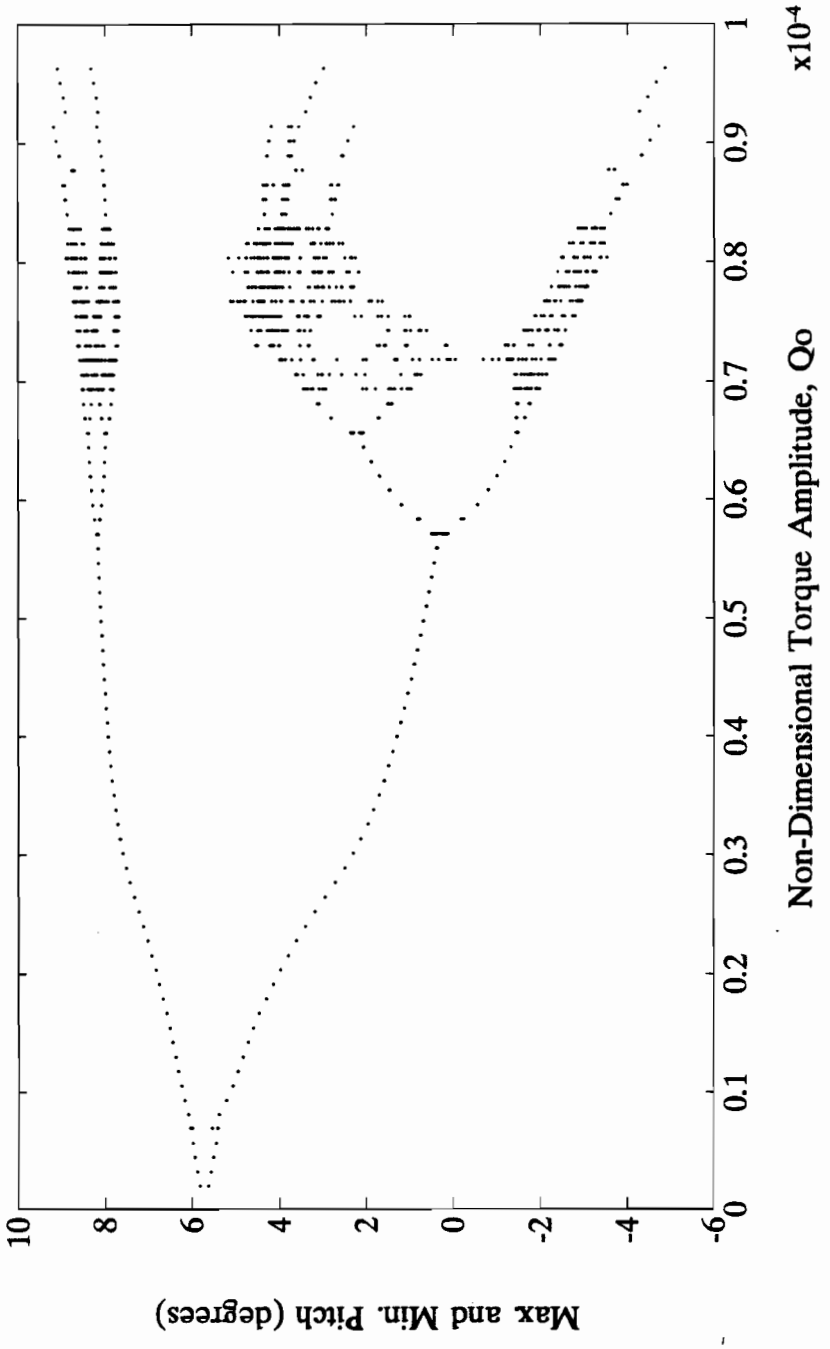

Figure 3.44: Bifurcation diagram for the case: $\alpha_o = 9.76°$, $U^* = 25.20$, $k = 0.088$ and $0.00 < Q_o < 1.00 * 10^{-4}$.

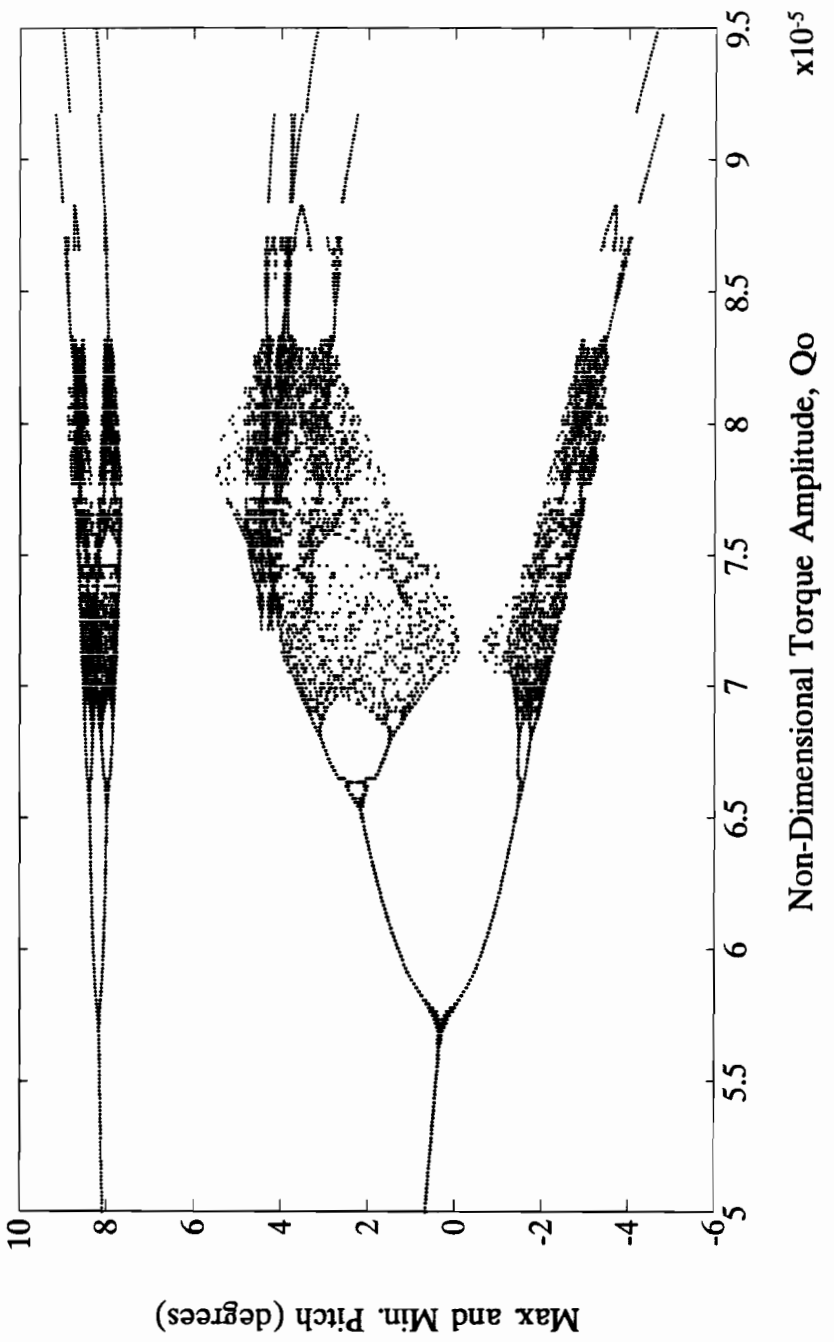

Figure 3.45: Bifurcation diagram for the case: $\alpha_o = 9.76^o$, $U^* = 25.20$, $k = 0.088$ and $5.00 * 10^{-5} < Q_o < 9.50 * 10^{-5}$.

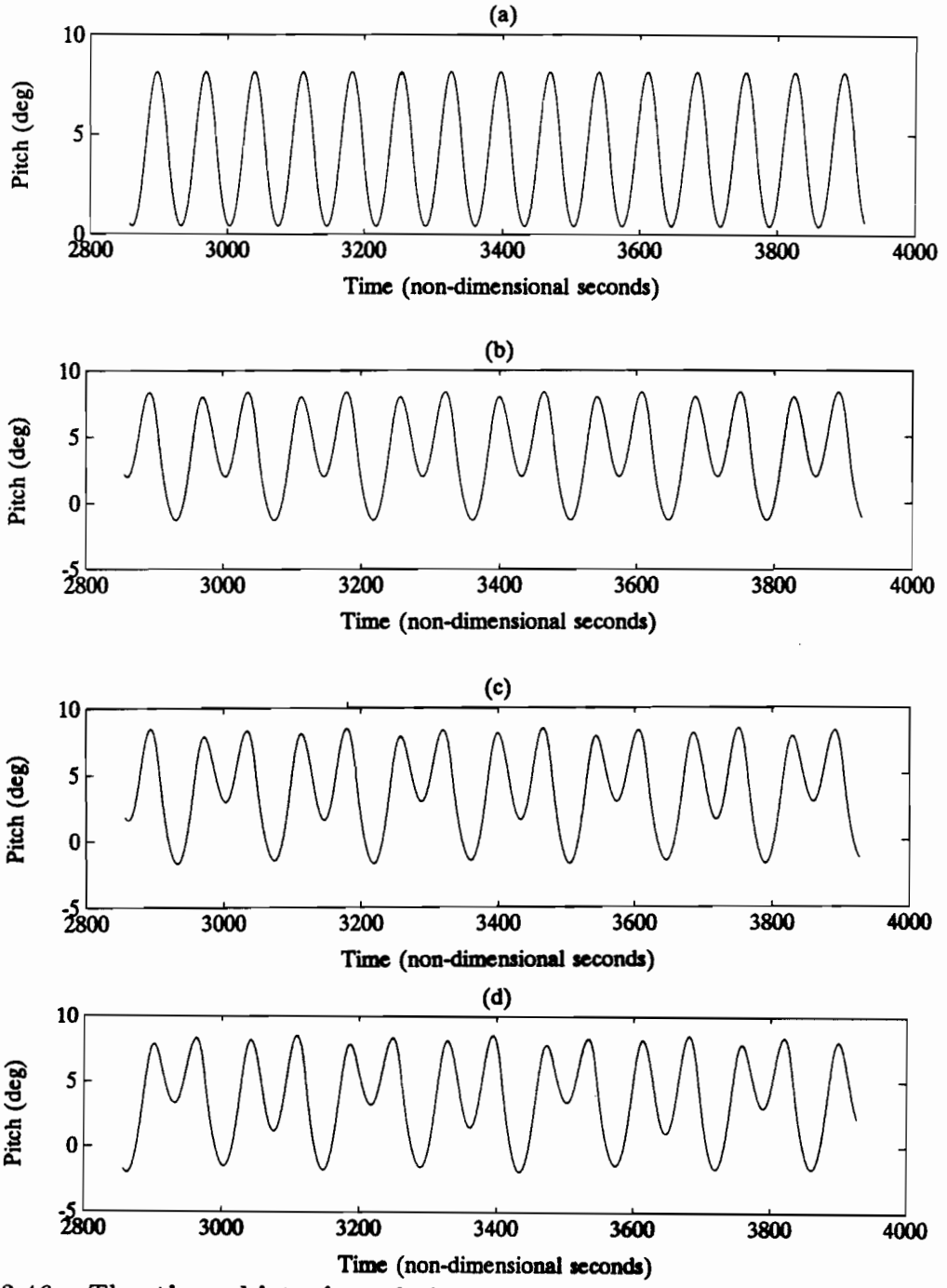

Figure 3.46: The **time histories** of the response of the airfoil for the cases: $\alpha_o = 9.76°$, $U^* = 25.20$ and $k = 0.088$ and (a) $Q_o = 0.550{*}10^{-4}$, (b) $Q_o = 0.640{*}10^{-4}$, (c) $Q_o = 0.675 * 10^{-4}$ and (d) $Q_o = 0.692 * 10^{-4}$.

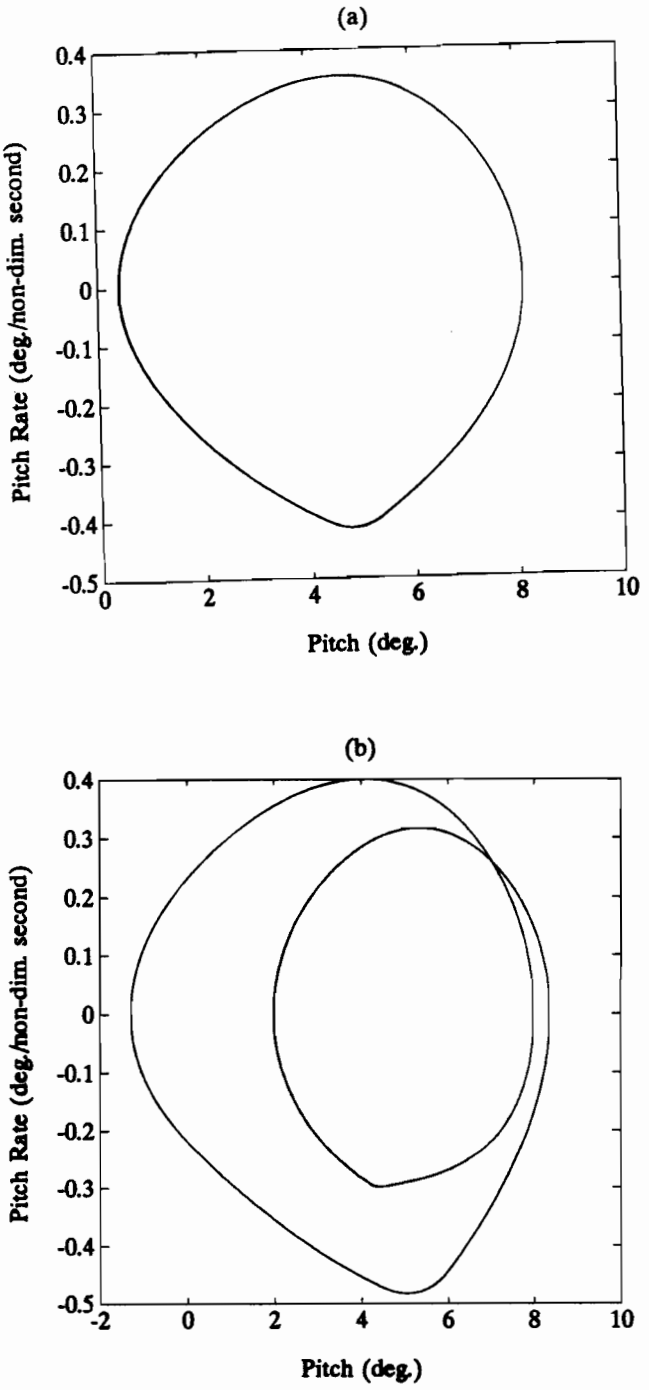

Figure 3.47: The **phase plane plots** of the response of the airfoil for the cases: $\alpha_o = 9.76°$, $U^* = 25.20$ and $k = 0.088$ and (a) $Q_o = 0.550{*}10^{-4}$, (b) $Q_o = 0.640{*}10^{-4}$, (c) $Q_o = 0.675 * 10^{-4}$ and (d) $Q_o = 0.692 * 10^{-4}$.

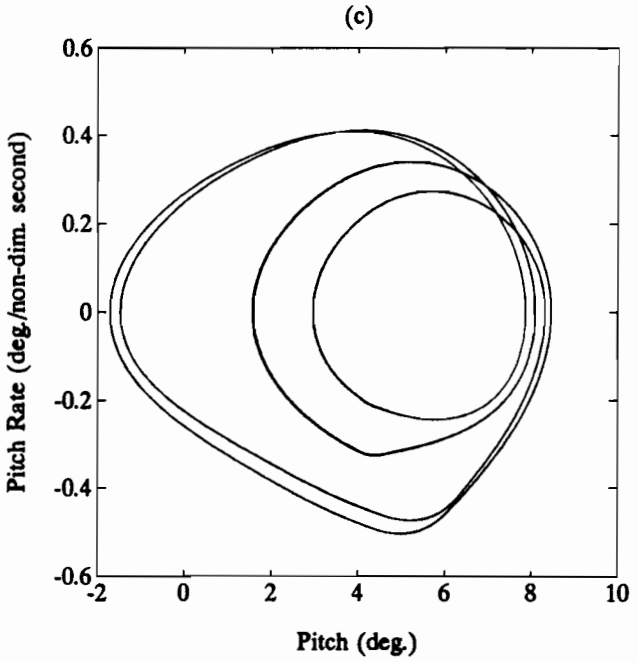
(c)
0.6
0.4
0.2
0
-0.2
-0.4
-0.6
-2
0
2
4
6
8
10
Pitch Rate (deg./non-dim. second)
Pitch (deg.)

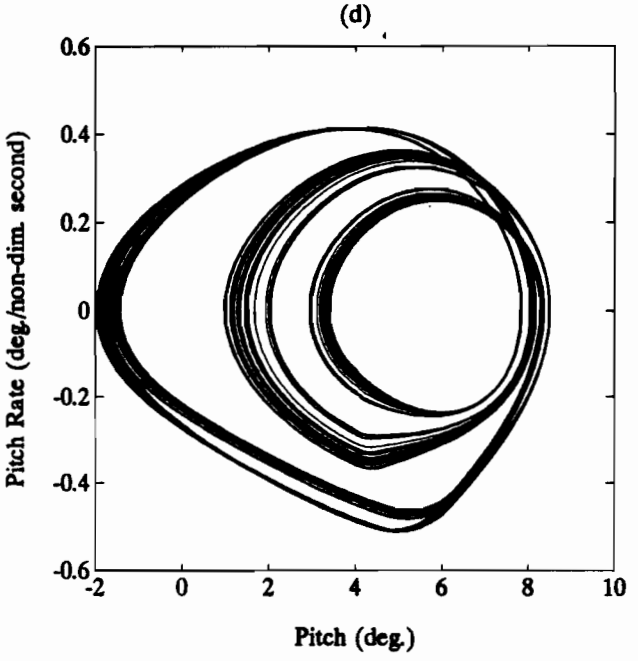
(d)
0.6
0.4
0.2
0
-0.2
-0.4
-0.6
-2
0
2
4
6
8
10
Pitch Rate (deg./non-dim. second)
Pitch (deg.)

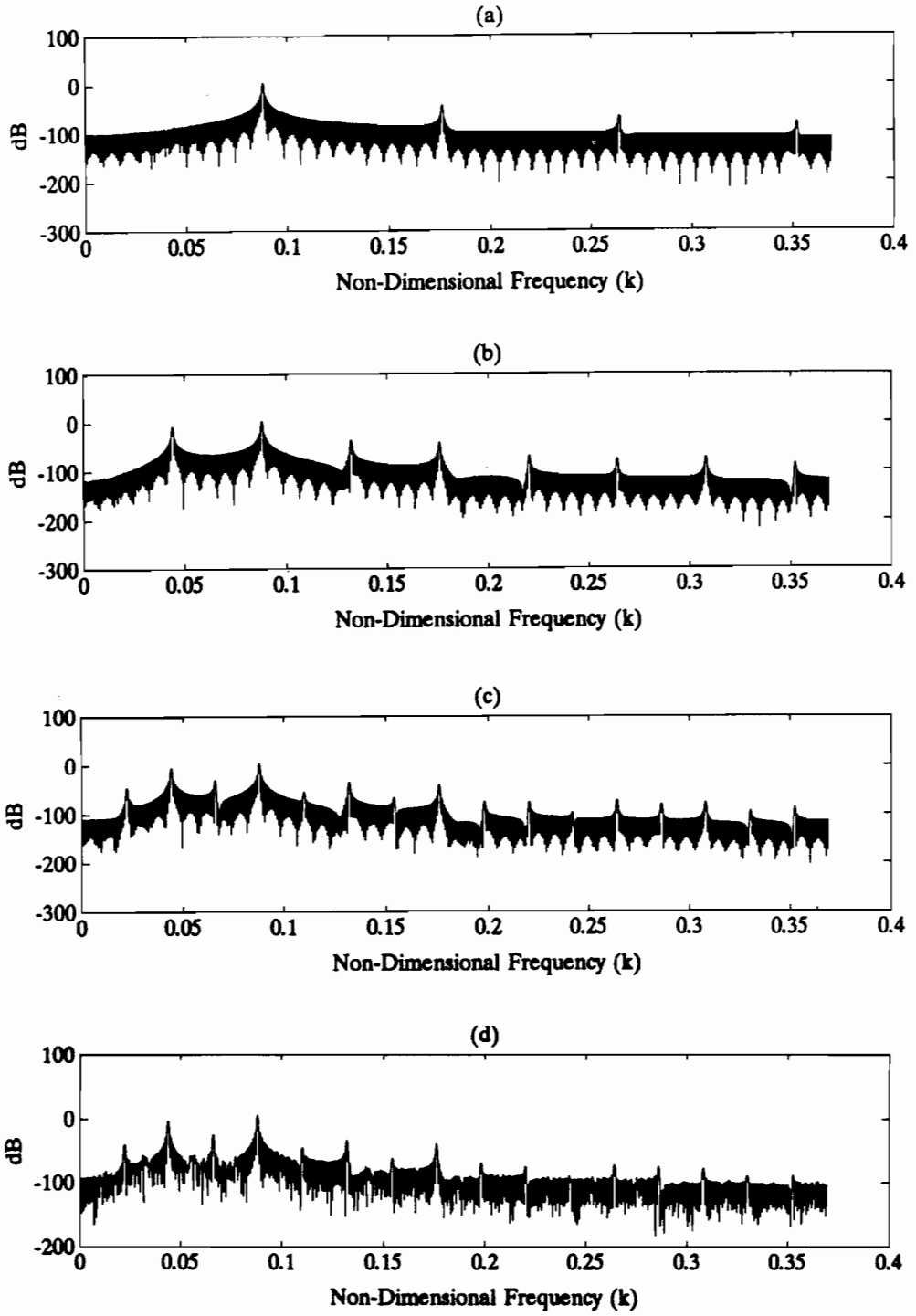

Figure 3.48: The **Fourier spectra** of the response of the airfoil for the cases: $\alpha_o = 9.76°$, $U^* = 25.20$ and $k = 0.088$ and (a) $Q_o = 0.550{*}10^{-4}$, (b) $Q_o = 0.640{*}10^{-4}$, (c) $Q_o = 0.675 * 10^{-4}$ and (d) $Q_o = 0.692 * 10^{-4}$.

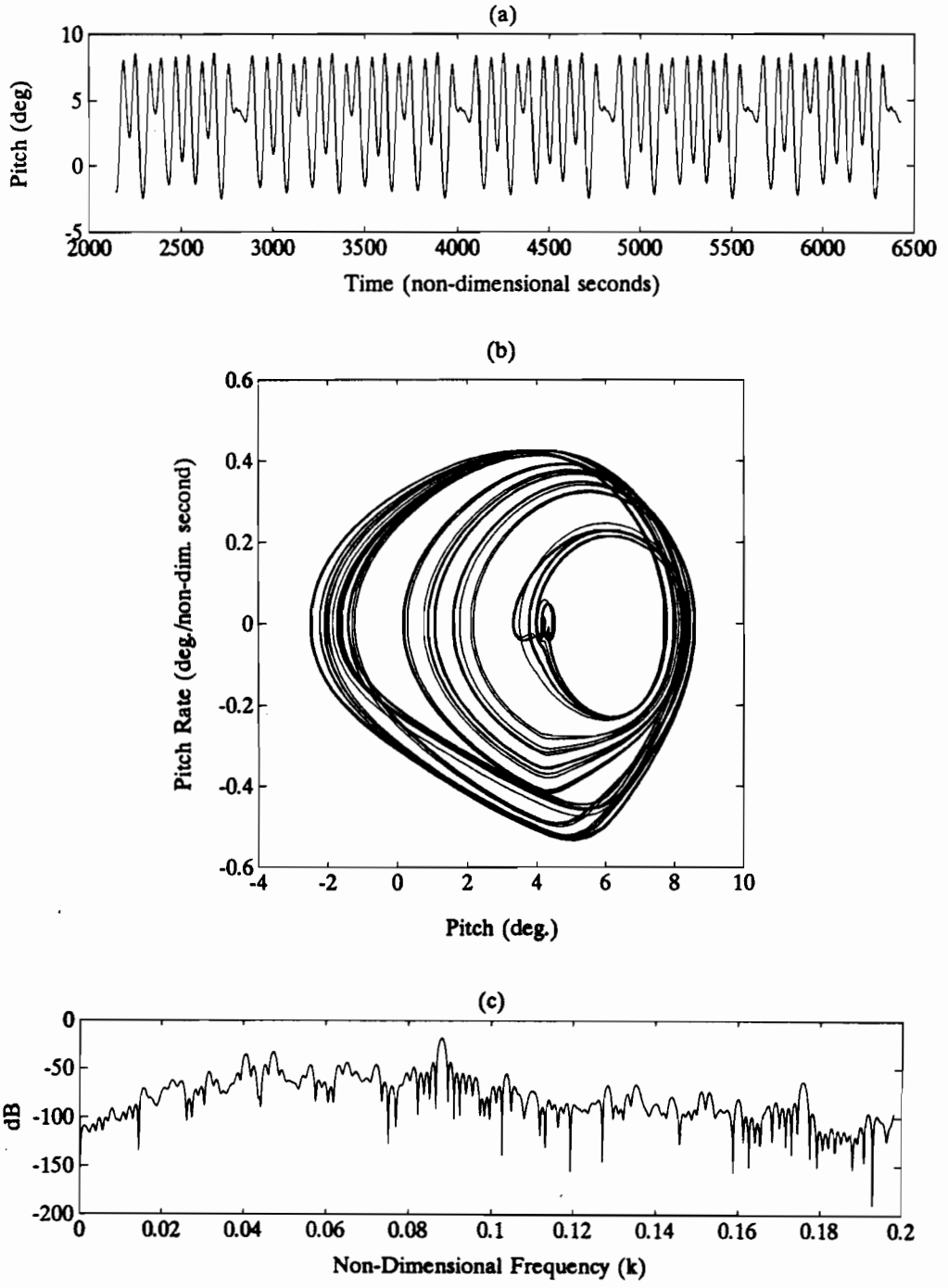

Figure 3.49: (a) The time history, (b) phase plane plot and (c) Fourier spectrum of the of the airfoil for the case: $\alpha_o = 9.76°$, $U^* = 25.20$ and $k = 0.088$ and $Q_o = 0.730 * 10^{-4}$.

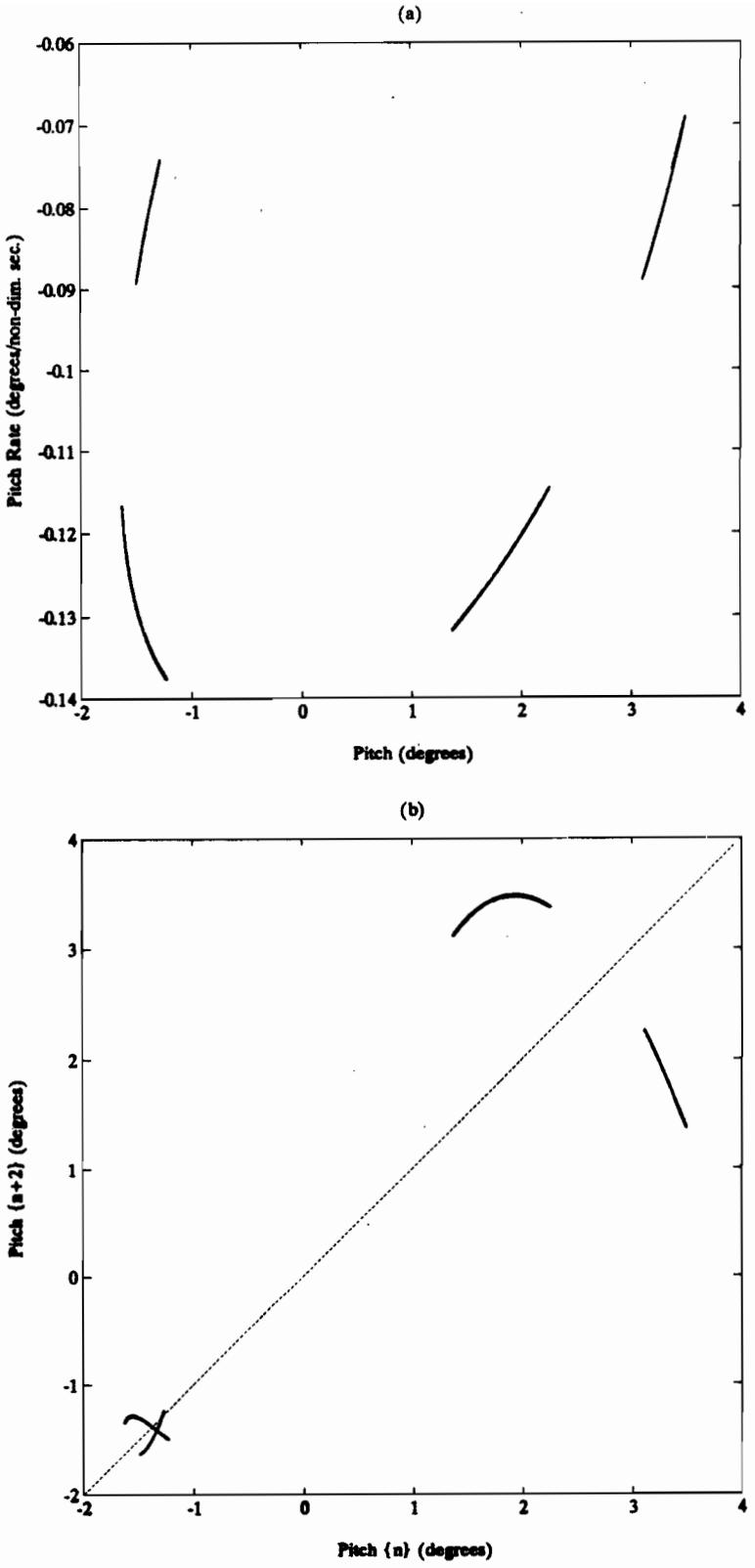

Figure 3.50: (a) The Poincaré section (b) second return map and (c) long term behaviour of the system for the case: $\mathbf{Q_o = 0.690 * 10^{-4}}$, $\alpha_o = 9.76^o$, $U^* = 25.20$ and $k = 0.088$.

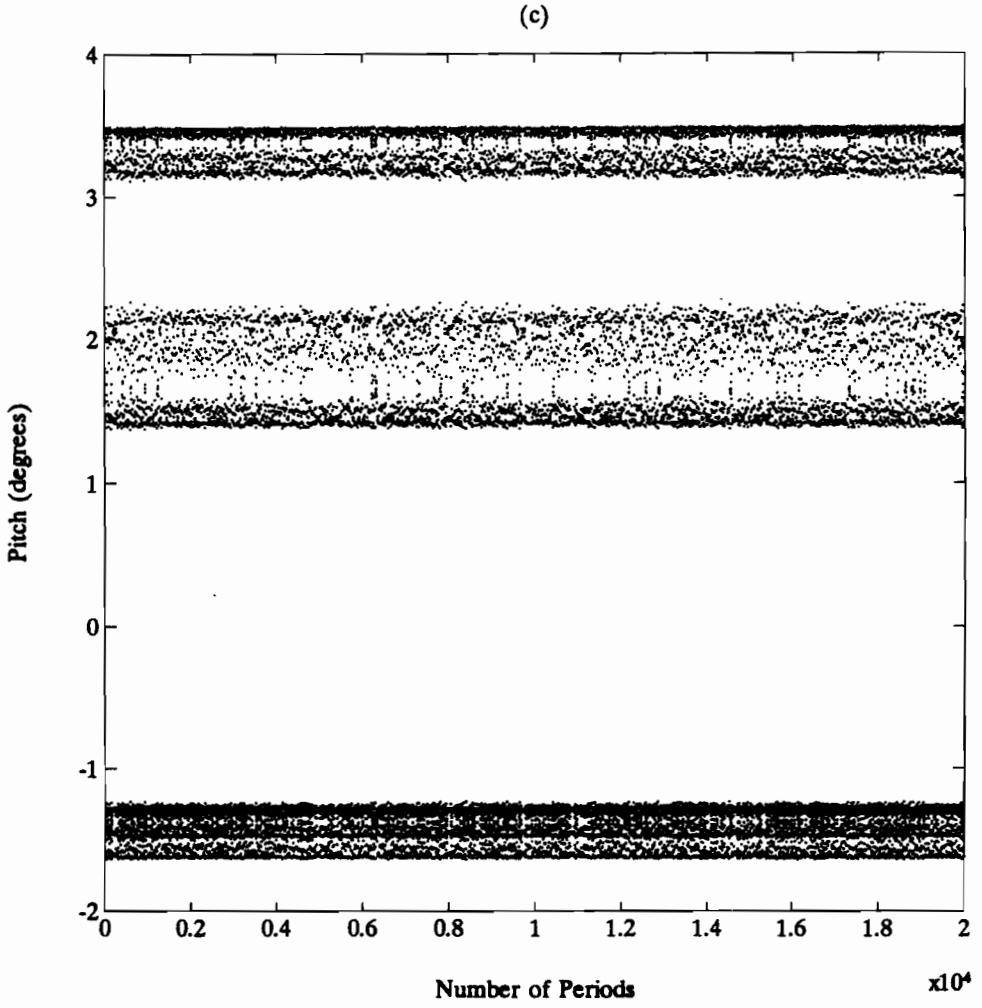
(c)
Pitch (degrees)
4
3
2
1
0
-1
-2
0
0.2
0.4
0.6
0.8
1
1.2
1.4
1.6
1.8
2
Number of Periods
x10⁴

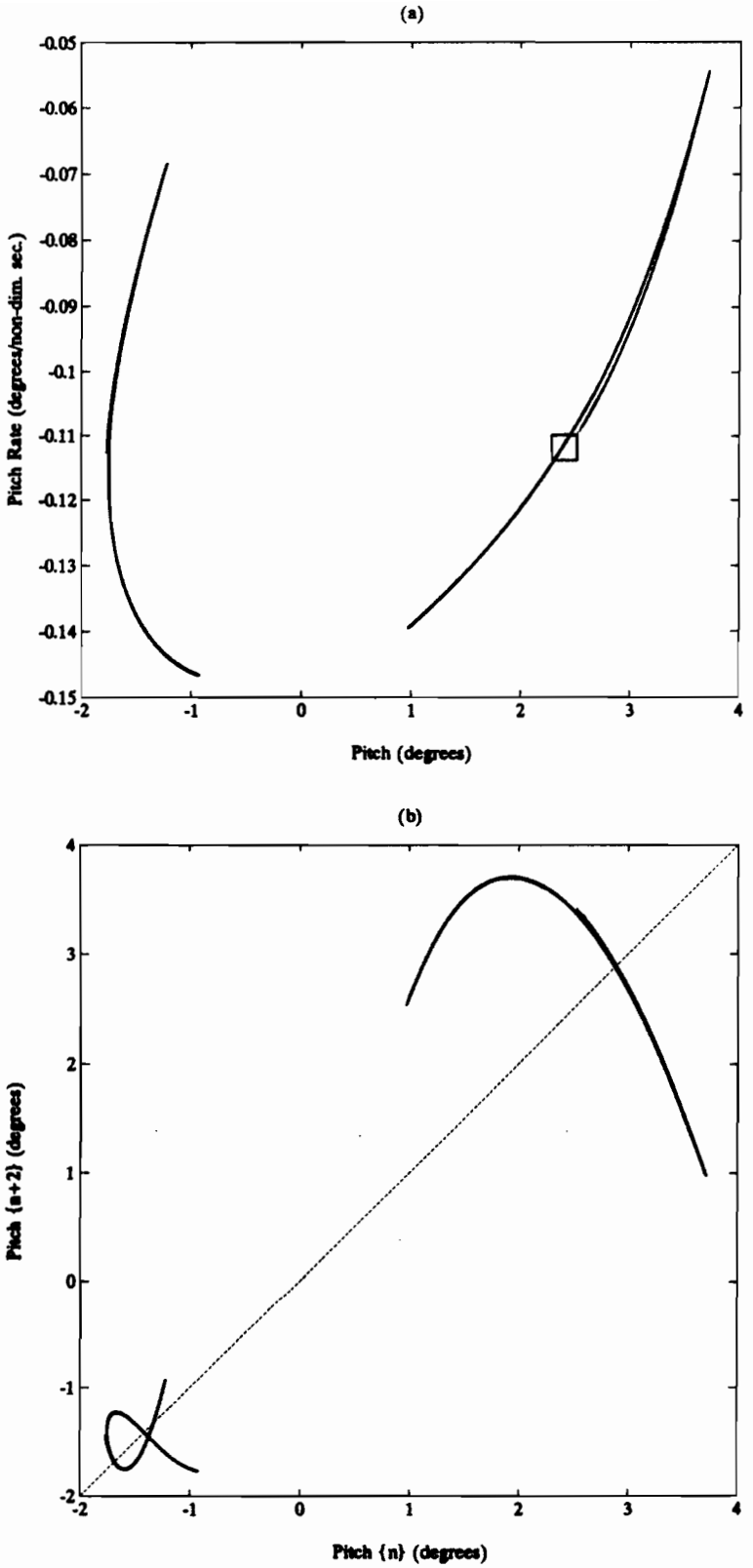

Figure 3.51: (a) The Poincaré section (b) second return map and (c) long term behaviour of the system for the case: $\mathbf{Q_o = 0.700 * 10^{-4}}$, $\alpha_o = 9.76^o$, $U^* = 25.20$ and $k = 0.088$.

(c)

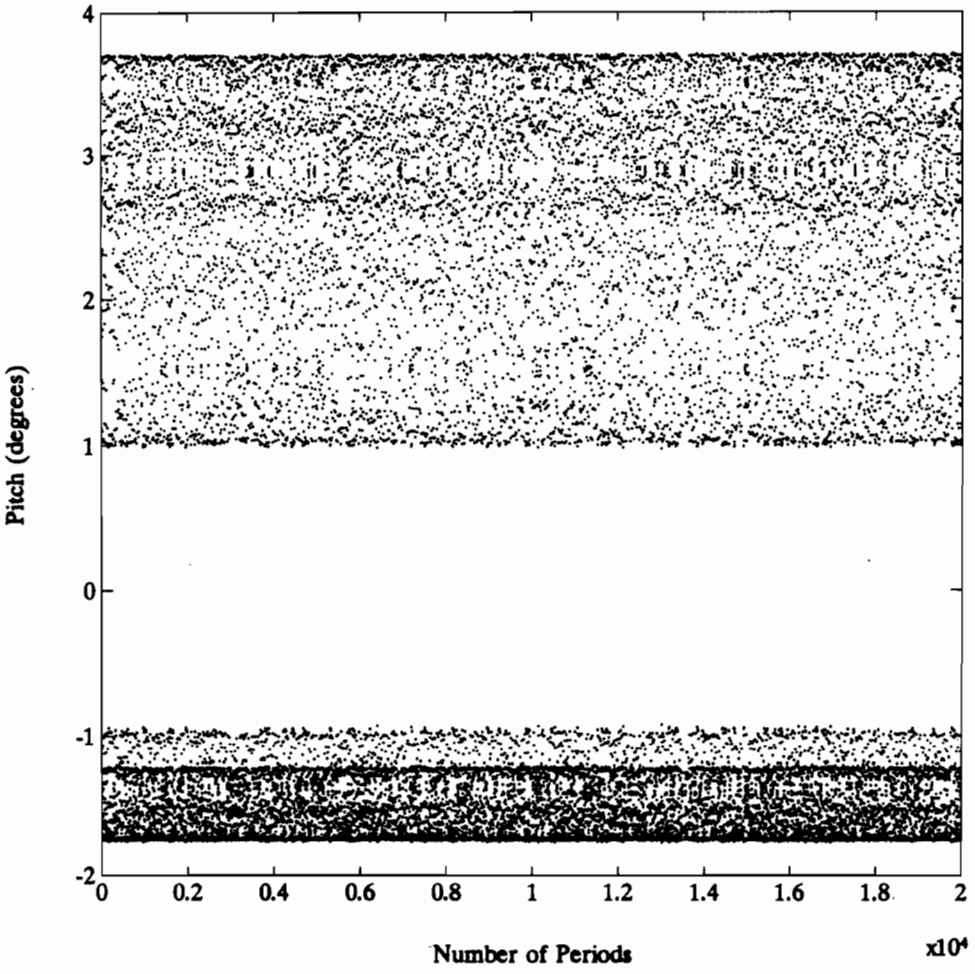
4
3
2
1
0
-1
-2
Pitch (degrees)
0
0.2
0.4
0.6
0.8
1
1.2
1.4
1.6
1.8
2
Number of Periods
x10⁴

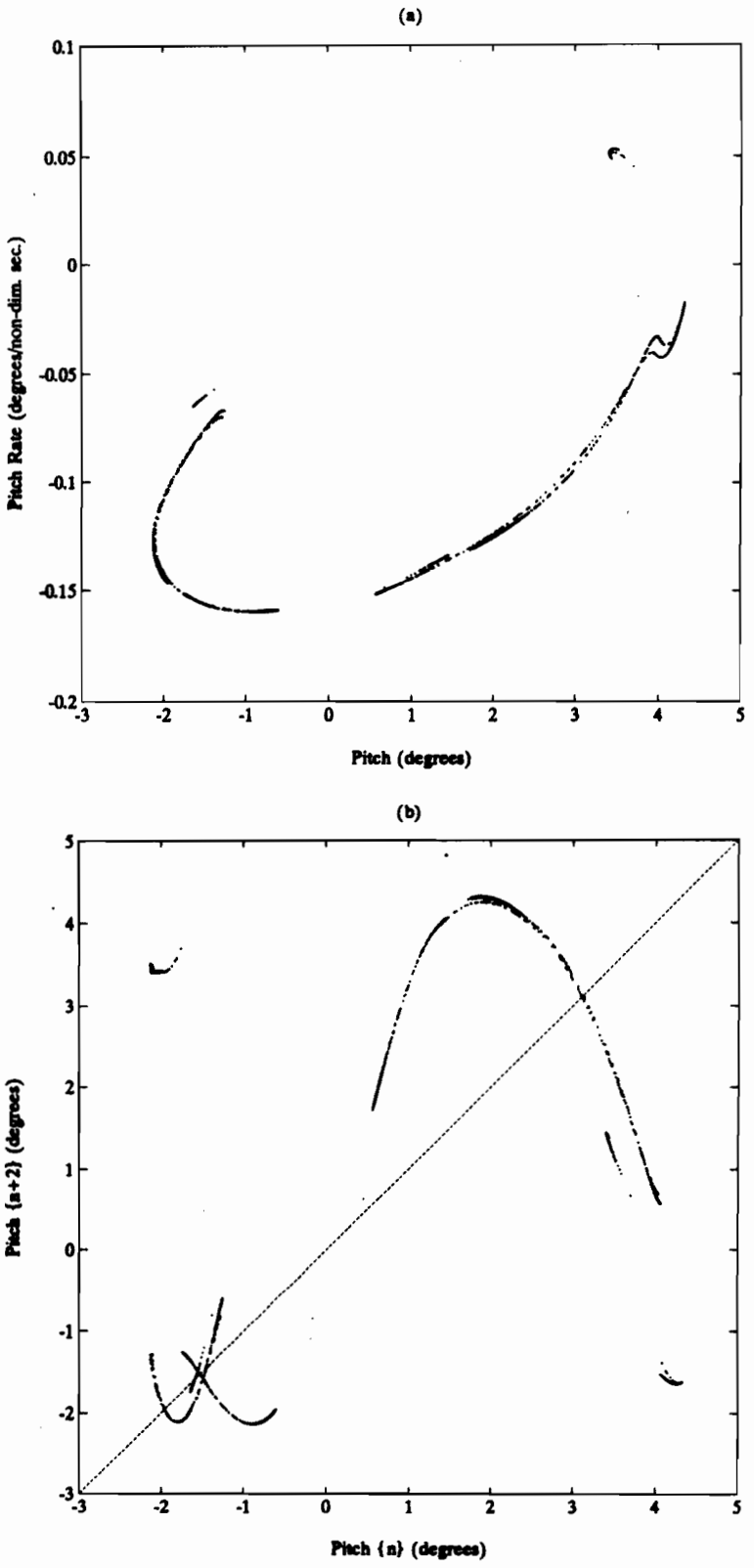

Figure 3.52: (a) The Poincaré section (b) second return map and (c) long term behaviour of the system for the case: $\mathbf{Q_o = 0.730 * 10^{-4}}$, $\alpha_o = 9.76^o$, $U^* = 25.20$ and $k = 0.088$.

(c)

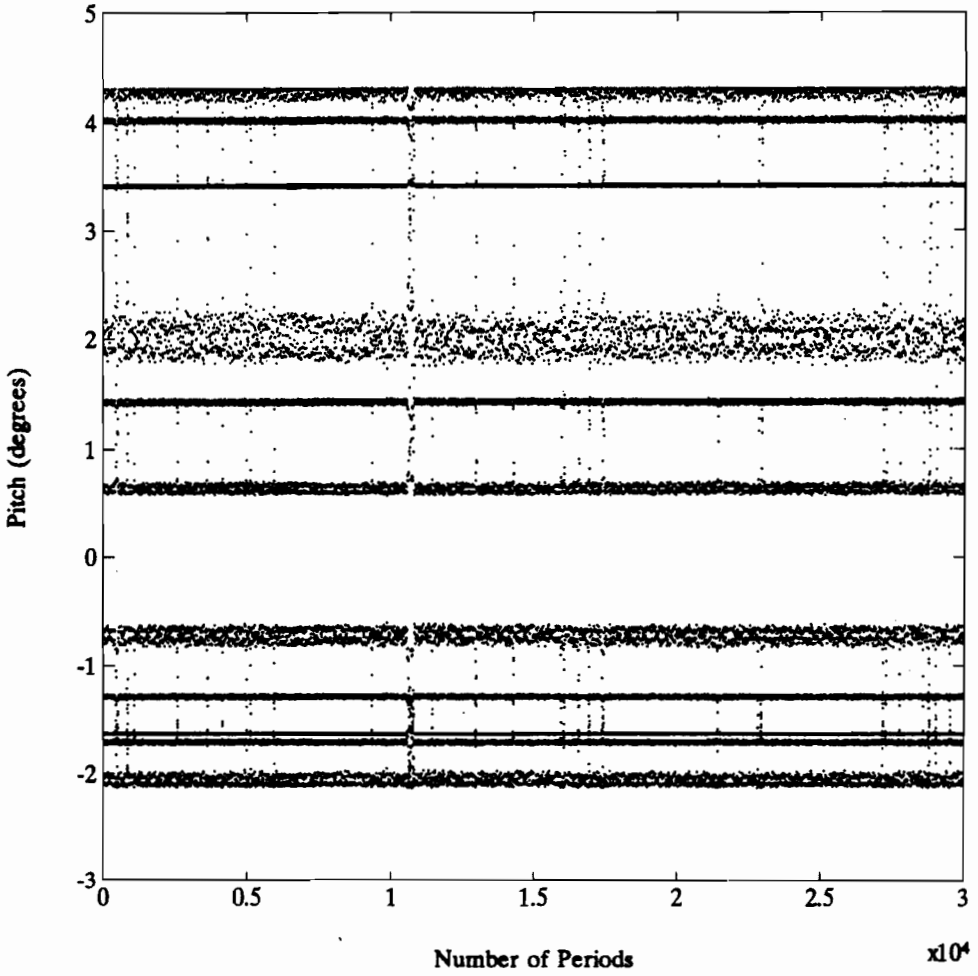
Pitch (degrees)
5
4
3
2
1
0
-1
-2
-3
0
0.5
1
1.5
2
2.5
3
Number of Periods
x10⁴

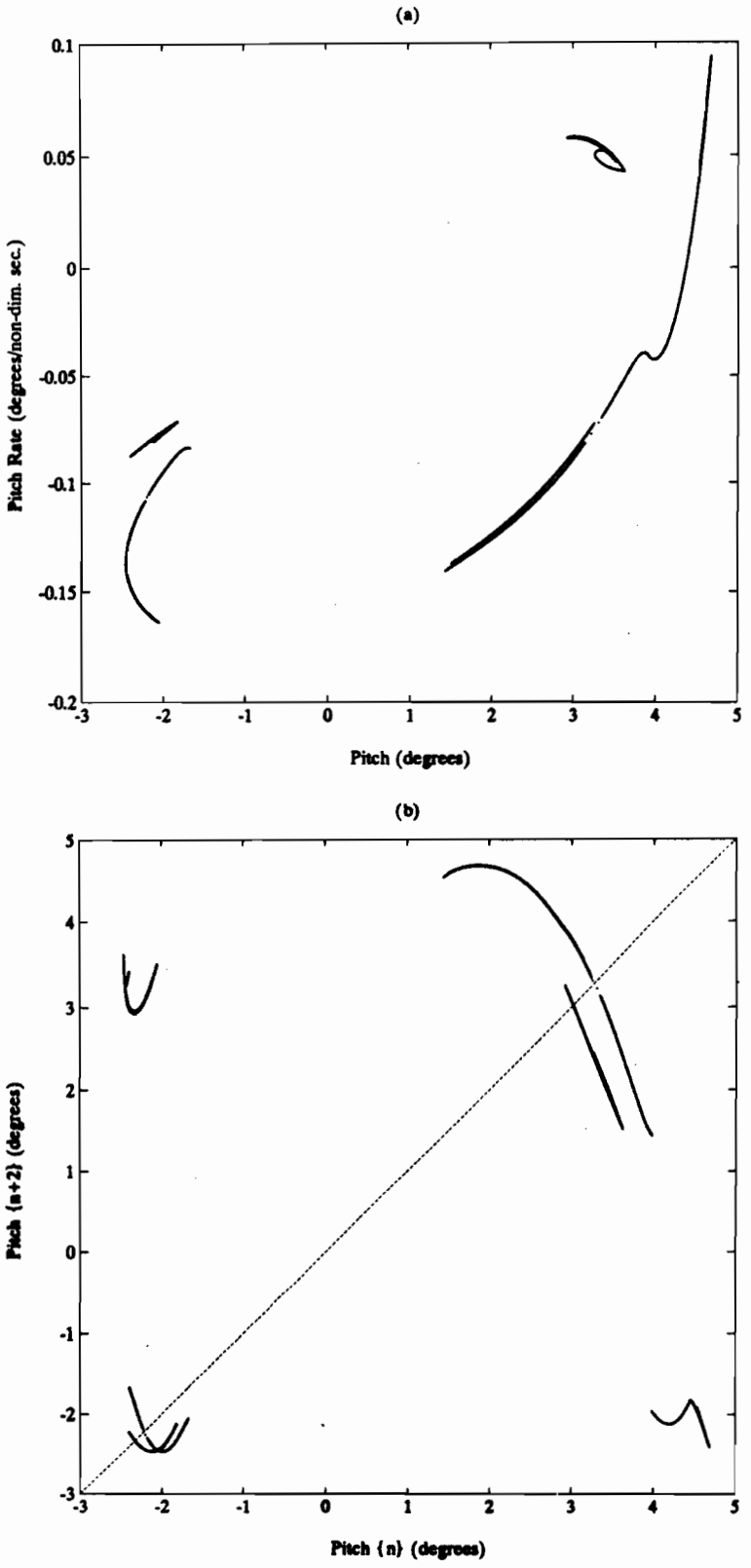

Figure 3.53: (a) The Poincaré section (b) second return map and (c) long term behaviour of the system for the case: $\mathbf{Q_o = 0.760 * 10^{-4}}$, $\alpha_o = 9.76°$, $U^* = 25.20$ and $k = 0.088$.

(c)

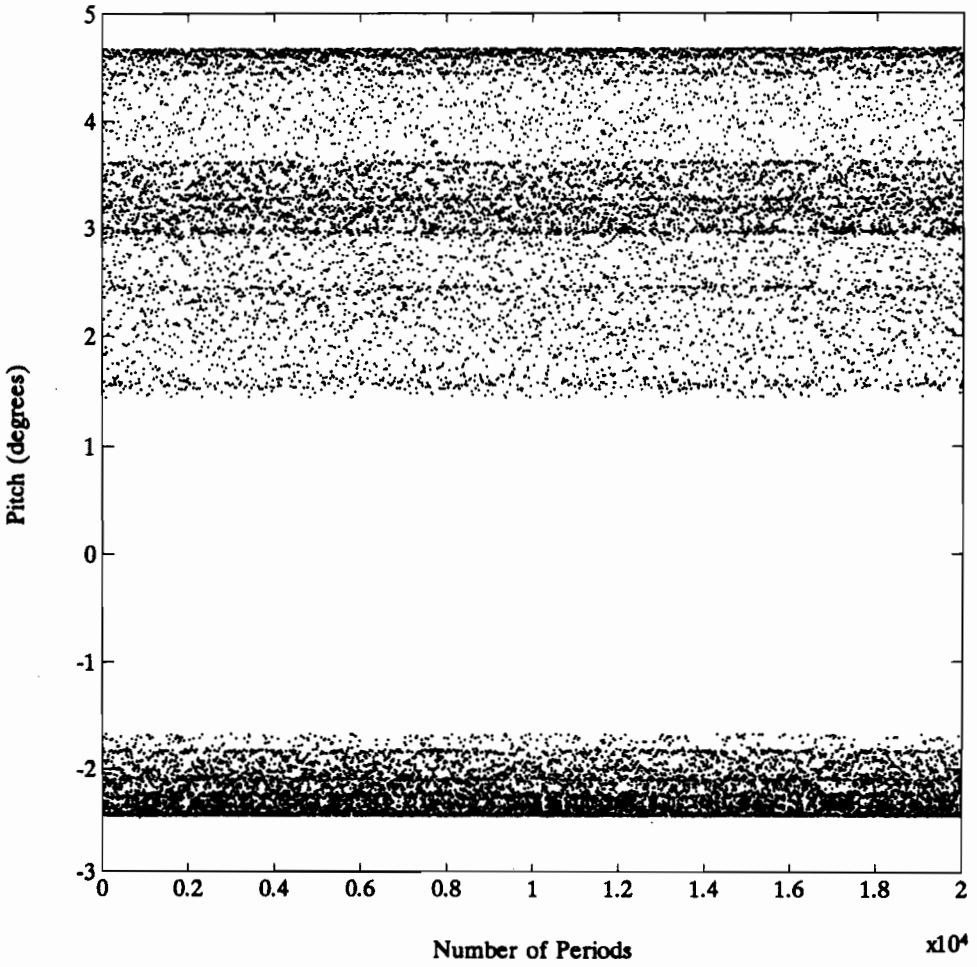
5
4
3
2
1
0
-1
-2
-3
Pitch (degrees)
0
0.2
0.4
0.6
0.8
1
1.2
1.4
1.6
1.8
2
Number of Periods
x10⁴

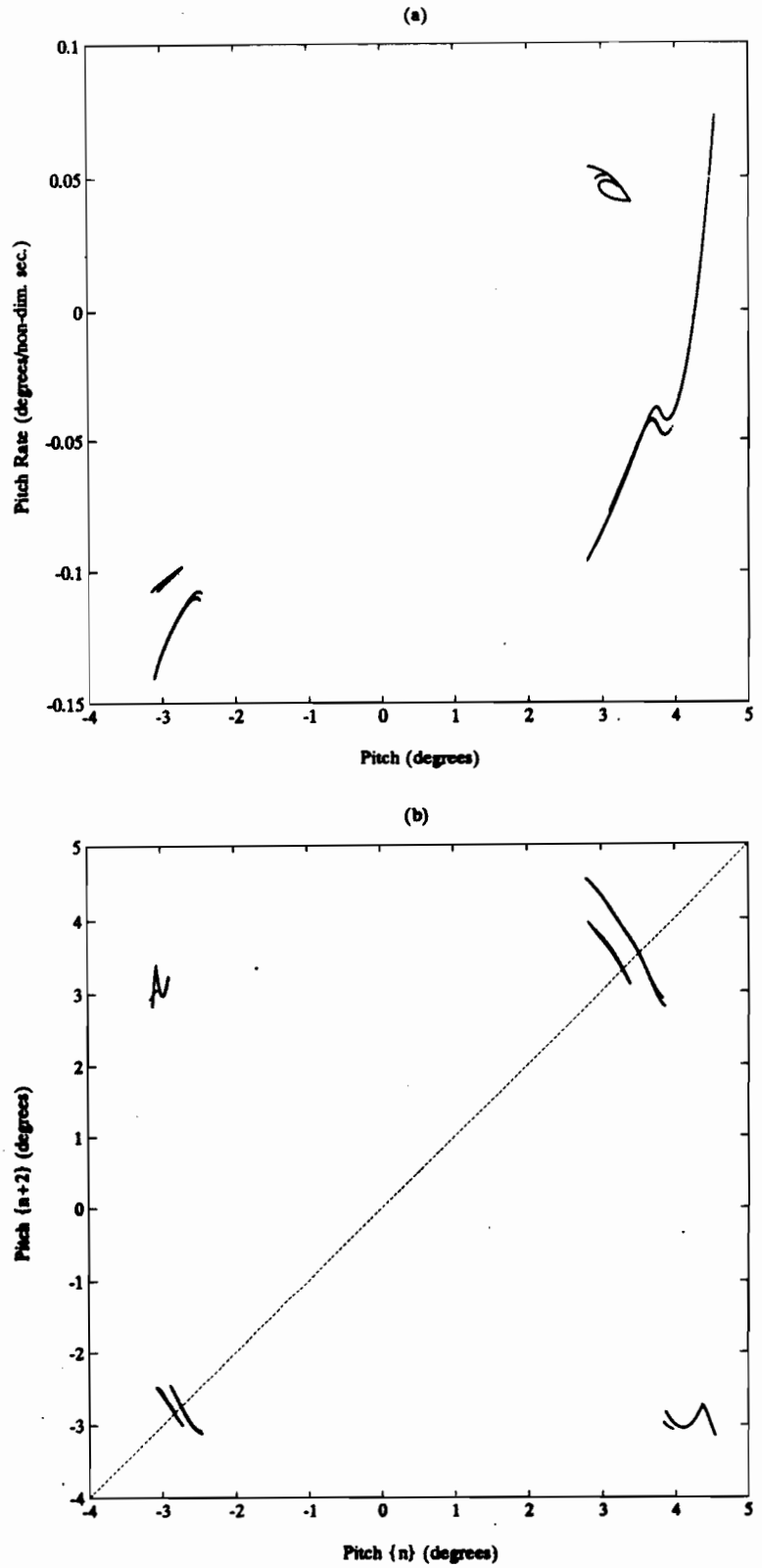

Figure 3.54: (a) The Poincaré section (b) second return map and (c) long term behaviour of the system for the case: $\mathbf{Q_o = 0.820 * 10^{-4}}$, $\alpha_o = 9.76°$, $U^* = 25.20$ and $k = 0.088$.

(c)

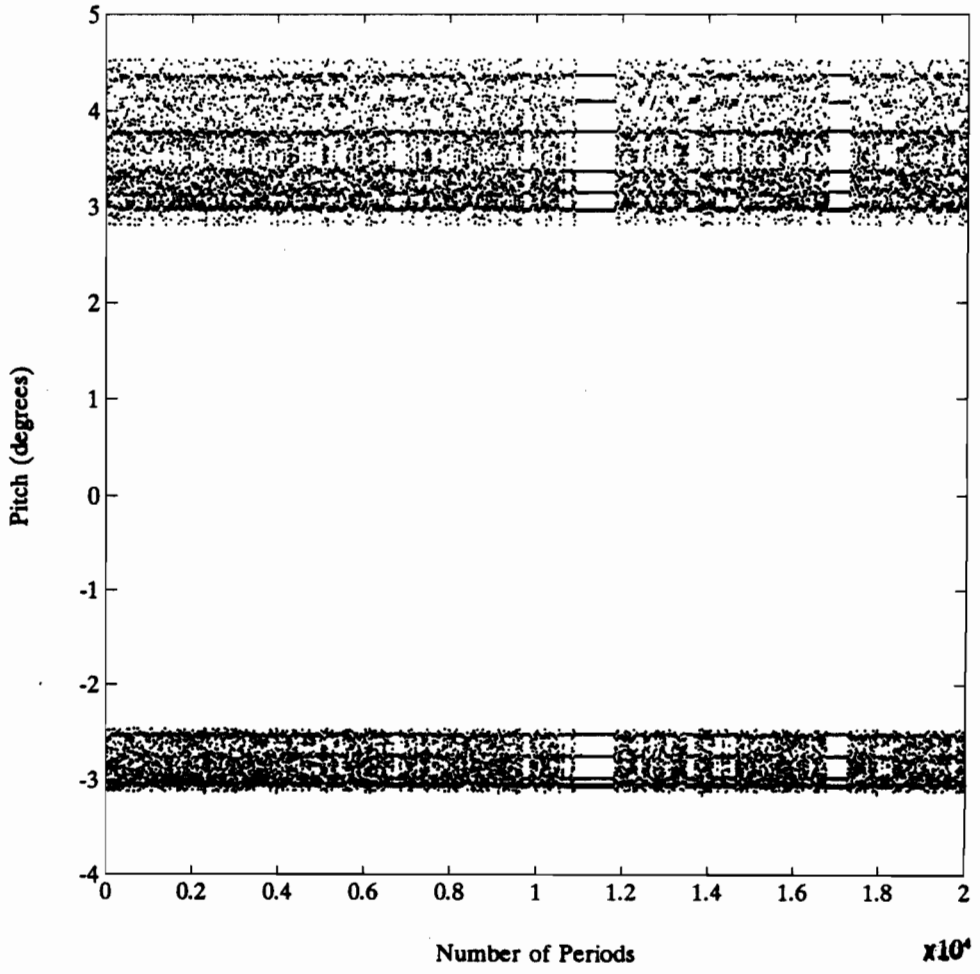
Pitch (degrees)
5
4
3
2
1
0
-1
-2
-3
-4
0
0.2
0.4
0.6
0.8
1
1.2
1.4
1.6
1.8
2
Number of Periods
x10⁴

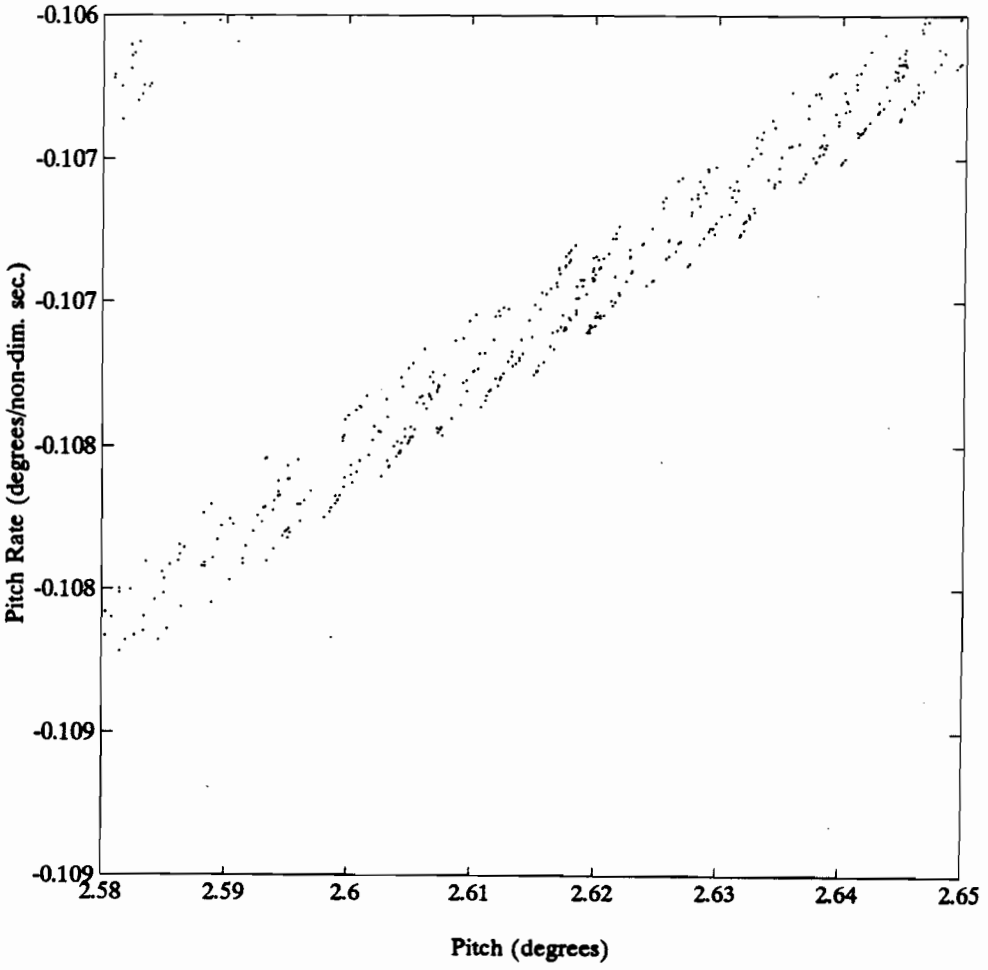

Figure 3.55: The micro-structure of the Poincaré attractor for the case: $Q_o = 0.700 * 10^{-4}$, $\alpha_o = 9.76°$, $U^* = 25.20$ and $k = 0.088$ (see Figure 3.51(a)).

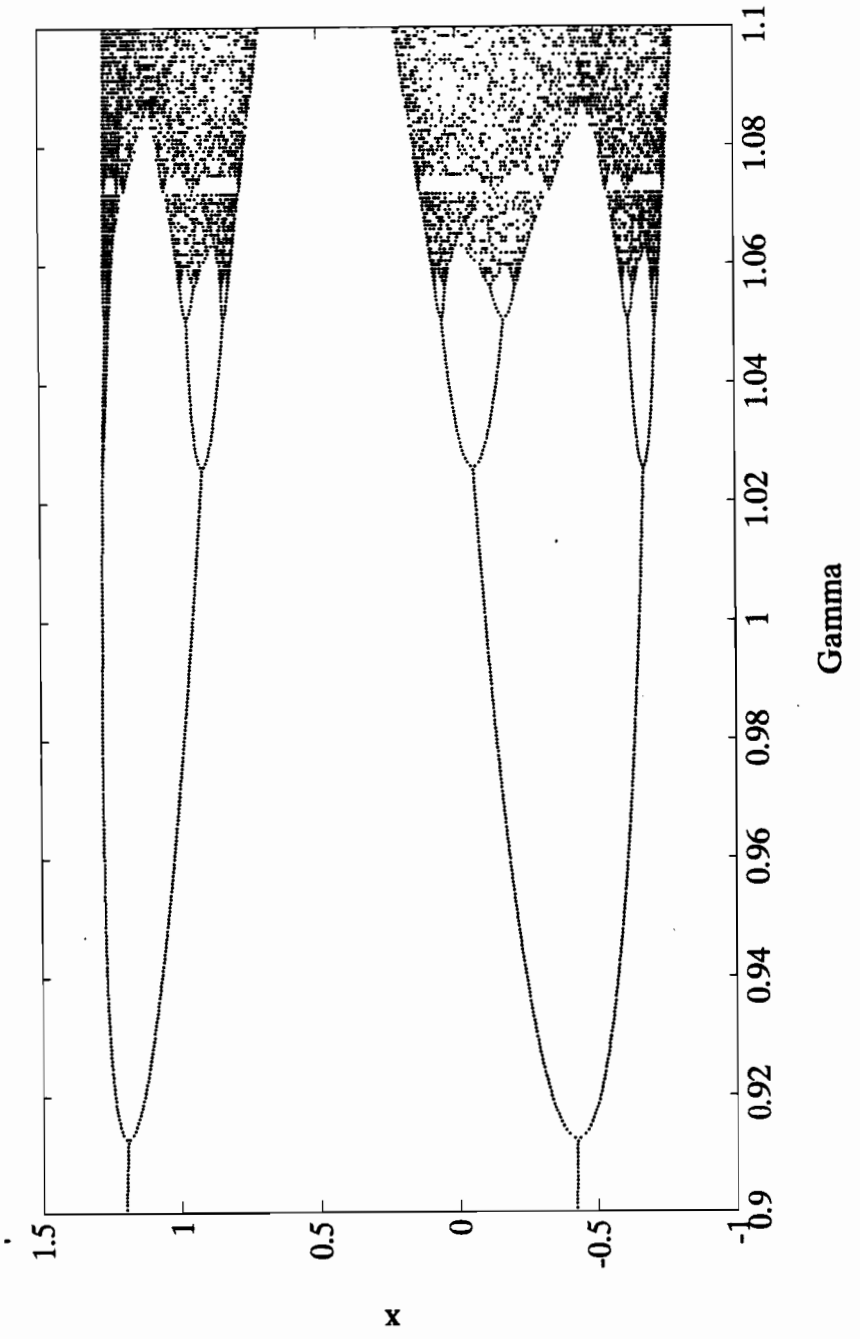

Figure 3.56: Bifurcation diagram for the 'x' variable of the Henon map [equation (3.3)] as a function the parameter ν for a fixed value of the parameter $J = -0.3$.

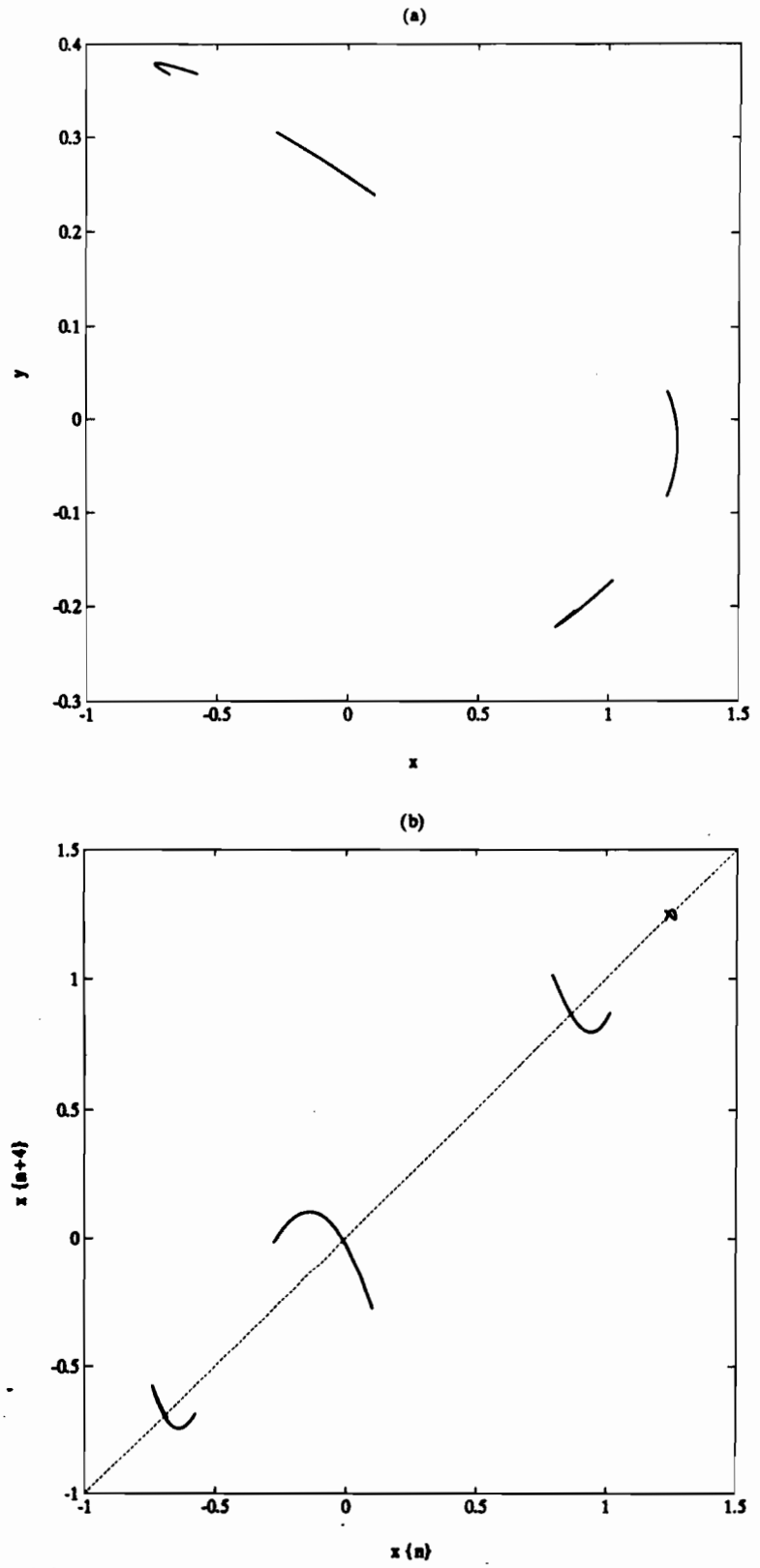

Figure 3.57: (a) y_n versus x_n, (b) the fourth return map and (c) the long term behaviour for the Henon map with parameters $\nu = 1.065$ and $J = -0.3$.

(c)

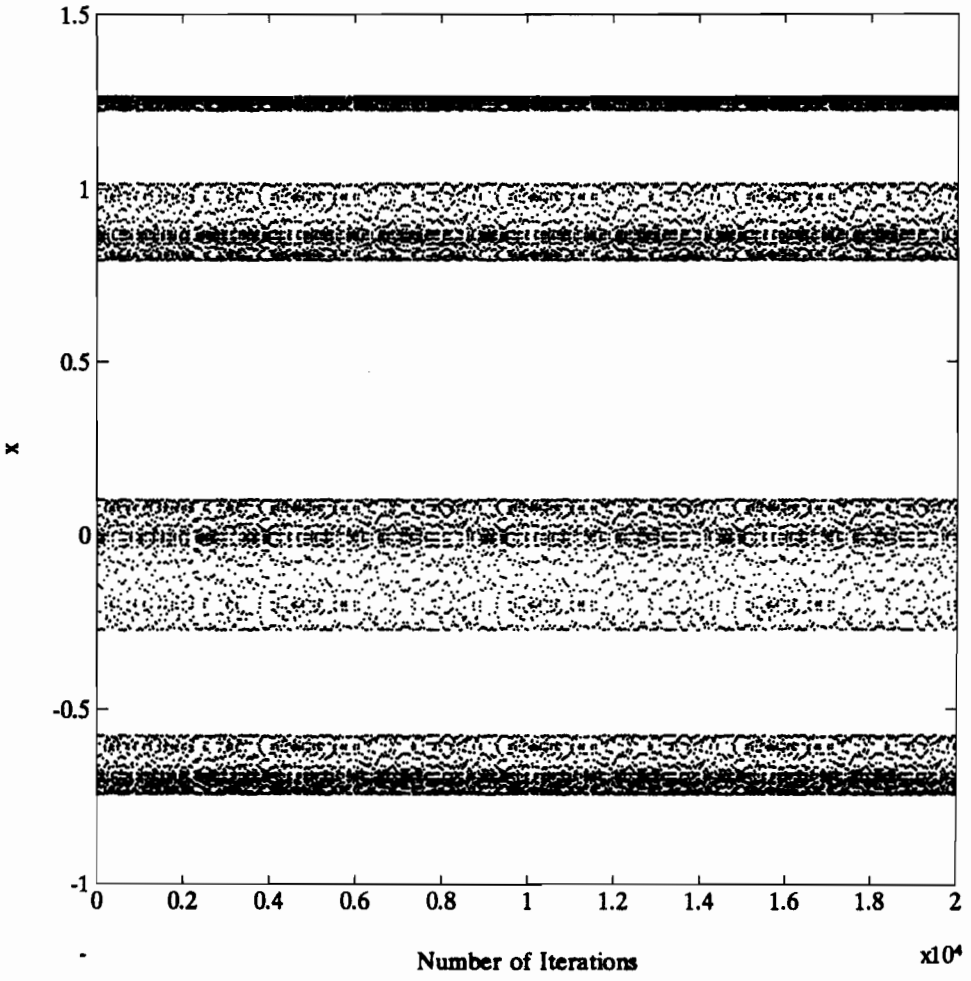
1.5
1
0.5
0
-0.5
-1
x
0
0.2
0.4
0.6
0.8
1
1.2
1.4
1.6
1.8
2
Number of Iterations
x10⁴

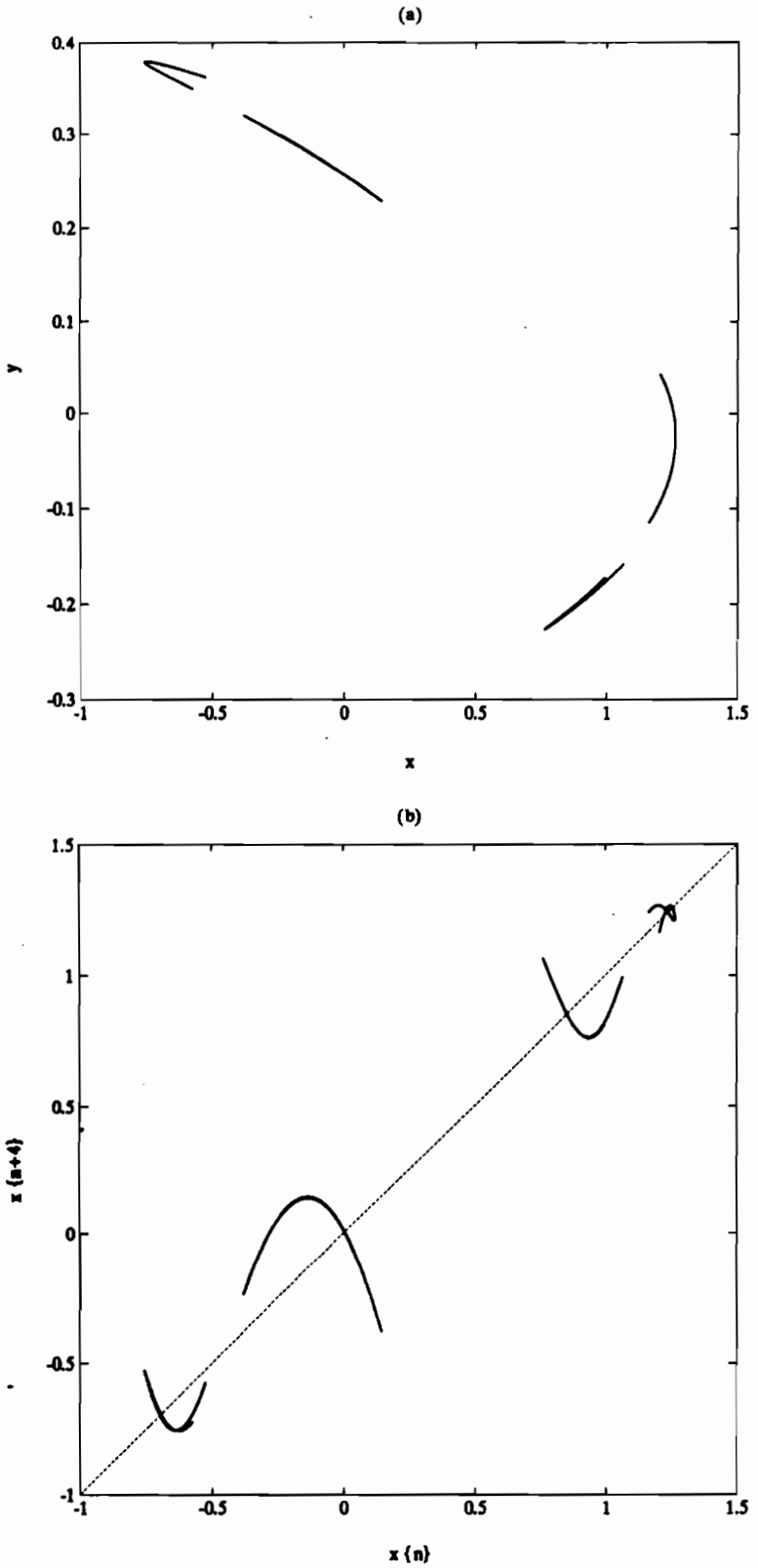

Figure 3.58: (a) y_n versus x_n, (b) the fourth return map and (c) the long term behaviour for the Henon map with parameters $\nu = 1.077$ and $J = -0.3$.

(c)

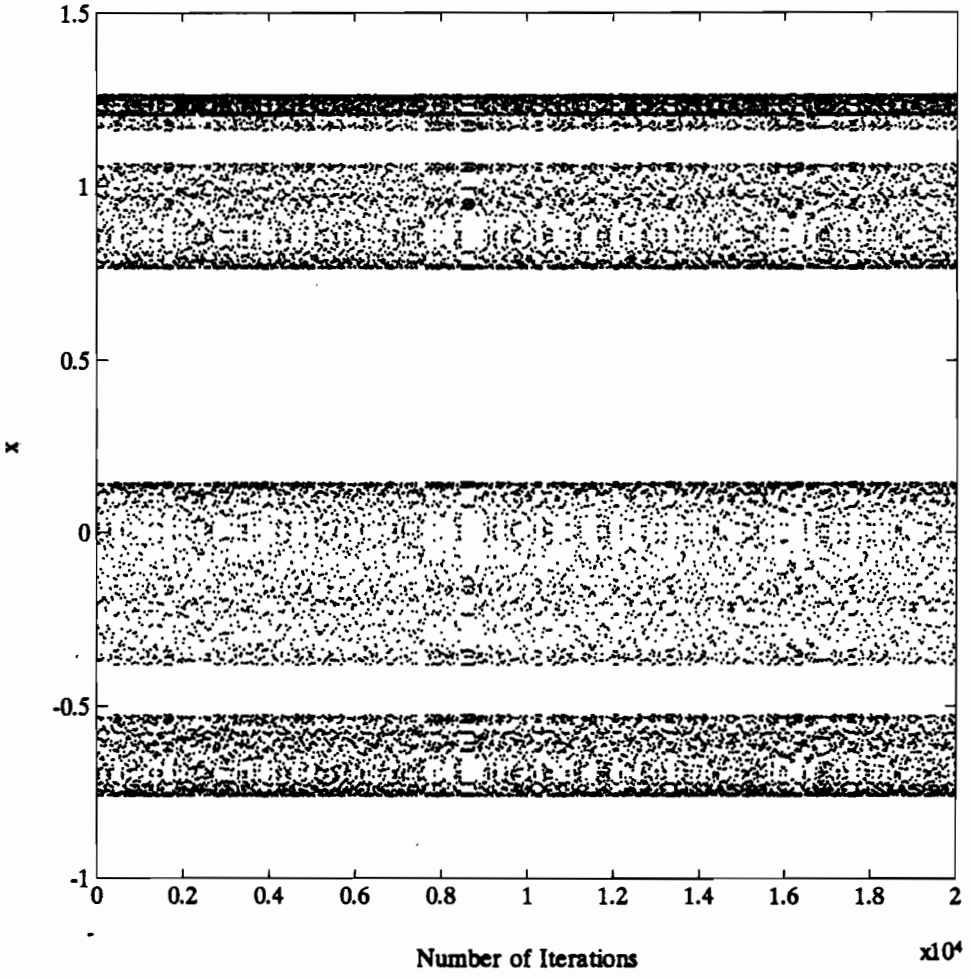
1.5
1
0.5
0
-0.5
-1
x
0
0.2
0.4
0.6
0.8
1
1.2
1.4
1.6
1.8
2
Number of Iterations
x10⁴

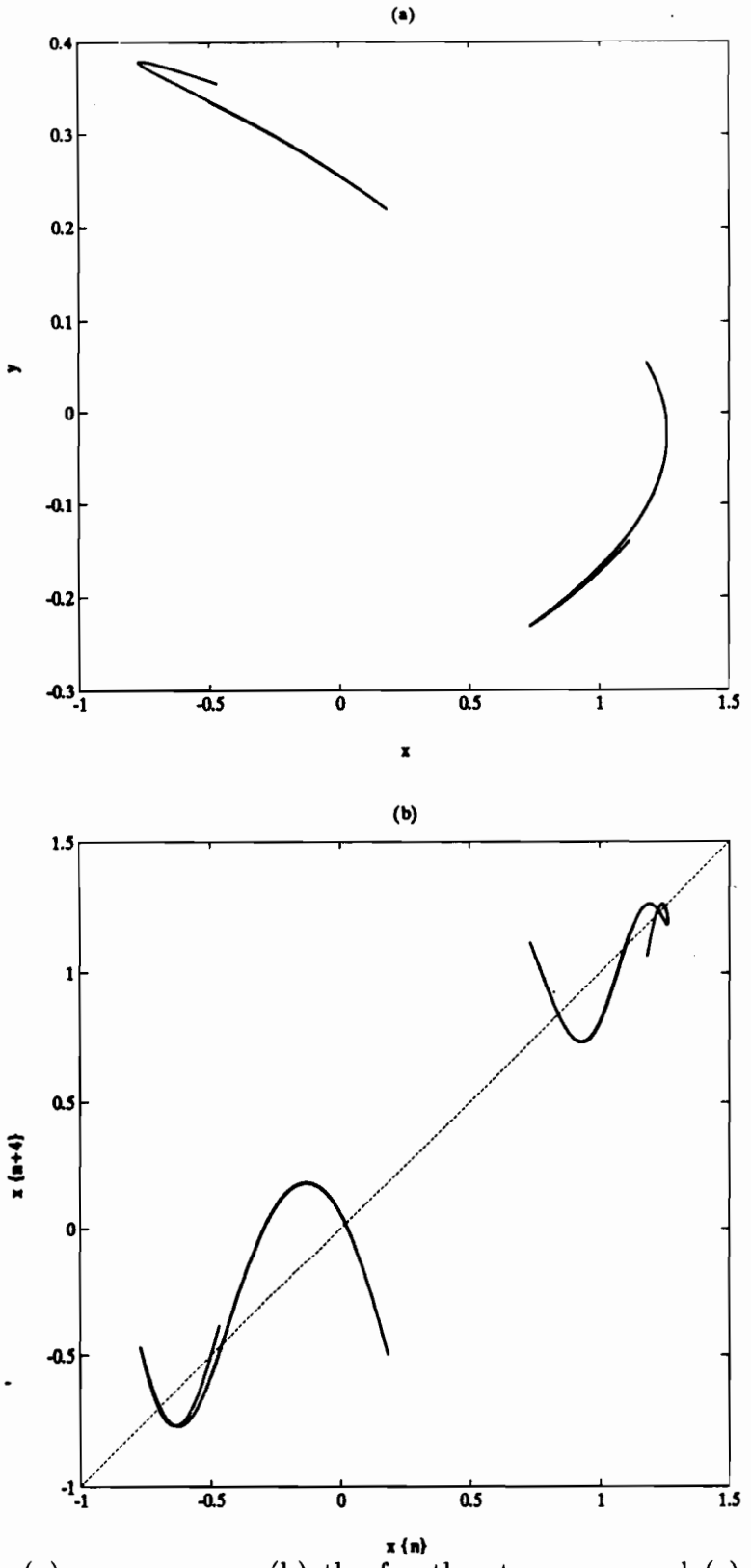

Figure 3.59: (a) y_n versus x_n, (b) the fourth return map and (c) the long term behaviour for the Henon map with parameters $\nu = 1.089$ and $J = -0.3$.

(c)

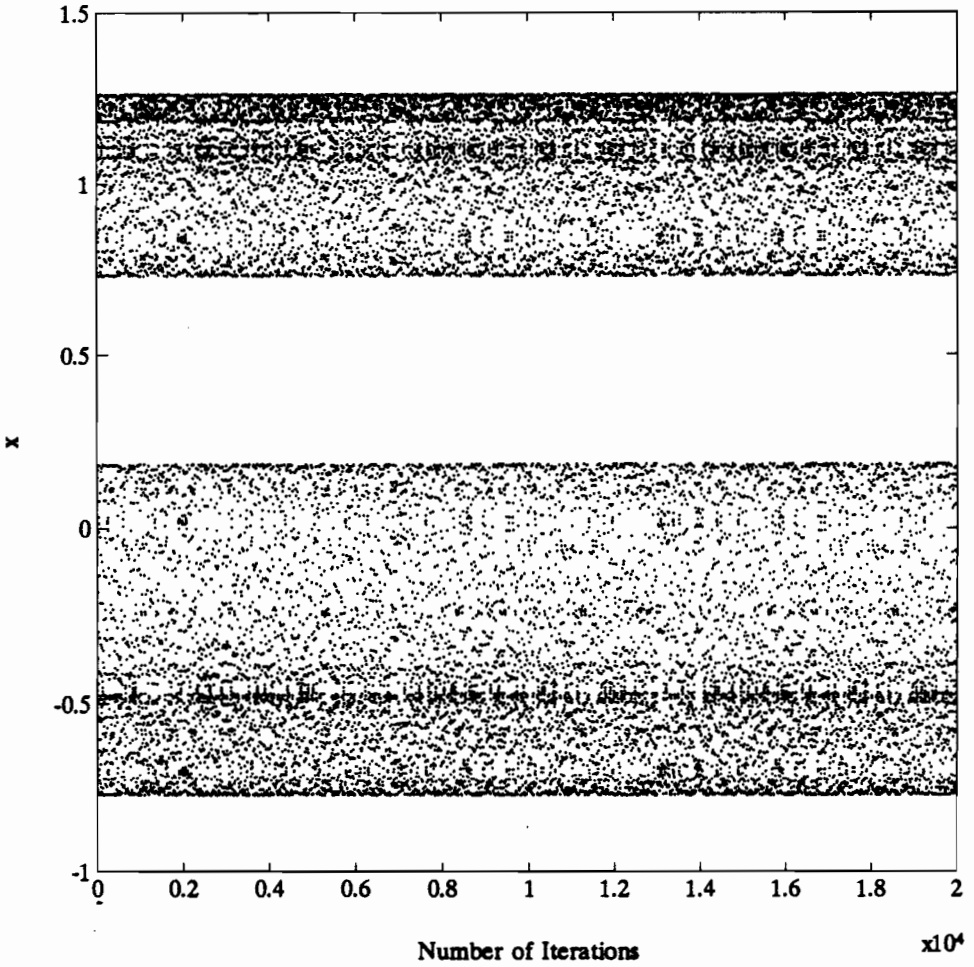
1.5
1
0.5
0
-0.5
-1
x
0
0.2
0.4
0.6
0.8
1
1.2
1.4
1.6
1.8
2
Number of Iterations
x10⁴

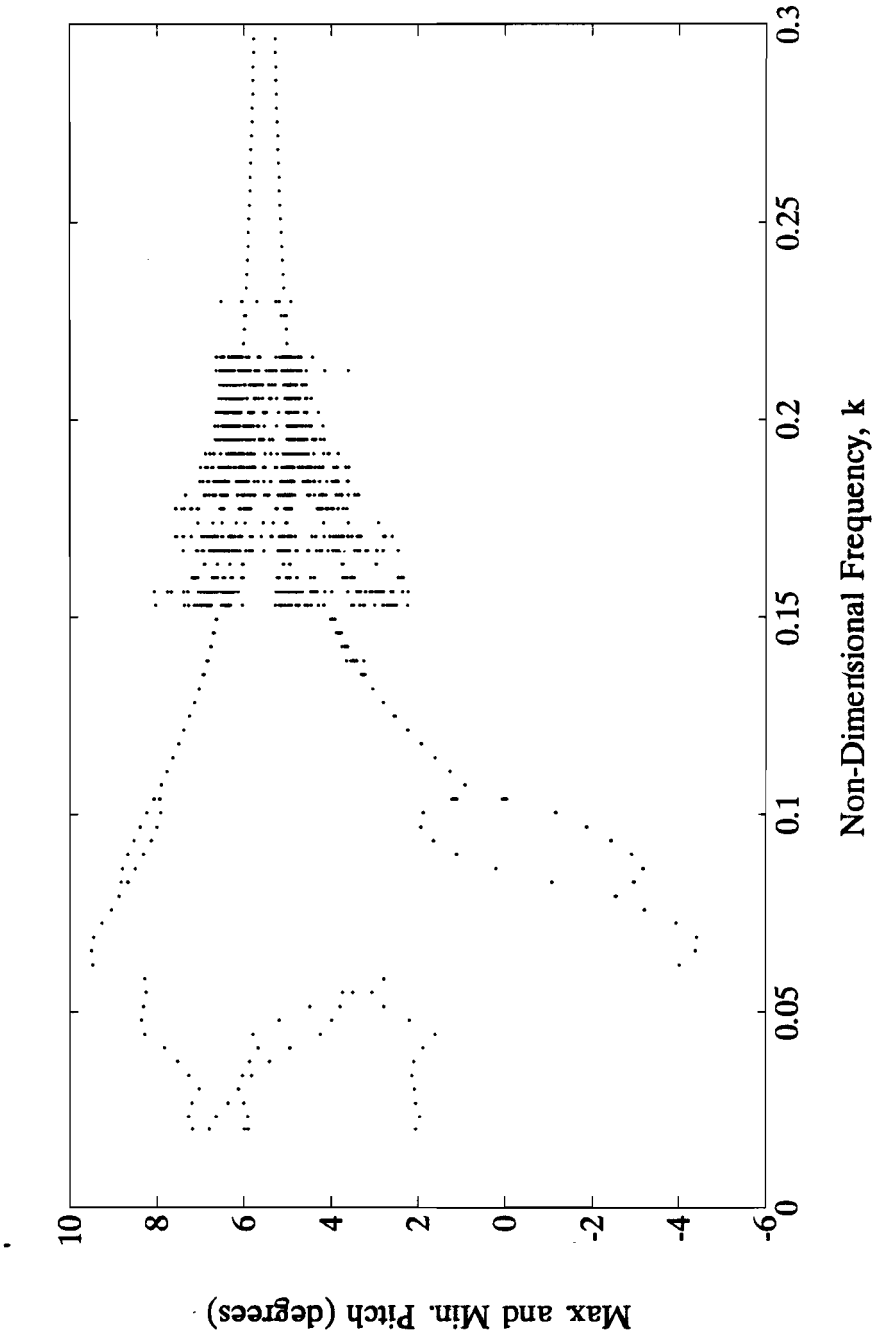

Figure 3.60: Bifurcation diagram for the case: $\alpha_o = 7.62°$, $U^* = 20.265$, $Q_o = 8.40 * 10^{-5}$ and $0.020 < k < 0.300$.

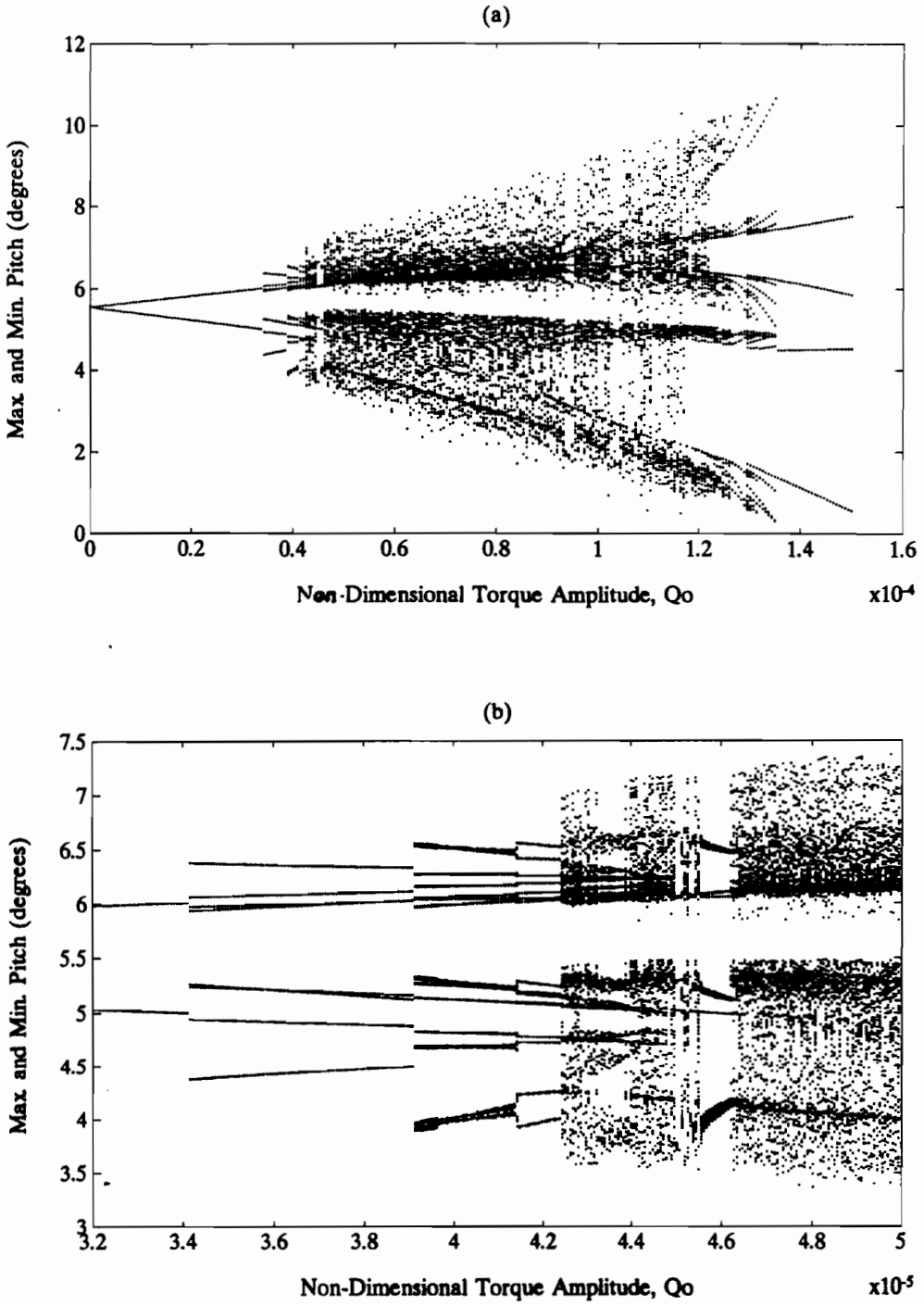

Figure 3.61: Bifurcation diagrams for the cases: $\alpha_o = 7.62^o$, $U^* = 20.265$, $k = 0.156$ and (a) $0.00 < Q_o < 1.5 * 10^{-4}$, (b) $3.2 * 10^{-5} < Q_o < 5.0 * 10^{-5}$.

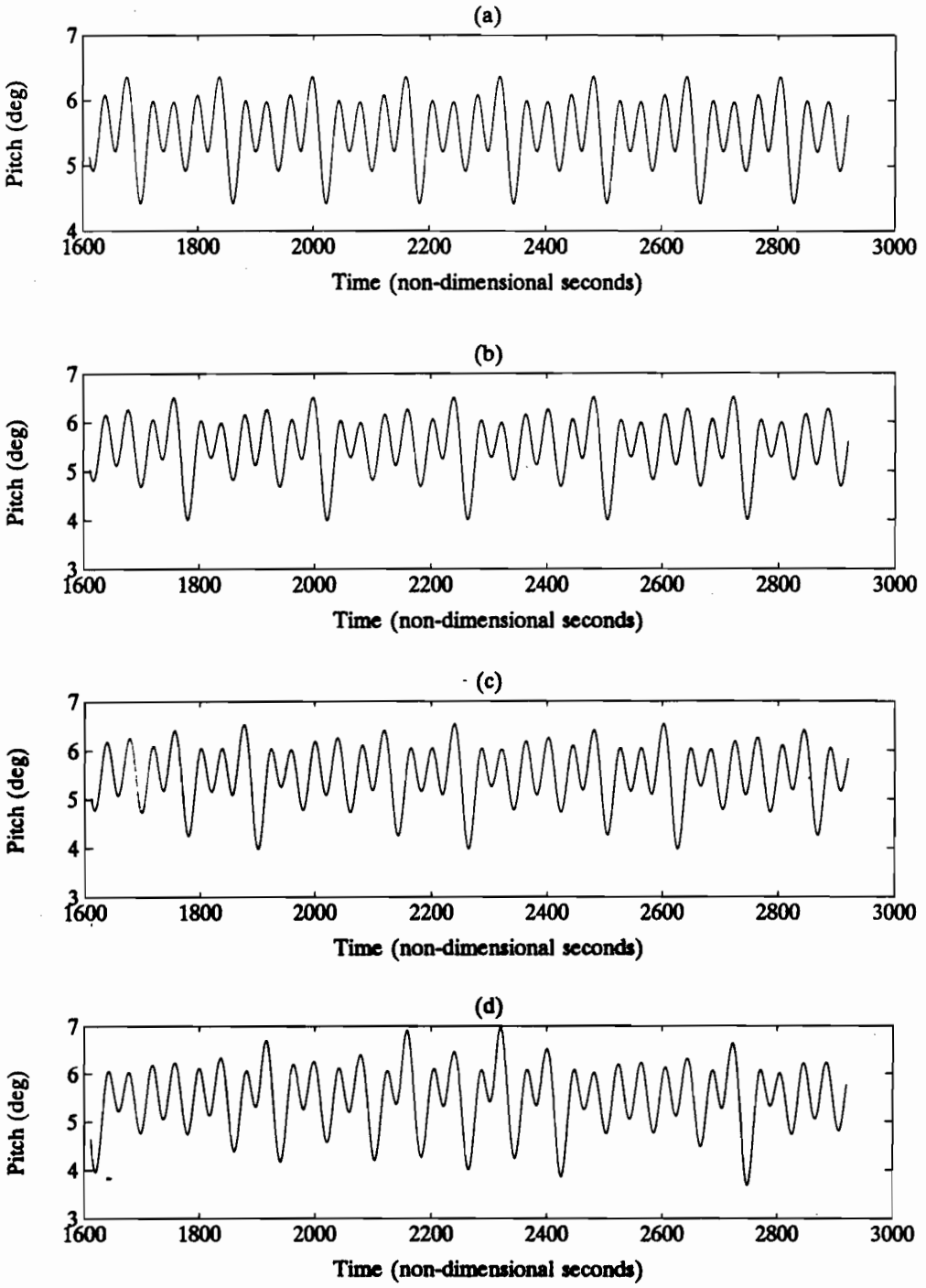

Figure 3.62: The **time histories** of the response of the airfoil for the cases: $\alpha_o = 7.62^o$, $U^* = 20.265$ and $k = 0.156$ and (a) $Q_o = 3.60 * 10^{-5}$, (b) $Q_o = 4.00 * 10^{-5}$, (c) $Q_o = 4.20 * 10^{-5}$ and (d) $Q_o = 4.30 * 10^{-5}$.

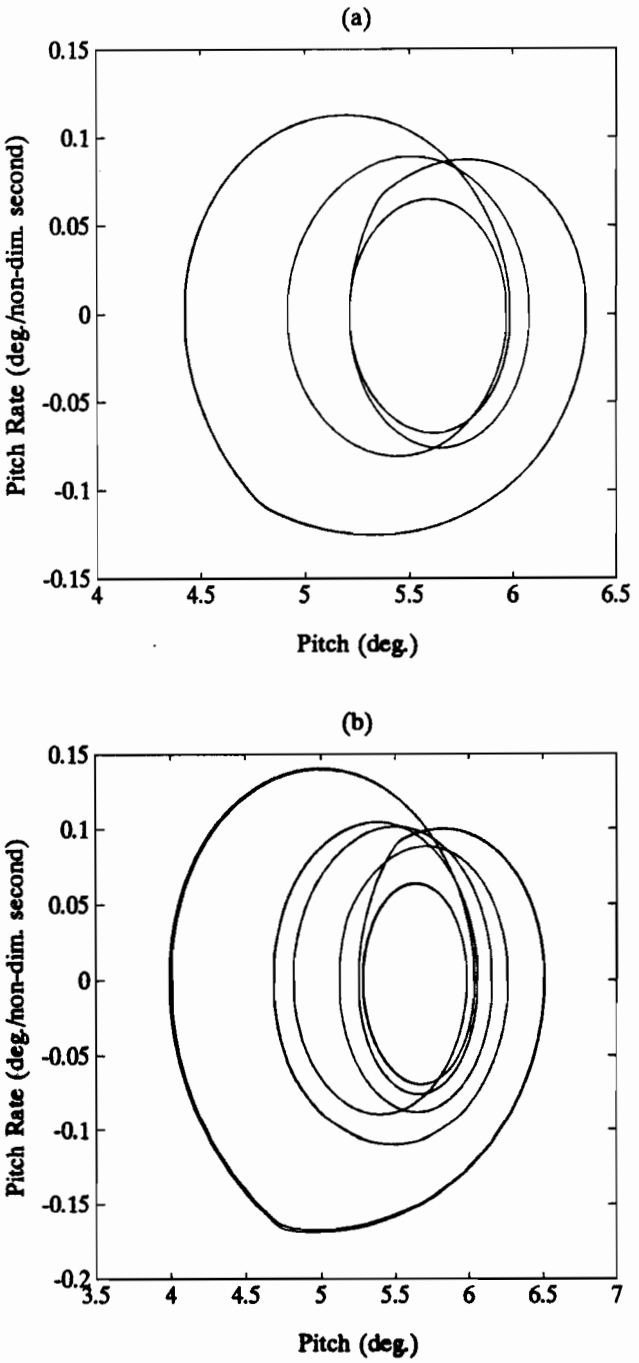

Figure 3.63: The **phase plane plots** of the response of the airfoil for the cases: $\alpha_o = 7.62^o$, $U^* = 20.265$ and $k = 0.156$ and (a) $Q_o = 3.60 * 10^{-5}$, (b) $Q_o = 4.00 * 10^{-5}$, (c) $Q_o = 4.20 * 10^{-5}$ and (d) $Q_o = 4.30 * 10^{-5}$.

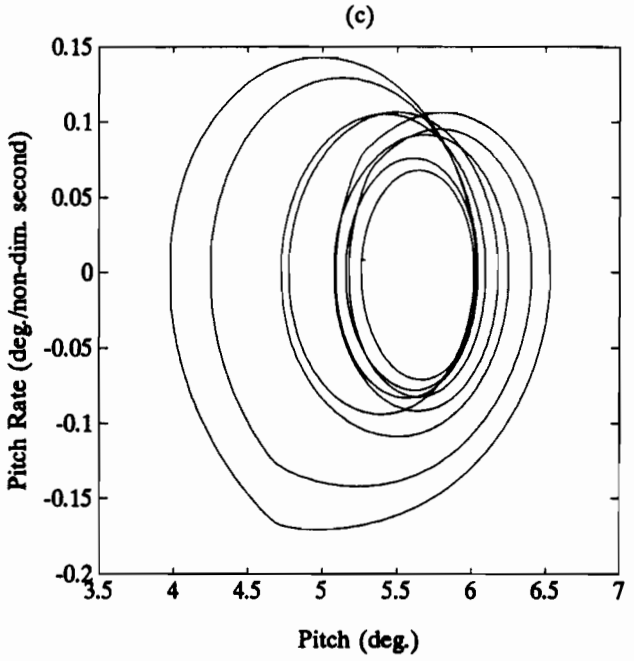
(c)
Pitch Rate (deg./non-dim. second)
0.15
0.1
0.05
0
-0.05
-0.1
-0.15
-0.2
3.5
4
4.5
5
5.5
6
6.5
7
Pitch (deg.)

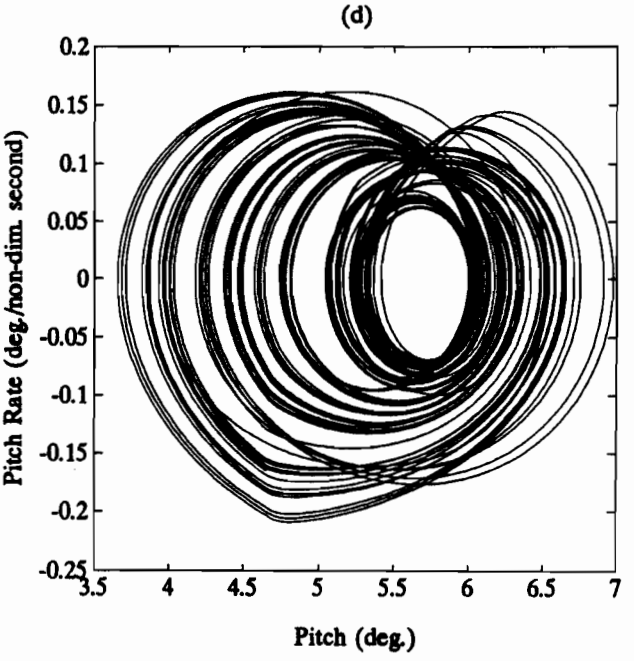
(d)
Pitch Rate (deg./non-dim. second)
0.2
0.15
0.1
0.05
0
-0.05
-0.1
-0.15
-0.2
-0.25
3.5
4
4.5
5
5.5
6
6.5
7
Pitch (deg.)

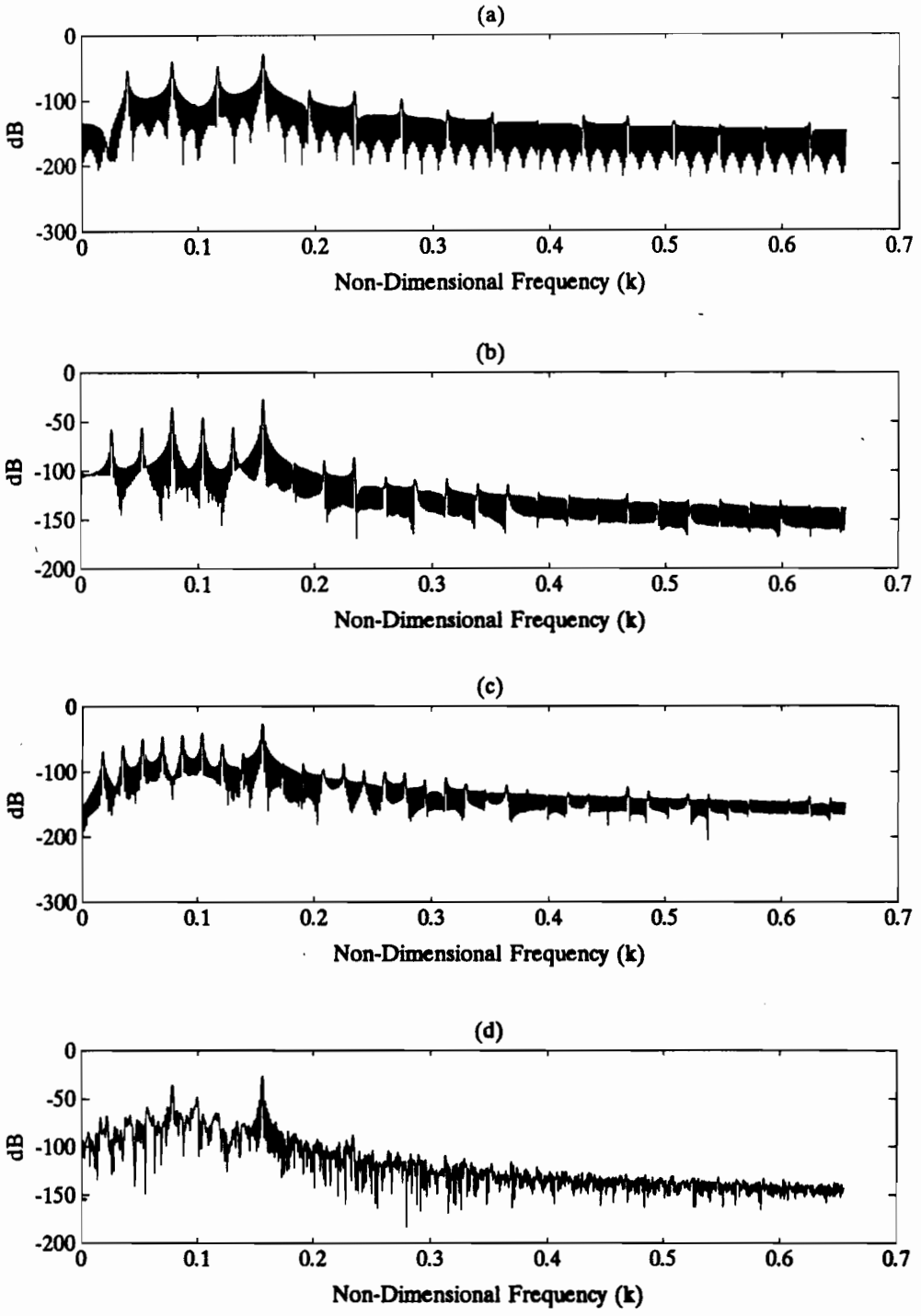

Figure 3.64: The **Fourier spectra** of the response of the airfoil for the cases: $\alpha_o = 7.62^o$, $U^* = 20.265$ and $k = 0.156$ and (a) $Q_o = 3.60 * 10^{-5}$, (b) $Q_o = 4.00 * 10^{-5}$, (c) $Q_o = 4.20 * 10^{-5}$ and (d) $Q_o = 4.30 * 10^{-5}$.

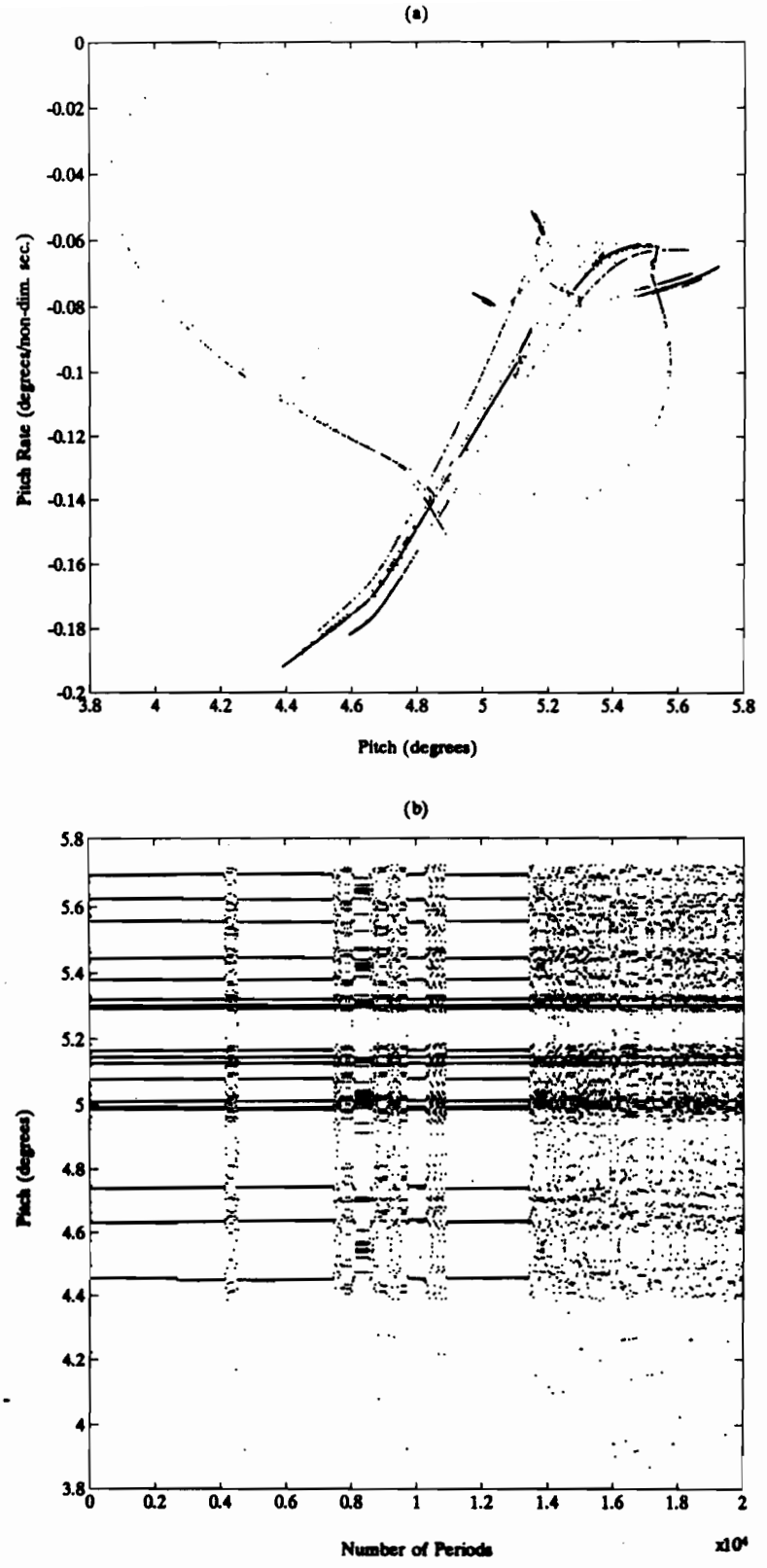

Figure 3.65: (a) The Poincaré section and (b) the long term behaviour of the system for the case: $\mathbf{Q_o = 0.430 * 10^{-4}}$, $\alpha_o = 7.62^o$, $U^* = 20.265$ and $k = 0.156$.

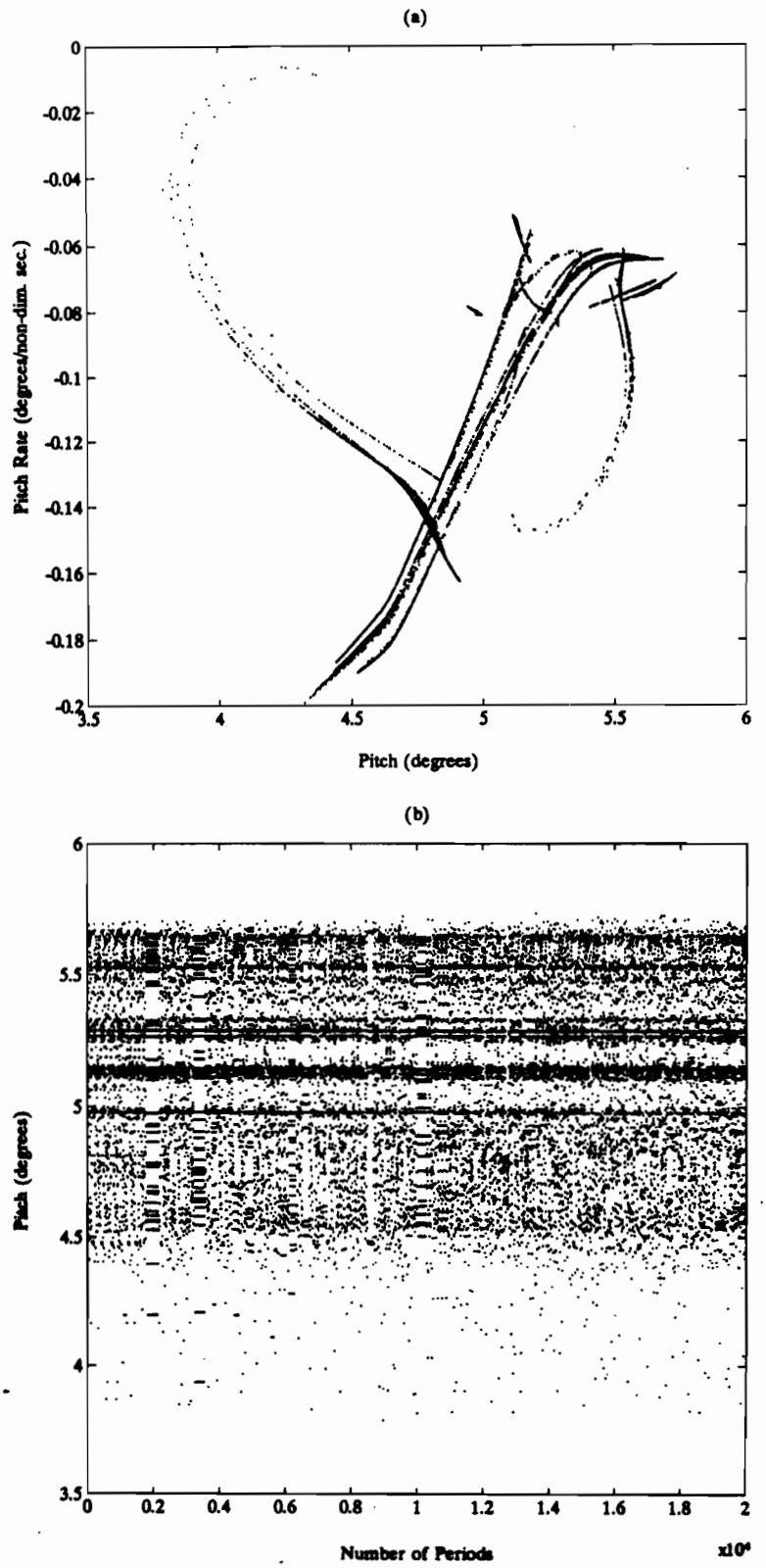

Figure 3.66: (a) The Poincaré section and (b) the long term behaviour of the system for the case: $\mathbf{Q_o = 0.445 * 10^{-4}}$, $\alpha_o = 7.62^o$, $U^* = 20.265$ and $k = 0.156$.

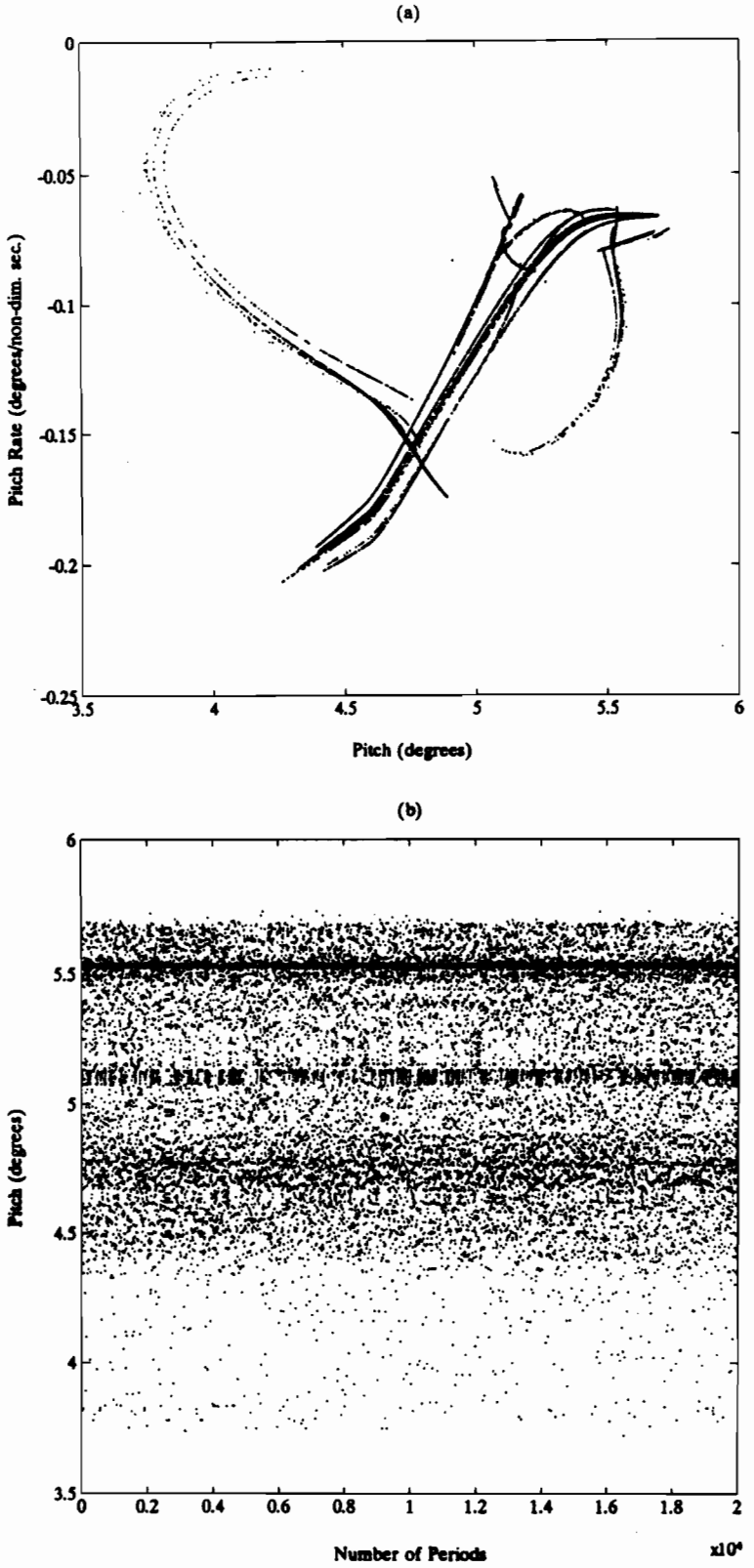

Figure 3.67: (a) The Poincaré section and (b) the long term behaviour of the system for the case: $\mathbf{Q_o = 0.470 * 10^{-4}}$, $\alpha_o = 7.62^o$, $U^* = 20.265$ and $k = 0.156$.

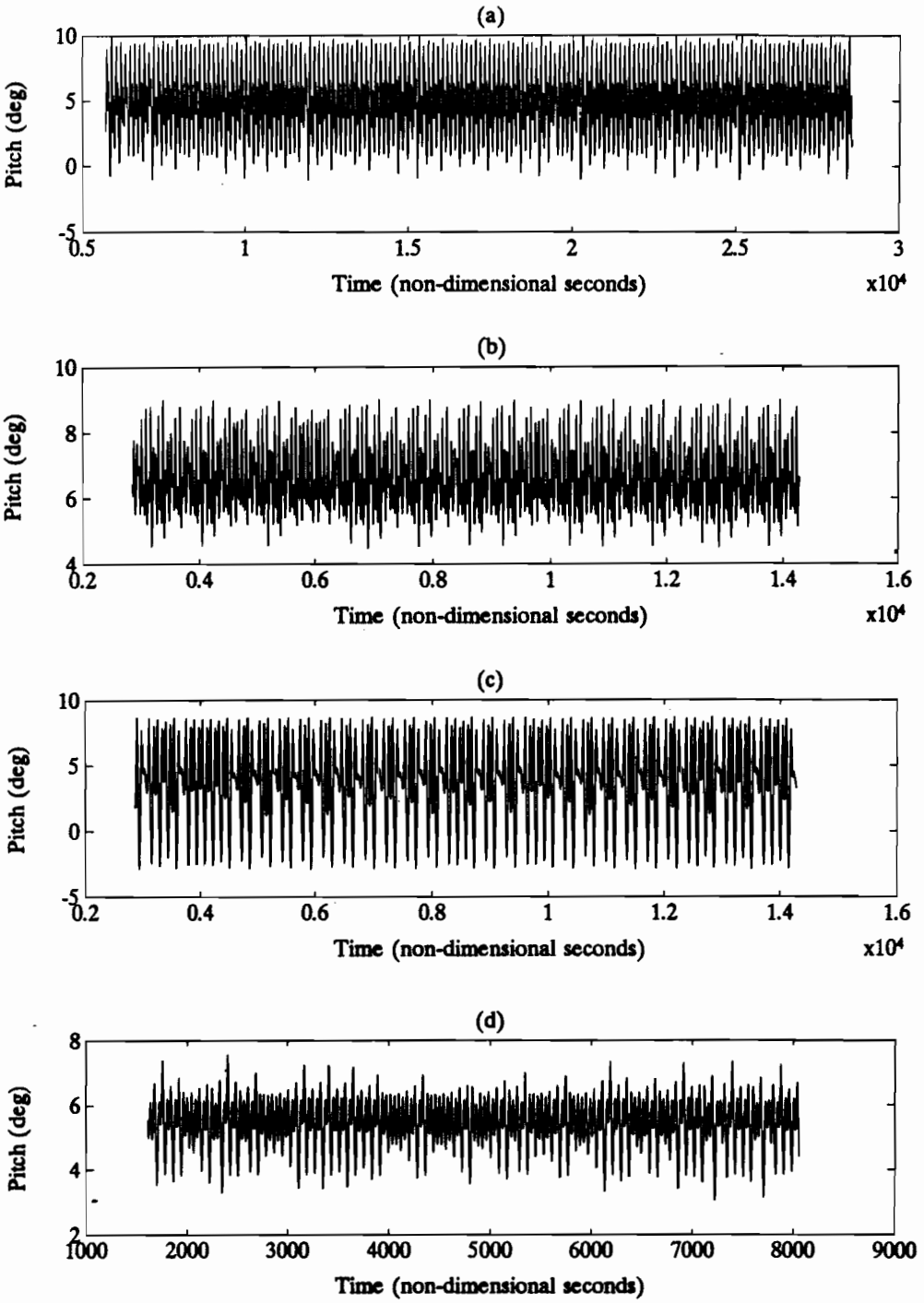

Figure 3.68: The time histories of the response of the airfoil for the chaotic cases: (a) $\alpha_o = 8.90^o$, $Q_o = 1.02 * 10^{-4}$, $U^* = 21.0227$, $k = 0.044$ (b) $\alpha_o = 9.76^o$, $Q_o = 0.70 * 10^{-4}$, $U^* = 12.20$, $k = 0.088$ (c) $\alpha_o = 9.76^o$, $Q_o = 0.76 * 10^{-4}$, $U^* = 25.20$, $k = 0.088$ (d) $\alpha_o = 7.62^o$, $Q_o = 0.55 * 10^{-4}$, $U^* = 20.265$, $k = 0.156$.

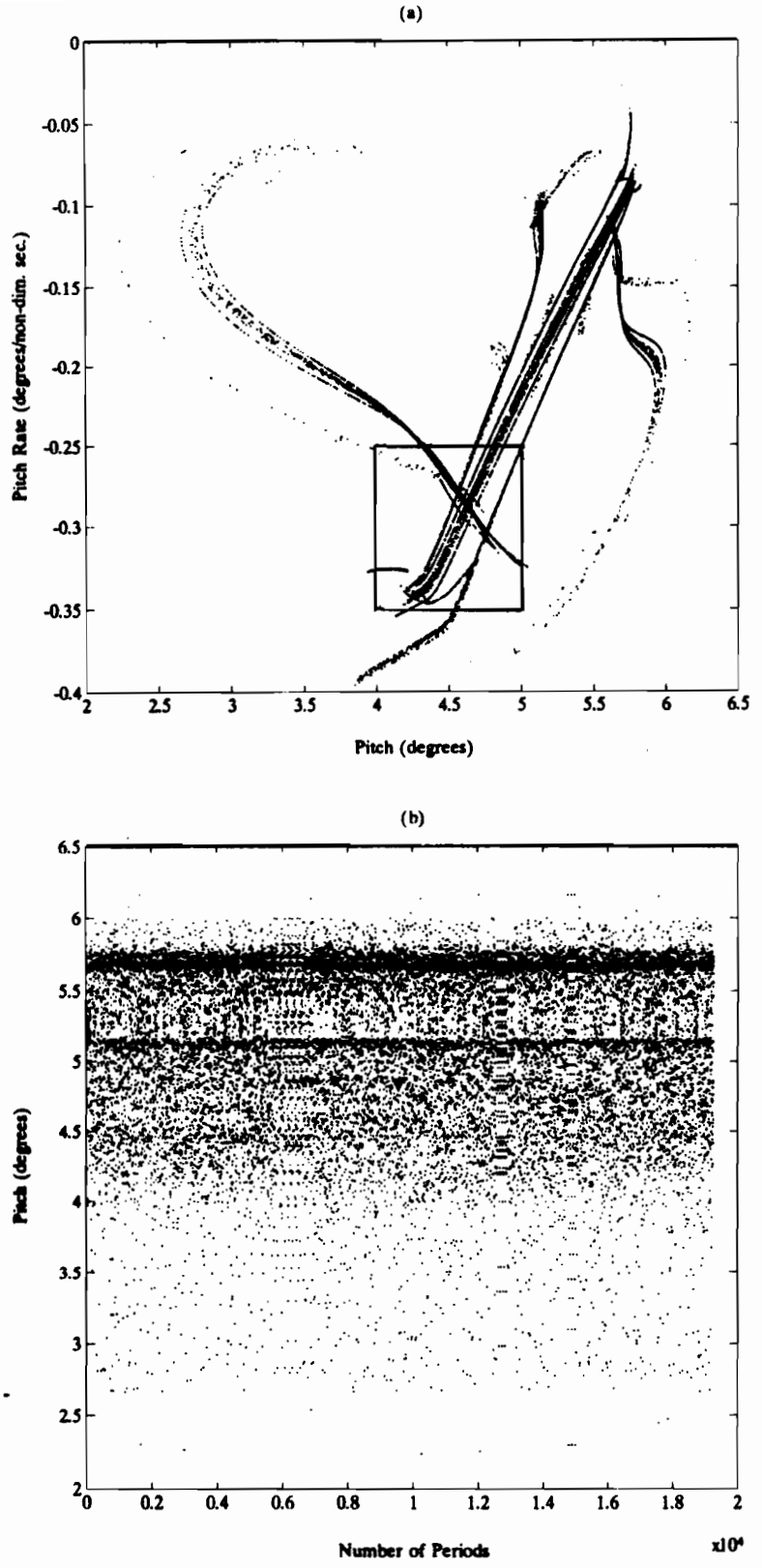

Figure 3.69: (a) The Poincaré section and (b) the long term behaviour of the system for the case: $\mathbf{Q_o = 1.02 * 10^{-4}}$, $\alpha_o = 8.90^o$, $U^* = 21.0227$ and $k = 0.170$.

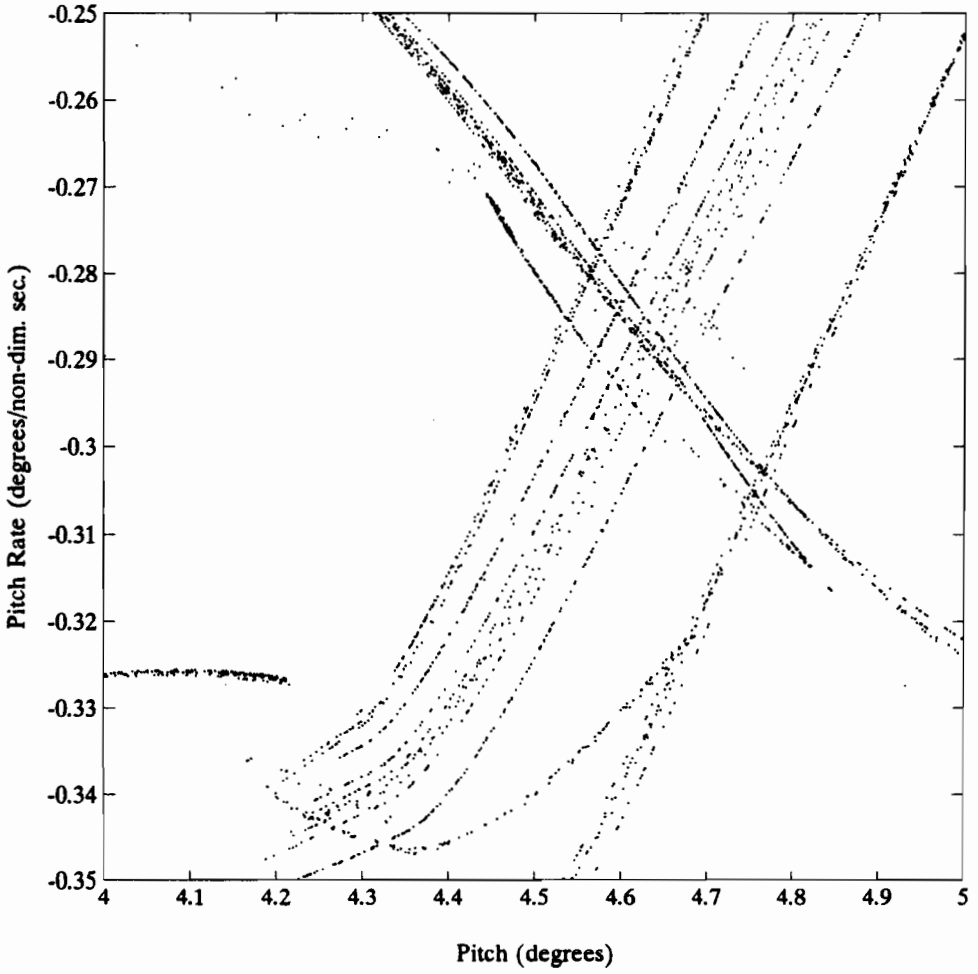

Figure 3.70: The micro-structure of the Poincaré attractor for the case: $Q_o = 1.02 * 10^{-4}$, $\alpha_o = 8.90°$, $U^* = 21.0227$ and $k = 0.170$ (see Figure 3.69(a)).

Chapter 4

The Two Degree of Freedom System

The non-dimensionalized aeroelastic equations for the two degree of freedom airfoil system, first introduced in Chapter 2, are given below:

$$\ddot{\xi} + x_\alpha \ddot{\alpha} + 2\zeta_\xi \frac{\bar{\omega}}{U^*}\dot{\xi} + \frac{(\bar{\omega})^2}{(U^*)^2}\xi = -\frac{1}{\pi\mu}C_N(s) + \frac{P(s)b}{mU^2} \tag{4.1}$$

$$x_\alpha \ddot{\xi} + r_\alpha^2 \ddot{\alpha} + \frac{r_\alpha^2 2\zeta_\alpha}{U^*}\dot{\alpha} + \frac{r_\alpha^2}{(U^*)^2}\alpha = \frac{2}{\pi\mu}C_M(s) + \frac{Q(s)}{mU^2} \tag{4.2}$$

where ζ_α and ζ_ξ are the viscous damping ratios in the pitch and plunge degrees of freedom, respectively, $\bar{\omega} = \omega_\xi/\omega_\alpha$ is the ratio of uncoupled natural frequencies in pitch and plunge and $U^* = U/b\omega_\alpha$ is the non-dimensional velocity. The airfoil air-mass ratio is defined as $\mu = m/\pi\rho b^2$, where m is the airfoil's mass per unit span, ρ is the air density and b is the semi-chord. The non-dimensionalized radius of gyration about the elastic axis is r_α. $C_N(s)$ and $C_M(s)$ are the lift and moment coefficients, respectively, taken about the elastic axis and $P(s)$ and $Q(s)$ are the externally applied force and torque, respectively, applied at the elastic axis. In all of the cases studied as part of this thesis the externally applied force $P(s)$ and the

viscous damping ratios, ζ_α and ζ_ξ are zero for all time. The two degree of freedom system is illustrated in Figure 4.1.

As mentioned in Chapter 2, the effect of the plunge degree of freedom on the aerodynamic loads is taken into account by a linear approximation: if the magnitude of the plunge motion is small compared to the pitch motion, then the effect of the plunge motion on the aerodynamic loads can be assumed small compared to the effect of the pitch motion. Therefore, for small plunge motions, the aerodynamic loads are predominantly a function of the pitch motion and the small adjustments for the plunge motion can be accounted for by superimposing linear aerodynamic theory (please see [Mazelsky, 1952] and [Mazelsky and Drischler, 1952]). Without this assumption calculating the aerodynamic loads becomes a very complicated problem that is beyond the scope of this thesis.

There are at least two flaws with the assumption of linear plunge motion effects. First of all, it is only strictly valid for large values of $\bar{\omega}$ and when the flow around the airfoil is attached. Therefore, when the airfoil is stalled this assumption is invalid and, in reality, the effect of the plunge motion on the aerodynamic loads is not well understood. Secondly, by adding the effects of the plunge motion to the aerodynamic loads as a linear correction the aerodynamic model fails to account for the effect of the plunge motion on the dynamic stall events. Thus, the effect of the plunge motion on the three main dynamic stall parameters, α_{DM}, s_{MT} and α_{RE}, is not taken into account.

Despite the flaws mentioned above, and for lack of more detailed theory, the assumption of linear plunge motion effects is maintained and the results presented in this chapter are based on this assumption.

4.1 Discussion of Results

As previously stated, the assumption that the effects of the plunge motion on the aerodynamics can be linearized is an essential part of the analysis presented here and, since the subsequent error due to this assumption is unavoidable, the analysis of the two degree of freedom system attempted herein is limited in scope. The goal of the analysis is to determine the effect of plunge motion on the chaotic oscillations discussed in the previous chapter, and also to qualitatively show the effect of the ratio of natural frequencies, $\bar{\omega}$, on the stability of the system. The time history, phase plane plot and Fourier spectrum are presented for a typical chaotic case and the effect of the ratio of natural frequencies on the stability of the response is presented in a series of bifurcation diagrams. The effect of the plunge motion on the long term stability and behaviour of the system is explored through the use of Poincaré sections.

4.1.1 The Effect of Adding Plunge Motion to a Typical Chaotic Case

The example studied in this section is a two degree of freedom version of case I (see section 3.3.1) with the following values of the system parameters: $\alpha_o = 8.90^o$, $Q_o = 1.02 * 10^{-4}$, $U^* = 21.0227$, $k = 0.044$ and the ratio of the natural frequencies is $\bar{\omega} = 10.67$.

In Figure 4.2 (a), (b) and (c), the time history, phase plane plot and Fourier spectrum, respectively, are presented for a short time interval of the response of the airfoil in pitch. The effect of the plunge motion on the response is not evident in the time history of the response, but, the phase plane plot clearly shows the effect of the plunge motion, especially when compared with the single degree of freedom

case, shown in Figure 3.9 (c). The plunging motion superimposes fluctuations on the pitch and pitch rate of the airfoil which are evident in the 'wavy' appearance of the phase plane plot. The Fourier transform of the response contains the same general characteristics as in the single degree of freedom case; the main frequency components are at the forcing frequency and higher order harmonics and the broadband structure of the spectrum between these frequencies indicates that the response is probably chaotic. The higher frequency components, present at approximately $k = 0.570$, are due to the higher non-dimensional structural natural frequency of the plunge motion. The non-dimensional structural natural frequency of the plunge motion can be calculated as approximately $\bar{\omega}/U^* = 0.508$ and the plunge natural frequency of the system will be slightly higher due to the effect of the aerodynamics.

The time history, phase plane plot and Fourier spectrum of the response of the airfoil in plunge, for the same set of conditions as above, are shown in Figure 4.3 (a), (b) and (c), respectively. The high frequency components of the plunge response, caused by the high plunge natural frequency, are evident in the time history of the response; a high frequency, small amplitude oscillation is superimposed on the main frequency of the response, which is at the forcing frequency. The high frequency components of the plunge response are also evident in the Fourier spectrum at approximately $k = 0.570$. The phase plane plot of the plunge response does not repeat itself over the time interval shown and the Fourier spectrum of the plunge response has a broadband structure with peaks at the forcing frequency and higher order harmonics. Together these plots suggest that the response may be chaotic.

4.1.2 The Effect of the Ratio of Natural Frequencies on the Stability of the Response

In this section, the effect of the natural frequency ratio, $\bar{\omega}$, on the stability of the system in pitch and the long term behaviour of the system is studied through the use of a series of bifurcation diagrams and Poincaré sections. Two separate examples are examined: the first is from case I (see section 3.3.1) for which $\alpha_o = 8.90°$, $Q_o = 1.02 * 10^{-4}$, $U^* = 21.0227$, and $k = 0.044$; and the second is from case III (see section 3.3.3) for which $\alpha_o = 9.76°$, $Q_o = 0.70 * 10^{-4}$, $U^* = 25.20$, and $k = 0.088$.

Example One

The bifurcation diagram, shown in Figure 4.4, shows the effect of increasing $\bar{\omega}$ on the stability of the pitch response for the case of $\alpha_o = 8.90°$, $Q_o = 1.02 * 10^{-4}$, $U^* = 21.0227$, and $k = 0.044$. As can be seen from the diagram, when $\bar{\omega}$ is less than approximately 6.8, the response of the system is stable and periodic. However, as the value of $\bar{\omega}$ is increased beyond this value the response suddenly changes from a stable periodic oscillation to what appears to be a chaotic oscillation. For $\bar{\omega}$ greater than approximately 10.0, the response appears to always be chaotic. This bifurcation diagram suggests that decreasing the ratio of natural frequencies can have a stabilizing effect on airfoils undergoing chaotic oscillations due to dynamic stall.

In Figure 4.5 (a), (b) and (c), the Poincaré sections are shown for three different values of $\bar{\omega}$. In each case the system parameters are the same as in the bifurcation diagram shown in Figure 4.4, but, $\bar{\omega}$ is equal to 8.54, 10.67 and 13.81 for the three cases, respectively. In Figure 4.6, the Poincaré section for the corresponding one degree of freedom system ($\bar{\omega}$ is infinite) has been reproduced because the effect of the plunge motion on the Poincaré attractors can best be seen when these three

sections are compared to the single degree of freedom case. The main curves that make up the one degree of freedom attractor can be identified in the two degree of freedom attractors but, they have been twisted into slightly modified orientations in the phase plane. These new orientations have a more two-dimensional appearance than the corresponding one degree of freedom attractor.

Figure 4.7 (a), (b) and (c) shows the long term behaviour of the system for the same cases discussed above and, in Figure 4.8, the long term behaviour of the system is shown for the corresponding one degree of freedom case. As can be seen from the diagrams, the marginally stable, intermittently chaotic behaviour, described in section 3.3.1, persists in the two degree of freedom systems with one interesting change. In the one degree of freedom case, a single marginally stable periodic state, such as the period-one oscillation beginning after approximately 17 000 periods, does not reoccur. However, in each of the two degree of freedom cases there is at least one marginally stable state that can be seen to repeat. For example, in Figure 4.7 (a) there are two stable periodic states that repeat; the first is approximately a period-twenty oscillation located at the beginning of the data and again after approximately 3000 periods and the second is a period-three oscillation which occurs after approximately 11 500 periods and again after approximately 14 500 periods.

This behaviour implies that while the one degree of freedom case wanders through a seemingly endless array of different marginally stable periodic attractors and never shows any indication of favouring one over the other, the two degree of freedom cases may wander near certain more favourable periodic attractors. Thus, it is possible that one of the effects of adding the plunge degree of freedom is to increase the strength of certain periodic attractors and in so doing increase the stability of the system.

Example Two

The bifurcation diagram shown in Figure 4.9 (a) is for the case $\alpha_o = 9.76^o$, $Q_o = 0.70 * 10^{-4}$, $U^* = 25.20$, $k = 0.088$ and the ratio of natural frequencies, $\bar{\omega}$, is varied from 7.00 to 70.00. As can be seen from the diagram, the chaotic behaviour of the system is greatly influenced by the value of $\bar{\omega}$. As $\bar{\omega}$ is varied, the response of the system undergoes many bifurcations alternating between regions of periodic and chaotic behaviour. In Figure 4.9 (b), the region of the bifurcation diagram for which the value of $\bar{\omega}$ is varied from 40.00 to 50.00 is shown in greater detail. From this magnified view of the bifurcation diagram, it is evident that the response is very sensitive to small changes in $\bar{\omega}$. The fact that the response is sensitive to small changes in the ratio of natural frequencies for very small amplitude plunge oscillations implies that one of the effects of adding even a small amount of plunge motion can be to stabilize the response of the system. However, the results shown here indicate that this newly acquired stability is very fragile. In other words, a small change in the ratio of natural frequencies could cause the response of the system to change from periodic to chaotic.

In Figure 4.10 (a), (b) and (c), the Poincaré sections for three different values of $\bar{\omega}$ are shown. In each of these examples the following system parameters remain constant: $\alpha_o = 9.76^o$, $Q_o = 0.70 * 10^{-4}$, $U^* = 25.20$, $k = 0.088$ and the values of $\bar{\omega}$ are 44.00, 46.50 and 48.00, respectively. In Figure 4.11, the Poincaré section for the corresponding one degree of freedom system is reproduced for the purpose of comparison. As in Example One, the effect of the plunge motion on the Poincaré section is to create waves on the attractor that cause it to change its shape and orientation in the phase plane. These changes in the orientation of the attractor lead to different types of long term behaviour of the response.

The long term behaviour of the three different two degree of freedom systems are shown in Figure 4.12 (a), (b) and (c), respectively and the long term behaviour of the one degree of freedom system is shown in Figure 4.13 for comparison purposes. In Figures 4.12 (a) and (c), the Poincaré data points are confined to within two bands, each band having its own internal structure of light and dark coloured bands; this behaviour is very similar to the single degree of freedom case shown in Figure 4.13. However, in Figure 4.12 (b), the Poincaré data points are loosely grouped into many more thinner bands, with occasional outbursts of data points outside of these bands. This behaviour is very similar to the type of behaviour exhibited by the one degree of freedom case for which $\alpha_o = 9.76°$, $Q_o = 0.73 * 10^{-4}$, $U^* = 25.20$ and $k = 0.088$ which is reproduced in Figure 4.14.

The aforementioned examples of the Poincaré sections for three separate values of $\bar{\omega}$ illustrate that the long term behaviour of the system is very sensitive to changes in the ratio of natural frequencies, even for very small plunge oscillations. Furthermore, by changing the value of $\bar{\omega}$ the long term behaviour of the two degree of freedom system can change in such a way as to mimic the changes of the one degree of freedom system as Q_o is varied. Both Example One and Two indicate that despite the assumptions that the effect of plunge motion on the aerodynamic loads is small and the plunge motion itself is small, the stability of the system can be very sensitive to changes in the ratio of natural frequencies. This causes some concern about whether it is reasonable to assume that the effect of plunge motion on the aerodynamic forces is small. Thus, until an improved two degree of freedom model of dynamic stall is developed, the usefulness of further work on the two degree of freedom system is questionable.

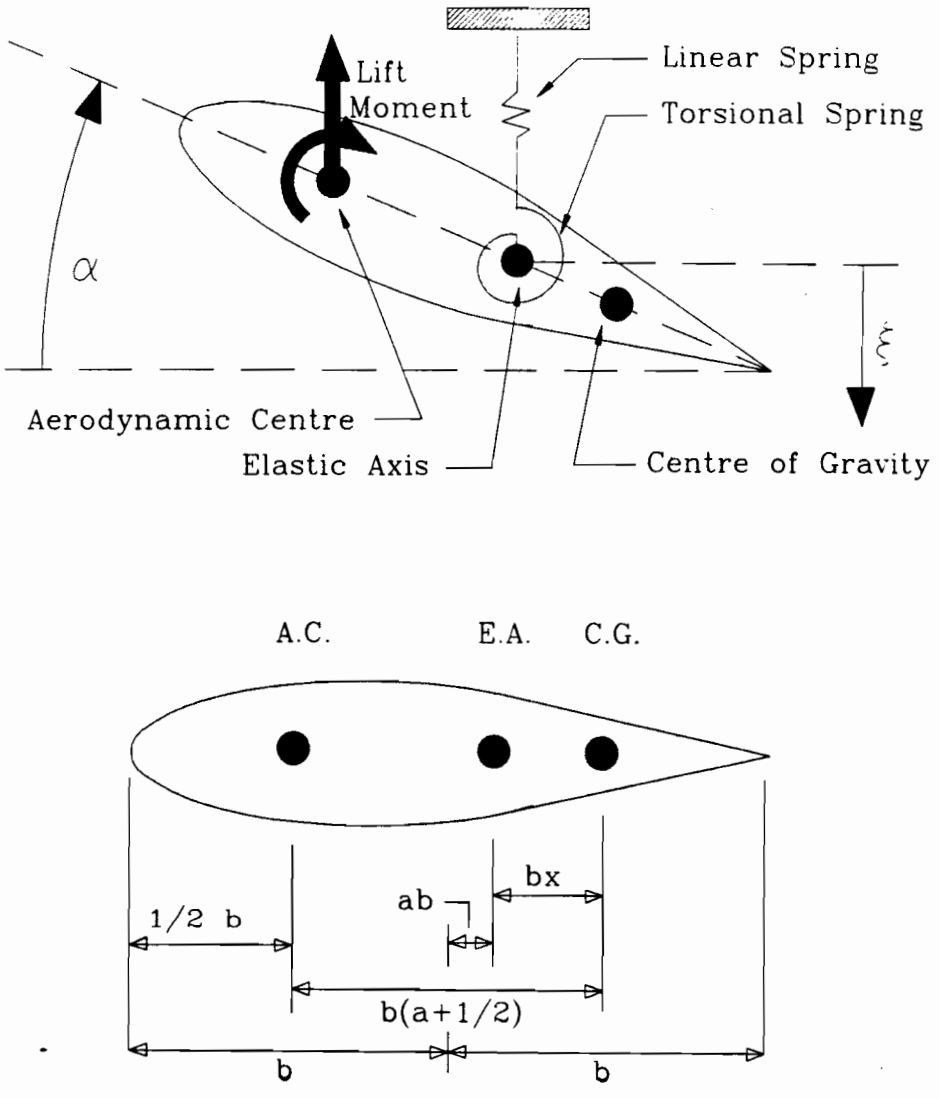

Figure 4.1: The two degree of freedom airfoil system.

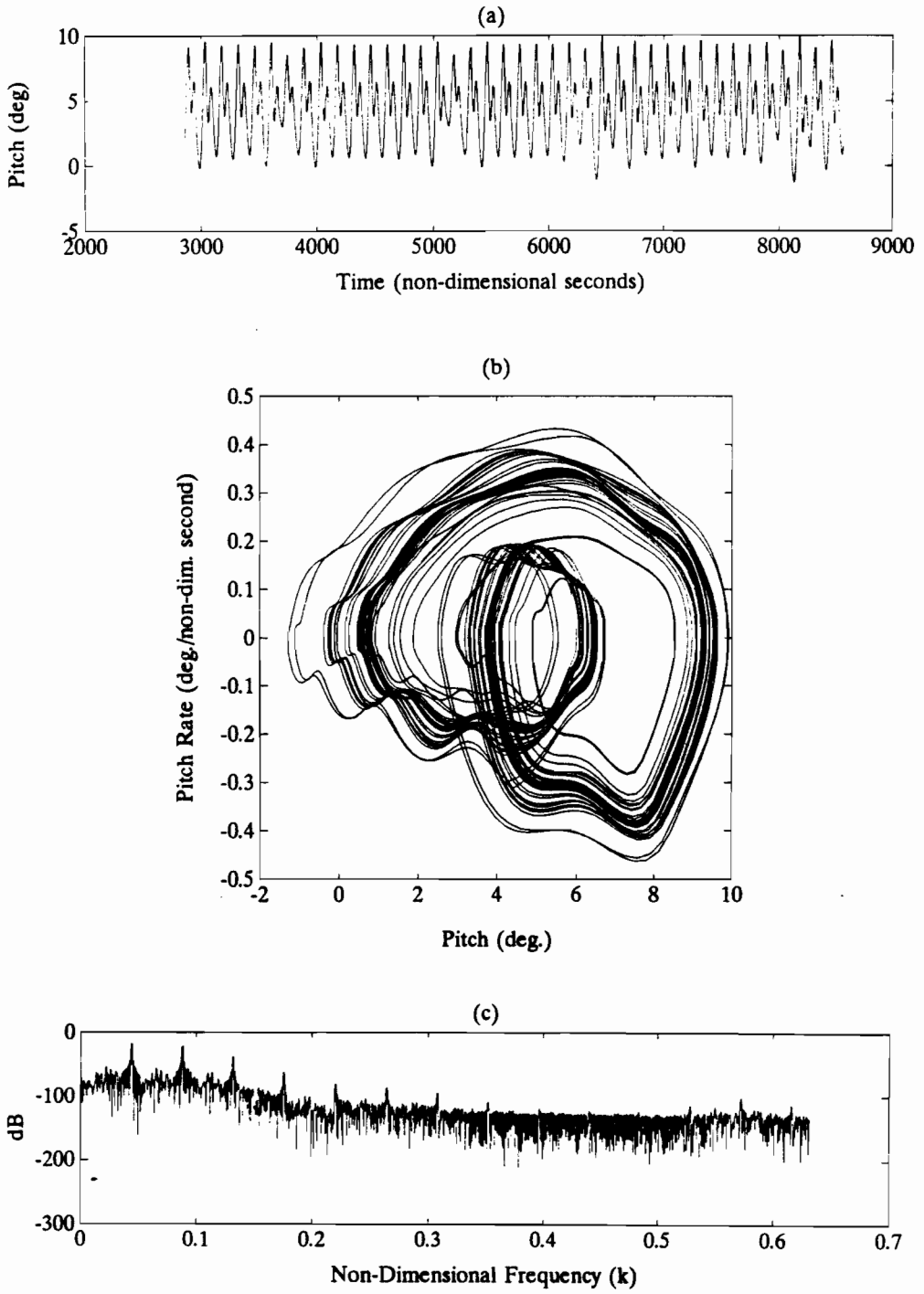

Figure 4.2: (a) The time history, (b) phase plane plot and (c) Fourier spectrum for the **pitch** degree of freedom for the case $\alpha_o = 8.90^o$, $Q_o = 1.02 * 10^{-4}$, $U^* = 21.0227$, $k = 0.044$ and $\bar{\omega} = 10.67$.

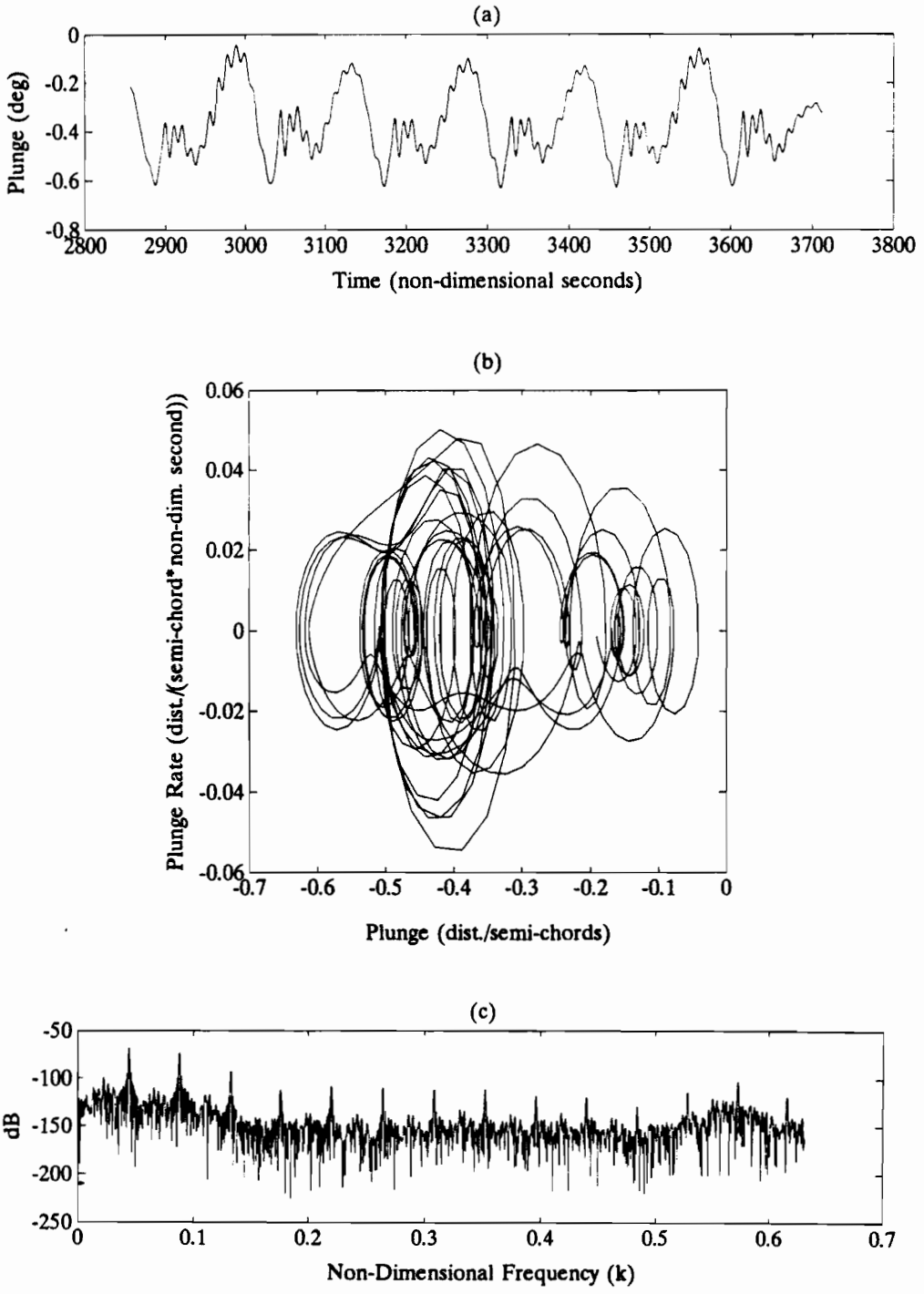

Figure 4.3: (a) The time history, (b) phase plane plot and (c) Fourier spectrum for the **plunge** degree of freedom for the case $\alpha_o = 8.90^o$, $Q_o = 1.02{*}10^{-4}$, $U^* = 21.0227$, $k = 0.044$ and $\bar{\omega} = 10.67$.

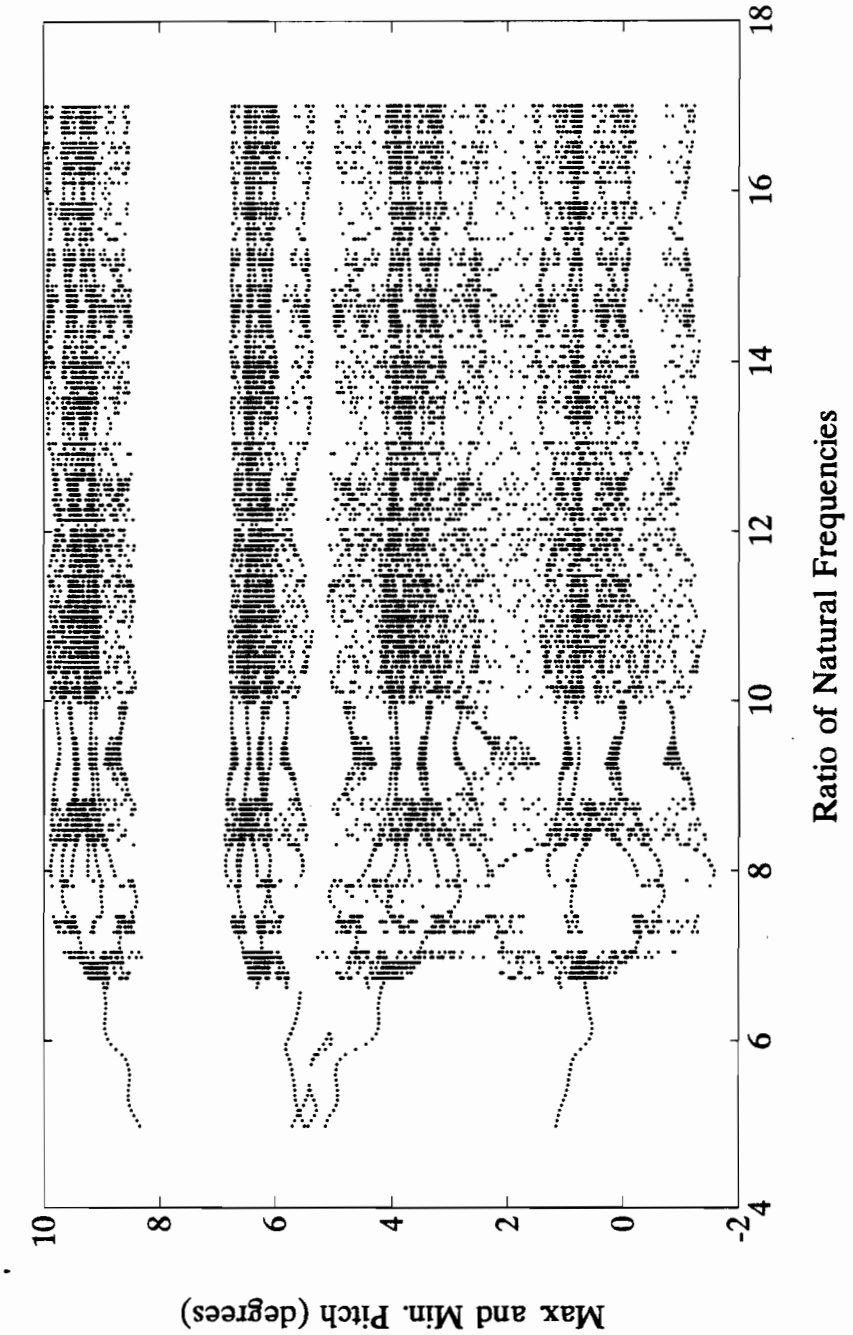

Figure 4.4: Bifurcation diagram for the case: $\alpha_o = 8.90^o$, $U^* = 21.0227$, $k = 0.044$, $Q_o = 1.02 * 10^{-4}$ and $5.00 < \bar{\omega} < 17.00$.

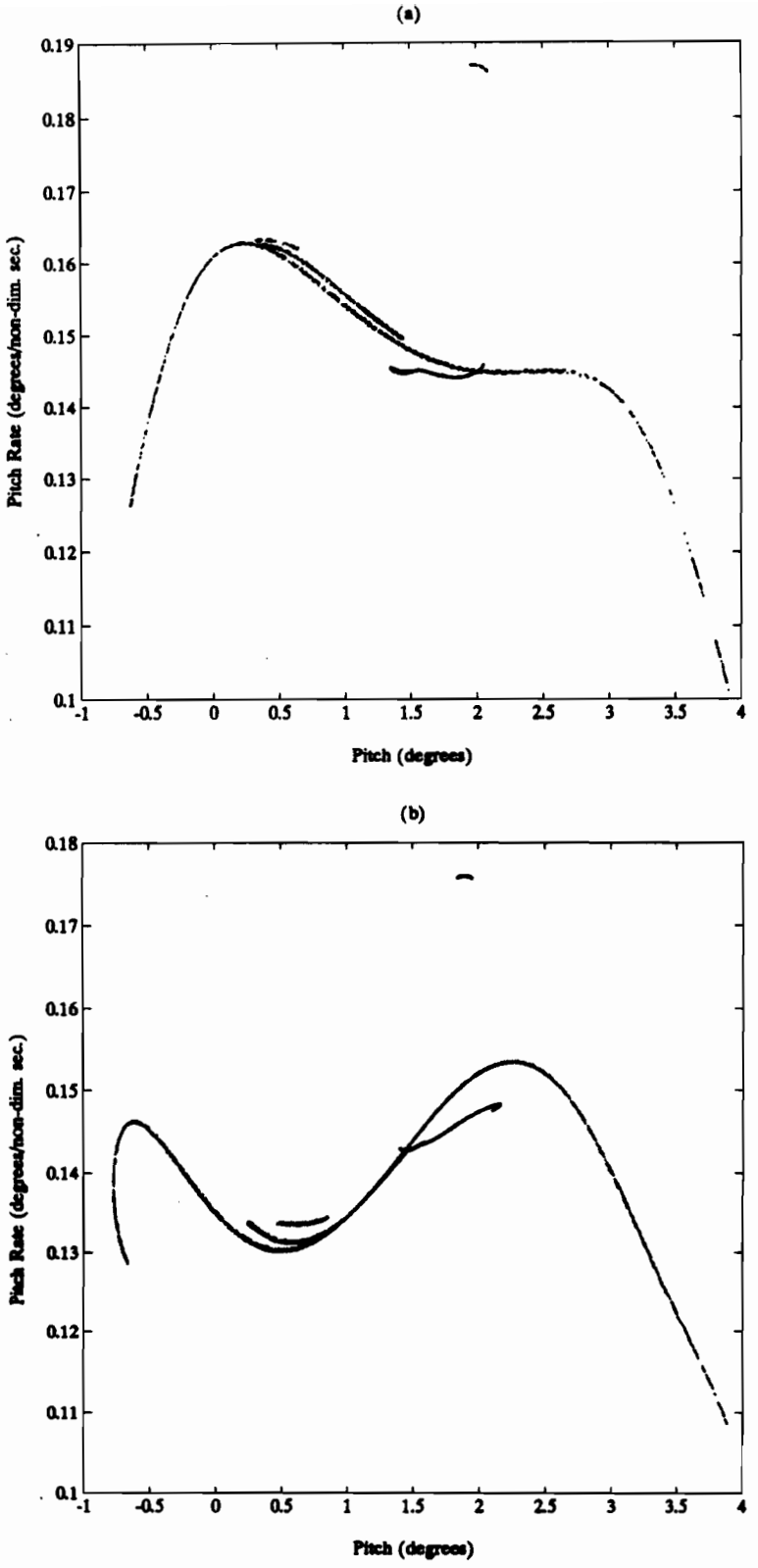

Figure 4.5: The Poincaré sections of the pitch variable for the two degree of freedom cases $\alpha_o = 8.90^o$, $Q_o = 1.02 * 10^{-4}$, $U^* = 21.0227$, $k = 0.044$ and (a) $\bar{\omega} = 8.54$, (b) $\bar{\omega} = 10.67$ and (c) $\bar{\omega} = 13.81$.

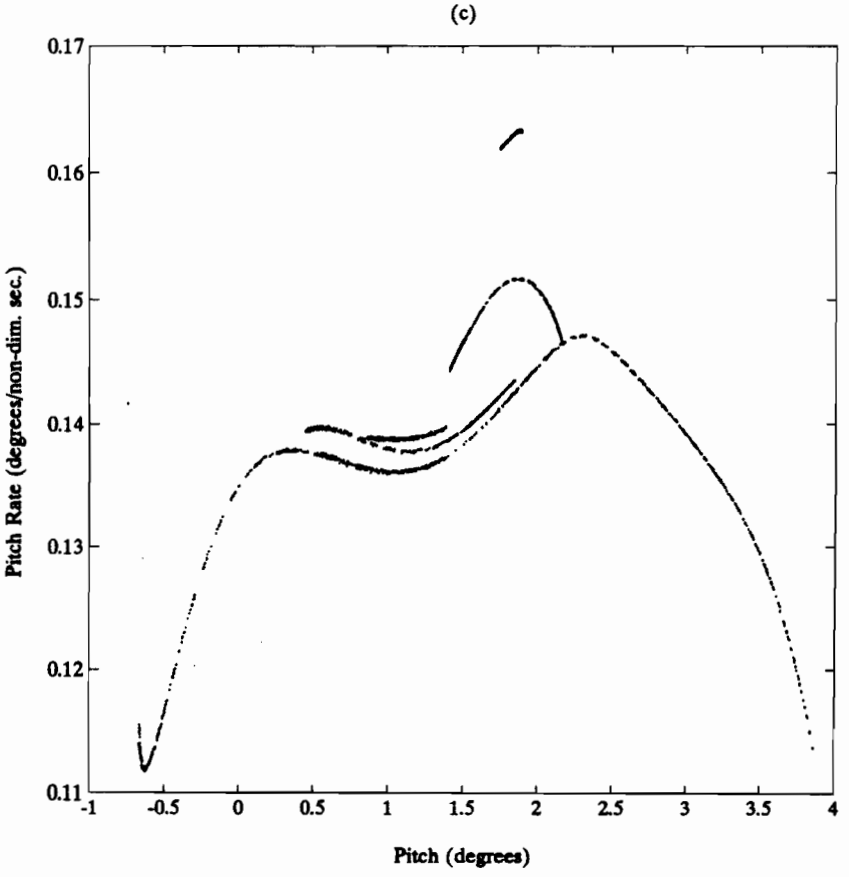
(c)
0.17
0.16
0.15
0.14
0.13
0.12
0.11
Pitch Rate (degrees/non-dim. sec.)
-1
-0.5
0
0.5
1
1.5
2
2.5
3
3.5
4
Pitch (degrees)

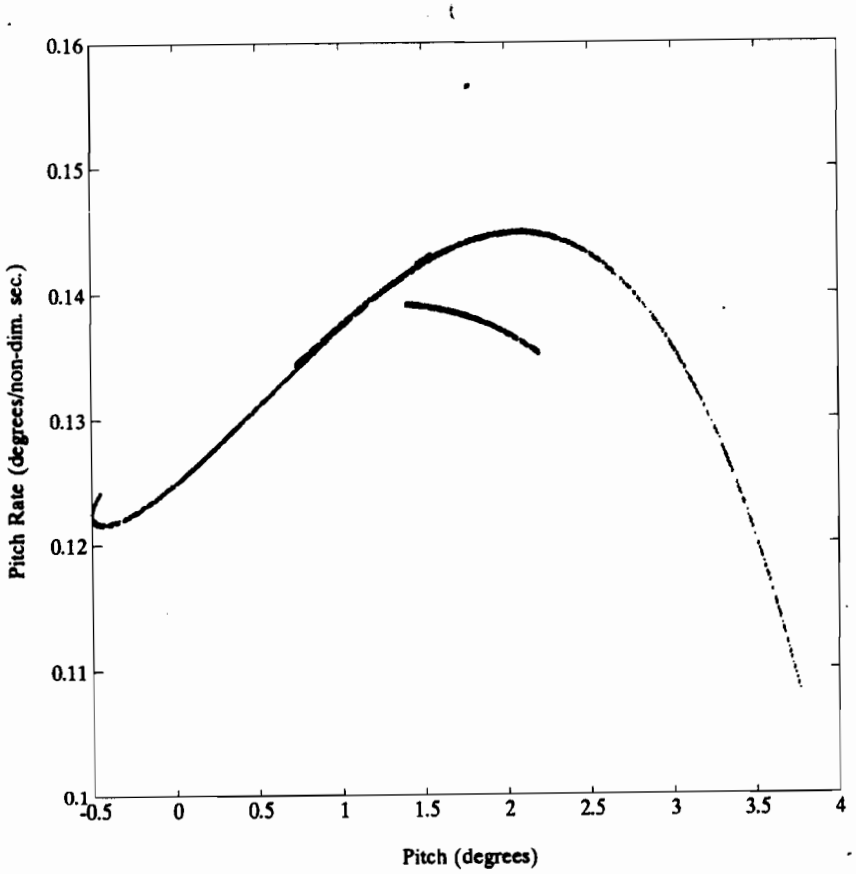

Figure 4.6: The Poincaré section of the pitch variable for the one degree of freedom system for which $\alpha_o = 8.90°$, $Q_o = 1.02 * 10^{-4}$, $U^* = 21.0227$ and $k = 0.044$.

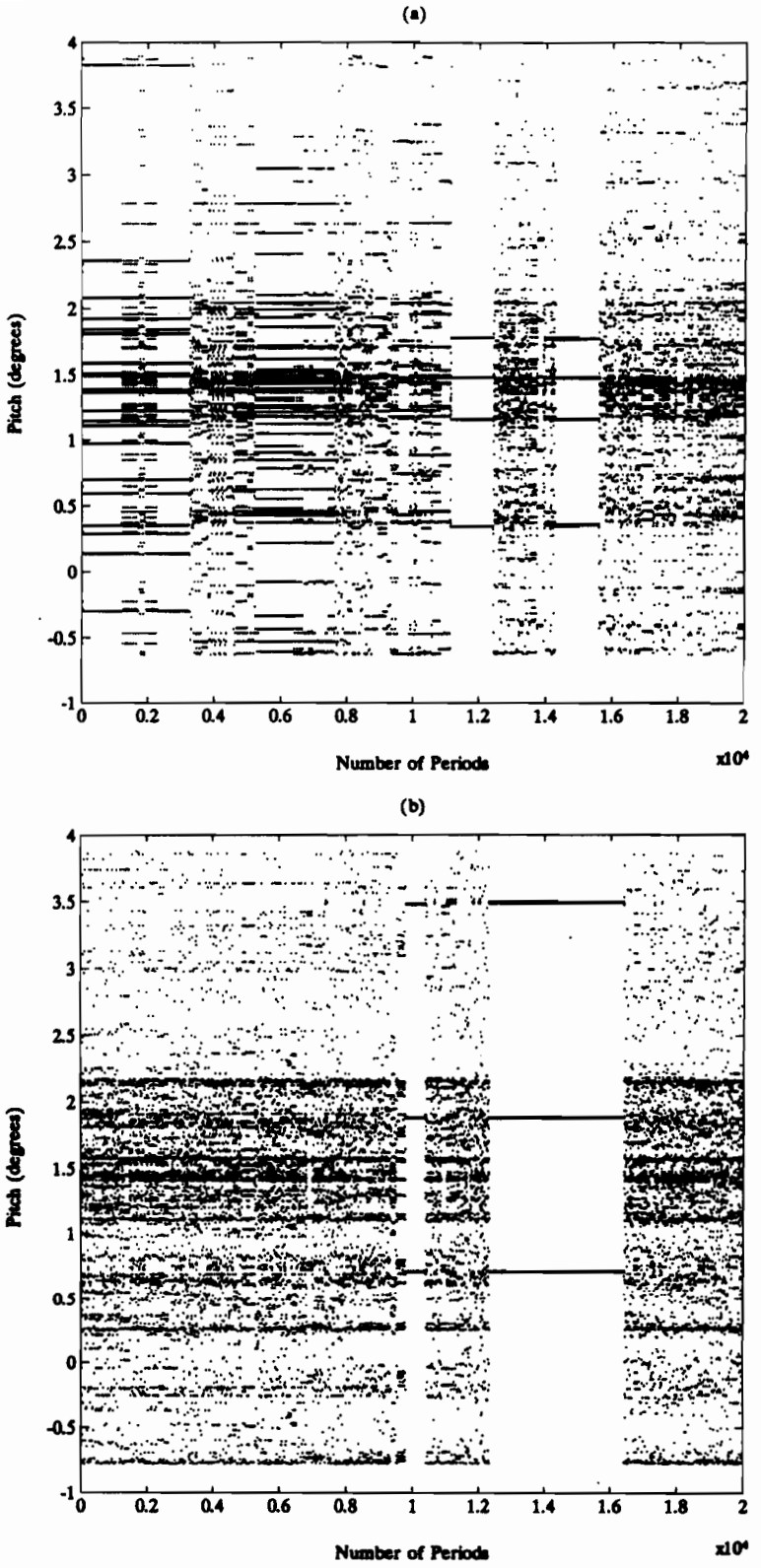

Figure 4.7: The long term behaviour of the pitch variable for the two degree of freedom cases $\alpha_o = 8.90°$, $Q_o = 1.02 * 10^{-4}$, $U^* = 21.0227$, $k = 0.044$ and (a) $\bar{\omega} = 8.54$, (b) $\bar{\omega} = 10.67$ and (c) $\bar{\omega} = 13.81$.

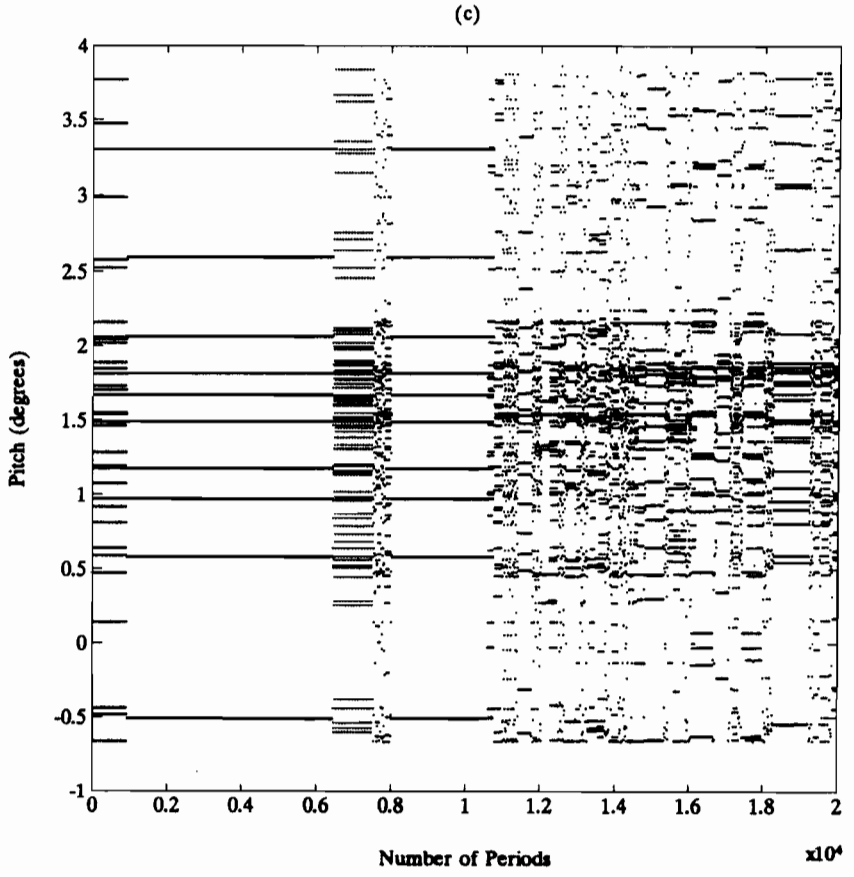
(c)
Pitch (degrees)
4
3.5
3
2.5
2
1.5
1
0.5
0
-0.5
-1
0
0.2
0.4
0.6
0.8
1
1.2
1.4
1.6
1.8
2
Number of Periods
x10⁴

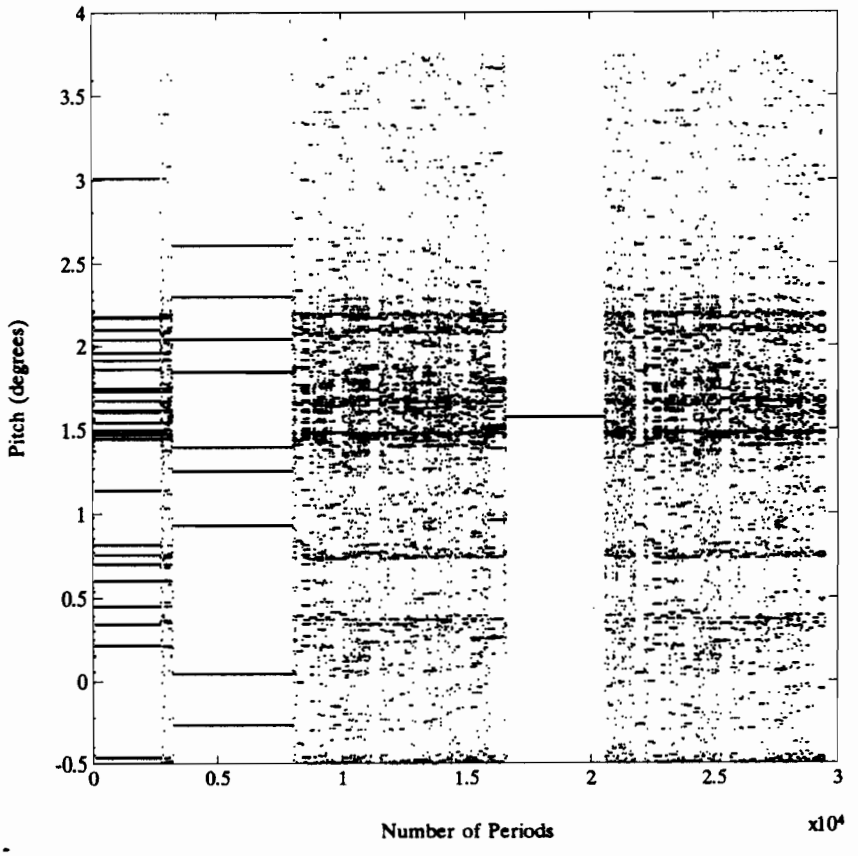

Figure 4.8: The long term behaviour of the pitch variable for the one degree of freedom system for which $\alpha_o = 8.90^o$, $Q_o = 1.02 * 10^{-4}$, $U^* = 21.0227$ and $k = 0.044$.

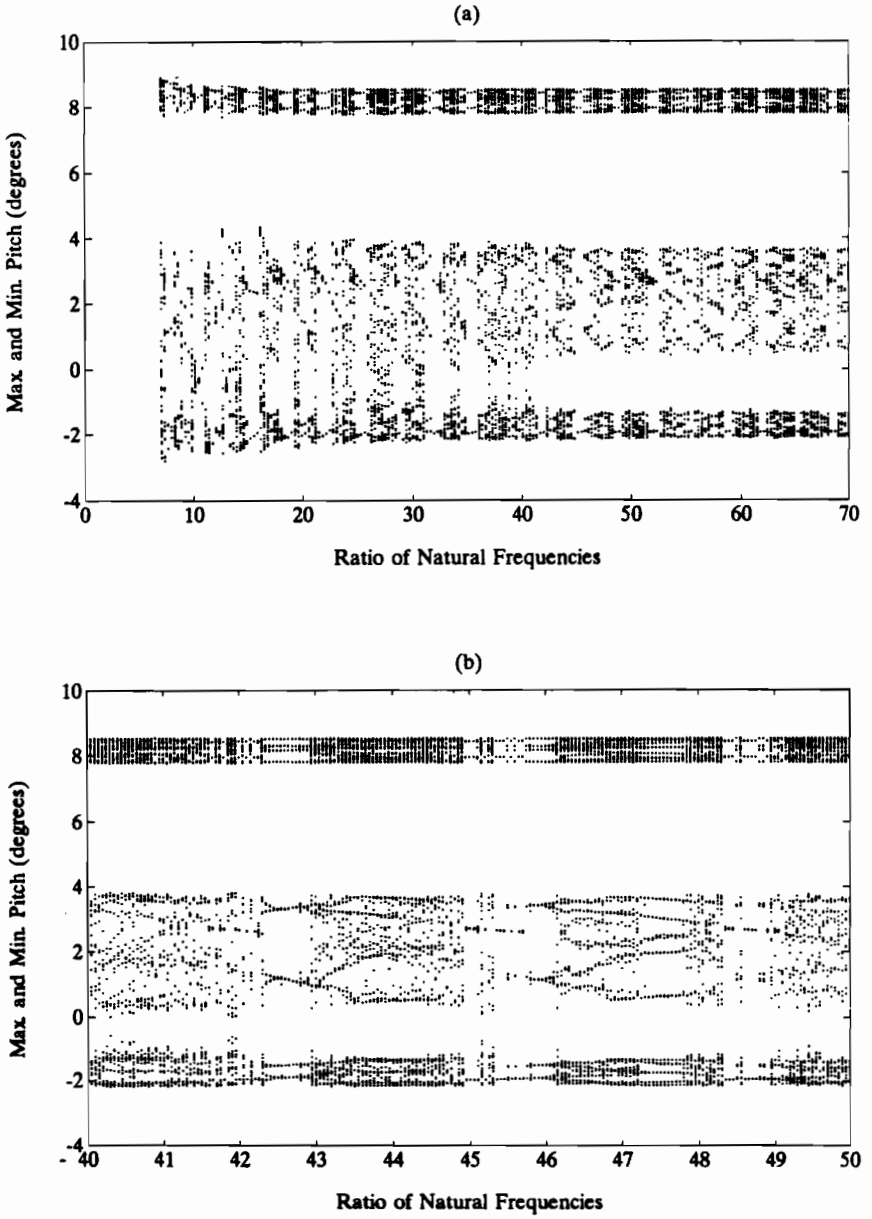

Figure 4.9: Bifurcation diagrams for the cases: (a) $\alpha_o = 9.76°$, $U^* = 25.20$, $k = 0.088$, $Q_o = 0.70 * 10^{-4}$ and $7.00 < \bar{\omega} < 70.00$ and (b) $\alpha_o = 9.76°$, $U^* = 25.20$, $k = 0.088$, $Q_o = 0.70 * 10^{-4}$ and $40.00 < \bar{\omega} < 50.00$.

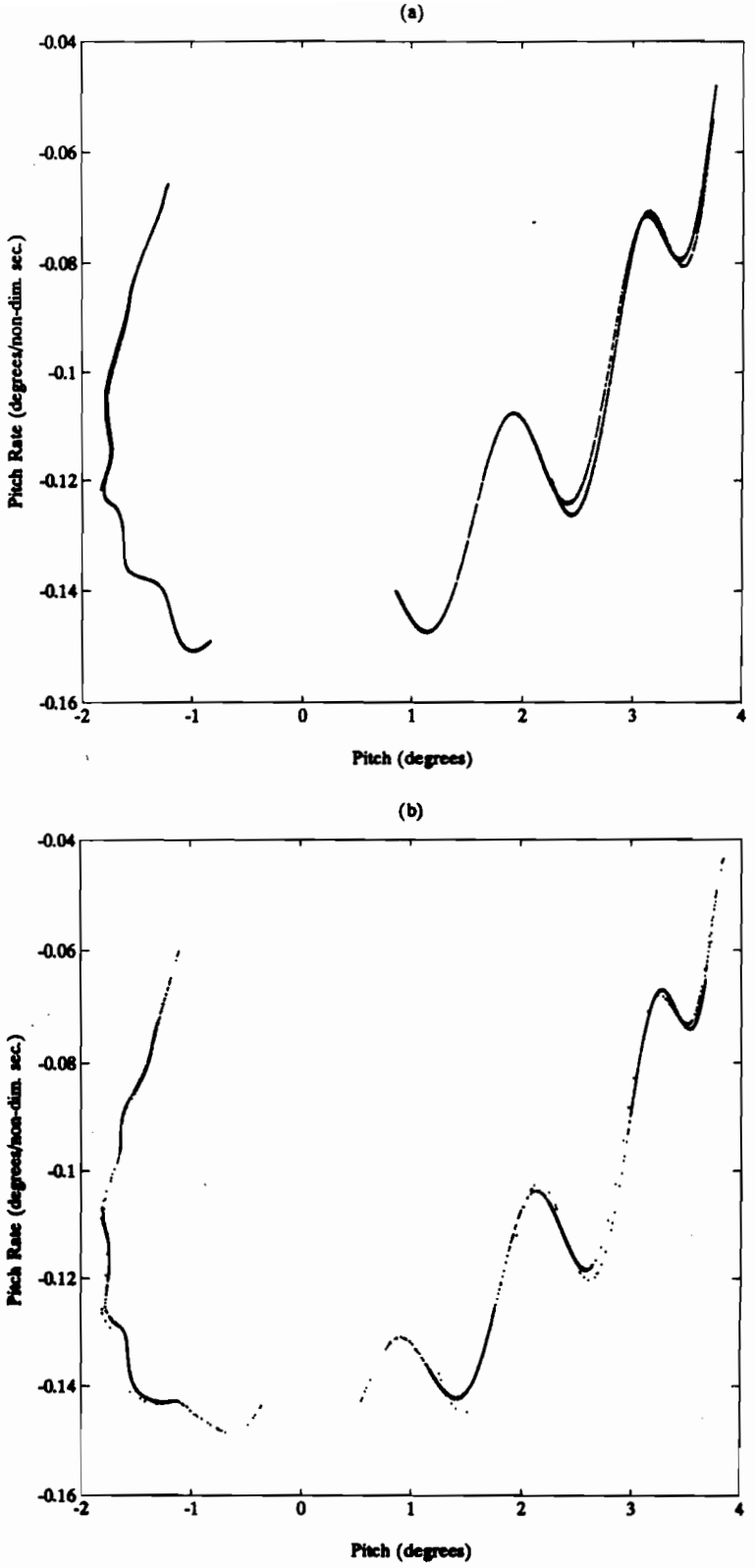

Figure 4.10: The Poincaré sections of the pitch variable for the two degree of freedom cases $\alpha_o = 9.76°$, $Q_o = 0.70 * 10^{-4}$, $U^* = 25.20$, $k = 0.088$ and (a) $\bar{\omega} = 44.00$, (b) $\bar{\omega} = 46.50$ and (c) $\bar{\omega} = 48.00$.

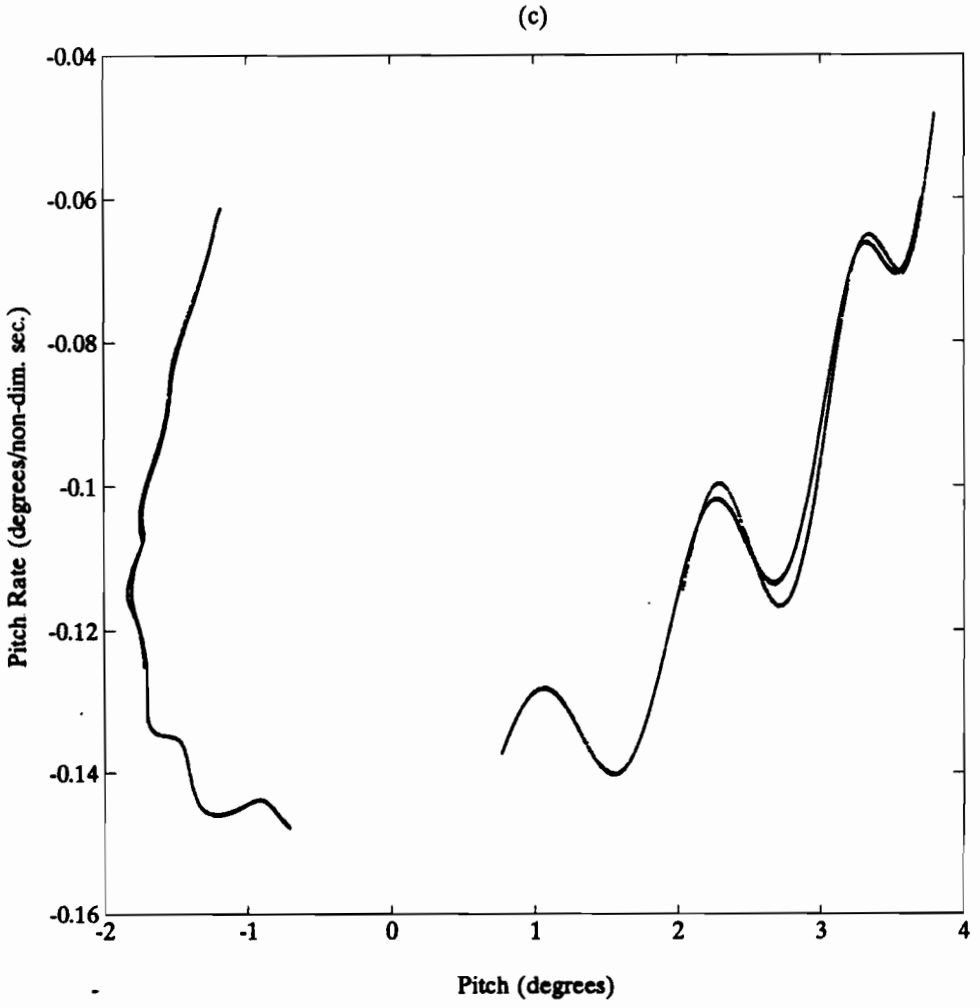
(c)
-0.04
-0.06
-0.08
-0.1
-0.12
-0.14
-0.16
Pitch Rate (degrees/non-dim. sec.)
-2
-1
0
1
2
3
4
Pitch (degrees)

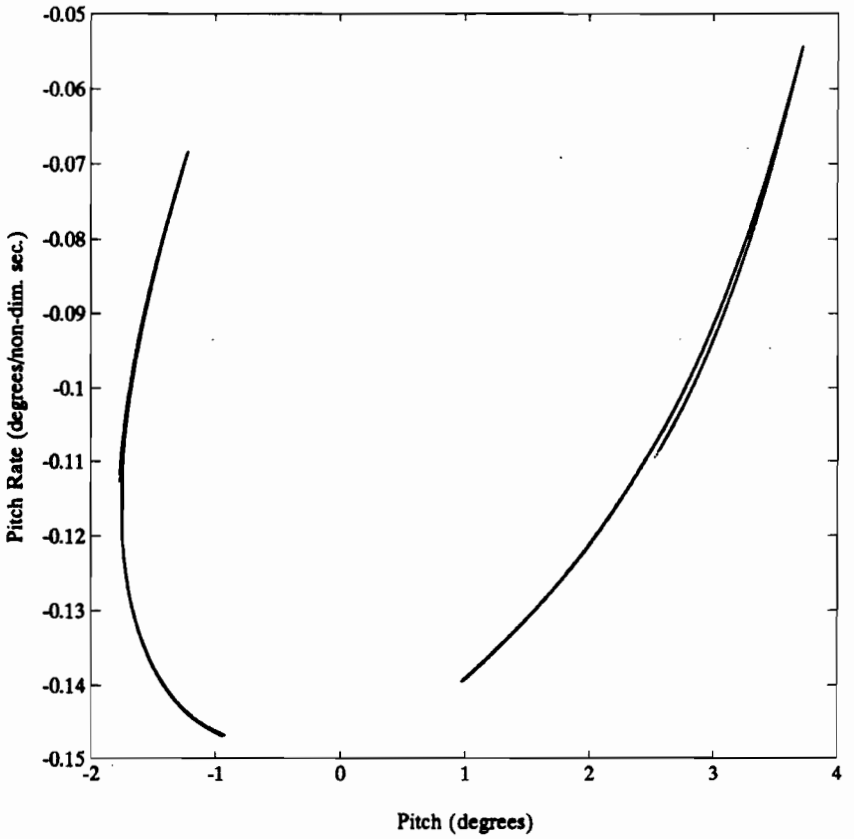

Figure 4.11: The Poincaré section of the pitch variable for the one degree of freedom system for which $\alpha_o = 9.76^o$, $Q_o = 0.70 * 10^{-4}$, $U^* = 25.20$ and $k = 0.088$.

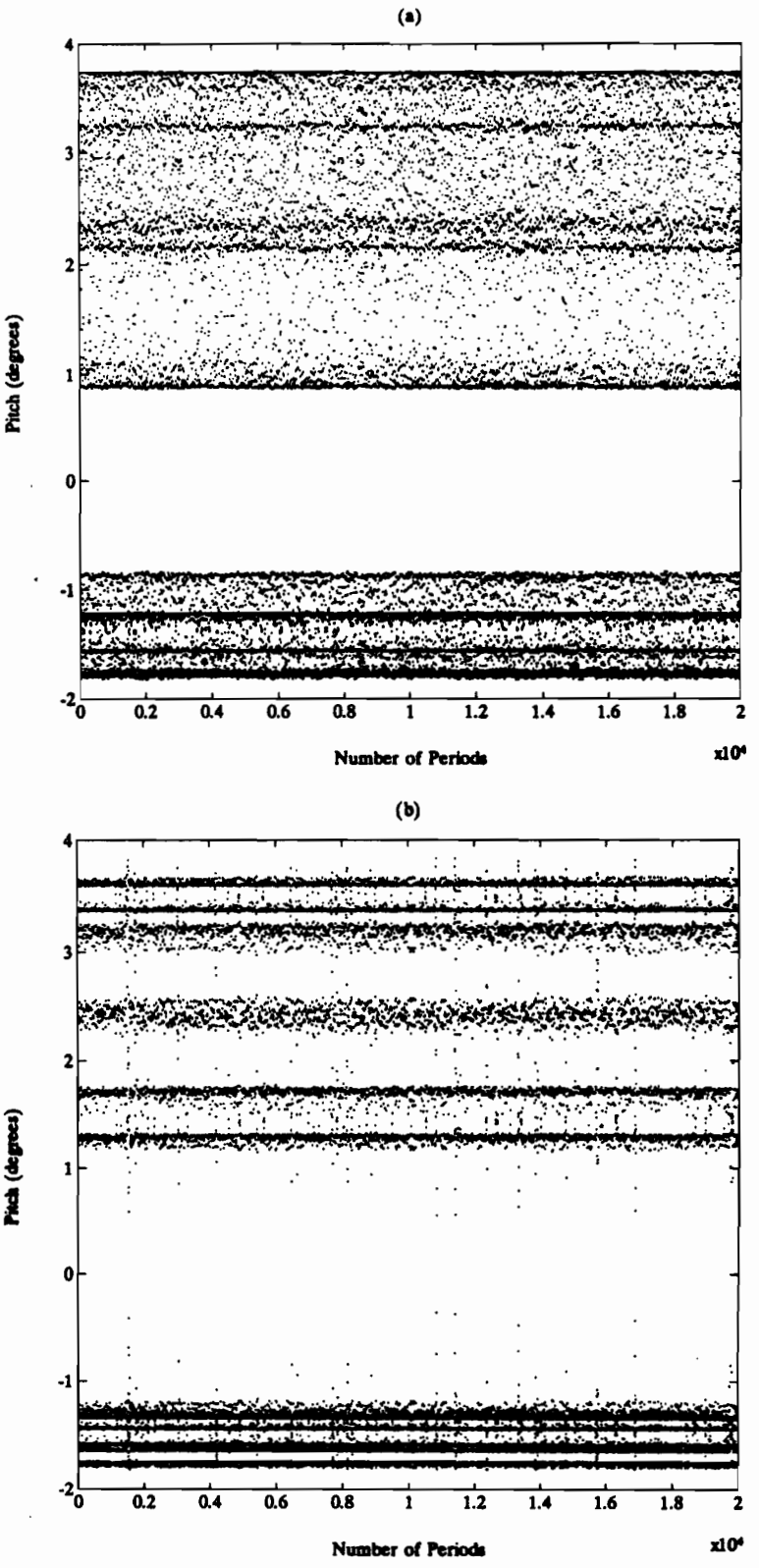

Figure 4.12: The long term behaviour of the pitch variable for the two degree of freedom cases $\alpha_o = 9.76°$, $Q_o = 0.70 * 10^{-4}$, $U^* = 25.20$, $k = 0.088$ and (a) $\bar{\omega} = 44.00$, (b) $\bar{\omega} = 46.50$ and (c) $\bar{\omega} = 48.00$.

(c)

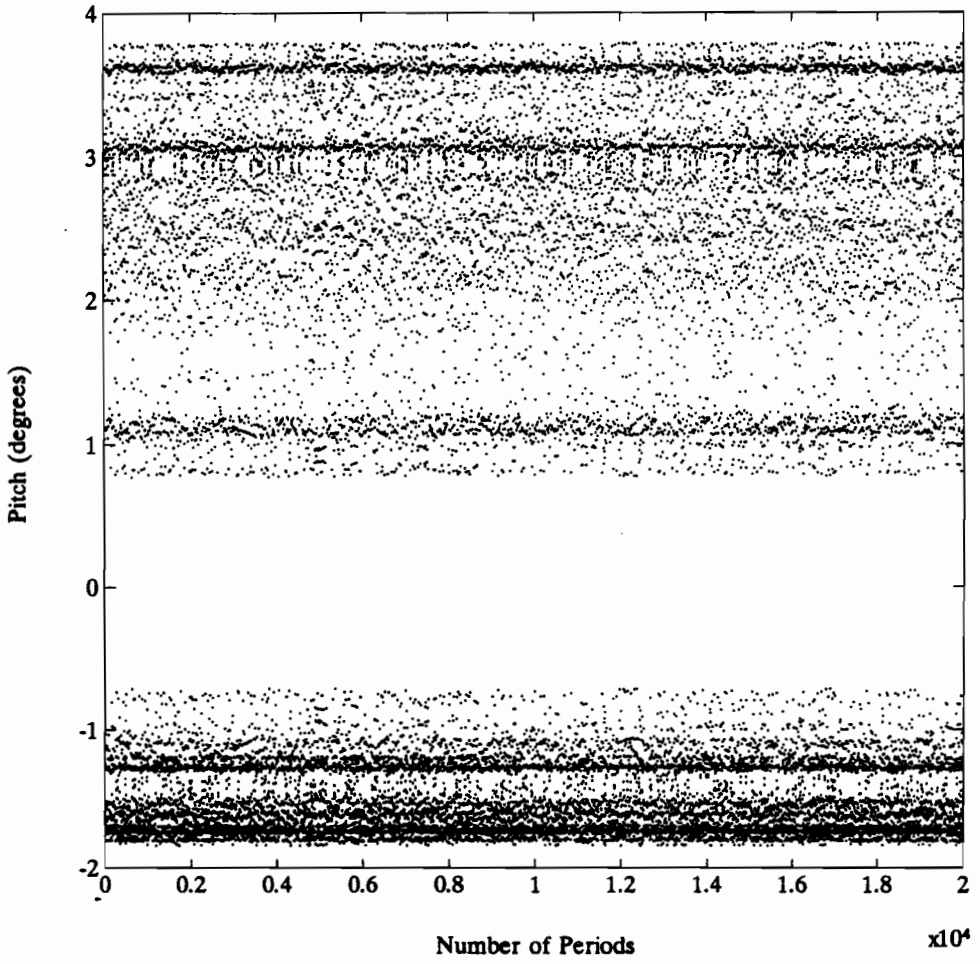
4
3
2
1
0
-1
-2
Pitch (degrees)
0
0.2
0.4
0.6
0.8
1
1.2
1.4
1.6
1.8
2
Number of Periods
x10⁴

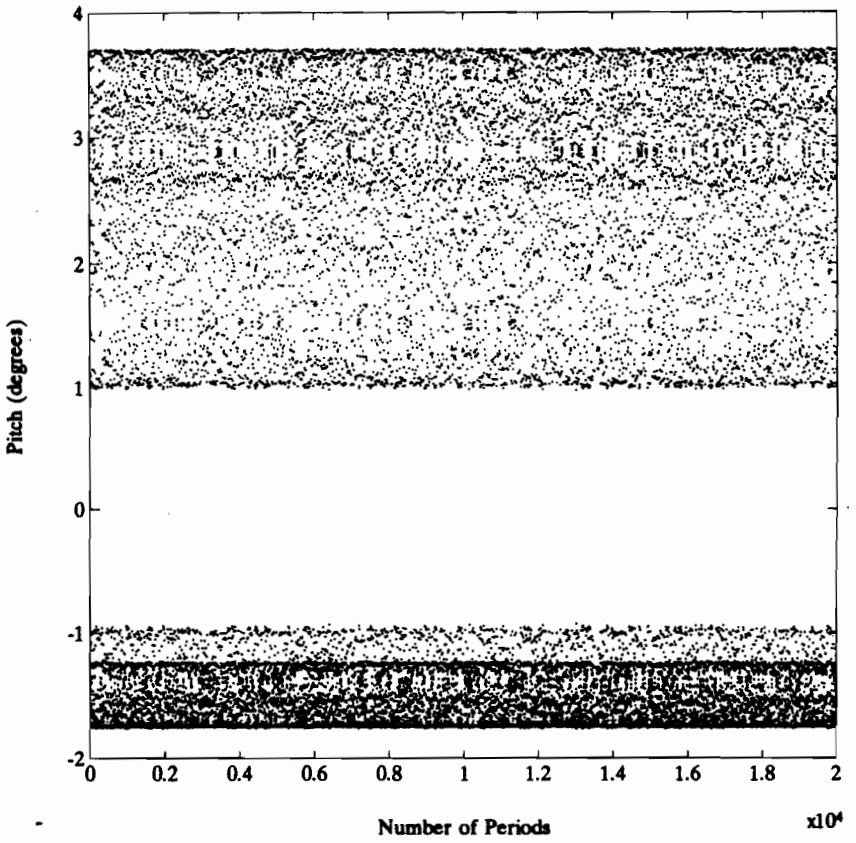

Figure 4.13: The long term behaviour of the pitch variable for the one degree of freedom system for which $\alpha_o = 9.76°$, $Q_o = 0.70 * 10^{-4}$, $U^* = 25.20$ and $k = 0.088$.

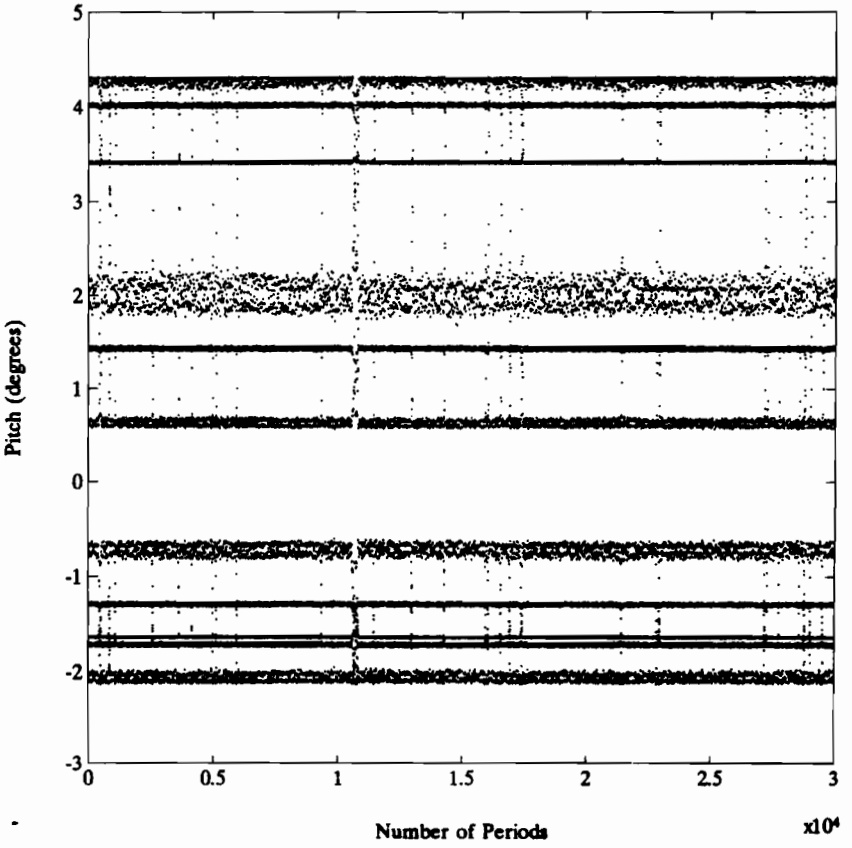

Figure 4.14: The long term behaviour of the pitch variable for the one degree of freedom system for which $\alpha_o = 9.76°$, $Q_o = 0.73 * 10^{-4}$, $U^* = 25.20$ and $k = 0.088$.

too faint !

Chapter 5

Conclusions and Recommendations

In this thesis, the dynamic response of a linear structural airfoil forced to oscillate at high angles of attack was studied. In the discussion sections, many conclusions about the dynamic behaviour of the airfoil system were made and, in this section, the most important of these conclusions are summarized and recommendations as to the direction of possible future research are given.

5.1 The Dynamic Stall Model

The Bielawa model of the dynamic stall process, discussed in Chapter 2, was developed based on windtunnel tests of airfoils constrained to oscillate in simple harmonic motion. As can be seen from the results of this model compared with experiment, shown in Appendix A, the model predicts the aerodynamic forces very well for airfoils oscillating in simple harmonic motion in pitch. However, this model has two main weaknesses that need to be addressed.

The Bielawa model of dynamic stall is based on the assumption that as an airfoil oscillates in dynamic stall a series of dynamic stall events occur in a specific order. It was found that, for an airfoil undergoing a general type of motion, these dynamic stall events do not always occur in this predetermined order. The result is that, in some cases, the dynamic stall model will predict aerodynamic forces that are discontinuous in the time domain. This problem was rectified by incorporating exponential terms into the model that make the aerodynamic loads at least piece-wise continuous in the time domain.

Another weakness of the dynamic stall model utilized herein is that it does not take into account the effect of the plunge degree of freedom on the main events of dynamic stall. Therefore, the results obtained in this thesis for the two degree of freedom airfoil system must be interpreted with this assumption in mind.

5.2 The One Degree of Freedom System

For the single degree of freedom system, discussed in Chapter 3, it was found that the nonlinearities present in the aerodynamic forces were sufficient to cause chaotic responses for several different values of the system parameters. Furthermore, the characteristics of the chaotic behaviour were found to differ substantially in some of these cases.

The first case of chaotic behaviour occurs at low values of the non-dimensional frequency and high values of the non-dimensional velocity. The type of behaviour exhibited by the system was classified as a marginally stable, chaotic response. This type of response is characterized by long periods of time in which the response is periodic, interrupted by periods of chaotic motion. The response also showed a tendency to change from one periodic state to another in a seemingly random fashion.

This marginally stable behaviour was shown to be neither type I nor type III classical intermittent chaos. However, the behaviour was defined to be intermittently chaotic because of two main characteristics: the system spends most of its time in some type of periodic oscillation, and the response can only be defined as chaotic, or unpredictable, if it is analyzed for a sufficiently long period of time.

Systems that exhibit classical intermittency can remain in a periodic oscillation for a very long period of time, but, eventually the response is interrupted by a short burst of chaotic activity and then the system returns to the original periodic oscillation. However, this system tends to remain in one type of periodic oscillation for a long period of time, until it is interrupted by a short burst of chaotic activity and then, instead of returning to its original periodic oscillation, the response changes to a new and different periodic oscillation. Furthermore, after many of these chaotic outbursts have been observed, there does not appear to be any preferred periodic state. In other words, the response wanders through a seemingly endless supply of periodic attractors.

The intermittent chaotic behaviour exhibited by this system was shown to be related to the microscopic internal structure of the chaotic attractor. The general shape of the first return map attractor was modelled by a simple set of equations and it was found that many different high-order periodic and chaotic states could be achieved by small changes in the orientation of this attractor in the phase plane. The Poincaré data of the aeroelastic system tends to be organized into a finite number of quasi-parallel groups of data points. The tendency of the Poincaré data to organize into these groups and not definite points allows the response to wander from one attractor to the next. Moreover, the orientation of these quasi-parallel groups occasionally permits the existence of marginally stable low-order periodic

oscillations. These periodic oscillations can persist for thousands of periods of the forcing function before going unstable.

There is evidence that this intermittent chaotic behaviour may be transient in nature. If the system is allowed to run for a very long time, it was shown that the response will eventually settle into a quasi-periodic oscillation. However, in general, the intermittent chaos persists for such an extremely long time (greater than thirty thousands periods of the forcing function) that it is not feasible to do an extensive analysis to determine if the intermittent chaotic behaviour is always transient.

The second case of chaotic behaviour was found to occur at much lower values of the non-dimensional velocity and at a slightly higher non-dimensional frequency than the first case. In this case, the shape of the Poincaré attractor was much more complicated than the first case but the same type of intermittent chaotic behaviour was shown to occur. It was also shown that for very small changes in the amplitude of the forcing function the response could suddenly change from stable and periodic behaviour to the intermittently chaotic behaviour discussed previously. This transition from periodic to chaotic behaviour could not always be predicted from the behaviour of the system prior to the bifurcation.

The similarities in the long term behaviour of the response shared by the first two case studies are undeniable. The intermittent chaotic behaviour was shown to exist at low values of the non-dimensional frequency for both high and low values of the non-dimensional velocity. This marginally stable long term behaviour of the system is only one type of chaotic behaviour predicted by the modified Bielawa model of dynamic stall.

The third type of chaotic behaviour for the single degree of freedom system was found to occur at relatively low non-dimensional frequencies and high non-

dimensional velocities. As the amplitude of the forcing function was increased, the response of the system was found to undergo a series of period doubling bifurcations that eventually lead to chaotic oscillations.

The period doubling route to chaos has been found to exist in many nonlinear systems; one such system is known as the Henon map. The Poincaré sections and maps that were obtained for this case study were compared qualitatively with those of the Henon map and many similarities were found to exist. Firstly, the two systems both become chaotic via the period doubling route. Secondly, the Poincaré attractors both consisted of a set of curves in the phase plane that appeared to fold back on themselves as a given system parameter was increased. Finally, the long term behaviour of both systems were found to be similar; the Poincaré data points were confined to within definite bands.

The Henon map is known to go unstable due to the infinite number of intersections of the stable and unstable manifolds of the Poincaré attractor. The intersection points of these two manifolds is called a homoclinic orbit. Further work is necessary to prove the existence of a homoclinic orbit in the aeroelastic system, but the similarities in the chaotic behaviour of this system and the Henon map suggest that the presence of a homoclinic orbit is the possible cause of the chaotic behaviour found in this particular case.

The final type of chaotic behaviour that was discussed in the single degree of freedom section was found to occur at relatively high non-dimensional frequencies and high non-dimensional velocities. The type of chaotic behaviour found in this case was shown to be more unstable than the previous cases.

A characteristic of the type of chaotic behaviour found in this case was a tendency for the amplitude of the response to suddenly increase. These outbursts of large

amplitude oscillations appear irregularly and do not last for a very long time, but, they are accompanied by sudden increases in the estimated error of the numerical scheme. This increase in the estimated error occasionally exceeded the pre-defined tolerance limit of the numerical method and the corrector iteration diverged. The divergence of the solution was found to occur even after many thousands of cycles of motion for which the numerical scheme converged. Further work is required to determine if the divergence of the response is a property of this type of chaotic behaviour or if it is due to the numerical procedure.

5.3 The Two Degree of Freedom System

The second degree of freedom, plunge motion, was added to the system with the assumptions that the motion must be small compared to the pitch motion and that the effect of the plunge motion on the main events of dynamic stall are small enough to be ignored. These assumptions, if correct, permit the use of linear aerodynamic theory to calculate the aerodynamic forces due to the plunge motion. Since the plunge degree of freedom was added as a linear approximation, the scope of the investigation of the two degree of freedom system was limited to a discussion of the effect of the plunge motion on the chaotic dynamics of the single degree of freedom system.

When the system parameters are set to values that cause the response of the single degree of freedom system to be chaotic, the stability of the response can be strongly influenced by the addition of a very small amount of plunge motion. The stability of the response was also found to be very dependent on the ratio of the natural frequencies in pitch and plunge. A small change in this ratio can change the response of the system from periodic to chaotic oscillations or vice-versa.

The sensitivity of the response of the system to the addition of small amplitude plunge motion and changes in the ratio of natural frequencies suggests that the assumption of small, linear effects of the plunge motion on the aerodynamic forces may not be valid. Further research into the two degree of freedom airfoil system with nonlinear aerodynamic forces requires a model of dynamic stall that explicitly incorporates the effect of plunge motion on the main events of dynamic stall and the unsteady aerodynamic forces.

Bibliography

[Abbott and von Doenhoff, 1959] Abbott, I.H., von Doenhoff, A.E., "Theory of Wing Sections, Including a Summary of Airfoil Data", Dover Publications, 1959.

[Bergé et al., 1986] Bergé, P., Pomeau, Y., Vidal, C., "Order Within Chaos", John Wiley and Sons, 1986.

[Bielawa et al., 1983] Bielawa, R.L., Johnson, S.A., Chi, R.M., Gangawani, S.T., "Aeroelastic Analysis for Propellers", *NASA Contractor Report 3729*, 1983.

[Bisplinghoff et al., 1957] Bisplinghoff, R.L., Ashley, H., Halfman, R.L., "Aeroelasticity", Addison-Wesley, 1957.

[Ericsson and Reding, 1988a] Ericsson, L.E., Reding J.P., "Fluid Mechanics of Dynamic Stall Part I. Unsteady Flow Concepts", *Journal of Fluids and Structures*, **Vol. 2**, pp. 1 to 33, 1988a.

[Ericsson and Reding, 1988b] Ericsson, L.E., Reding J.P., "Fluid Mechanics of Dynamic Stall Part II. Prediction of Full Scale

Characteristics", *Journal of Fluids and Structures*, **Vol. 2**, pp. 113 to 143, 1988b.

[Fung, 1955] Fung, Y.C., "An Introduction to the Theory of Aeroelasticity", John Wiley and Sons, 1955.

[Gray and Liiva, 1968] Gray, L., Liiva, J., "Two Dimensional Tests of Airfoils Oscillating Near Stall", *USAAVLABS Technical Report 68-13B*, **Vol. 11**, 1968.

[Houbolt, 1950] Houbolt, J.C., "A Recurrence Matrix Solution for the Dynamic Response of Elastic Aircraft", *Journal of Aeronautical Sciences*, **Vol. 17**, pp. 540 to 550, 1950.

[Lee and LeBlanc, 1986a] Lee, B.H.K., LeBlanc, P., "Flutter Analysis of a Two-Dimensional Airfoil with Cubic Non-Linear Restoring Force", National Research Council Canada, NAE-AN-36, 1986a.

[Lee and LeBlanc, 1986b] Lee, B.H.K., LeBlanc, P., "Forced Oscillation of a Two-Dimensional Airfoil with Nonlinear Aerodynamic Loads", National Research Council Canada, LR-617, 1986b.

[Mazelsky, 1952] Mazelsky, B., "Numerical Determination of Indicial Lift and Moment Functions for a Two-Dimensional Pitching Airfoil at Subsonic Mach Numbers from Oscillatory Coefficients with

Numerical Calculations for a Mach Number of 0.7", *NACA Technical Note 2739*, 1952.

[Mazelsky and Drischler, 1952] Mazelsky, B., Drischler, J.A., "Numerical Determination of Indicial Lift and Moment Functions for a Two-Dimensional Sinking and Pitching Airfoil at Mach Numbers 0.5 and 0.6", *NACA Technical Note 2739*, 1952.

[Moon, 1987] Moon, F.C., "Chaotic Vibrations, An Introduction for Applied Scientists and Engineers", John Wiley and Sons, 1987.

[Press et al., 1986] Press, W.H., Flannery, B.P., Teukolsky, S.A., Vetterling, W.T., "Numerical Recipes, The Art of Scientific Computing", Cambridge University Press, 1986.

[Price et al., 1993] Price, S.J., Alighanbari, H., Lee, B., "An Analysis of the Post-Instability Behaviour of a Two-Dimensional Airfoil with a Structural Nonlinearity", *34th AIAA/ASME/ASCE/AHS/ASC Structures, Structural Dynamics and Materials Conference*, 1993.

[Tang and Dowell, 1992] Tang, D.M., Dowell, E.H., "Flutter and Stall Response of a Helicopter Blade with Structural

Nonlinearity", *Journal of Aircraft*, **Vol. 29**, No. 5, 1992.

[Thompson and Stewart, 1986] Thompson J.M.T., Stewart, H.B., "Nonlinear Dynamics and Chaos", John Wiley and Sons, 1986.

[Tran and Falchero, 1982] Tran, C.T., Falchero, D., "Application of the ONERA Dynamic Stall Model to a Helicopter Blade in Forward Flight", *Vertica*, **Vol. 6**, pp. 219 to 239, 1982.

[Tran and Petot, 1981] Tran, C.T., Petot, D., "Semi-Empirical Model for the Dynamic Stall of Airfoils in View of the Application to the Calculation of Responses of a Helicopter Blade in Forward Flight", *Vertica*, **Vol. 5**, pp. 35 to 53, 1981.

Appendix A

Coefficients of the Dynamic Stall Model

In this Appendix, the coefficients of the dynamic stall model are listed.

The coefficients of the dynamic stall model are:

$$P_1 = 10.593687777057760;\ P_2 = 10.832854524817120;\ P_3 = -0.018632566823462;$$

$$P_4 = -1.367529319089629;\ P_5 = -4.164299690698649;\ P_6 = -0.184990006133694;$$

$$P_7 = 0.051047607973315;\ P_8 = 0.382202466218984;\ P_9 = 2.669455333726313;$$

$$P_{10} = -1.743978009850223$$

$$Q_1 = -1.757201145145348;\ Q_2 = -0.082550541677624;\ Q_3 = 0.006018886629636;$$

$$Q_4 = -0.062061284628051;\ Q_5 = 0.048939583548136;\ Q_6 = -0.777320074011365;$$

$$Q_7 = -5.964050461851018$$

$$\beta_1 = 0.18;\ C_{AR} = 16.6502;\ C_{AM} = 54.9273;\ C_{WM} = 10.5179;\ C_{WR} = -8.6689;$$

$$C_{AT} = 5.4204;\ C_{\alpha T} = 0.4884;\ \epsilon = -0.0139;$$

Appendix B

Comparison of the Modified Bielawa Model with Experiment

This Appendix contains graphical comparisons of the lift and moment coefficients predicted by the modified Bielawa dynamic stall model with the experimental lift and moment coefficients obtained by Gray, L. and Liiva, J. (1968) for the NACA 0012 airfoil. The lift coefficient data is given first followed by the moment coefficient data.

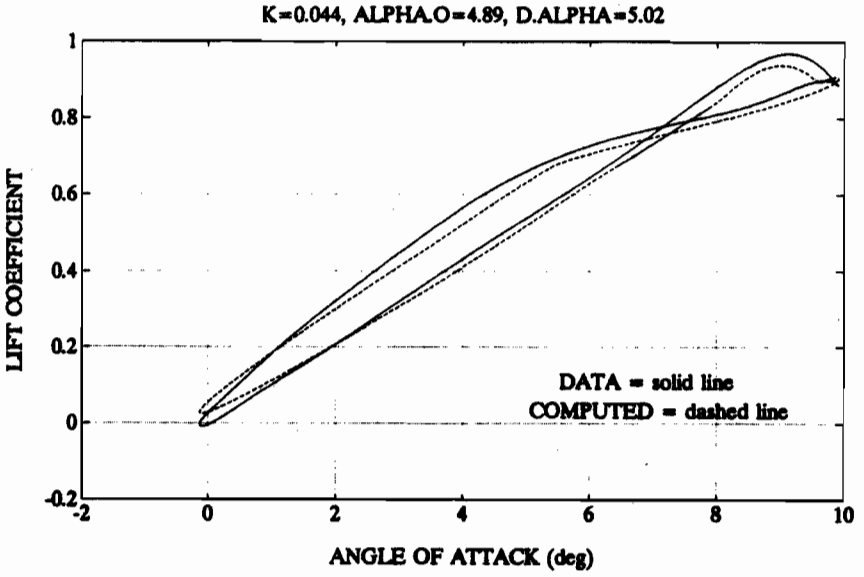
K=0.044, ALPHA.O=4.89, D.ALPHA=5.02
LIFT COEFFICIENT
ANGLE OF ATTACK (deg)
DATA = solid line
COMPUTED = dashed line
1
0.8
0.6
0.4
0.2
0
-0.2
-2
0
2
4
6
8
10

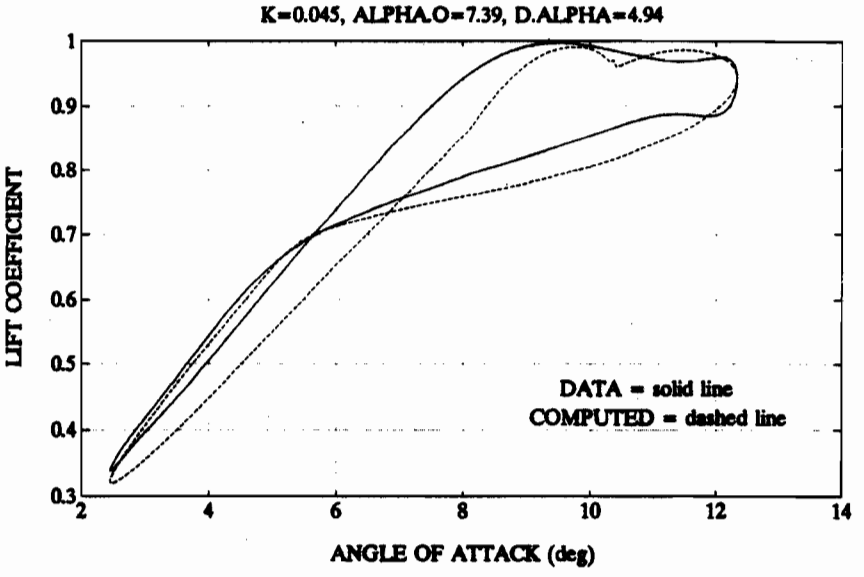
K=0.045, ALPHA.O=7.39, D.ALPHA=4.94
LIFT COEFFICIENT
ANGLE OF ATTACK (deg)
DATA = solid line
COMPUTED = dashed line
1
0.9
0.8
0.7
0.6
0.5
0.4
0.3
2
4
6
8
10
12
14

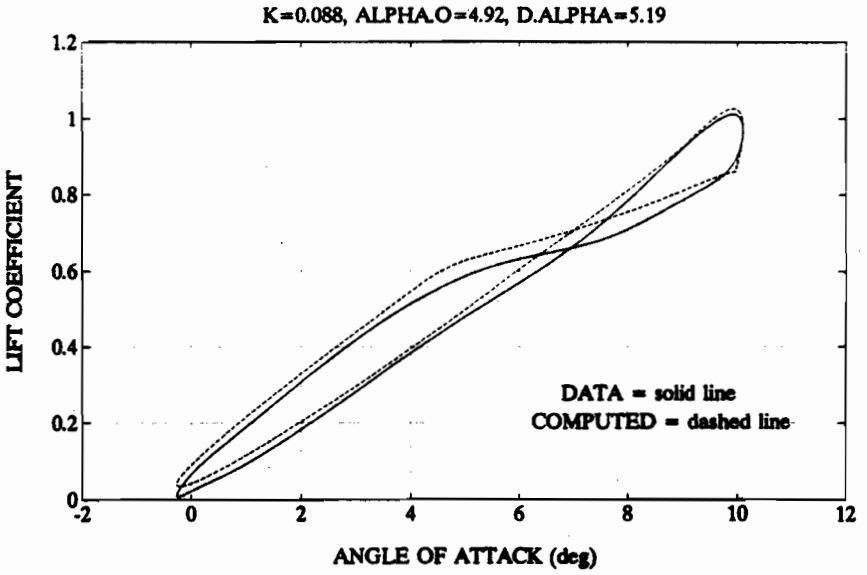
K=0.088, ALPHA.O=4.92, D.ALPHA=5.19
LIFT COEFFICIENT
ANGLE OF ATTACK (deg)
DATA = solid line
COMPUTED = dashed line
1.2
1
0.8
0.6
0.4
0.2
0
-2
0
2
4
6
8
10
12

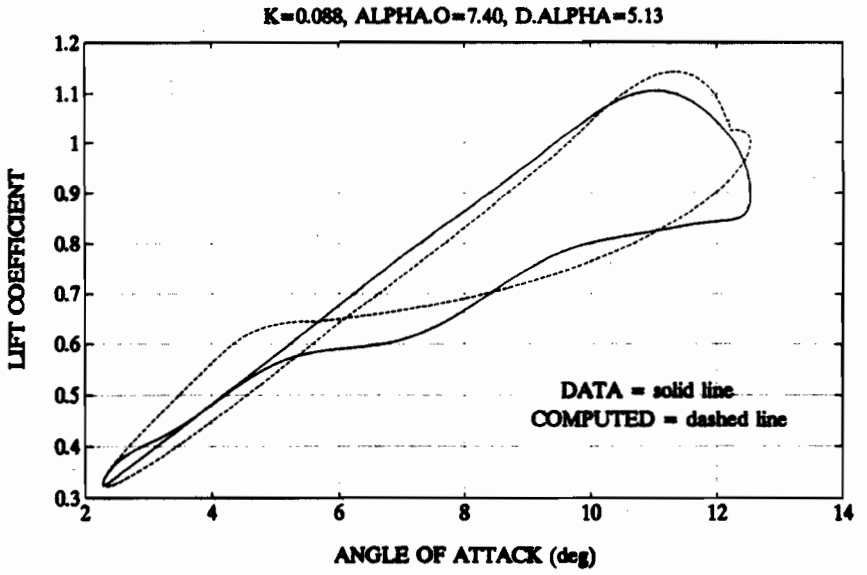
K=0.088, ALPHA.O=7.40, D.ALPHA=5.13
LIFT COEFFICIENT
ANGLE OF ATTACK (deg)
DATA = solid line
COMPUTED = dashed line
1.2
1.1
1
0.9
0.8
0.7
0.6
0.5
0.4
0.3
2
4
6
8
10
12
14

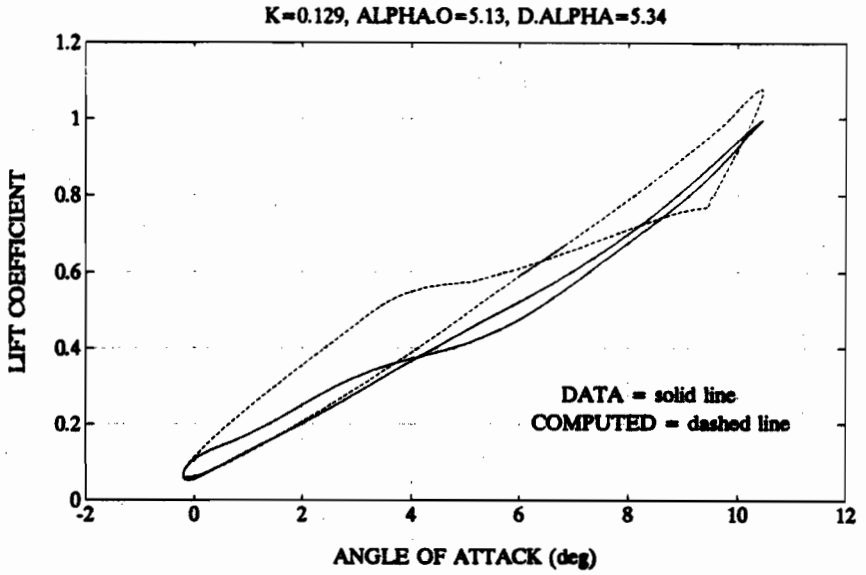
K=0.129, ALPHA.O=5.13, D.ALPHA=5.34
LIFT COEFFICIENT
ANGLE OF ATTACK (deg)
DATA = solid line
COMPUTED = dashed line
1.2
1
0.8
0.6
0.4
0.2
0
-2
0
2
4
6
8
10
12

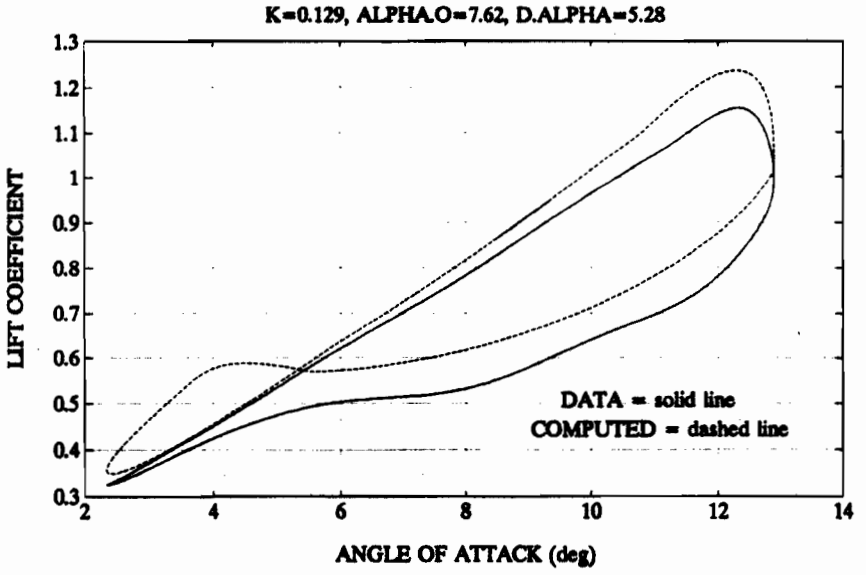
K=0.129, ALPHA.O=7.62, D.ALPHA=5.28
LIFT COEFFICIENT
ANGLE OF ATTACK (deg)
DATA = solid line
COMPUTED = dashed line
1.3
1.2
1.1
1
0.9
0.8
0.7
0.6
0.5
0.4
0.3
2
4
6
8
10
12
14

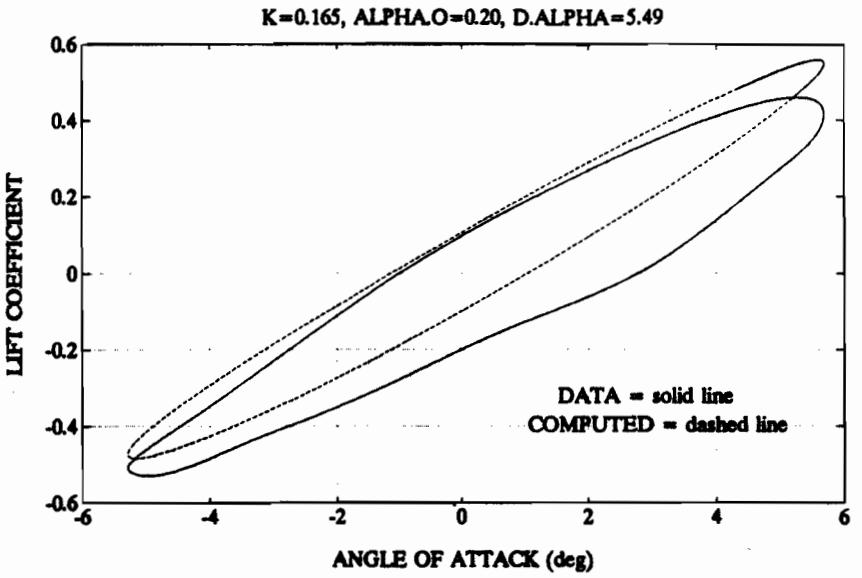
K=0.165, ALPHA.O=0.20, D.ALPHA=5.49
LIFT COEFFICIENT
ANGLE OF ATTACK (deg)
DATA = solid line
COMPUTED = dashed line
0.6
0.4
0.2
0
-0.2
-0.4
-0.6
-6
-4
-2
0
2
4
6

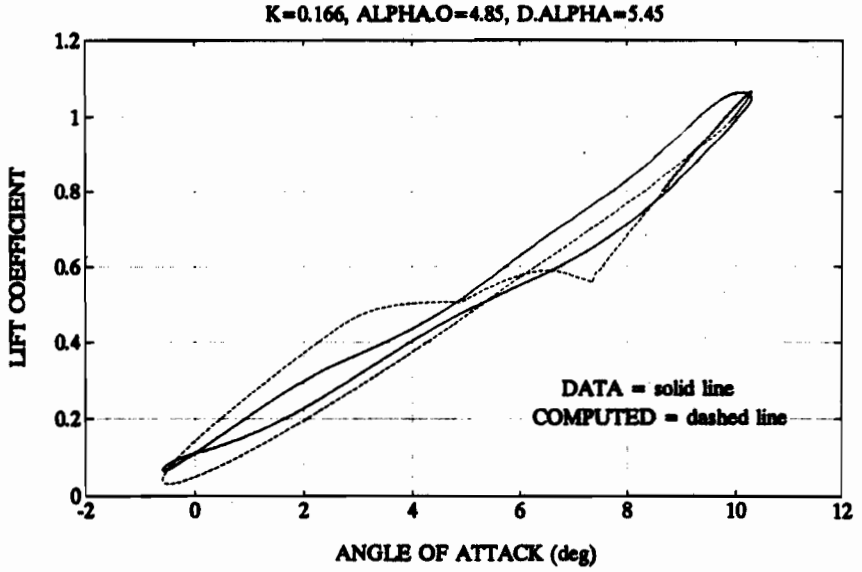
K=0.166, ALPHA.O=4.85, D.ALPHA=5.45
LIFT COEFFICIENT
ANGLE OF ATTACK (deg)
DATA = solid line
COMPUTED = dashed line
1.2
1
0.8
0.6
0.4
0.2
0
-2
0
2
4
6
8
10
12

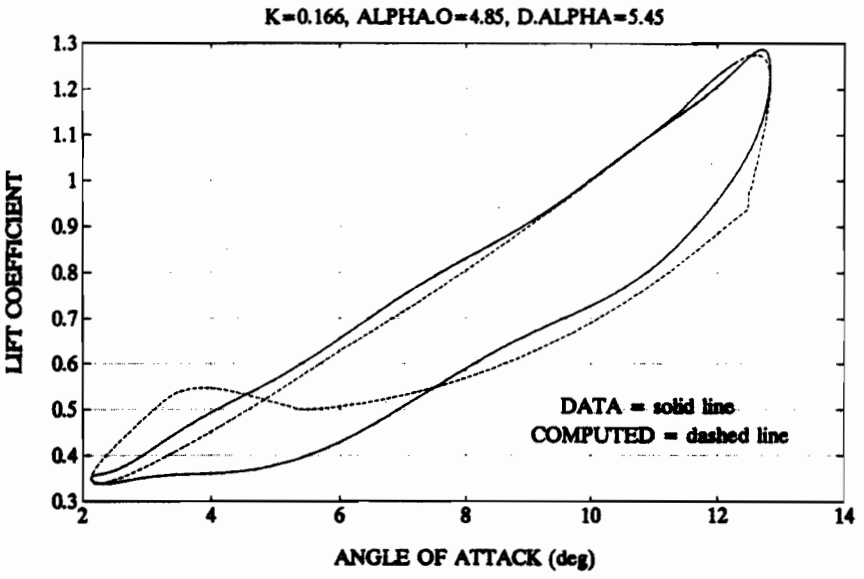
K=0.166, ALPHA.O=4.85, D.ALPHA=5.45
LIFT COEFFICIENT
ANGLE OF ATTACK (deg)
DATA = solid line
COMPUTED = dashed line
1.3
1.2
1.1
1
0.9
0.8
0.7
0.6
0.5
0.4
0.3
2
4
6
8
10
12
14

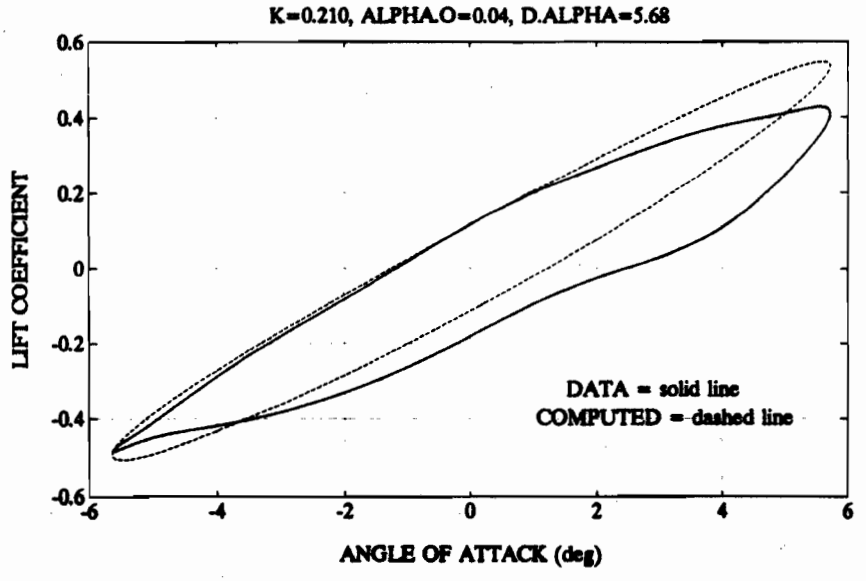
K=0.210, ALPHA.O=0.04, D.ALPHA=5.68
LIFT COEFFICIENT
ANGLE OF ATTACK (deg)
DATA = solid line
COMPUTED = dashed line
0.6
0.4
0.2
0
-0.2
-0.4
-0.6
-6
-4
-2
0
2
4
6

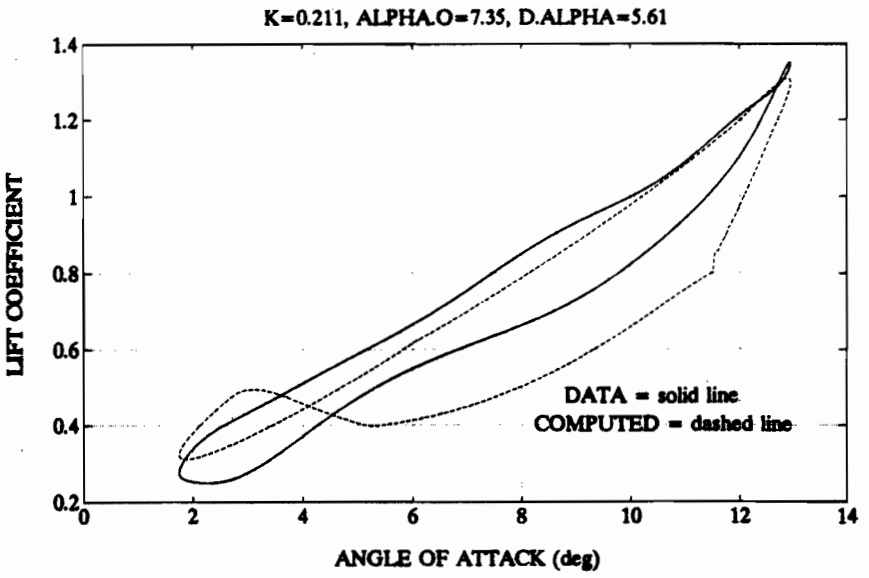
K=0.211, ALPHA.O=7.35, D.ALPHA=5.61
LIFT COEFFICIENT
ANGLE OF ATTACK (deg)
DATA = solid line
COMPUTED = dashed line
1.4
1.2
1
0.8
0.6
0.4
0.2
0
2
4
6
8
10
12
14

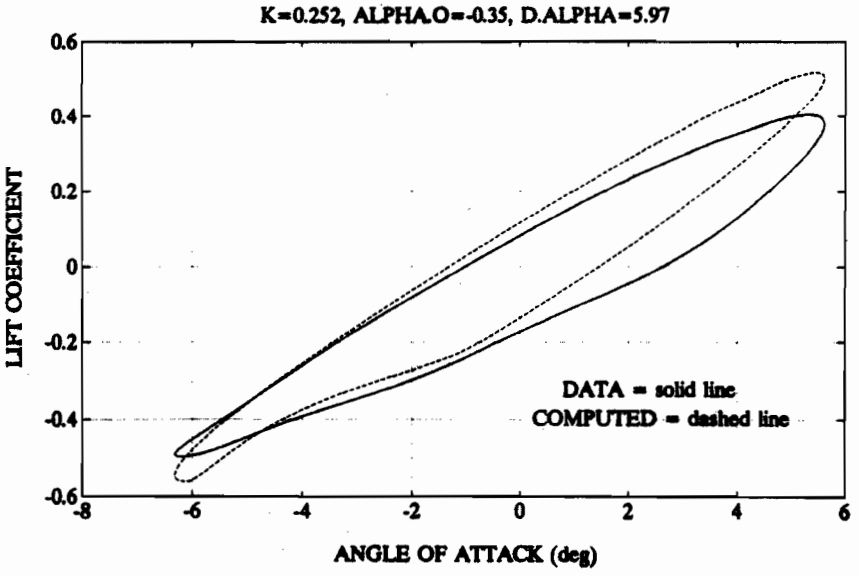
K=0.252, ALPHA.O=-0.35, D.ALPHA=5.97
LIFT COEFFICIENT
ANGLE OF ATTACK (deg)
DATA = solid line
COMPUTED = dashed line
0.6
0.4
0.2
0
-0.2
-0.4
-0.6
-8
-6
-4
-2
0
2
4
6

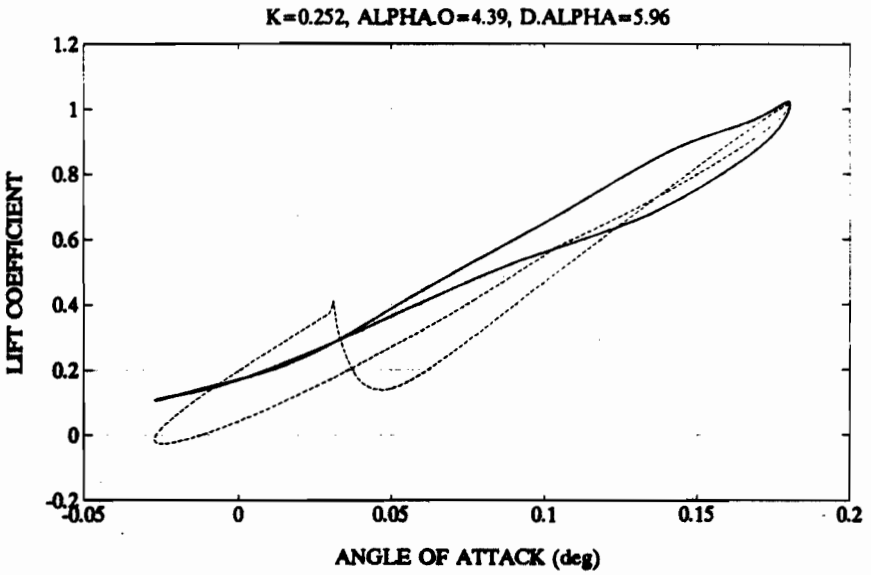
K=0.252, ALPHA.O=4.39, D.ALPHA=5.96
LIFT COEFFICIENT
1.2
1
0.8
0.6
0.4
0.2
0
-0.2
-0.05
0
0.05
0.1
0.15
0.2
ANGLE OF ATTACK (deg)

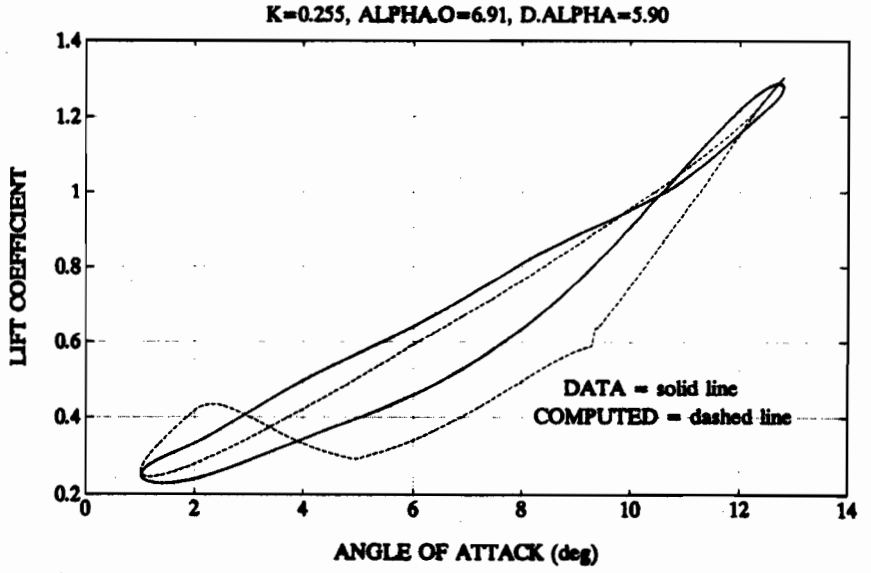
K=0.255, ALPHA.O=6.91, D.ALPHA=5.90
LIFT COEFFICIENT
1.4
1.2
1
0.8
0.6
0.4
0.2
0
2
4
6
8
10
12
14
DATA = solid line
COMPUTED = dashed line
ANGLE OF ATTACK (deg)

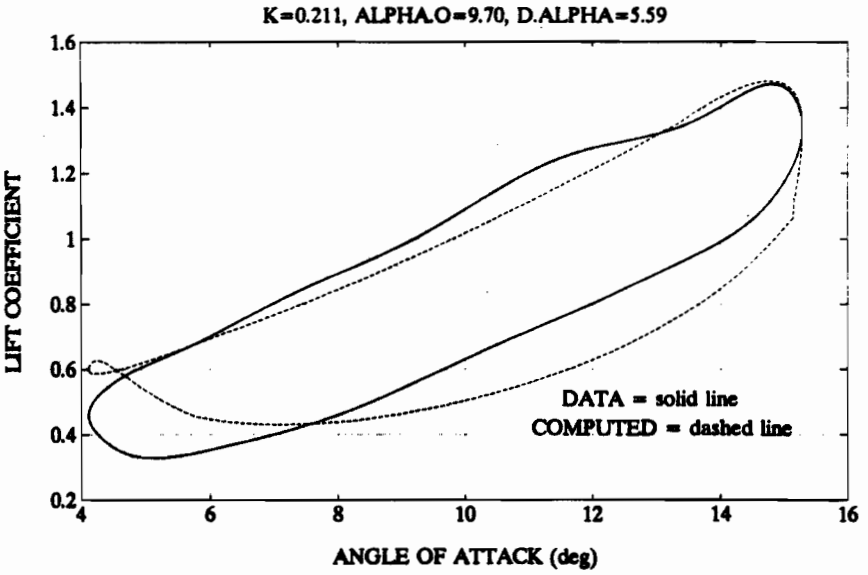
K=0.211, ALPHA.O=9.70, D.ALPHA=5.59
LIFT COEFFICIENT
1.6
1.4
1.2
1
0.8
0.6
0.4
0.2
4
6
8
10
12
14
16
ANGLE OF ATTACK (deg)
DATA = solid line
COMPUTED = dashed line

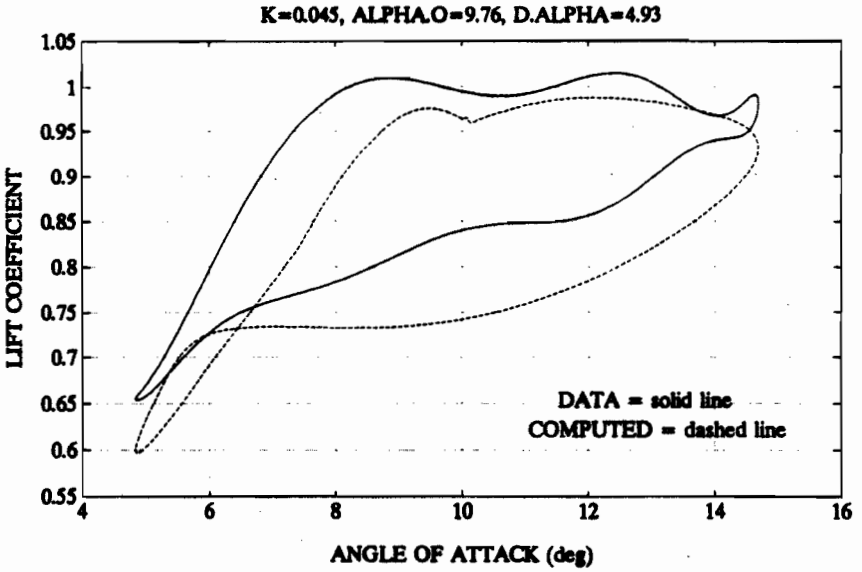
K=0.045, ALPHA.O=9.76, D.ALPHA=4.93
LIFT COEFFICIENT
1.05
1
0.95
0.9
0.85
0.8
0.75
0.7
0.65
0.6
0.55
4
6
8
10
12
14
16
ANGLE OF ATTACK (deg)
DATA = solid line
COMPUTED = dashed line

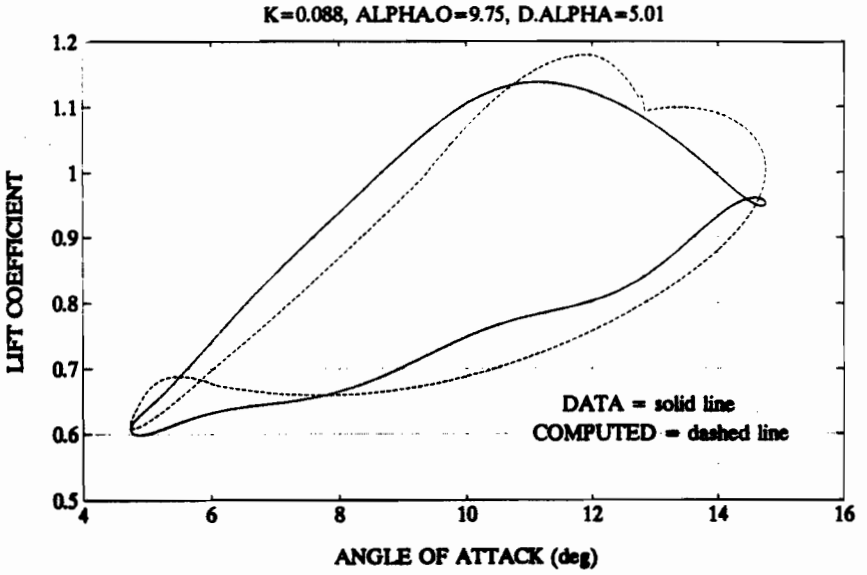
K=0.088, ALPHA.O=9.75, D.ALPHA=5.01
LIFT COEFFICIENT
ANGLE OF ATTACK (deg)
DATA = solid line
COMPUTED = dashed line
1.2
1.1
1
0.9
0.8
0.7
0.6
0.5
4
6
8
10
12
14
16

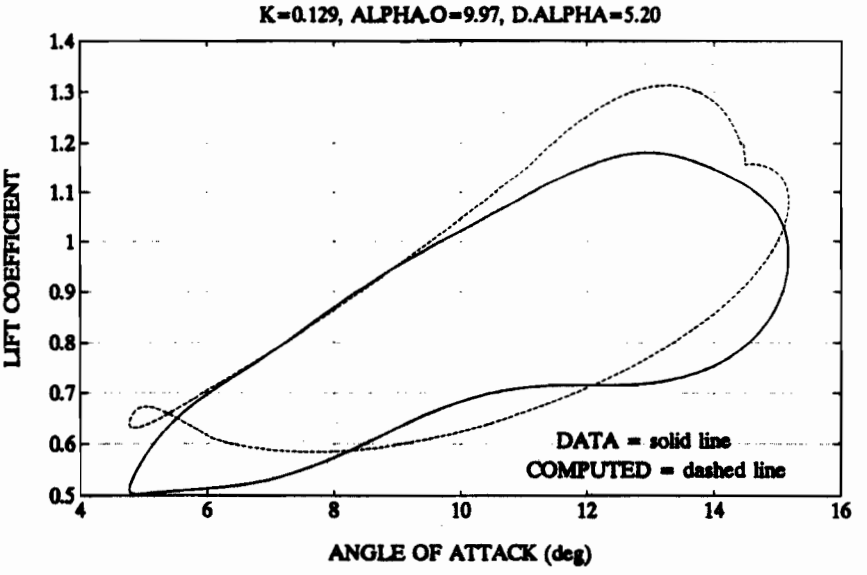
K=0.129, ALPHA.O=9.97, D.ALPHA=5.20
LIFT COEFFICIENT
ANGLE OF ATTACK (deg)
DATA = solid line
COMPUTED = dashed line
1.4
1.3
1.2
1.1
1
0.9
0.8
0.7
0.6
0.5
4
6
8
10
12
14
16

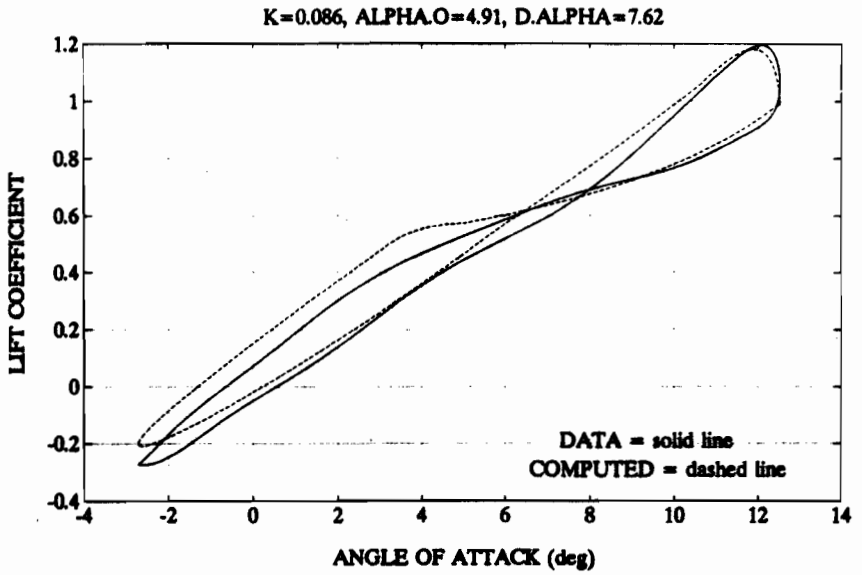
K=0.086, ALPHA.O=4.91, D.ALPHA=7.62
LIFT COEFFICIENT
ANGLE OF ATTACK (deg)
DATA = solid line
COMPUTED = dashed line
1.2
1
0.8
0.6
0.4
0.2
0
-0.2
-0.4
-4
-2
0
2
4
6
8
10
12
14

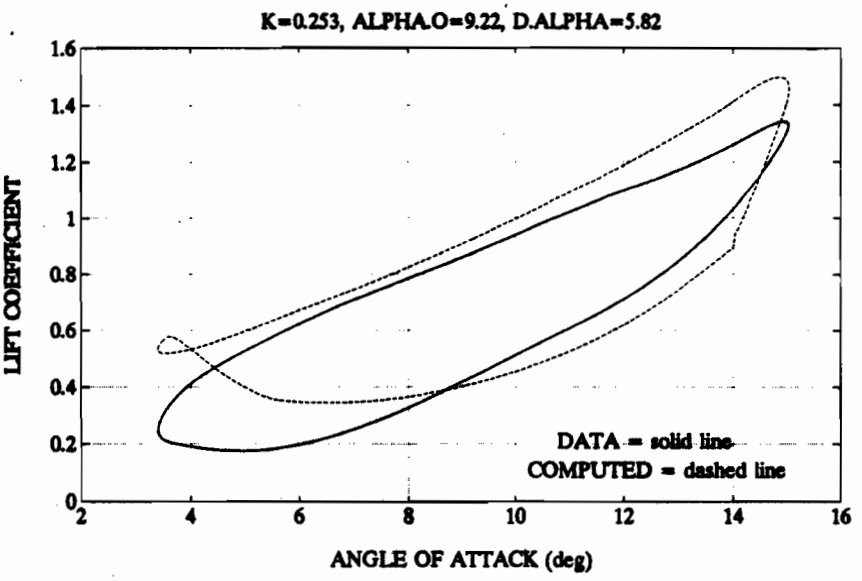
K=0.253, ALPHA.O=9.22, D.ALPHA=5.82
LIFT COEFFICIENT
ANGLE OF ATTACK (deg)
DATA = solid line
COMPUTED = dashed line
1.6
1.4
1.2
1
0.8
0.6
0.4
0.2
0
2
4
6
8
10
12
14
16

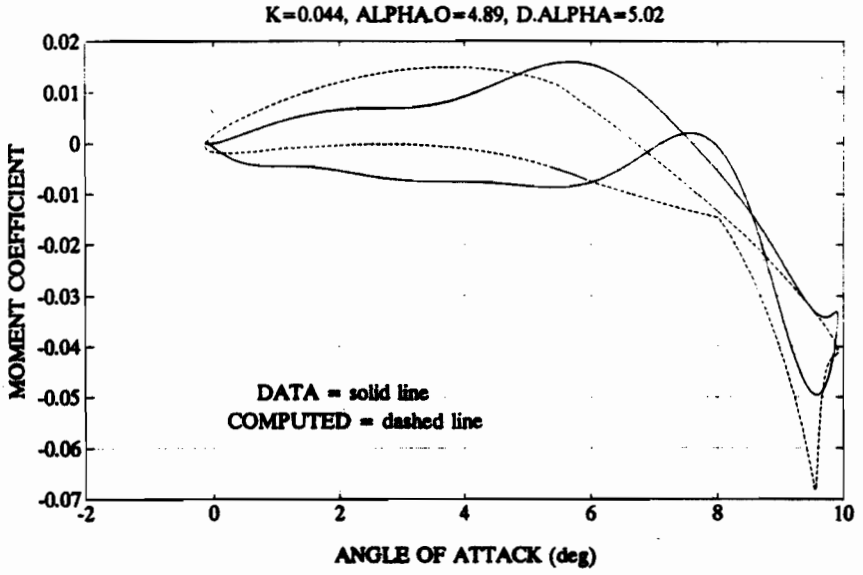
K=0.044, ALPHA.O=4.89, D.ALPHA=5.02
MOMENT COEFFICIENT
0.02
0.01
0
-0.01
-0.02
-0.03
-0.04
-0.05
-0.06
-0.07
DATA = solid line
COMPUTED = dashed line
-2
0
2
4
6
8
10
ANGLE OF ATTACK (deg)

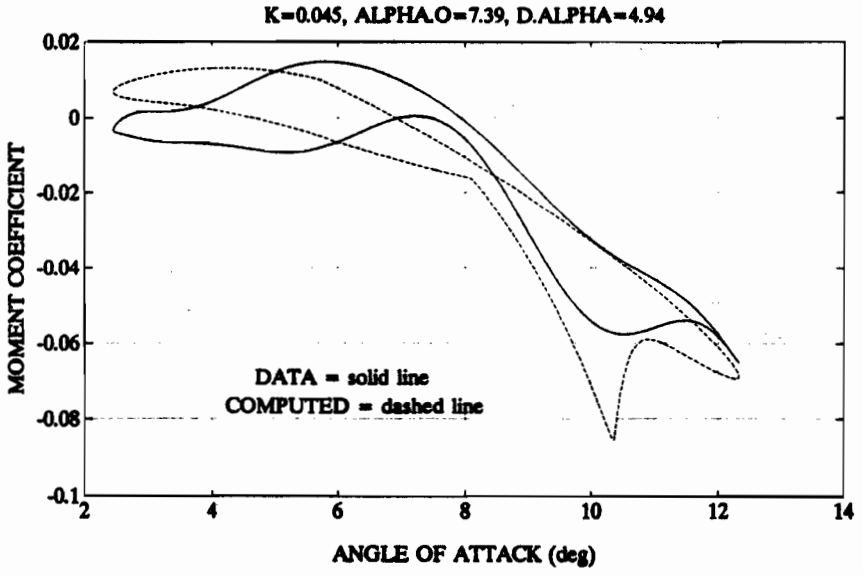
K=0.045, ALPHA.O=7.39, D.ALPHA=4.94
MOMENT COEFFICIENT
0.02
0
-0.02
-0.04
-0.06
-0.08
-0.1
DATA = solid line
COMPUTED = dashed line
2
4
6
8
10
12
14
ANGLE OF ATTACK (deg)

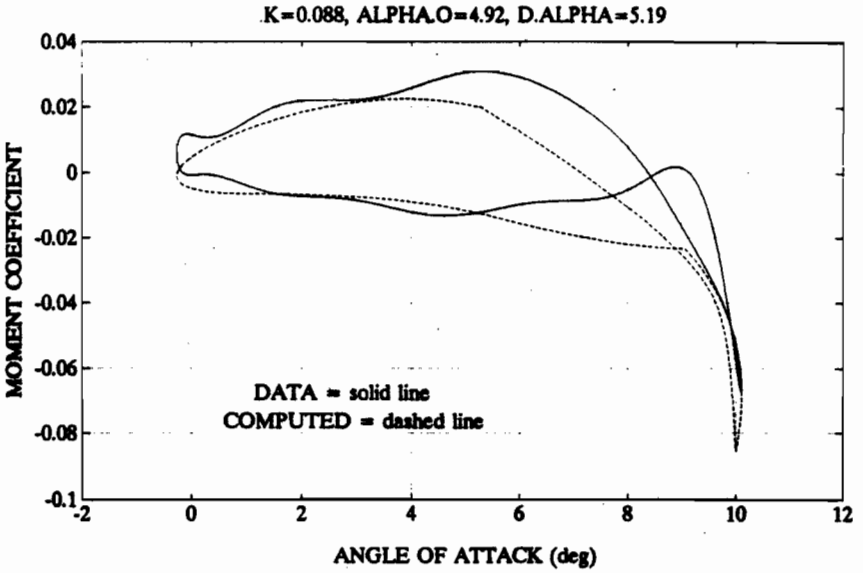
K=0.088, ALPHA.O=4.92, D.ALPHA=5.19
MOMENT COEFFICIENT
0.04
0.02
0
-0.02
-0.04
-0.06
-0.08
-0.1
-2
0
2
4
6
8
10
12
DATA = solid line
COMPUTED = dashed line
ANGLE OF ATTACK (deg)

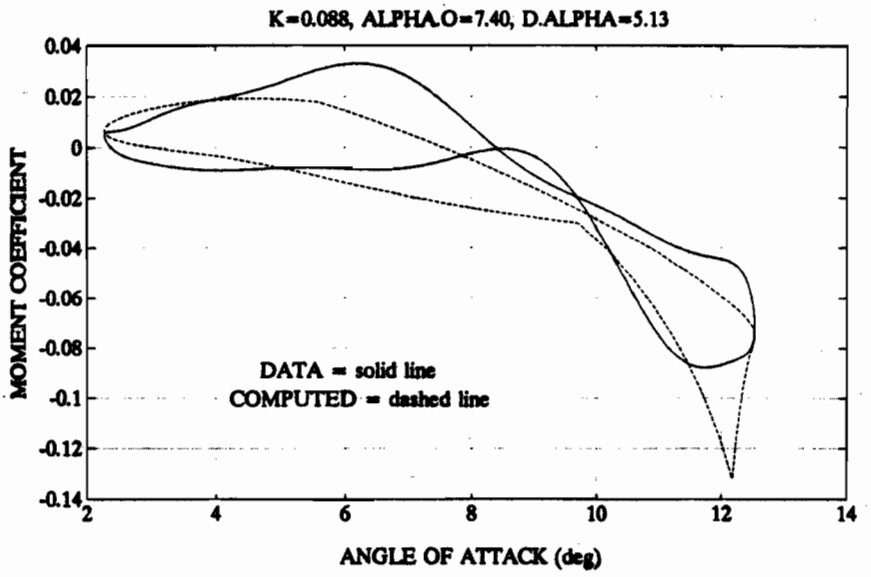
K=0.088, ALPHA.O=7.40, D.ALPHA=5.13
MOMENT COEFFICIENT
0.04
0.02
0
-0.02
-0.04
-0.06
-0.08
-0.1
-0.12
-0.14
2
4
6
8
10
12
14
DATA = solid line
COMPUTED = dashed line
ANGLE OF ATTACK (deg)

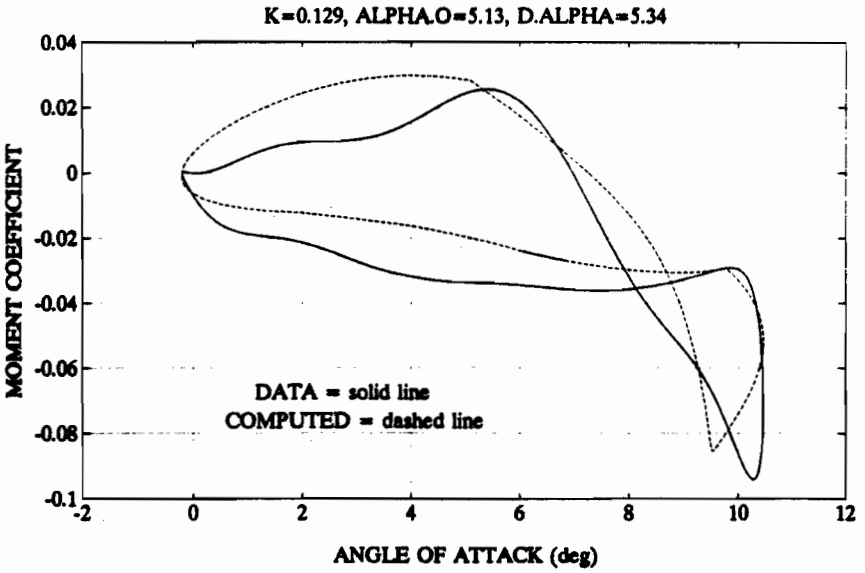
K=0.129, ALPHA.O=5.13, D.ALPHA=5.34
MOMENT COEFFICIENT
0.04
0.02
0
-0.02
-0.04
-0.06
-0.08
-0.1
-2
0
2
4
6
8
10
12
DATA = solid line
COMPUTED = dashed line
ANGLE OF ATTACK (deg)

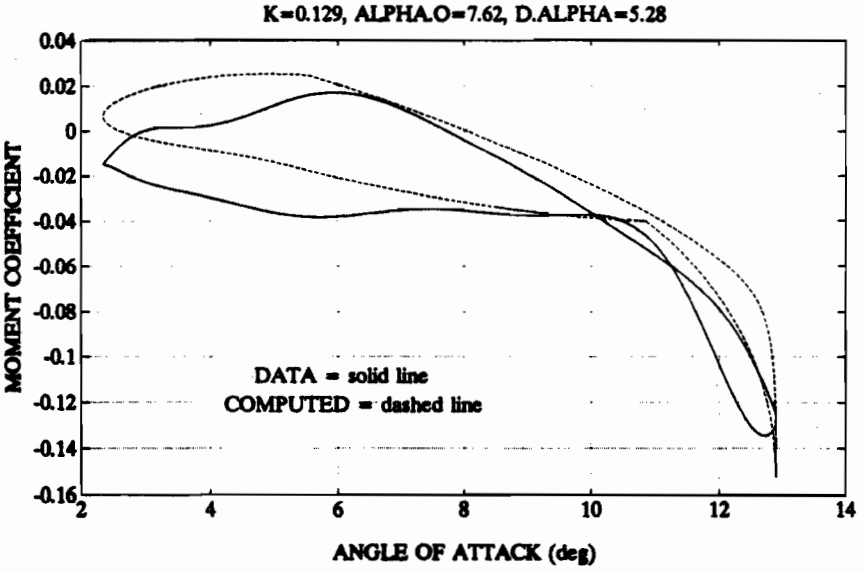
K=0.129, ALPHA.O=7.62, D.ALPHA=5.28
MOMENT COEFFICIENT
0.04
0.02
0
-0.02
-0.04
-0.06
-0.08
-0.1
-0.12
-0.14
-0.16
2
4
6
8
10
12
14
DATA = solid line
COMPUTED = dashed line
ANGLE OF ATTACK (deg)

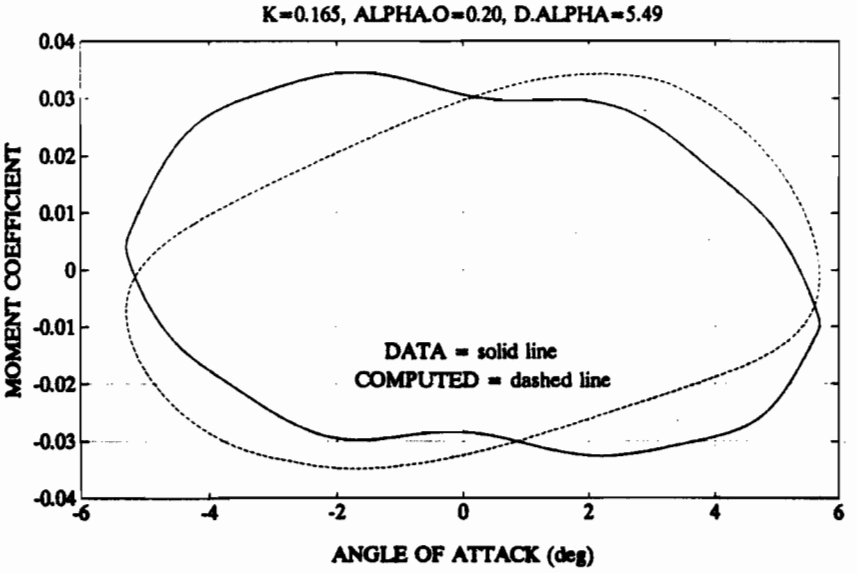
K=0.165, ALPHA.O=0.20, D.ALPHA=5.49
MOMENT COEFFICIENT
ANGLE OF ATTACK (deg)
DATA = solid line
COMPUTED = dashed line
0.04
0.03
0.02
0.01
0
-0.01
-0.02
-0.03
-0.04
-6
-4
-2
0
2
4
6

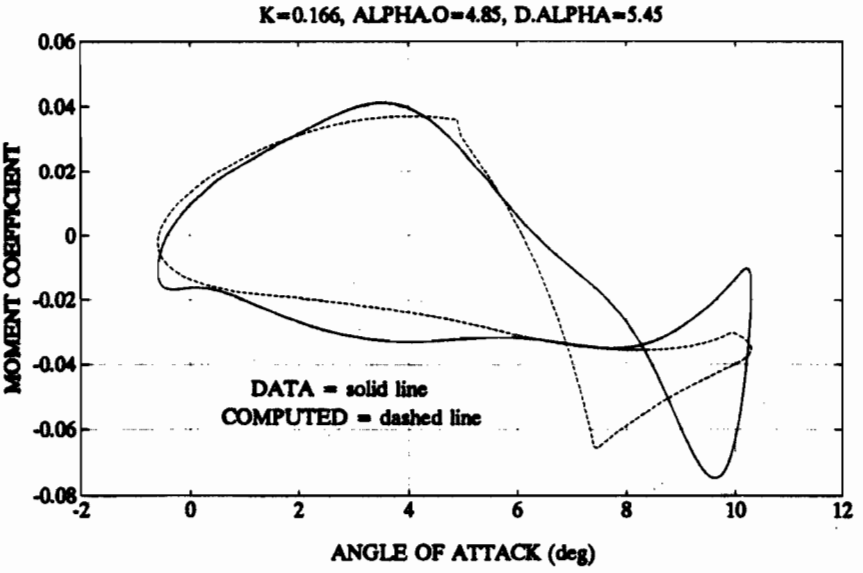
K=0.166, ALPHA.O=4.85, D.ALPHA=5.45
MOMENT COEFFICIENT
ANGLE OF ATTACK (deg)
DATA = solid line
COMPUTED = dashed line
0.06
0.04
0.02
0
-0.02
-0.04
-0.06
-0.08
-2
0
2
4
6
8
10
12

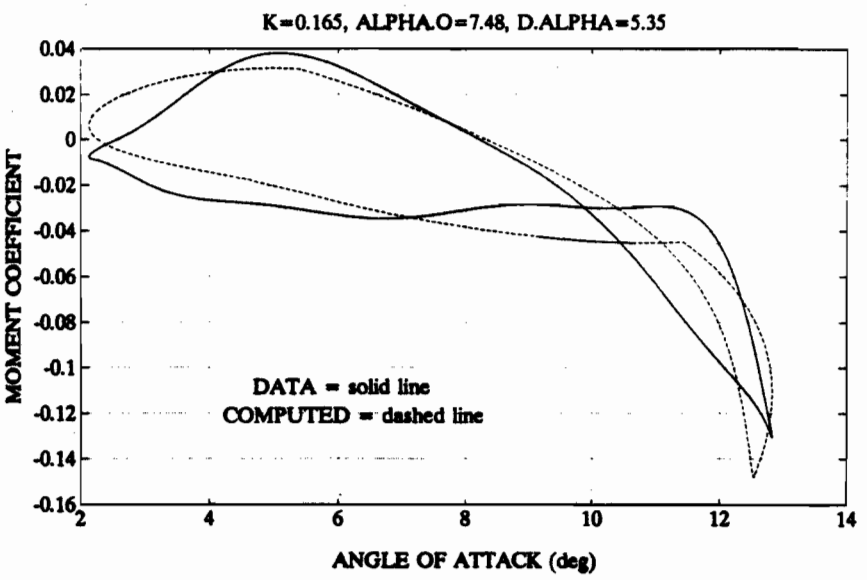
K=0.165, ALPHA.O=7.48, D.ALPHA=5.35
MOMENT COEFFICIENT
0.04
0.02
0
-0.02
-0.04
-0.06
-0.08
-0.1
-0.12
-0.14
-0.16
DATA = solid line
COMPUTED = dashed line
2
4
6
8
10
12
14
ANGLE OF ATTACK (deg)

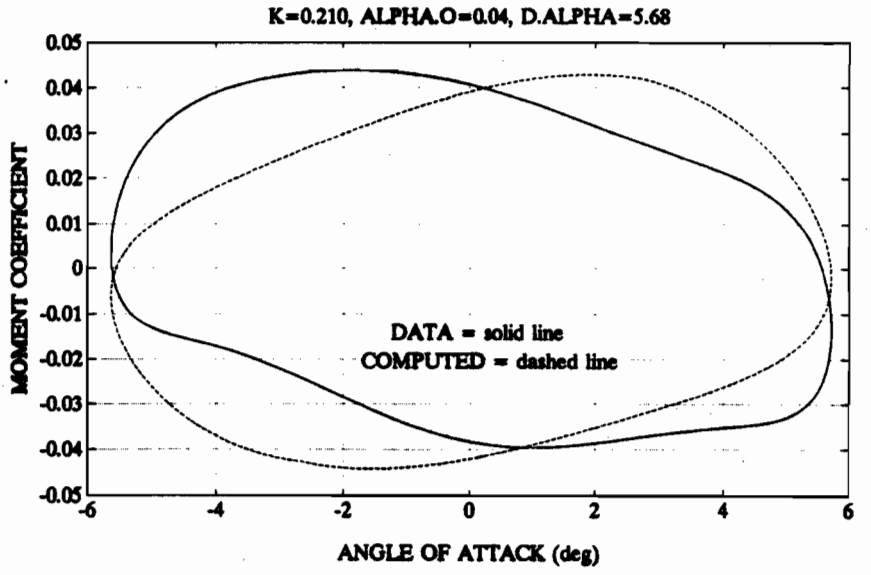
K=0.210, ALPHA.O=0.04, D.ALPHA=5.68
MOMENT COEFFICIENT
0.05
0.04
0.03
0.02
0.01
0
-0.01
-0.02
-0.03
-0.04
-0.05
DATA = solid line
COMPUTED = dashed line
-6
-4
-2
0
2
4
6
ANGLE OF ATTACK (deg)

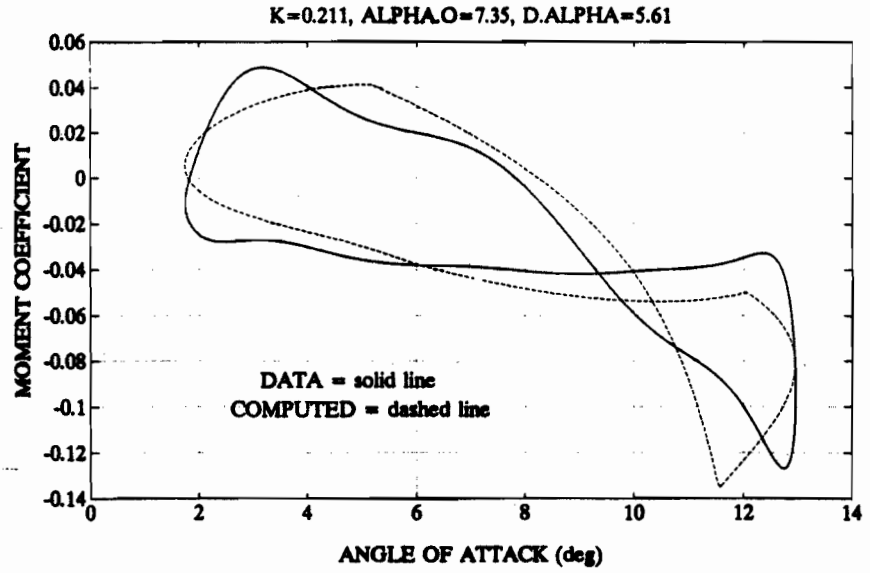
K=0.211, ALPHA.O=7.35, D.ALPHA=5.61
MOMENT COEFFICIENT
0.06
0.04
0.02
0
-0.02
-0.04
-0.06
-0.08
-0.1
-0.12
-0.14
DATA = solid line
COMPUTED = dashed line
0
2
4
6
8
10
12
14
ANGLE OF ATTACK (deg)

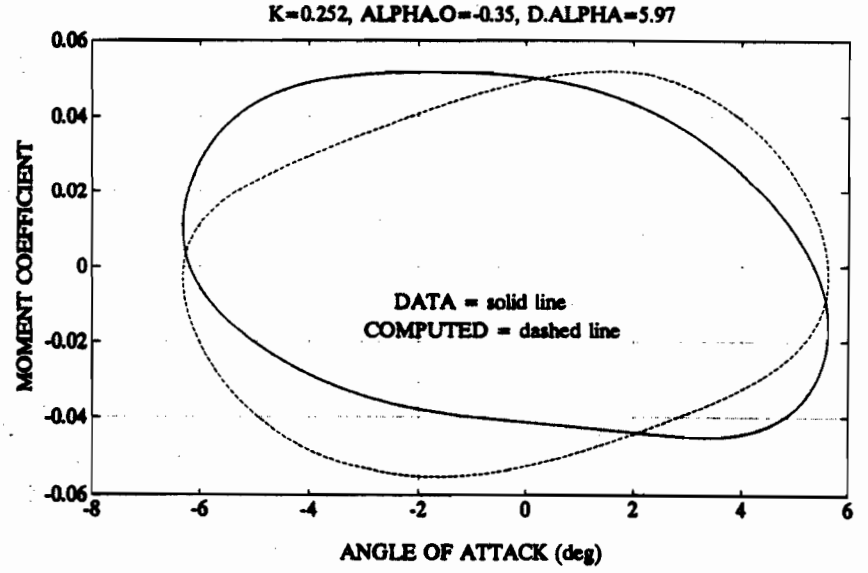
K=0.252, ALPHA.O=-0.35, D.ALPHA=5.97
MOMENT COEFFICIENT
0.06
0.04
0.02
0
-0.02
-0.04
-0.06
DATA = solid line
COMPUTED = dashed line
-8
-6
-4
-2
0
2
4
6
ANGLE OF ATTACK (deg)

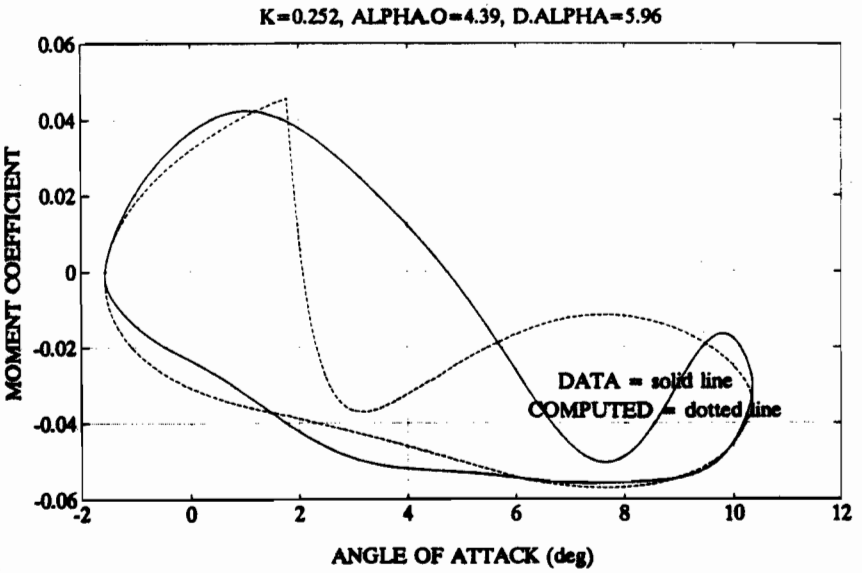
K=0.252, ALPHA.O=4.39, D.ALPHA=5.96
MOMENT COEFFICIENT
ANGLE OF ATTACK (deg)
DATA = solid line
COMPUTED = dotted line
0.06
0.04
0.02
0
-0.02
-0.04
-0.06
-2
0
2
4
6
8
10
12

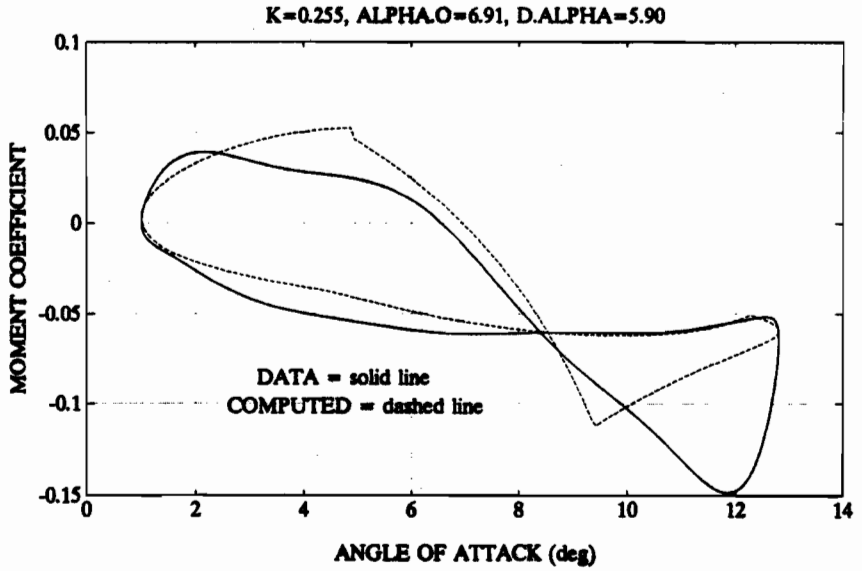
K=0.255, ALPHA.O=6.91, D.ALPHA=5.90
MOMENT COEFFICIENT
ANGLE OF ATTACK (deg)
DATA = solid line
COMPUTED = dashed line
0.1
0.05
0
-0.05
-0.1
-0.15
0
2
4
6
8
10
12
14

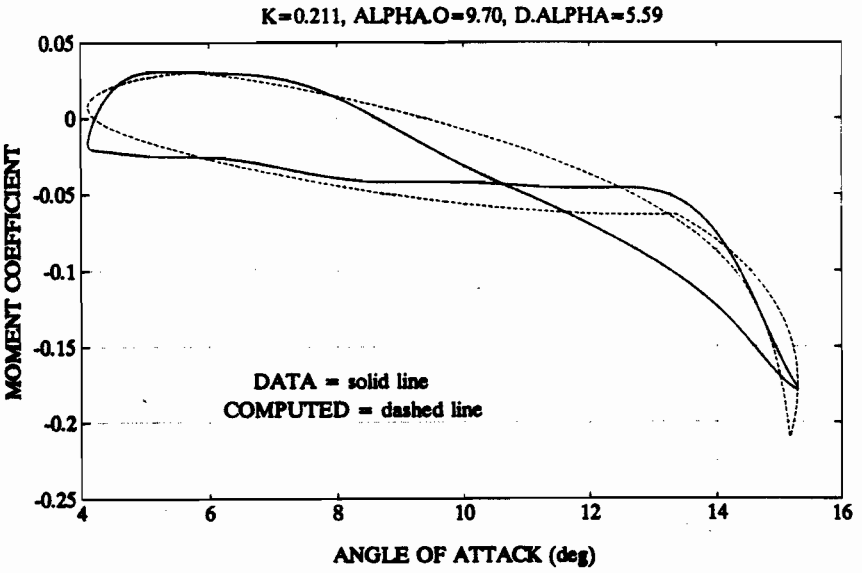
K=0.211, ALPHA.O=9.70, D.ALPHA=5.59
MOMENT COEFFICIENT
0.05
0
-0.05
-0.1
-0.15
-0.2
-0.25
DATA = solid line
COMPUTED = dashed line
4
6
8
10
12
14
16
ANGLE OF ATTACK (deg)

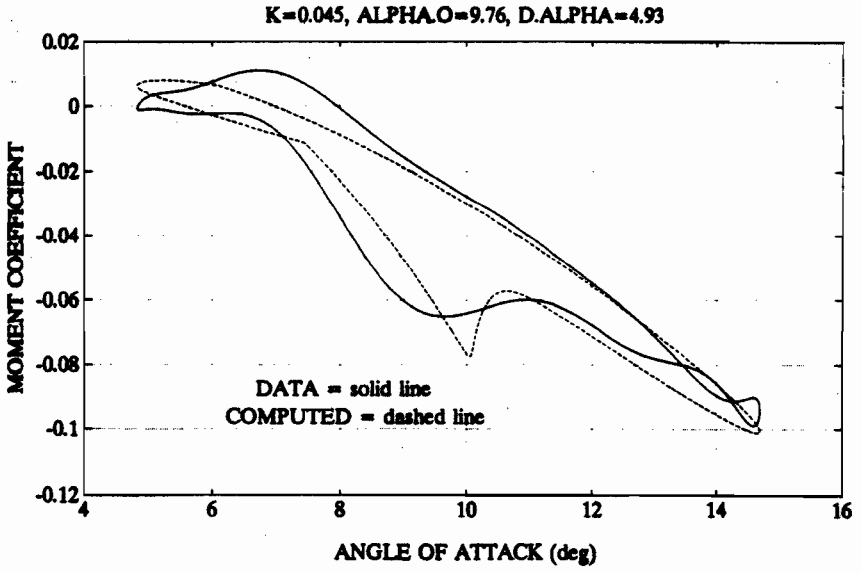
K=0.045, ALPHA.O=9.76, D.ALPHA=4.93
MOMENT COEFFICIENT
0.02
0
-0.02
-0.04
-0.06
-0.08
-0.1
-0.12
DATA = solid line
COMPUTED = dashed line
4
6
8
10
12
14
16
ANGLE OF ATTACK (deg)

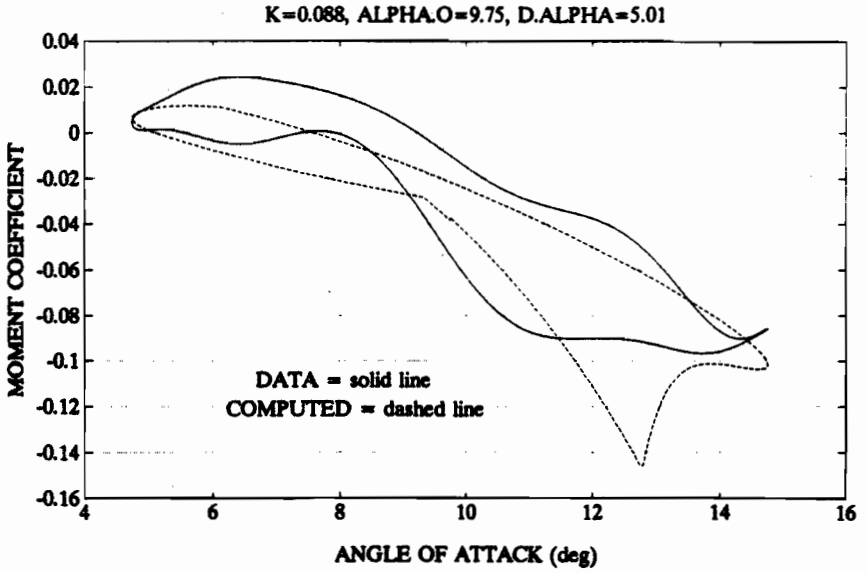
K=0.088, ALPHA.O=9.75, D.ALPHA=5.01
MOMENT COEFFICIENT
0.04
0.02
0
-0.02
-0.04
-0.06
-0.08
-0.1
-0.12
-0.14
-0.16
4
6
8
10
12
14
16
ANGLE OF ATTACK (deg)
DATA = solid line
COMPUTED = dashed line

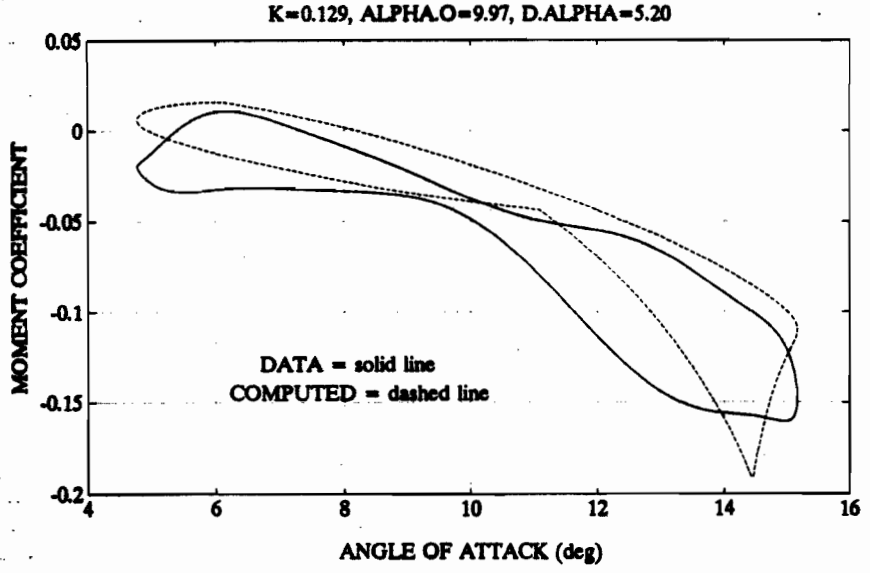
K=0.129, ALPHA.O=9.97, D.ALPHA=5.20
MOMENT COEFFICIENT
0.05
0
-0.05
-0.1
-0.15
-0.2
4
6
8
10
12
14
16
ANGLE OF ATTACK (deg)
DATA = solid line
COMPUTED = dashed line

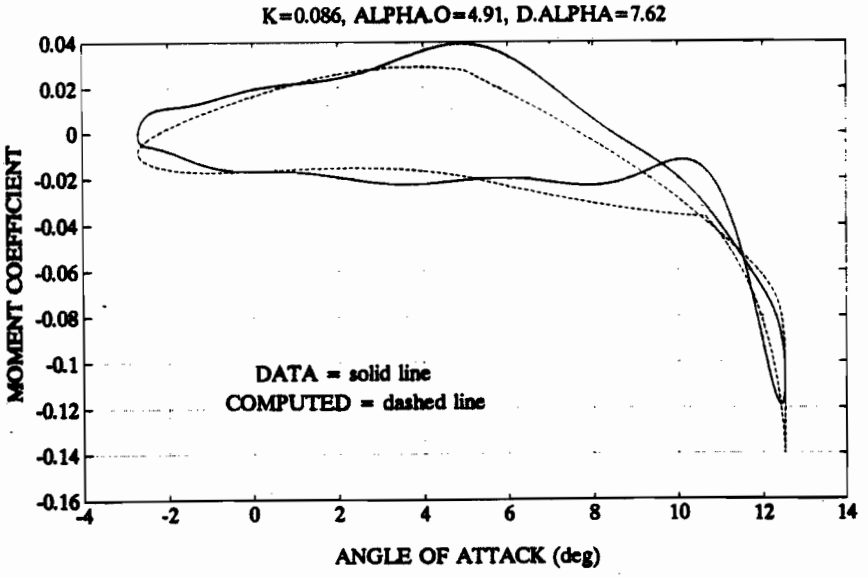
K=0.086, ALPHA.O=4.91, D.ALPHA=7.62
MOMENT COEFFICIENT
0.04
0.02
0
-0.02
-0.04
-0.06
-0.08
-0.1
-0.12
-0.14
-0.16
DATA = solid line
COMPUTED = dashed line
-4
-2
0
2
4
6
8
10
12
14
ANGLE OF ATTACK (deg)

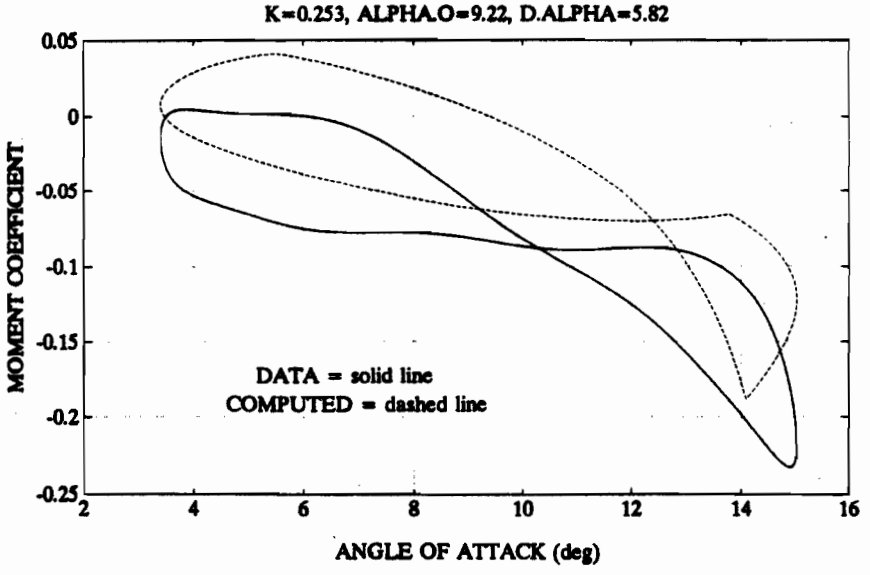
K=0.253, ALPHA.O=9.22, D.ALPHA=5.82
MOMENT COEFFICIENT
0.05
0
-0.05
-0.1
-0.15
-0.2
-0.25
DATA = solid line
COMPUTED = dashed line
2
4
6
8
10
12
14
16
ANGLE OF ATTACK (deg)

Appendix C

Coefficients for the Recursive Matrix

The complete equations for α_n and ξ_n, from equation (2.29) are:

$$\alpha_n = [Z_6 - \frac{Z_3 Z_4}{Z_1}][Z_5 - \frac{Z_2 Z_4}{Z_1}]^{-1} \tag{C.1}$$

$$\xi_n = \frac{1}{Z_1}(Z_3 - Z_2[Z_6 - \frac{Z_3 Z_4}{Z_1}][Z_5 - \frac{Z_2 Z_4}{Z_1}]^{-1}) \tag{C.2}$$

where the following definitions apply:

$$Z_1 = \frac{2}{\epsilon^2}\frac{a_1}{a_5} \tag{C.3}$$

$$Z_2 = \frac{2}{\epsilon^2} + \frac{11}{6\epsilon}\frac{a_6}{a_5} + \frac{a_7}{a_5} \tag{C.4}$$

$$\begin{aligned} Z_3 = C_{M_n}(\frac{a_8}{a_5}) + Q_n(\frac{1}{a_5}) + \alpha_{n-1}(\frac{5}{\epsilon^2} + \frac{3}{\epsilon}\frac{a_6}{a_5}) - \alpha_{n-2}(\frac{4}{\epsilon^2} + \frac{3}{2\epsilon}\frac{a_6}{a_5}) + \\ \alpha_{n-3}(\frac{1}{\epsilon^2} + \frac{1}{3\epsilon}\frac{a_6}{a_5}) + \xi_{n-1}(\frac{5}{\epsilon^2}\frac{a_1}{a_5}) - \xi_{n-2}(\frac{4}{\epsilon^2}\frac{a_1}{a_5}) + \xi_{n-3}(\frac{1}{\epsilon^2}\frac{a_1}{a_5}) \end{aligned} \tag{C.5}$$

$$Z_4 = \frac{2}{\epsilon^2} + \frac{11}{6\epsilon}a_2 + a_3 \tag{C.6}$$

$$Z_5 = \frac{2}{\epsilon^2}a_1 \tag{C.7}$$

$$Z_6 = C_{N_n}(a_4) + P_n + \alpha_{n-1}(\frac{5}{\epsilon^2}a_1) - \alpha_{n-2}(\frac{4}{\epsilon^2}a_1) + \alpha_{n-3}(\frac{a_1}{\epsilon^2}) +$$

$$\xi_{n-1}(\frac{5}{\epsilon^2} + \frac{3}{\epsilon}a_2) - \xi_{n-2}(\frac{4}{\epsilon^2} + \frac{3}{2\epsilon}a_2) + \xi_{n-3}(\frac{1}{\epsilon^2} + \frac{1}{\epsilon}a_2) \tag{C.8}$$

where ϵ is the constant time step size and the coefficients, $a_1 \ldots a_8$ are the coefficients of equations (2.25) and (2.26). These coefficients are given below:

$$a_1 = x_\alpha \tag{C.9}$$

$$a_2 = 2\zeta_\xi \frac{\bar{\omega}}{(U^*)} \tag{C.10}$$

$$a_3 = \frac{\bar{\omega}^2}{(U^*)^2} \tag{C.11}$$

$$a_4 = -\frac{1}{\pi\mu} \tag{C.12}$$

$$a_5 = r_\alpha^2 \tag{C.13}$$

$$a_6 = \frac{2r_\alpha^2\zeta_\alpha}{U^*} \tag{C.14}$$

$$a_7 = \frac{r_\alpha^2}{(U^*)^2} \tag{C.15}$$

$$a_8 = \frac{2}{\pi\mu} \tag{C.16}$$

Appendix C

Coefficients for the Recursive Matrix

The complete equations for α_n and ξ_n, from equation (2.29) are:

$$\alpha_n = \quad {}_5 - \frac{Z_2 Z_4}{Z_1}]^{-1} \tag{C.1}$$

$$\xi_n = \quad \frac{Z_4}{Z_1}][Z_5 - \frac{Z_2 Z_4}{Z_1}]^{-1}) \tag{C.2}$$

where the following

$$Z_1 = \frac{2}{\epsilon^2}\frac{a_1}{a_5} \tag{C.3}$$

$$Z_2 = \frac{2}{\epsilon^2} + \frac{11}{6\epsilon}\frac{a_6}{a_5} + \frac{a_7}{a_5} \tag{C.4}$$

$$Z_3 = C_{M_n}(\frac{a_8}{a_5}) + Q_n(\frac{1}{a_5}) + \alpha_{n-1}(\frac{5}{\epsilon^2} + \frac{3}{\epsilon}\frac{a_6}{a_5}) - \alpha_{n-2}(\frac{4}{\epsilon^2} + \frac{3}{2\epsilon}\frac{a_6}{a_5}) +$$
$$\alpha_{n-3}(\frac{1}{\epsilon^2} + \frac{1}{3\epsilon}\frac{a_6}{a_5}) + \xi_{n-1}(\frac{5}{\epsilon^2}\frac{a_1}{a_5}) - \xi_{n-2}(\frac{4}{\epsilon^2}\frac{a_1}{a_5}) + \xi_{n-3}(\frac{1}{\epsilon^2}\frac{a_1}{a_5}) \tag{C.5}$$